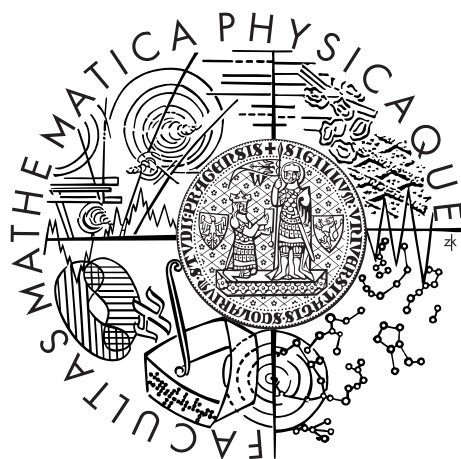


Charles University
Faculty of Mathematics and Physics
Department of Chemical Physics and Optics

HABILITATION THESIS



LUCIE D. AUGUSTOVIČOVÁ

QUANTUM DYNAMICS OF SMALL MOLECULAR SYSTEMS
FROM DIATOMICS TO POLYATOMICS

Prague 2020

ACKNOWLEDGMENTS

At the first place, I address my deepest thanks to my husband, and my whole family for their understanding and endless love, their support and patience during my years of research.

I am also grateful to all my colleagues and students I worked with at Charles University in Prague, at Czech Academy of Sciences, at Max-Planck-Institute of Astrophysics MPG in Garching, Germany, at JILA, National Institute of Standards and Technology and at University of Colorado in the USA.

I thank my colleague and former advisor Pavel Soldán for bringing me to the vast and interesting field of atomic and molecular physics in which I met wonderful collaborators and friends, especially Vladimír Špirko, Wolfgang P. Kraemer, people from group of Juraj Glosík and foremost John L. Bohn with whom I could spend two splendid years in Boulder and whom I am still regularly visiting as well as my beloved adoptive family.

My work was financially supported by the Grant Agency of the Czech Republic, the Grant Agency of the Charles University, the US National Science Foundation, the US Army Research Office, and by the JILA NSF Physics Frontier Center as acknowledged in the published papers.

LIST OF PUBLICATIONS

PUBLICATIONS IN SCIENTIFIC JOURNALS WITH IF

- Augustovičová, L. D. and J. L. Bohn (2017). “No evaporative cooling of nitric oxide in its ground state.” In: *Physical Review A* 96, p. 042712.
DOI: [10.1103/PhysRevA.96.042712](https://doi.org/10.1103/PhysRevA.96.042712).
- Augustovičová, L. D. and J. L. Bohn (2018a). “Manifestation of quantum chaos in Fano-Feshbach resonances.” In: *Physical Review A* 98, p. 023419.
DOI: [10.1103/PhysRevA.98.023419](https://doi.org/10.1103/PhysRevA.98.023419).
- Augustovičová, L. D. and J. L. Bohn (2018b). “NO evaporative cooling in the $^2\Pi_{3/2}$ state.” In: *Physical Review A* 97, p. 062703.
DOI: [10.1103/PhysRevA.97.062703](https://doi.org/10.1103/PhysRevA.97.062703).
- Augustovičová, L. D. and J. L. Bohn (2019). “Ultracold collisions of polyatomic molecules: CaOH.” In: *New Journal of Physics* 21.10, p. 103022.
DOI: [10.1088/1367-2630/ab4720](https://doi.org/10.1088/1367-2630/ab4720).
- Augustovičová, L. D. and J. L. Bohn (2020). “Ultracold collisions of the lithium monoxide radical.” In: submitted.
- Augustovičová, L., W. P. Kraemer, and P. Soldán (2014a). “Depopulation of metastable helium by radiative association with hydrogen and lithium ions.” In: *The Astrophysical Journal* 782, 46.
DOI: [10.1088/0004-637X/782/1/46](https://doi.org/10.1088/0004-637X/782/1/46).
- Augustovičová, L., W. P. Kraemer, and P. Soldán (2014b). “Depopulation of metastable helium He(2^1S) by radiative association with hydrogen and lithium cations.” In: *Journal of Quantitative Spectroscopy and Radiative Transfer*, 148, pp. 27–37.
DOI: [10.1016/j.jqsrt.2014.06.012](https://doi.org/10.1016/j.jqsrt.2014.06.012).
- Augustovičová, L., W. P. Kraemer, V. Špirko, and P. Soldán (2015a). “The role of molecular quadrupole transitions in the depopulation of metastable helium.” In: *Monthly Notices of the Royal Astronomical Society* 446, pp. 2738–2743.
DOI: [10.1093/mnras/stu2317](https://doi.org/10.1093/mnras/stu2317).
- Augustovičová, L. and P. Soldán (2012). “Ab initio properties of MgAlk (Alk = Li, Na, K, Rb, Cs).” In: *Journal of Chemical Physics* 136, 084311.
DOI: [10.1063/1.3690459](https://doi.org/10.1063/1.3690459).
- Augustovičová, L., P. Soldán, W. P. Kraemer, and V. Špirko (2014c). “Potential microwave probes of the proton-to-electron mass ratio

- at very high redshifts." In: *Monthly Notices of the Royal Astronomical Society* 439, pp. 1136–1139.
DOI: [10.1093/mnras/stu060](https://doi.org/10.1093/mnras/stu060).
- Augustovičová, L., P. Soldán, W. P. Kraemer, and V. Špirko (2014d).
"Potential microwave probes of the proton-to-electron mass ratio at very high redshifts (supplementary material)." In: *Monthly Notices of the Royal Astronomical Society*, pp. 1–8.
DOI: [10.1093/mnras/stu060](https://doi.org/10.1093/mnras/stu060).
- Augustovičová, L., P. Soldán, and V. Špirko (2016). "Effective hyperfine structure functions of ammonia." In: *The Astrophysical Journal* 824, p. 147.
DOI: [10.3847/0004-637x/824/2/147](https://doi.org/10.3847/0004-637x/824/2/147).
- Augustovičová, L., V. Špirko, W. P. Kraemer, and P. Soldán (2012a).
"Radiative association of LiHe⁺." In: *Chemical Physics Letters* 531, pp. 59–63.
DOI: [10.1016/j.cplett.2012.02.038](https://doi.org/10.1016/j.cplett.2012.02.038).
- Augustovičová, L., V. Špirko, W. P. Kraemer, and P. Soldán (2013a).
"Radiative association of He₂⁺ revisited." In: *Astronomy & Astrophysics* 553, A42.
DOI: [10.1088/0004-637X/749/1/22](https://doi.org/10.1088/0004-637X/749/1/22).
- Augustovičová, L., V. Špirko, W. P. Kraemer, and P. Soldán (2013b).
"Radiative association of He₂⁺: the role of quartet states." In: *Monthly Notices of the Royal Astronomical Society* 435, pp. 1541–1546.
DOI: [10.1093/mnras/stt1395](https://doi.org/10.1093/mnras/stt1395).
- Augustovičová, L. D. and V. Špirko (2020a). "Morphing radial molecular property functions of hydroxyl." In: submitted.
- Augustovičová, L. D. and V. Špirko (2020b). "Zeeman molecular probe for tests of fundamental physical constants." In: *Monthly Notices of the Royal Astronomical Society* 494.2, pp. 1675–1680.
DOI: [10.1093/mnras/staa792](https://doi.org/10.1093/mnras/staa792).
- Augustovičová, L., M. Zámečnicková, W. P. Kraemer, and P. Soldán (2015b). "Radiative association of He(2³P) with lithium cations." In: *Chemical Physics* 462. Inelastic Processes in Atomic, Molecular and Chemical Physics, pp. 65–70.
DOI: [10.1016/j.chemphys.2015.07.003](https://doi.org/10.1016/j.chemphys.2015.07.003).
- Belyaev, A. K., L. Augustovičová, P. Soldán, and W. P. Kraemer (2014).
"Non-radiative inelastic processes in lithium-helium ion-atom collisions." In: *Astronomy & Astrophysics* 565, A106.
DOI: [10.1051/0004-6361/201423578](https://doi.org/10.1051/0004-6361/201423578).
- Belyaev, A. K., D. S. Rodionov, L. Augustovičová, P. Soldán, and W. P. Kraemer (2015). "Full quantum study of non-radiative inelastic processes in lithium-helium ion-atom collisions." In: *Monthly Notices of the Royal Astronomical Society* 449, pp. 3323–3332.
DOI: [10.1093/mnras/stv391](https://doi.org/10.1093/mnras/stv391).

Glosík, J., P. Dohnal, Á. Kálosi, L. D. Augustovičová, D. Shapko, Š. Roučka, and R. Plašil (2017). "Electron-ion recombination in low temperature hydrogen/deuterium plasma." In: *The European Physical Journal Applied Physics* 80, p. 30801.

DOI: [10.1051/epjap/2017170228](https://doi.org/10.1051/epjap/2017170228).

Kálosi, Á., P. Dohnal, L. Augustovičová, Š. Roučka, R. Plašil, and J. Glosík (2016). "Monitoring the removal of excited particles in He/Ar/H₂ low temperature afterglow plasma at 80-300 K." In: *The European Physical Journal Applied Physics* 75, p. 24707.

DOI: [10.1051/epjap/2016150587](https://doi.org/10.1051/epjap/2016150587).

Shapko, D., P. Dohnal, M. Kassayová, Á. Kálosi, S. Rednyk, Š. Roučka, R. Plašil, L. D. Augustovičová, et al. (2020). "Dissociative recombination of N₂H⁺ ions with electrons in the temperature range of 80–350 K." In: *The Journal of Chemical Physics* 152.2, p. 024301.

DOI: [10.1063/1.5128330](https://doi.org/10.1063/1.5128330).

OTHER PEER-REVIEW PUBLICATIONS

(REGISTERED IN THE WOS/ISI DATABASE)

Zámečníková, M., L. Augustovičová, W. P. Kraemer, and P. Soldán (2015). "Formation of molecular ion LiHe⁺ by radiative association of metastable helium He(2³P) with lithium ions." In: *Journal of Physics: Conference Series* 635, p. 022038.

DOI: [10.1088/1742-6596/635/2/022038](https://doi.org/10.1088/1742-6596/635/2/022038).

CONTENTS

SUMMARY OF NOTATION	8
PREFACE	10
Overview of selected topics in my research	11
1 RADIATIVE PROCESSES IN ASTROCHEMISTRY	12
1.1 Methodology	14
1.2 Summary of results in the attached papers	18
2 SPECTRAL PROBES OF POSSIBLE VARIABILITY OF FUNDAMENTAL CONSTANTS	26
2.1 Results for selected systems	29
3 TOWARD ABSOLUTE ZERO TEMPERATURE	36
3.1 Results of ultracold dipolar molecular collisions	37
4 QUANTUM CHAOS EMERGING FROM COLLISIONS OF COLD MAGNETIC ATOMS	45
5 CONCLUDING REMARKS	51
A MOLECULAR DESCRIPTION AND THEORY DETAILS: OH	53
A.1 Molecular Hamiltonian in the absence of field	53
A.2 Zeeman Hamiltonian	55
A.3 Estimations of transition intensities	56
BIBLIOGRAPHY	57
Attached Publications	75
Depopulation of metastable helium by radiative association with hydrogen and lithium ions (Augustovicova, 2014)	76
Depopulation of metastable helium He(2^1S) by radiative association with hydrogen and lithium cations (Augustovicova, 2014)	84
The role of molecular quadrupole transitions in the depopulation of metastable helium (Augustovicova, 2015)	96
Radiative association of He(2^3P) with lithium cations (Augustovicova, 2015)	103
Non-radiative inelastic processes in lithium-helium ion-atom collisions (Belyaev, 2014)	110
Full quantum study of non-radiative inelastic processes in lithium-helium ion-atom collisions (Belyaev, 2015)	116

- Potential microwave probes of the proton-to-electron mass ratio at very high redshifts (Augustovicova, 2014) [127](#)
- Potential microwave probes of the proton-to-electron mass ratio at very high redshifts (supplementary material) (Augustovicova, 2014) [132](#)
- Effective hyperfine structure functions of ammonia (Augustovicova, 2016) [141](#)
- No evaporative cooling of nitric oxide in its ground state (Augustovicova, 2017) [149](#)
- NO evaporative cooling in the $^2\Pi_{3/2}$ state (Augustovicova, 2018) [156](#)
- Manifestation of quantum chaos in Fano-Feshbach resonances (Augustovicova, 2018) [164](#)
- Ultracold collisions of polyatomic molecules: CaOH (Augustovicova, 2019) [172](#)
- Zeeman molecular probe for tests of fundamental physical constants (Augustovicova, 2020) [185](#)

SUMMARY OF NOTATION

Scalar quantities and variables, and symbols for constants are written in upright glyphs (Latin or Greek), as a, b, c, π . Vector quantities are printed in boldface as $\mathbf{L}, \mathbf{S}, \mathbf{J}$ and their quantum numbers are denoted by the same letters in upright glyphs: L, S, J . The meanings of some common symbols used throughout the text are listed below. More specific quantities are explained directly in the text. Prime or double prime is used to distinguish the upper (') and lower (") levels in a transition. They occur as superscripts on the quantum numbers. The subscripts g or u indicate the molecular states associated with the gerade (even) or ungerade (odd) symmetry, respectively.

v	vibrational quantum number
E	energy
\mathbf{L}	orbital angular momentum
\mathbf{S}	electron spin angular momentum
\mathbf{J}	total angular momentum excluding nuclear spin
\mathbf{N}	total angular momentum excluding electron and nuclear spin, in the case where electron spin is present
\mathbf{I}	nuclear spin angular momentum
\mathbf{F}	total angular momentum including electron and nuclear spin
Λ	projection of \mathbf{L} along internuclear axis (body-fixed projection)
Σ	projection of \mathbf{S} along internuclear axis (body-fixed projection)
$\Omega = \Lambda + \Sigma$	projection of total electronic angular momentum along internuclear axis
M	projection of \mathbf{J} on the space-fixed quantization axis
k	projection of \mathbf{J} along the intermolecular z -axis
K	unsigned projection quantum number $K = k $
Σ, Π, Δ	electronic state designation for which $ \Lambda = 0, 1, 2$, respectively
(ϕ, θ, γ)	Euler angles
k_B	Boltzmann constant
R	internuclear distance
R_e	equilibrium internuclear distance
$U(R)$	potential energy curve

ϵ_0	permittivity of vacuum
μ_0	permeability of vacuum
c	speed of light in vacuum
T	temperature
μ	reduced mass

The formulas presented in this thesis are reported in SI units unless explicitly noted otherwise; the exceptions to this rule are spectroscopic properties and characteristics (such as distances, e.g.), which are normally reported in atomic units (a.u.). Energies are here most frequently reported in K, cm^{-1} or in eV. In the atomic units system, four frequently used quantities (Planck's constant \hbar divided by 2π [\hbar], elementary charge [e], electron mass [m_e], and inverse Coulomb's constant [$4\pi\epsilon_0$]) are all unity by definition, making formulas more simple to read. The atomic unit of length is the *bohr*

$$a_0 = \frac{4\pi\epsilon_0\hbar^2}{m_e e^2},$$

where $a_0 \approx 0.529\,177\,210\,92(17) \times 10^{-10}\text{m}$.

The atomic unit of energy is the *hartree*

$$E_h = \frac{e^2}{4\pi\epsilon_0 a_0},$$

and it has the value $E_h \approx 4.359\,744\,722\,2071(85) \times 10^{-18}\text{J}$, or $E_h/(hc) \approx 2.194\,746\,313\,6320(43) \times 10^5\text{cm}^{-1}$. Units for other quantities can be readily worked out from these basic few.

PREFACE

The main scientific results of the research that I carried out in the years 2014–2020 are written up in this habilitation thesis. This is mirrored in the selected publications that can be found in the attachment to this thesis. The covered topics encompass broad field of molecular physics of small systems, ranging from radiative and non-radiative processes in early Universe, stellar environments and interstellar medium, through quantum studies on possible cosmological variation of fundamental constants to physics of ultracold molecules and quantum chaos. Therefore, the main part of this thesis is divided into four fundamental chapters according to their focus. The purpose of this work is to briefly describe the current state and summarize the author's contributions to these issues.

This thesis is organized as follows: it consists of two parts, the topical overview of my research followed by the attached scientific papers, available only in the printed version.

Chapter 1 gives an introduction to radiative processes and discusses its importance for astrochemistry together with a review of relevant literature. This is followed by a theoretical description of the transition processes forming molecular ions or deexcitation of collisional partners, and a summary of main results and findings.

In Chapter 2 the critical exploration of the possibility that the fundamental constants of nature may depend on time and space in the evolving Universe is considered. The possibility of using spectra of light homonuclear molecular ions, ammonia isotopomers or diatomic hydride radicals as potential probes of the variations of the proton-to-electron mass ratio is investigated.

Chapter 3 focuses on the possibility of cooling polar molecules to nanoKelvin temperature range. The ultracold collisions of several molecular systems are investigated with emphasis on the influence of external electric or magnetic field on elastic or inelastic collisional rates.

Chapter 4 summarizes the results on the emergence of quantum chaos in collisions of ultracold magnetic lanthanide atoms. In this systems quantum chaos is manifested in Fano-Feshbach resonances due to dense distribution of levels near the dissociation threshold of the formed dimer.

A summary of the main results and findings of this thesis as well as conclusion and outlook can be found in Chapter 5.

All relevant papers, published in peer-reviewed international scientific journals with impact factor, of which I am the main author or a coauthor are attached in the appendices.

OVERVIEW OF SELECTED TOPICS IN MY
RESEARCH

RADIATIVE PROCESSES IN ASTROCHEMISTRY

The first chapter is dedicated to the study of quantum dynamics of radiative processes in molecules and molecular ions with astrophysical importance. Such processes include spontaneous emission, emission and absorption stimulated by black-body radiation, and radiative association. All these processes have to be taken into account when studying wide range of phenomena from the past and present, e.g. the physical and chemical processes involved in the formation and evolution of interstellar molecules (Tielens, 2013). Of particular importance is the formation of the first molecules in the Universe (Lepp et al., 2002). The computational approach developed for calculation of radiative processes in molecules is useful even for the search for the possible space-time variations of fundamental constants (Augustovičová et al., 2014c) as will be demonstrated in Chapter 2.

One important avenue of research is focused on the growth of molecular complexity in the early Universe, when after the period of fast initial expansion a decrease in number densities and temperature occurred, ending nucleosynthesis. During the recombination epoch, the neutral atoms He, H and D and singly charged ions He^+ and Li^+ were produced in collisions of H^+ , D^+ , He^{2+} and Li^{3+} with electrons. With the formation of the very first neutral atom – helium – the creation of the first molecular ions (HeH^+ and then H_2^+ (Lepp et al., 2002)) could proceed via spontaneous radiative association process (and at the same time be enhanced due to a stimulating background radiation field). It is interesting to note that, although HeH^+ was a cornerstone of early Universe chemistry, it was detected only recently (Güsten et al., 2019) in planetary nebula NGC 7027. The subsequent formation of the neutral H_2 molecule (via charge transfer reaction of H_2^+ with H (Lepp et al., 2002) and at later times through associative detachment reaction of H^- with H (Kreckel et al., 2010; Gerlich et al., 2012)) led to cooling of primordial clouds allowing them to collapse. Thus the radiative association stands at the beginning of the chain of processes leading to the formation of the first structures in the early Universe. Hydrogen and helium containing diatomic ions H_2^+ , HeH^+ and He_2^+ are assumed to be present in significant abundances in the atmospheres of white dwarf stars, either in the helium-rich ones or in the more numerous hydrogen-dominated DA-type stars, respectively (Koester and Chanmugam, 1990).

In addition to cooling, radiation due to spontaneous depopulation has important astrophysical implications, as metastable atomic states are considered to provide most of the light emitted from planetary nebulae. The measured intensities of the relevant radiation lines can yield information on temperatures, densities and chemical compositions in these environments.

Helium is an important atomic species for primordial chemistry with cosmic abundance second only to hydrogen. Its metastable triplet state He 2^3S with electronic configuration $1s2s$ (19.75 eV above the helium ground state) has an extremely long lifetime - about two hours (Drake, 1971; Hodgman et al., 2009) because the direct radiative transition to the ground state is doubly forbidden by quantum mechanical selection rules. The relatively large amount of helium in interstellar space, led the author and her co-workers to study the depopulation of the metastable levels (both singlet and triplet) of He by radiative collisions with hydrogen, helium and lithium ions - i.e. species present in abundance in early Universe. These collisions result in the formation of molecular cations, either in high-spin or low-spin electronic state through the process of radiative association.

Radiative association reaction proceeds through collision of two smaller species that can remain close together for a considerable time and form an unstable collisional complex even on the excited state potentials. The barrier that holds the two species (either ion-atom pairs or reactive neutrals) together is most commonly caused by centrifugal potential, but there are many adiabatic potential curves which exhibit barriers even for zero angular momentum. Stabilization of the complex against redissociation is finally ensured by radiative transition to bound levels of the ground or other lower-lying electronic state.

Studies of collisional complexes on different excitation levels can provide reaction rates crucial for the primordial and interstellar chemistry, especially when the efficiencies of radiative processes at different temperatures are compared. Due to the difficulty of corresponding laboratory experiments (Gerlich and Horning, 1992), most of the cross sections and rate coefficients for radiative association processes must be obtained by theoretical methods, although in recent years there was a promising development in experimental techniques for radiative association rate coefficient determination (Beyer and Merkt, 2018).

Radiative association was proposed as an effective formation mechanism in the interstellar medium already in the early forties (Swings, 1942). Bates (Bates and Spitzer, 1951; Bates, 1951) derived a semi-classical formula for the cross sections based on the unrestricted transition rate and calculated the rate coefficients for radiative association of CH, CH⁺, N₂⁺ and H₂⁺.

Building on the results of these pioneering studies were groups of Dalgarno (e. g. Stancil et al., 1993; Babb and Dalgarno, 1995; Dalgarno

et al., 1996; Zygelman et al., 1998), Dickinson (e. g. Bennett et al., 2003; Dickinson, 2005), Gianturco (e. g. Gianturco and Giorgi, 1996; Gianturco and Giorgi, 1997; Bovino et al., 2011), Talbi (e. g. Bacchus-Montabonel and Talbi, 1999; Talbi and Bacchus-Montabonel, 2007), Kraemer and Špirko (e. g. Juřek et al., 1995; Mrugała et al., 2003; Mrugała and Kraemer, 2005) and others who performed thorough investigations on radiative association of various species.

My theoretical work focused on simple interacting systems such as $\text{He} + \text{H}^+$, $\text{He} + \text{He}^+$, $\text{Li}^+ + \text{He}$, $\text{Li} + \text{He}^+$, and similar. The choice of considered systems was governed mainly by the importance of the corresponding reactions for astrophysics and chemistry of the early Universe.

I and my collaborators have published a number of detailed studies of spontaneous and stimulated radiative association of molecular ions HeH^+ , LiHe^+ , and He_2^+ (Augustovičová et al., 2012; Augustovičová et al., 2013a; Augustovičová et al., 2013b; Augustovičová et al., 2014a; Augustovičová et al., 2014b; Augustovičová et al., 2015a; Augustovičová et al., 2015b; Zámečníková et al., 2015). The theoretical framework will be introduced further followed by a section giving a description and discussion of selected results.

1.1 METHODOLOGY

Disclaimer: This section may contain similarities with my dissertation thesis (Augustovičová, 2014). Text coincidence in definitions, formulas, *termini technici*, methods, or references to earlier works in this field is hard to avoid.

Continuous-bound transitions

The reactive processes occurring in ion-atom collisions include two possibilities: Either a (positive) charge is transferred from an ion to an atom (or molecule), the respective reaction is referred to as a charge transfer reaction, or the reaction results in molecule/molecular ion formation in the radiative association process. The energy conservation is maintained by a transition accompanied by the emission of a photon of energy.

In quantum mechanics, the total cross sections $\sigma(E; T_b)$ for radiative association of a diatomic bound species in the field of black-body radiation (characterized by temperature T_b) can be expressed as a sum of the partial cross sections over allowed transitions between a continuum state with a positive energy E and orbital angular momentum J' to bound ro-vibrational states (labeled by vibrational quantum number v'' and orbital angular momentum J'') (Zygelman and Dalgarno, 1990). Each of such contributions corresponds to a

radiative-association cross section from the channel E, J' towards the level ν'', J'' being expressed as (Stancil and Dalgarno, 1997)

$$\sigma_{J';\nu'',J''}^{\text{dip.}}(E; T_b) = \frac{1}{4\pi\epsilon_0} \frac{64}{3} \frac{\pi^5}{c^3 k^2} p \nu_{E;\nu'',J''}^3 \mathcal{S}_{J',J''}^{\text{dip.}} M_{E,J';\nu'',J''}^2 \times \left[\frac{1}{1 - \exp[-h\nu_{E;\nu'',J''}/(k_B T_b)]} \right] \quad (1)$$

for transitions driven by dipole moment and

$$\sigma_{J';\nu'',J''}^{\text{quad.}}(E; T_b) = \frac{1}{4\pi\epsilon_0} \frac{32}{5} \frac{\pi^7}{c^5 k^2} p \nu_{E;\nu'',J''}^5 \mathcal{S}_{J',J''}^{\text{quad.}} M_{E,J';\nu'',J''}^2 \times \left[\frac{1}{1 - \exp[-h\nu_{E;\nu'',J''}/(k_B T_b)]} \right] \quad (2)$$

for transitions driven by quadrupole moment.

The variables in this formula represent: c the speed of light in vacuum, the wave number k of the scattered particle is related to the relative energy E by $k^2 = 2\mu E/\hbar^2$, μ is the reduced mass of the molecular species, p is the probability in the input channel, $\nu_{E;\nu'',J''}$ the emitted photon frequency, $h\nu_{E;\nu'',J''} = E + \Delta E - E_{\nu'',J''}$, where ΔE is the difference in energies of the initial collision partners in an infinity distance and of the dissociation products of the final electronic states, and

$$M_{E,J';\nu'',J''} = \int_0^\infty \chi_{J'}(E, R) T_{|\sigma|}^\kappa(R) \psi_{\nu'',J''}(R) dR \quad (3)$$

is the transition matrix element of the irreducible spherical tensor operator $T_{|\sigma|}^\kappa$ of rank κ , $\sigma = -\kappa, \dots, \kappa$, (the dipole moment operator μ_m has rank 1; $\sigma = 0$ for the $\Sigma - \Sigma$ transitions and $\sigma = \pm 1$ for the $\Pi - \Sigma$ transitions, the quadrupole moment Q_m has rank 2; $\sigma = 0$ for the $\Sigma - \Sigma$ transitions considered here) between the initial continuum energy-normalized radial wave function $\chi_{J'}(E, R)$ for the partial wave J' and the final \mathcal{L}^2 -normalized bound-state radial wave function $\psi_{\nu'',J''}(R)$. The wave functions $\chi_{J'}(E, R)$ and $\psi_{\nu'',J''}(R)$ were calculated by numerical integration of the corresponding radial Schrödinger equations using the Numerov-Cooley method (Numerov, 1923; Cooley, 1961).

Finally, $\mathcal{S}_{J',J''}$ are the rotational line strength factors (so-called Hönl-London coefficient) for a dipole/quadrupole transition governed by the rotational selection rules for $\Delta J = J' - J''$. They were derived and reported in Augustovičová, 2011 for the nine and fifteen possible types of linear Hund's case (a) molecules transitions. In particular, for $\Sigma^\pm - \Sigma^\pm$

$$\mathcal{S}_{J',J'+1}^{\text{dip.}} = J' + 1, \quad \mathcal{S}_{J',J'-1}^{\text{dip.}} = J', \quad (4)$$

and

$$\begin{aligned}\mathcal{S}_{J',J'}^{\text{quad.}} &= \frac{(2J'+1)J'(J'+1)}{(2J'-1)(2J'+3)}, \quad \mathcal{S}_{J',J'+2}^{\text{quad.}} = \frac{3(J'+1)(J'+2)}{2(2J'+3)}, \\ \mathcal{S}_{J',J'-2}^{\text{quad.}} &= \frac{3J'(J'-1)}{2(2J'-1)},\end{aligned}\quad (5)$$

where the superscript denotes dipole/quadrupole transition, respectively. Note that a set of Hönl-London factors for an allowed $2S'+1\Lambda'_{-}2S''+1\Lambda''$ transition connected to a given J' (or J'') obey a standard sum rule

$$\sum \mathcal{S}_{J',J''} = (2 - \delta_{0\Lambda'}\delta_{0\Lambda''})(2S+1)(2J+1), \quad (6)$$

with the sum over all ΔJ and any Λ -doublets (Bernath, 2005).

The rate constants for formation of a molecule by (spontaneous $T_b = 0$ and stimulated) radiative association at temperature T are then derived from the total cross sections $\sigma(E; T_b) = \sum \sigma_{J',\nu'',J''}(E; T_b)$ by averaging over a Maxwellian velocity distribution of the collisional continuum

$$\alpha(T; T_b) = \left(\frac{8}{\mu\pi}\right)^{1/2} \left(\frac{1}{k_B T}\right)^{3/2} \int_0^\infty E \sigma(E; T_b) e^{-E/k_B T} dE, \quad (7)$$

assuming that the system is found in thermodynamic equilibrium.

We improved the theoretical approach of Dalgarno and coworkers (Zygelman and Dalgarno, 1990; Stancil and Dalgarno, 1997) by taking into account the numbers of shape resonances, which are not negligible in some studied processes, in order to evaluate this integral as accurately as possible. In the actual calculation the total reaction rates can be obtained by summing over all resonant and non-resonant contributions. The inclusion of these resonances in the computation can increase the RA rate coefficients by up to 15% (Augustovičová et al., 2012). The resonance partial-wave J'_r contribution is counted in the rate coefficient calculation according to the numerical value of the ratio $\Gamma_{E_r, J'_r}^t/E_r$, where Γ_{E_r, J'_r}^t is the resonance tunneling width and E_r is its energy position. Resonances satisfying the criterion $\Gamma_{E_r, J'_r}^t \ll E_r$ are assumed to be “narrow” and vice versa. So we follow the approach of (Augustovičová et al., 2012), where contributions from wide and narrow resonances are treated separately from the background contribution. I hope the readers will forgive me that I will not depict details about calculation of adiabatic Born-Oppenheimer molecular state potentials, dipole and quadrupole moment functions of specific electronic states of studied molecular species, bound-state, orbiting resonance and continuum wave functions as well as interpolation and extrapolation of potential curves and their molecular characteristics and refer readers to the attached publications and other Refs. (Soldán and Kraemer, 2012; Augustovičová et al., 2012; Augustovičová et al.,

2013a; Augustovičová et al., 2013b; Augustovičová et al., 2014a; Augustovičová et al., 2014b; Belyaev et al., 2015; Augustovičová et al., 2015b)

Bound-bound transitions

For ability of molecular species to electronic transitions and chemical elementary processes the knowledge of radiative lifetimes of molecular species is of key importance. While transition probabilities can be obtained indirectly by measurements of radiative lifetimes, experimental measurements of emission spectral line intensities are difficult to obtain for many high temperature molecular species. Calculated line intensities then provide an alternative to measurements burdened by systematic errors and means for calibration in experiments.

Depopulation of a given level J' with energy E' and number density N' (in molecules/m³) is given in the absence of an external radiation field by the rate equation

$$\frac{dN'}{dt} = -A_{f \leftarrow i} N', \quad (8)$$

where the constant of proportionality $A_{f \leftarrow i}$ is the Einstein coefficient for emission. It implies that an excited-level population decays exponentially with time at rate $A_{f \leftarrow i}$. This decay rate determines the radiative lifetime of level E' as

$$(\tau_{i=E'})^{-1} = \sum_{f=E''} A_{f \leftarrow i}. \quad (9)$$

The Einstein A -coefficient can be approximated by the leading term in the multipole moment expansion, which can be written for electric-dipole allowed transitions as

$$A_{f \leftarrow i} = \frac{64\pi^4 \nu_{if}^3}{(4\pi\epsilon_0)3hc^3} \frac{1}{g_i} S_{f \leftarrow i}^{\text{dip.}}, \quad (10)$$

where $S_{f \leftarrow i}^{\text{dip.}}$ is the line strength of an electric dipole transition between all substates of the initial upper and final lower levels. The degeneracy factor (statistical weight) g_i of the initial state takes into account electronic, vibration, rotation, nuclear etc. statistics.

Line intensity for electric dipole transition arising between upper state with energy E' and lower state with energy E'' is given by (Bernath, 2005)

$$I_{f \leftarrow i} = \frac{8\pi^3 \tilde{\nu}_{if}}{(4\pi\epsilon_0)3hc Q(T)} \left[e^{-E''/k_B T} - e^{-E'/k_B T} \right] S_{f \leftarrow i}^{\text{dip.}}, \quad (11)$$

where $\tilde{\nu}_{if} = (E' - E'')/hc$ is the wavenumber of the transition (in cm⁻¹) and $Q(T)$ is the total internal partition function, which has

been scaled such that the minimum possible rotational-vibrational level has zero energy. The intensity is related to a single molecule event. Note that there are many other definitions and notations of the line intensity as numerous choices for quantities ν or N_{tot} (molecular number density) are possible, which causes confusion concerning units. $I_{f \leftarrow i}$ has the dimension of $\text{cm}^{-1}/(\text{molecule} \times \text{cm}^{-2})$, commonly referred to as HITRAN unit defined as wavenumber per column density (Rothman et al., 1998). This quantity is often called the integrated absorption coefficient.

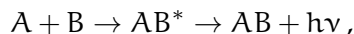
Combination of Equations (11) and (10) yields a relation between the line intensity and the Einstein A-coefficient corresponding to the transition $f \leftarrow i$

$$I_{f \leftarrow i} = \frac{g_i}{Q(T)} \frac{A_{f \leftarrow i}}{8\pi c \tilde{\nu}_{if}^2} \left[e^{-E''/k_B T} - e^{-E'/k_B T} \right].$$

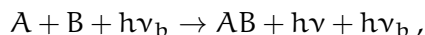
1.2 SUMMARY OF RESULTS IN THE ATTACHED PAPERS

The research presented in this section is based on papers that are included in the full printed version. Therefore, this section provides merely an abstract and accents high points of the obtained results. For full details I refer the reader to the appended part of this thesis that contains the corresponding papers.

In the attached papers (Augustovičová et al., 2014a; Augustovičová et al., 2014b; Augustovičová et al., 2015a; Augustovičová et al., 2015b) we investigated thoroughly the two-body association process



in which the collision complex AB^* is stabilized against dissociation by spontaneous emission of a photon with frequency ν . Apart from spontaneous emission, processes stimulated by the cosmic background radiation were also considered. The cosmic background radiation can enhance molecule formation by stimulated radiative association



where ν_b is the frequency of the background radiation field with effective temperature T_b . In this context, detailed studies of spontaneous and stimulated radiative association resulting in the formation of the HeH^+ (HeD^+), He_2^+ , and LiHe^+ molecular ions have been performed.

These calculations were performed employing the Born-Oppenheimer approximation, and the processes studied were characterized by means of energy-dependent cross sections and temperature-dependent rate coefficients. Contrary to previous works, highly excited electronic states were also included in these studies.

Due to the eminence of considered molecules and their formation processes for astrochemistry the emphasis is on the calculation of the rate coefficients of the corresponding reactions.

Among the main outcomes of these studies were realizations that the metastable helium atoms in planetary nebulae are significantly depopulated due to spontaneous radiative association process, and that the black-body background radiation enhances radiative association rates predominantly at low collision temperatures and only for those processes with small energy of emitted photons, e.g. for inelastic processes within one electronic state (see Fig. 1). The absence of this phenomenon in the majority of two-state processes, where emitted photon frequencies are very large, is caused by the factor $[1 - \exp(-h\nu_{E;v'',J''}/k_B T_b)]^{-1}$ in Eqs. (1) and (2) being almost 1. For reaction temperatures below a few thousand K the increase of rate coefficients due to black-body background radiation can be by an order of magnitude or more, for larger temperatures stimulation appears to be ineffective.

The cross sections for spontaneous ($T_b = 0$ K) and stimulated radiative association were calculated as functions of the relative collision energy of the reactants in the range of 10^{-6} and 10 eV. Typical quantum-mechanical cross sections obtained in our studies (see e.g. Fig. 2) are generally decreasing with increasing collision energy and have a rapid drop-off in the energy range between 0.1 and 10 eV. This is a typical behavior for radiative collision processes including radiative charge transfer (cf. e.g. Zygelman et al., 1989; Belyaev et al., 2014).

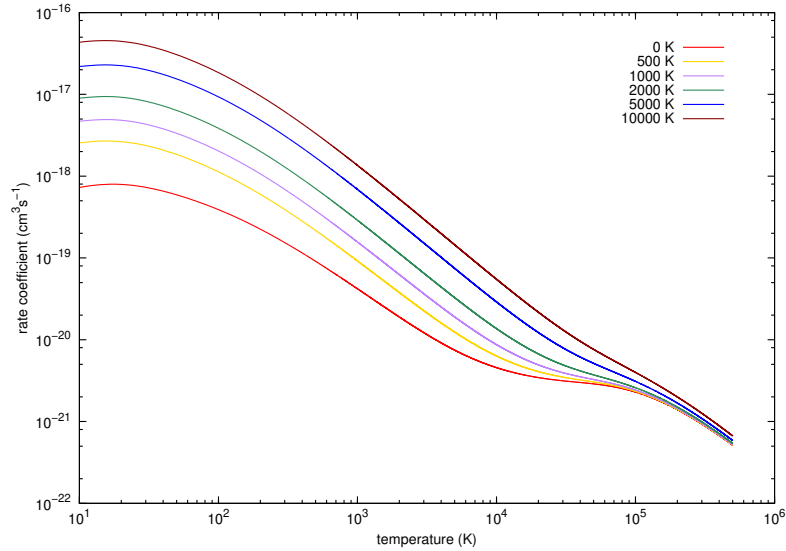


Figure 1: Adapted from Ref. Augustovičová et al. (2014b): Rate coefficients for the stimulated and spontaneous radiative association of H^+ and $He(2^1S)$ (continuum-bound $B(1^1\Sigma^+) \rightarrow B(1^1\Sigma^+)$ process) at different background temperatures.

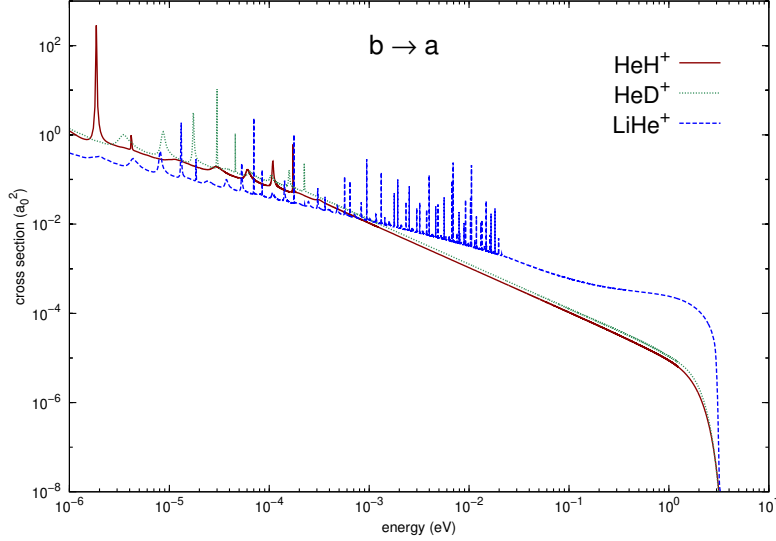


Figure 2: Adapted from Ref. Augustovičová et al. (2014a): Cross sections versus energy for spontaneous ($T_b = 0$ K) radiative association process $b(^3\Sigma^+) \rightarrow a(^3\Sigma^+)$ of formation three different molecular ions. Displayed are only the contributions of resonances with widths wider than 0.01 cm^{-1} .

The downhill background profile is usually complemented by a complex resonance structure while some of the resonance widths can be vanishingly small. Such features exceedingly complicate the numerical evaluation of the integral in Eq. (7). We bypassed this issue by treatment of wide and narrow resonance contributions to the radiative-association rate coefficients in a separate calculation following the procedure outlined in Section 1.1. For further details interested readers are referred to the Ref. (Augustovičová et al., 2012).

The low-energy resonance structure arises from the existence of quasi-bound states trapped behind centrifugal barriers in the reactant channel and is mostly determined by the depth and anharmonicity of the target potential. Provided one-state process the resonance structure is most pronounced, but for the two-state processes it is practically missing unless the final potential supports a large number of bound-state partners.

Different sizes of spontaneous cross sections, and hence rate coefficients, varying even by orders of magnitude can be attributed to the very large difference in ionization potentials of respective atomic species. This can be seen e.g. in Fig. 3 in which three target molecular potentials of LiHe^+ are involved, or in Fig. 4 showing formation of He_2^+ via various processes. Apart from the fact that the third power of the emitted photon frequency overwhelmingly dominates the total cross section, the number of terms in the sum of partial cross sections that is determined by the number of target rovibra-

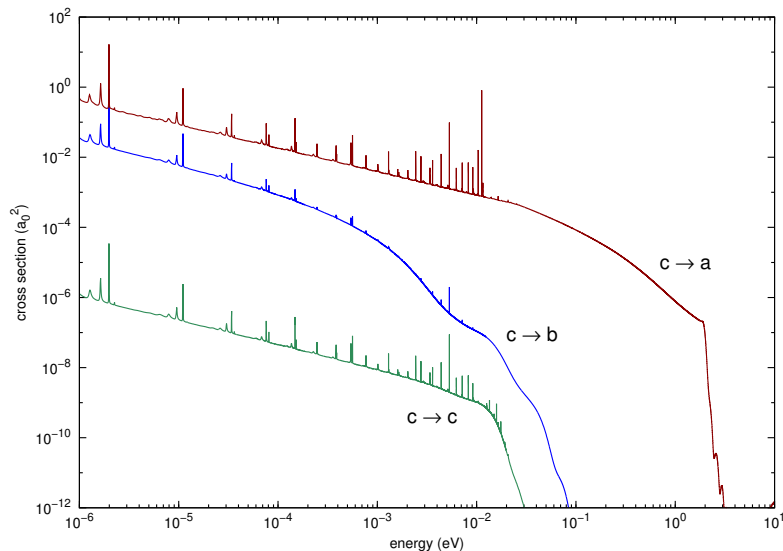


Figure 3: Adapted from Ref. Augustovičová et al. (2015a): Cross sections versus energy for spontaneous ($T_b = 0$ K) radiative association of LiHe^+ involving molecular states $a(^3\Sigma^+)$, $b(^3\Sigma^+)$, and $c(^3\Sigma^+)$. Displayed are only the contributions of resonances with widths wider than 0.01 cm^{-1} .

tional states also substantially affects the total cross section. Another considerable impact on increase of $\sigma(E)$ is the number of appropriate symmetry-allowed resonances as such, for which the corresponding Hönl-London coefficients are non-zero, throughout the character of a quasi-bound state wave function $\chi_{J'}(E, R)$. The wave function for a resonant energy picks up amplitude at the barrier and generates then a larger overlap in the well region with a transition dipole (quadrupole) moment function for the transition to a lower-lying level as the integral (3) depicts.

The corresponding rates of formation of the selected molecular ions of astrophysical importance (HeH^+ , HeD^+ , LiHe^+ , and He_2^+) were calculated as functions over a wide range of temperatures. Since the rate coefficient can be seen as a Laplace-transform image that smoothens the resonance structure (Eq. 7), the rates on the temperature scale are thus mimicking the cross-section behavior (cf. Fig. 4 and Fig. 5) on the energy scale.

Barred some noteworthy exceptions rates for all studied association processes are generally decreasing with increasing reaction temperatures.

Out of all the presented papers I will to focus in more detail on one, the outcomes of which I consider most interesting. The four processes that were shown in Fig. 4 illustrate a comparison of spontaneous radiative association driven by quadrupole transitions to those driven by dipole transitions. To my best knowledge, the study (Au-

gustovičová et al., 2015a) presents for the first time a direct comparison between molecular formations of homonuclear diatomic ions induced by electric quadrupole transitions with those induced by electric dipole transitions.

Within this work four ${}^2\Sigma^+$ states of He_2^+ were involved (from the lowest in energy $X({}^2\Sigma_u^+)$, $A({}^2\Sigma_g^+)$, $B({}^2\Sigma_u^+)$, and $D({}^2\Sigma_u^+)$), whereby the extra symmetry classification of gerade (g) and ungerade (u), which is available in homonuclear molecules such as H_2^+ and He_2^+ , introduces new selection rules that are applied to radiative transitions. The transitions from the initial Σ_u^+ states proceed towards Σ_g^+ states via dipole moment, while Σ_u^+ states are only achievable via quadrupole moment transitions. In principle, the quadrupole transitions conserving $g \leftrightarrow g$ symmetry may be considered, but a shallow potential well of the $A^2\Sigma_g^+$ electronic state supports only a few target rovibrational states, so the corresponding transition moments are expected to be inconsiderable. These processes in the mentioned scheme are labelled as $B \rightarrow A$ or $D \rightarrow A$ (dipole), and $B \rightarrow X$ or $D \rightarrow X$ (quadrupole), respectively.

Normally, one expects the cross sections for quadrupole-induced transitions to be at least four orders of magnitude smaller than those for dipole-induced transitions, where the major argument comes from c^5 dependence in contrast to c^3 in the denominator of the respective cross-section formulas (1) and (2). Nevertheless, the combina-

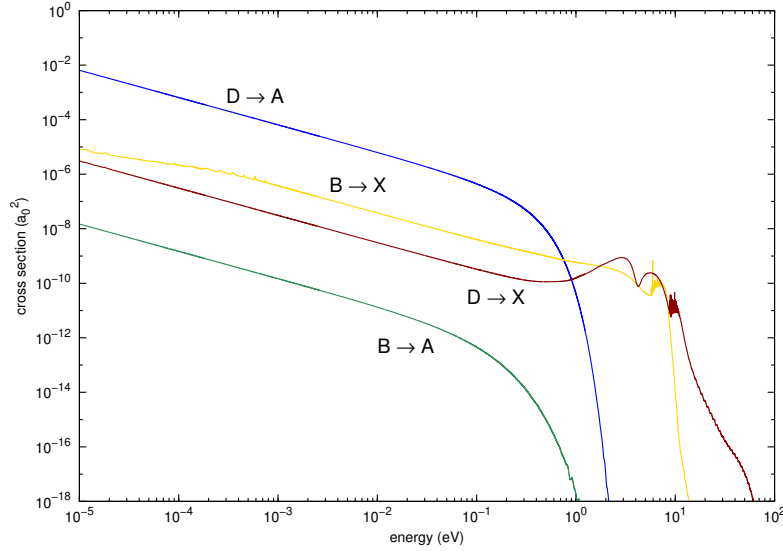


Figure 4: Adapted from Ref. Augustovičová et al. (2015a): Cross sections versus energy for spontaneous ($T_b = 0$ K) radiative association of He_2^+ involving molecular states $D({}^2\Sigma_u^+)$, $B({}^2\Sigma_u^+)$, $A({}^2\Sigma_g^+)$, and $X({}^2\Sigma_u^+)$. Transitions labeled $B \rightarrow A$ and $D \rightarrow A$ are dipole-driven, $B \rightarrow X$ and $D \rightarrow X$ are quadrupole-driven. Displayed are only the contributions of resonances with widths wider than 0.01 cm^{-1} .

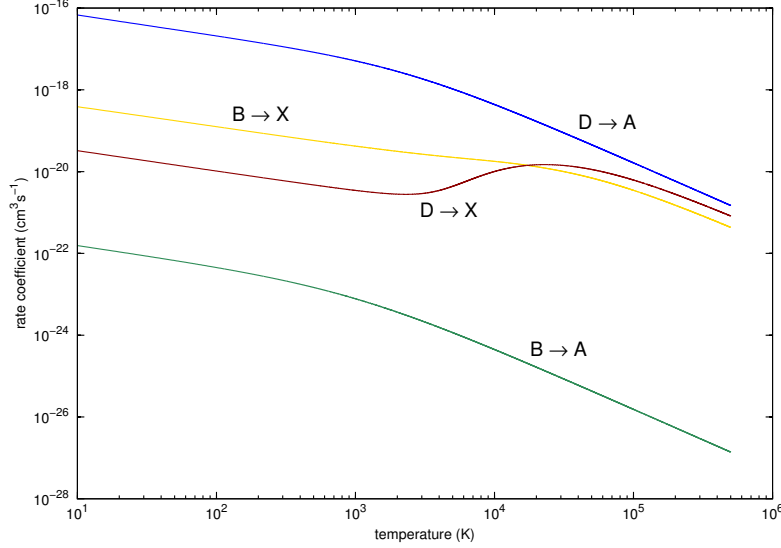


Figure 5: Adapted from Ref. Augustovičová et al. (2015a): Rate coefficients versus temperature for spontaneous ($T_b = 0$ K) radiative association of He_2^+ involving molecular states $D(^2\Sigma_u^+)$, $B(^2\Sigma_u^+)$, $A(^2\Sigma_g^+)$, and $X(^2\Sigma_u^+)$. Transitions labeled $B \rightarrow A$ and $D \rightarrow A$ are dipole-driven, $B \rightarrow X$ and $D \rightarrow X$ are quadrupole-driven.

tion of several factors can favorably influence the size of quadrupole-induced cross sections. The factors that play a significant role are: First, the depth of the target potential, thus the number of accessible rovibrational levels supported by this electronic state. Second, the Franck–Condon overlaps between the initial and target state wave functions. Third, the size of the corresponding transition moments (see Fig. 2 in Augustovičová et al., 2015a).

The calculated cross sections and rate coefficients inferred from them are displayed in Figs. 4 and 5 for the four considered processes. Surprisingly, all these aspects give rise to the quadrupole cross sections that are fairly comparable to the dipole ones. A couple of additional reasons can be named which may give a better explanation to this outcome. Mainly, it is the large difference in the numbers of rovibrational bound states in the target X and A states, 409 in X versus 6 in A. Moreover, quadrupole-induced transitions allow for three branches (O, Q, and S) within a band of a molecular spectrum of He_2^+ , while dipole-induced transitions offer only two branches (P and R). Their relative strengths are indicated by the Hönl–London factors (4) and (5). These facts result in that the quadrupole-driven radiative association processes $B \rightarrow X$ or $D \rightarrow X$ have many more (by approximately a factor of 100) summands contributing to the total cross sections. The large difference between the efficiencies of two association reactions induced by electric dipole $D \rightarrow A$ and $B \rightarrow A$ can be explained through different Franck–Condon conditions as Fig. 4

in Augustovičová et al. (2015a) demonstrates, and through the non-vanishing dipole moment function for large internuclear distances (see Fig. 2 in the same reference).

The radiative association results have been compared to non-radiative inelastic and de-excitation processes treated beyond the Born-Oppenheimer approximation (Belyaev et al., 2014; Belyaev et al., 2015). Studies of non-adiabatic effects performed on different excitation levels of collisional complexes $\text{Li}^+ + \text{He}$ and $\text{Li} + \text{He}^+$ can contribute to a better understanding of primordial and interstellar lithium chemistry, especially when comparing the efficiencies of radiative and non-radiative processes at different temperatures in astrophysical environments.

Quantum non-adiabatic nuclear dynamics takes into account radial non-adiabatic coupling matrix elements between states of the same symmetry of the low-lying $^1,3\Sigma^+$ and $^1,3\Pi$ states of the LiHe^+ ion to determine non-radiative inelastic cross sections and rate coefficients for all partial processes between the scattering channels. In contrast to radiative cross sections, the non-radiative ones generally increase with increasing collision energy (see Figs. 5 and 6 in Belyaev et al., 2015), owing to the fact that dominating partial channels are essentially endothermic. This behavior is reflected in a general increase of

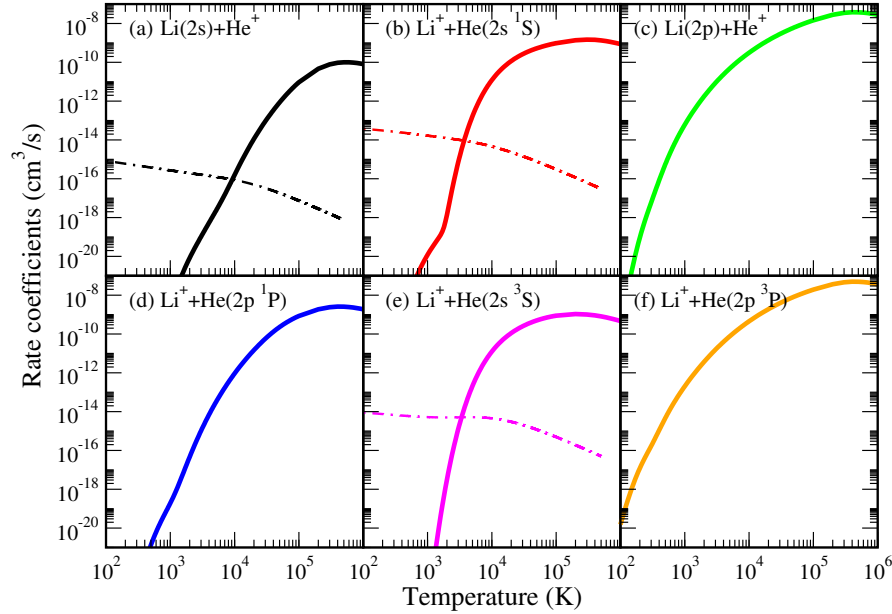


Figure 6: Adapted from Ref. Belyaev et al. (2015): Total rate coefficients for non-radiative (solid lines) and radiative (dot-dashed lines) inelastic processes in lithium–helium ion–atom collisions for different initial channels as a function of temperature. The initial collisional channel is indicated in each panel. The data for radiative depopulation are taken from (Augustovičová et al., 2012; Augustovičová et al., 2014a; Augustovičová et al., 2014b).

the corresponding rate coefficients as a function of temperature (Fig. 3 in Belyaev et al., 2014 and Fig. 7 in Belyaev et al., 2015).

They are compared with available total radiative rate coefficients (Augustovičová et al., 2012; Augustovičová et al., 2014a; Augustovičová et al., 2014b) for the same initial channels. As shown in Fig. 6, whereas the rate coefficients of the non-radiative processes increase rapidly with increasing temperature, the rate coefficients of the radiative processes drop slowly for high temperatures.

The findings evidence that at low temperatures the radiative depopulation in $\text{Li}^+ + \text{He}$ and $\text{Li} + \text{He}^+$ collisions dominates over the non-radiative processes at temperatures up to $\sim 9\,000$ K, while in $\text{Li}^+ + \text{He}(2^3\text{S})$ or $\text{Li}^+ + \text{He}(2^1\text{S})$ collisions only up to a critical temperature $\sim 3\,400$ K or $\sim 3\,700$ K, respectively. Thus the latter reactions are expected to have some influence on depopulations of metastable He in high temperature astrophysical environments.

Based on these results, we can summarize that at relatively high temperatures a non-radiative decay (due to non-adiabatic transitions) is expected to be more efficient than a radiative decay for higher-lying excited states. A critical temperature separating radiative and non-radiative reactions needs to be determined in each particular case.

More broadly, it appears that non-radiative and radiative processes apply to different areas in interstellar environments when surveying atomic or molecular astrophysical questions. In particular, non-radiative collision processes can, therefore, be expected to be dominant in stellar atmospheres. On the other hand, the radiative processes are typically the more efficient ones at low temperatures, such as in molecular clouds or in other cold astrophysical environments.

SPECTRAL PROBES OF POSSIBLE VARIABILITY OF FUNDAMENTAL CONSTANTS

The two cornerstones of modern physics – Standard Model (SM) of particle physics and General Relativity (GR) theory have been remarkably successful in the description of existing phenomena and prediction of new ones (Patrignani C. et al. (Particle Data Group), 2016). In contrast to their great success, there are major problems inseparably intertwined with these theories. The imbalance of matter and antimatter (Dine and Kusenko, 2003), the existence and properties of the dark matter (Bertone, 2013), the accelerating expansion of the Universe (Perlmutter, 2012) connected with dark energy and the frustrating failure of all attempts to combine physics of Standard Model with gravity are the most glaring examples. Thus, the search for possible physics beyond the Standard Model can have profound impact on our understanding of the nature of Universe and its laws.

The SM considers all fundamental constants as invariable in time and space. Many theories that go beyond GR and SM allow variability of these constants (Uzan, 2011). Most recent studies on variation of fundamental constants focus on dimensionless constants, especially the proton to electron mass ratio μ and the fine structure constant α as their values are not dependent on the chosen system of units of measurement (Safronova et al., 2018).

As the possible space or time variability of μ or α is reflected in the spectra of atoms and molecules that are dependent on these constants, the most accurate tests of their variability in modern era are performed using atomic clocks. The combination of constraints from atomic clock experiments carried out with different species (Godun et al., 2014) gives the following limits to the present day variation of μ and α (Safronova et al., 2018):

$$\begin{aligned}\frac{\dot{\mu}}{\mu} &= (0.2 \pm 1.1) \times 10^{-16} \text{ year}^{-1}, \\ \frac{\dot{\alpha}}{\alpha} &= (-0.7 \pm 2.1) \times 10^{-17} \text{ year}^{-1}.\end{aligned}$$

Similar values were reported by Huntemann et al. (2014) who analyzed different sets of atomic clock frequencies related to Cs microwave clock.

Molecules possess rich spectra that enable many different types of transitions. In the Born-Oppenheimer approximation the energy (frequency) of the rovibronic transitions depend on μ as

$$E \sim E_{\text{elec}} + c_{\text{vib}}\mu^{-1/2} + c_{\text{rot}}\mu^{-1},$$

where c_{elec} , c_{vib} and c_{elec} are not functions of μ . Hence, the purely vibrational and rotational transitions have sensitivity factors to variation of μ , $K_{\mu} = -1/2$ and $K_{\mu} = -1$, respectively. The sensitivity factor describes the relative change of energy (frequency) of given transition due to relative change of the value of the proton to electron mass ratio:

$$\frac{\Delta E}{E_0} = K \frac{\Delta \mu}{\mu_0},$$

where the subscript 0 denotes the present value of transition energy or μ . Additional types of dependences of K on μ arise after inclusion of fine and hyperfine structure, Λ -doubling etc. (Chin et al., 2009).

Pioneering experiments on utilization of molecular clocks for studies of fundamental constants variation were performed by Shelkovnikov et al. (2008) who used Ramsey spectroscopy to probe rovibrational transition in a supersonic beam of SF_6 . Theoretical studies by Beloy et al. (2010) and Flambaum and Kozlov (2007) have shown that accidental degeneracies between vibrational and fine structure levels can lead to a substantial enhancement of the sensitivities to variation of both α and μ in many diatomic systems, such as Cl^+ , CuS , HfF^+ , IrC , and SiBr . An increase of sensitivities on variation of α by 2 to 3 orders of magnitude due to cancellation between the hyperfine and rotational intervals was reported by Flambaum (2006).

Chin and Flambaum (2006), and Gacesa and Côté (2014) proposed to probe the possible variation of fundamental constants using precise measurement of scattering lengths in Bose-Einstein condensate and in photoassociation of ultracold molecules near a Feshbach resonance. An incremental progress was made in laboratory spectroscopic tests on variation of μ for ultracold deuterated ammonia released from an electrostatic trap and recaptured after chosen time (Quintero-Pérez et al., 2014) and for high resolution spectroscopy of methanol and its deuterated isotopologue in a Stark-deflected molecular beam (Jansen et al., 2013). The main aim of the latter studies has been an improvement in precision in reference to the astrophysical searches of μ variation.

While the laboratory studies focus on possible present variation of fundamental constants on a time scale of years, a complementary avenue of research aims to probe their variation in distant past, wherein the time scale is given by the age of the Universe. A distant bright astrophysical light source such as quasar is needed to provide illumination of high-redshift interstellar gas clouds enabling observation of atomic and molecular spectra with an age of up to several billion years. Such spectra can then be compared to the results from the high resolution laboratory experiments.

As the Universe expands, the light from distant objects is redshifted with a cosmological redshift z defined as

$$z = \frac{\lambda_{\text{obs}} - \lambda_{\text{lab}}}{\lambda_{\text{lab}}},$$

where λ_{lab} is the wavelength of the absorbed or emitted radiation and λ_{obs} is the wavelength of the light as observed on Earth. The higher the redshift z the longer the look-back time in the history of the Universe.

Presently the best astrophysical constraint on variation of μ for high redshifts of up to $z = 4.2$ (12.4 billion years) was obtained by Ubachs et al. (2016) from the 10 absorption systems of the H_2 molecule using UV transitions in the Lyman and Weber bands that are redshifted to the visible spectrum with z in the range of 2.0 to 4.2. Although the maximum sensitivity coefficient of these transitions was only $\Delta K_\mu \approx 0.06$ (Kozlov and Levshakov, 2013), the limit on temporal variation of μ set by the study of Ubachs et al. (2016) was

$$\left| \frac{\Delta\mu}{\mu} \right| = \left| \frac{\mu_{\text{obs}} - \mu_{\text{lab}}}{\mu_{\text{lab}}} \right| \leq 5 \times 10^{-6} \quad (3\sigma), \quad (12)$$

where μ_{obs} was inferred from the astrophysical observations and corresponds to the value of μ in distant past and μ_{lab} is the current value of μ obtained from contemporary laboratory studies.

The most stringent constraint on possible time variation of μ , albeit for lower redshifts ($z = 0.89$), was set by Bagdonaite et al. (2013a) and Bagdonaite et al. (2013b) using several absorption lines of methanol molecule observed towards PKS 1830-211. Methanol is present in sufficient densities in many interstellar environments and has relatively high sensitivity coefficients with $\Delta K_\mu \approx 60$ (Kozlov and Levshakov, 2013). The obtained limit of $\Delta\mu/\mu = (-1 \pm 0.8_{\text{stat}} \pm 1.0_{\text{sys}}) \times 10^{-7}$ (Bagdonaite et al., 2013a) gives assuming linear change of μ with time $\dot{\mu}/\mu = 2 \times 10^{-17} \text{year}^{-1}$. This is more strict than the corresponding limit inferred from atomic clocks (Huntemann et al., 2014; Godun et al., 2014).

Other astrophysical systems were considered for studies of temporal variation of μ . The transitions of ammonia isotopologues (especially inverse transitions) promise to potentially improve limits on μ variation (Augustovičová et al., 2016; Špirko, 2014; Flambaum and Kozlov, 2007; Murphy et al., 2008; Henkel, C. et al., 2009; Kanekar, 2011) as ammonia is ubiquitous in the interstellar medium and possess several transitions with very high sensitivities (Jansen et al., 2014 reported sensitivity coefficient of -938 , while Špirko (2014) and Owens et al. (2016) found a transition with $K_\mu = -16737.52$). Rather high sensitivity coefficients were also reported for H_3O^+ and D_3O^+ molecular ions (Owens et al., 2015) and for the phosphine molecule (Owens et al., 2018). Unfortunately, in all these cases the highest sensitivity coefficients correspond to forbidden transitions and therefore the

particular lines are very weak. Recently, primordial diatomic cations H_2^+ , D_2^+ and He_2^+ were suggested as feasible probes of μ variation at very high redshifts owing to the high sensitivity coefficients of their microwave rovibronic transitions (Augustovičová et al., 2014c). The search for possible spatial or temporal variation of fundamental constants is also substantially facilitated by rapid evolution of astronomical detection techniques such as VLBI, ALMA and FAST telescope (Martí-Vidal, I. et al., 2013).

2.1 RESULTS FOR SELECTED SYSTEMS

The sensitivity coefficient K_μ for transition between two states with energies E_u (upper state) and E_l (lower state) can be described by a linear proportionality (Jansen et al., 2014)

$$K_\mu \equiv K_{u,l} = \frac{\mu}{E_u - E_l} \left(\frac{dE_u}{d\mu} - \frac{dE_l}{d\mu} \right). \quad (13)$$

The frequency shift ($\Delta\nu = \nu_{\text{obs}} - \nu_0$) of a given transition due to a temporal variation of μ (where $\Delta\mu = \mu_{\text{obs}} - \mu_0$) depends on K_μ through the expression

$$\Delta\nu = \nu_0 K_\mu \frac{\Delta\mu}{\mu_0} = (E_u - E_l) K_\mu \frac{\Delta\mu}{\mu_0} = S_\mu \frac{\Delta\mu}{\mu_0}. \quad (14)$$

The subscript 0 denotes present day values of μ or ν , while those inferred from observations of distant objects are labelled by the subscript "obs".

When choosing promising systems for astrophysical studies of possible μ variation several considerations have to be taken into account. First, the sensitivity coefficient itself of a given transitions. Several transitions with high absolute value and different sign of K_μ are desirable. Second, the intensity of the particular transitions as often the highest K_μ are related to forbidden transitions with very low Einstein A coefficients. Third, the abundance of the studied molecular specie in the Universe and especially at high redshifts - only such species whose laboratory spectra can be compared to the astrophysical observations are suitable candidates.

The publication (Augustovičová et al., 2014c) predicts the sensitivity coefficients and various spectral characteristics of ro-vibrational transitions between the lowest lying electronic states of H_2^+ , D_2^+ and He_2^+ cations that are supposed to had played a key role in the chemical evolution of the early Universe and as such can be expected to be observable at very high redshifts. It is necessary to point out that the studied cations H_2^+ , D_2^+ and He_2^+ have not yet been detected in the extraterrestrial environments and their very detection is considered a daunting task. On the bright side, the characteristic time scale for H_2^+ destruction in reactive collisions with atomic or molecular hydrogen is much longer than the radiative lifetimes (up to 1000 s) of the

H_2^+ states whose microwave transitions were covered in the presented study with details in Ref. (Augustovičová et al., 2014c).

To obtain sensitivity coefficient K_μ for a spectral transition between an upper and lower state with their energies, E_u and E_l , respectively, we adopted an indirect approach, in which we relied on extensive high-level ab initio calculations that were subsequently morphed by fitting to extremely accurate experimental data. The calculations themselves for H_2^+ , D_2^+ and He_2^+ were based on direct non-linear fit of the spectroscopic data in microwave range (e.g. Carrington, 1996) and of the available theoretical rovibrational energies to obtain reliable potential energy curves. To respect the fact that the available experimental data are rather scarce, we performed our fitting in the framework of the Jenč’s Reduced Potential Curve (RPC) approach (Jenč, 1983; Jenč et al., 1993). The RPC method provides a suitable tool for a quantitative morphing of accurate ab initio potential energy curves in terms of only a small number of morphing parameters (Patkowski et al., 2009; Špirko, 2016). Moreover, the accuracy of resulting potentials can be enhanced by incorporating ab initio calculated coefficients to the fits when available.

In addition, the approach of computing sensitivity coefficients for a molecular system made use of an effective Hamiltonian model to probe how the parameters of this model depend on μ . The required numerical derivatives, $dE_x/d\mu$, for $x = u, l$, were obtained from the calculated dependences of particular energies on μ . The variational approach is advantageous in that along with sensitivity coefficients, reliable theoretical transition frequencies can be predicted if no experimental data are available, and it also allows a comprehensive

Table 1: Adapted from Ref. Augustovičová et al. (2014c): The $A^2\Sigma_u^+ \leftrightarrow X^2\Sigma_g^+$ microwave transitions of H_2^+ (frequencies ν in MHz, line strengths S in D^2 , Einstein coefficients A in s^{-1}). Experimental data from Ref. Carrington et al. (1995).

ν', N'	ν'', N''	ν_{fit}	ν_{exp}	S	A	T
$A \rightarrow X$						
0,0	18,1	514956.6		3.073	2.038×10^{-01}	31.669
0,1	18,0	645722.3		2.484	1.083×10^{-01}	26.982
0,1	18,2	352014.8		7.493	5.293×10^{-02}	39.683
0,2	18,1	593778.1		4.452	9.055×10^{-02}	27.400
0,2	18,3	156614.7	156633	15.406	5.751×10^{-03}	65.568
$X \rightarrow A$						
19,0	0,1	52907.5	52895	8.884	6.400×10^{-04}	-17.594
19,1	0,0	96431.6	96432	5.268	7.659×10^{-04}	-5.739
19,1	0,2	17610.2	17610	24.113	2.135×10^{-05}	-29.230

treatment of a molecule to be undertaken. For all transitions analyzed Einstein A coefficients and line strengths S have been calculated to guide future laboratory and astronomical observations using theoretical concepts described in Section 1.1. The values of the calculated sensitivity coefficients are comparable to their ‘record-breaking’ methanol counterparts (see Table 1 and the supplemental material to Ref. Augustovičová et al., 2014c for the complete list of studied transitions, their sensitivities and other spectral parameters). The largest absolute value of K_μ obtained in this study, $K_\mu = -407$, involved the ($\nu_A = 0, N_A = 3 \leftarrow \nu_X = 26, N_X = 4$) transition of D_2^+ molecular ion. The fact, that the resulting sensitivity coefficients were of both signs allowing simple analysis without need for reference molecules coupled with the relatively large line strengths of the studied transitions, hints that H_2^+ (and to a lesser extend also D_2^+ and He_2^+) could be a promising candidate for astrophysical tests of μ variation at high redshifts.

The theoretical approach utilized in the above mentioned study of primordial cations H_2^+ , D_2^+ and He_2^+ (Augustovičová et al., 2014c) was refined in my subsequent study (Augustovičová et al., 2016) focused on hyperfine structure of rotational-inverse ($\nu_2 = 0^+, 0^-, 1^+, 1^-$) states of ammonia isotopomers $^{14}\text{NH}_3$ and $^{15}\text{NH}_3$ by addition of efficient roinverse hyperfine functions. These functions were obtained by simultaneous fitting of available measured transitions using ef-

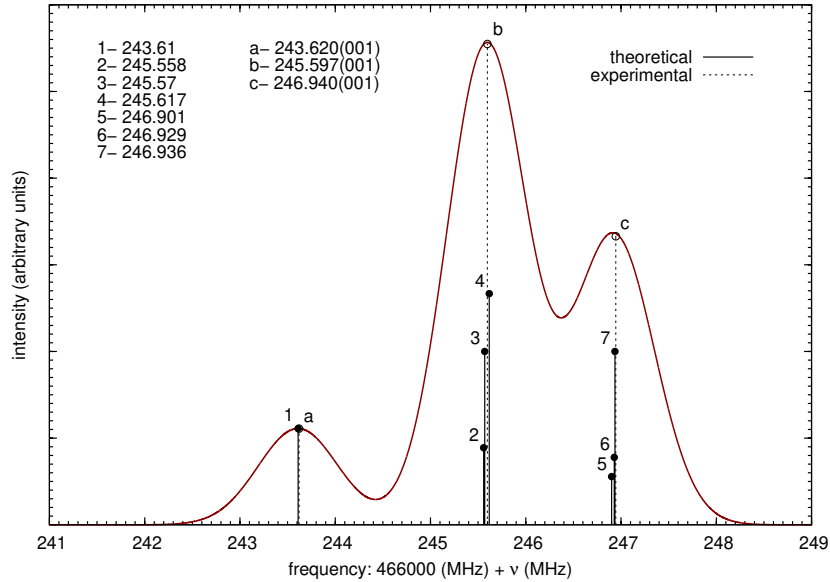


Figure 7: Adapted from Ref. Augustovičová et al. (2016): Theoretical ammonia $^{14}\text{NH}_3$ $\nu_2 = 1, (J, K) = (1, 0)^+ \rightarrow (0, 0)^-$ spectrum vs. saturation dip position lines of the hyperfine components from (Belov et al., 1998) at temperature 150 K. Frequencies are given in MHz relative to the value of 466,000 MHz.

fective Hamiltonian within the non-rigid inverter theory. The results obtained with the inclusion of only a small number of mass independent fit parameters allowed to provide reliable predictions of hyperfine interactions for a large number of so far unobserved transitions involving roinverse states of ammonia isotopomers as well as critical revision of fits based on mass and state dependent spectroscopic constants.

Precise determination of the hyperfine-structure parameters allows to account for energy level patterns imprinted in the Doppler profile of ro-inversion transitions (e.g. see Figs. 7 and 8), and hence for explanation of physical characteristics that are dependent on these patterns - for example, an accurate determination of Boltzmann constant by Doppler spectroscopy (Lemarchand et al., 2011) or modeling of the laser-induced population transfers. In particular, the published predictions can be used to derive the true centers of astronomical line bands that come to the forefront of fundamental physics and seem promising for critical testing of the cosmological variability of μ .

Ammonia is abundant in a variety of interstellar environments and has been detected not only in our Galaxy but also in very distant astronomical objects with redshifts $z \sim 0.685$ and $z \sim 0.886$ (Henkel, C. et al., 2005; Henkel, C. et al., 2008) currently providing spectral lines that allow a critical limitation regarding changes in ratio of proton mass to electron mass on cosmological timescales.

As documented in the case of ammonia molecule, the dependence of sensitivity coefficient K_μ on the reciprocal value of the transition

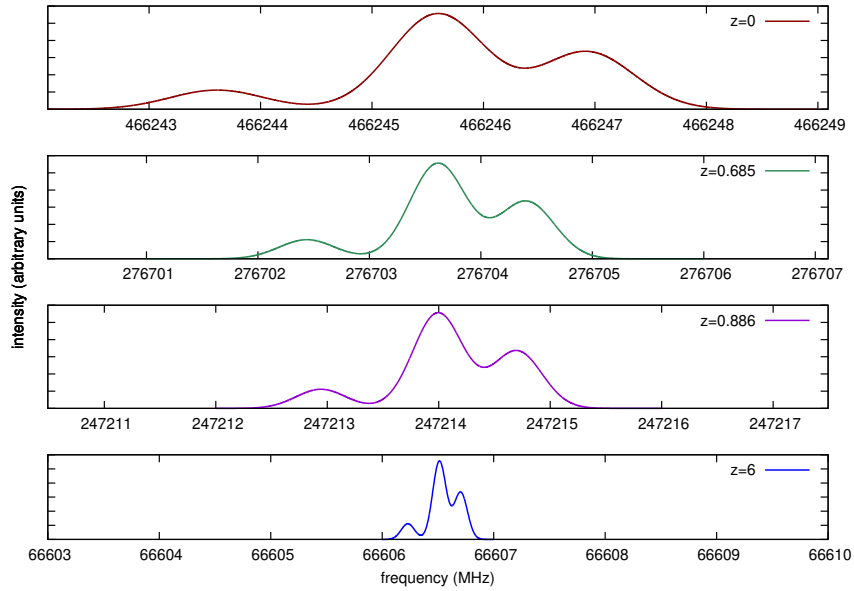


Figure 8: Theoretical ammonia $^{14}\text{NH}_3$ $v_2 = 1, (J, K) = (1, 0)^+ \rightarrow (0, 0)^-$ Doppler spectra lineshapes for various redshifts at temperature 150 K.

frequency can lead to its strong enhancement in case of accidental degeneracies of the corresponding energy levels. Thus by tuning the energy levels degeneracy, such as in the Zeeman-tuned level-crossing spectroscopy (Cahn et al., 2014), a dramatic increase of the value of K_{μ} can be achieved. The magnetic field, detected in almost every astrophysical object in the Universe, and believed to play an important role in the dynamics of the interstellar medium (Crutcher, 1999; Crutcher, 2012), could be utilized not only for significant enhancement of the sensitivities but also for reduction of the Doppler broadening of the studied transitions that often hinders precise astrophysical observations.

The hydroxyl radical (OH) was chosen as a model system for the study on the effects of the magnetic fields on the mass sensitivities of the spectral transitions of molecular radicals exhibiting Zeeman splittings (Augustovičová and Špirko, 2020). OH is present in large quantities in many astrophysical objects including those with very high redshifts. Recently the study by Spilker et al. (2018) reported observation of OH spectra towards SPT2319-55 with $z \sim 5.3$ corresponding to the look back time of 12 billion years. Moreover, the energy level pattern of the rotational ground state is especially suitable for Zeeman tuning of relative distance of particular hyperfine energy levels.

The hydroxyl radical in its electronic ground state X possesses a ${}^2\Pi$ configuration. Each rotational level, labelled by quantum number J consists of a Λ doublet with states described by $+$ and $-$ parities (and labelled here by the usual spectroscopic notation e and f , respectively). Under the influence of the magnetic field each of these components splits into several sublevels (see upper panel of Fig. 9 and a detailed analysis in the Appendix A), and as a result, the Zeeman level patterns corresponding to the e and f parity topologically almost coincide.

The Zeeman energy and mass sensitivity patterns of the rotational states of the paramagnetic OH radical in its ground electronic state were probed using a complete molecular Hamiltonian. The Zeeman energy splittings exhibit nearly coinciding magnetic dependences with their corresponding ‘reduced’ mass sensitivities. For the low magnetic fields that are too weak to compete with the hyperfine interactions rather nonlinear shapes of the Zeeman spectra occur, while for the fields dominating the hyperfine interactions the Zeeman effect is nearly linear with the change of B . As the slopes of the individual split Zeeman lines acquire positive and negative values, the energy levels in the imposed magnetic field undergo level-crossings.

The decrease in the transition frequencies related to these crossovers provides a dramatic enhancement of the mass sensitivity coefficients K_{μ} of the involved transitions and also a substantial reduction of their spectral line broadenings. The intensities of $e \leftrightarrow e$ and $f \leftrightarrow f$ magnetic dipole allowed transitions are diminished to zero

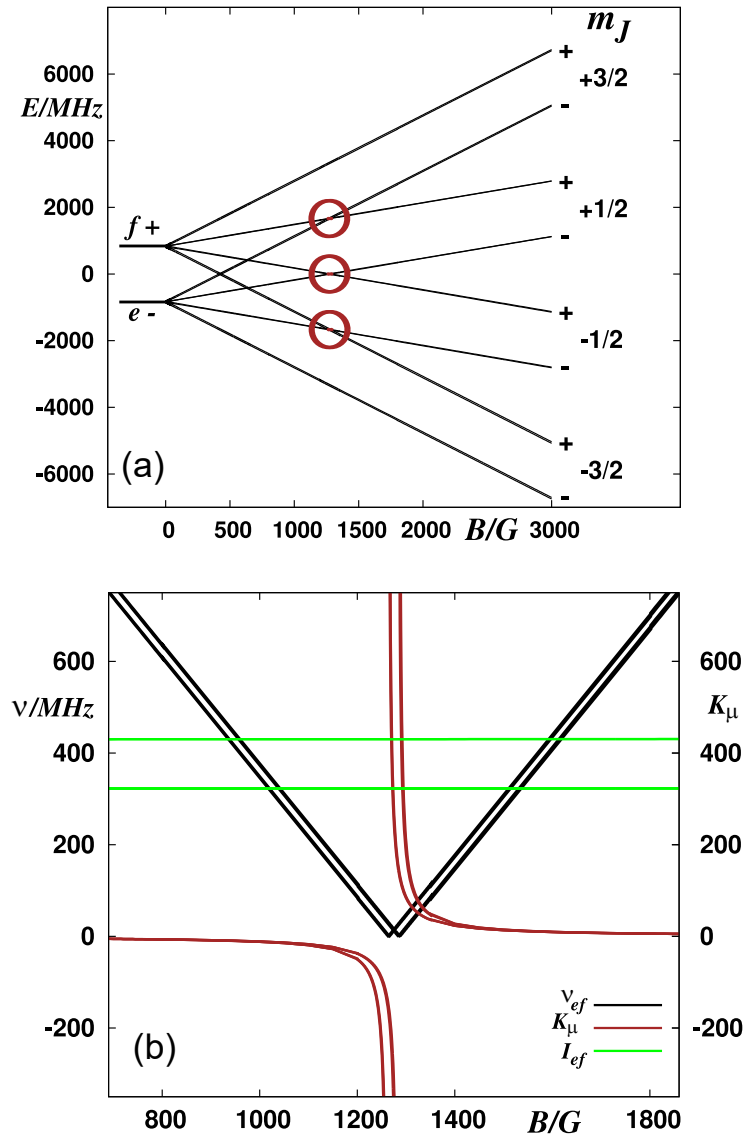


Figure 9: Adapted from Ref. Augustovičová and Špirko (2020): Energy level patterns E [panel (a)], allowed transition frequencies ν , mass sensitivities K_μ and relative intensities I (in arbitrary units) [panel (b)] of ^{16}OH in its $J = 3/2$ rotational state. Colored circles label level-crossing states supporting allowed transitions [colored curves in panel (b)].

as the values of the corresponding frequencies are reduced. Therefore, their possible use in astrophysical analysis of cosmological constant variability is limited. On the other hand, the intensities of the $e \leftrightarrow f$ electric dipole allowed transitions are almost constant in the imposed field as shown in the lower panel of Fig. 9. Moreover, these transitions are much stronger than their magnetic counterparts and thus they appear to be very promising astronomical probes for the cosmological variability of the proton-to electron mass ratio.

Paramagnetic spectrum analysis obtained in the presence of extremely strong magnetic fields seems to be particularly interesting, because the absolute sensitivity factors S_{μ} of the corresponding transitions increase monotonously with the field strength. It therefore seems conceivable that these analyzes could improve the current limit of the temporal variation of μ .

However, it should be emphasized that current results were obtained using constant molecular g -factors with total neglect of higher order diamagnetic contributions. The diamagnetic contributions are quadratic in B and their role in the case of extremely strong magnetic fields could become important.

Cooling atoms to ultralow temperatures has offered new insights into fundamental physics (e.g. Bose-Einstein condensate, superfluidity, degenerated Fermi gases), precision measurement, quantum information processing and quantum optics. Ultracold physics as well as its applications have undergone a remarkable progress thanks especially to very recent experimental developments such as molecular laser cooling (Shuman et al., 2010; Barry et al., 2014; Yeo et al., 2015; Kozyryev et al., 2016; Chae et al., 2017) and buffer-gas-loaded beams (Hutzler et al., 2012). With sophisticated cooling techniques – resulting in several Nobel Prizes (Chu, Cohen-Tannoudji, Phillips, Haroche, Wineland) – applied to molecules, whose implementation has been more challenging due to the complexity of molecular structures, the longstanding goal of accurately controlling molecular degrees of freedom and the resulting interaction processes seems to be finally within reach. Further insight on how molecules interact can in turn lead to more precise control of reaction chemistry (Bohn et al., 2017).

In particular, the technology of laser cooling molecules has paved the way for the production of a long list of truly ultracold molecular species, with temperatures reaching microKelvin rather than the milliKelvin scale (McCarron et al., 2018a). At such low temperatures the molecules can be confined in magnetic (Williams et al., 2018; McCarron et al., 2018b) or optical dipole traps (Anderegg et al., 2018; Cheuk et al., 2018), it is possible to prepare them in individual quantum states, their collisions are governed by individual partial waves and are strongly influenced by laboratory electric and magnetic fields (Krems, 2019). However this technique is at present limited to a particular subset of molecules. In comparison, although still limited to sample temperatures of hundreds of mK, the buffer-gas-loaded beams prove to be very versatile sources.

One of the methods utilized to reach the ultracold regime for a number of chemically relevant species, for which additional cooling is desirable, is the process known as evaporative cooling. Evaporative cooling is a continuous process of decreasing the average energy of a system of trapped particles. This is maintained by flying off atoms in the high-energy tail of Maxwell-Boltzmann distribution away and then by allowing the rest to rethermalize at a lower temperature. However, the cooling efficiency is subject to repopulation of the thermal distribution tail by collisions which requires a relatively high elastic collision rate and initially a high number density of the ensemble related to rethermalization rate (Bohn and Jin, 2014). Yet fulfill-

ment of the rethermalization condition is slowed down by chemical, or primarily, by inelastic collisions during which one or both collision partners change their internal state. The internal state conversion manifests itself in a spin-flip transition or parity change, leading to associated particle losses. Moreover, the inelastic collisions are typically exothermic which leads to additional heating of the trapped atoms or molecules. The technique works well for alkali atoms, where it was noted long ago that the ratio of elastic to inelastic collision rates should exceed ~ 100 for evaporation to be effective (Monroe et al., 1993). For molecules, it has been somewhat difficult to achieve this ratio, because they possess rotational structure and dipole moments ensuing in a substantial number of energy levels, in which they end up after collision. Thus the extension of the evaporative cooling method to molecules, as a secondary cooling process, is not straightforward and has not yet been clearly demonstrated (with a possible exception of OH radical).

A ground state of a polar molecule tends to align dipole moments parallel to the field, known as a high-field seeker. But this state is not trappable because of Earnshaw's theorem. Hence, a desire for finding a configuration with local minimum of the field vector modulus with the purpose of confining cold atoms or molecules in the low-field-seeking states has led experimentalists to design various trapping arrangements employing static or time-varying inhomogeneous fields, such as TOP trap, Ioffe-Pritchard trap, Paul RF trap etc (Ketterle and Drueten, 1996; Pérez-Ríos and Sanz, 2013).

It is necessary to point out that for certain ultracold collisions, the scattering rates and their dependences on external fields are determined by physics occurring on scales larger than the range given by the exchange potentials between the collision partners, i. e. when the molecules are far apart. A molecule in a weak-electric-field seeking state can experience torques due to this long range forces and ends up in a strong-field seeking state after collision resulting in losses of trapped particles. One of the advantages of laser-cooled molecules is that they can be optically trapped in strong-field-seeking states being thus more resistant to such state-changing collisions.

In this regard, understanding collision cross sections and their response to applied electromagnetic fields is vital for controlling collisions, which could allow for experimental observation of predicted quantum mechanical effects applicable, e.g. in quantum simulation and computation.

3.1 RESULTS OF ULTRACOLD DIPOLAR MOLECULAR COLLISIONS

In this section I will briefly describe the structure of the studied molecules, the theoretical approach of molecular scattering and present outcomes. In the absence of an applied field, the effective

Hamiltonian for the fine and hyperfine structure of a free diatomic radical in its ground ${}^2\Pi$ state includes the spin-orbit interaction, rotational energy of the molecule in the treatment of the rigid body, spin-rotation interaction, Λ -doubling terms, and nuclear hyperfine interaction. The theoretical analysis of the NO spectra is similar to that already described for OH radical, but with features arising from different nuclear spin (${}^{14}\text{N}$ nucleus has spin $I = 1$, the spin of the hydrogen nucleus is $1/2$). Therefore, we can utilize most of the matrix elements derived earlier for OH in Chapter 2 and Appendix A. Components of Λ -doubling are $|\Omega| = 1/2$ and $|\Omega| = 3/2$, both doubly degenerate, of which ${}^2\Pi_{1/2}$ is the lower-lying state because the spin-orbit coupling constant (for the ground vibrational state) is positive $A = 123.146 \text{ cm}^{-1}$ (Varberg et al., 1999), unlike that of OH, SH or LiO. As indicated in Appendix A we work in a Hund's case (a) basis while the basis functions are of the form

$$|\eta, |\Omega|, (J, I), F, M_F; p\rangle \quad (15)$$

in the hyperfine-coupled basis set. Here η is a general index which represents all other considered quantum numbers and p labels parity.

The list of laser-coolable diatomic species has been recently extended to include classes of polyatomic molecules that are expected to be amenable based on Franck-Condon factors calculations (Isaev and Berger, 2016). Soon after, experimental success in Sisyphus laser cooling of the polyatomic molecules SrOH and YbOH has been reported (Kozyryev et al., 2017; Augenbraun et al., 2020). Augustovičová and Bohn (2019) extended cold collision theory of linear polyatomic molecules, treating ${}^{40}\text{Ca}{}^{16}\text{OH}$ molecules colliding with each other.

In comparison to laser cooled diatomic molecules, alkaline earth monohydroxide radicals, including CaOH, possess more complicated structure. It has three vibrational modes: a symmetric stretch ν_1 , an antisymmetric stretch ν_3 , and doubly degenerate bending vibrations ν_2 without a direct analog in diatomics. Additionally, an effect of molecular rotations and vibrations on the electronic spectra of linear molecular species in degenerate electronic states ($\Lambda \neq 0$), the Renner-Teller effect, which is missing in diatomic molecules, further complicates molecular structure. For optical trapping purposes we have focused on the specific state, the lowest bending excitation with $\nu_2^{|\ell|} = 1$ of the ground electronic $X^2\Sigma^+$ state. This is because it is the lowest-lying state with a doublet and therefore can be easily polarized in a small electric field. The superscript ℓ next to the vibrational quantum number ν_2 labels the projection of the vibrational angular momentum on the molecular axis and takes values of $\ell = -\nu_2, -\nu_2 + 2, \dots, \nu_2$. The appropriate hyperfine-coupled case (b) basis set is

$$|X(0, 1^{|\ell|=1}, 0); [(N, S)J, I] F, M_F; p\rangle \quad (16)$$

of definite parity $(-1)^{N-l}$ and the spin $I = 1/2$ is of the hydrogen atom. The matrix elements of the effective Hamiltonian that includes vibrational and rotational energies, the spin-rotation coupling, the l -type doubling, and the hyperfine interaction are given in Augustovičová and Bohn (2019).

Polar molecules are susceptible to external electromagnetic fields via their electric and magnetic moments. In the case of both considered molecules, NO and CaOH, a magnetic field is less relevant as the molecular magnetic moment due to the electron's orbital motion and spin is insignificant. The Stark Hamiltonian for the molecular dipole – electric field interaction is given by $H_S = -\mathbf{d}_s \cdot \mathcal{E}$, where direction of the homogenous electric field vector \mathcal{E} coincides with the space-fixed Z -axis. Fig. 10 demonstrates the electric-field dependence of the $(0, 1^1, 0)$, $N = 1$ levels of CaOH.

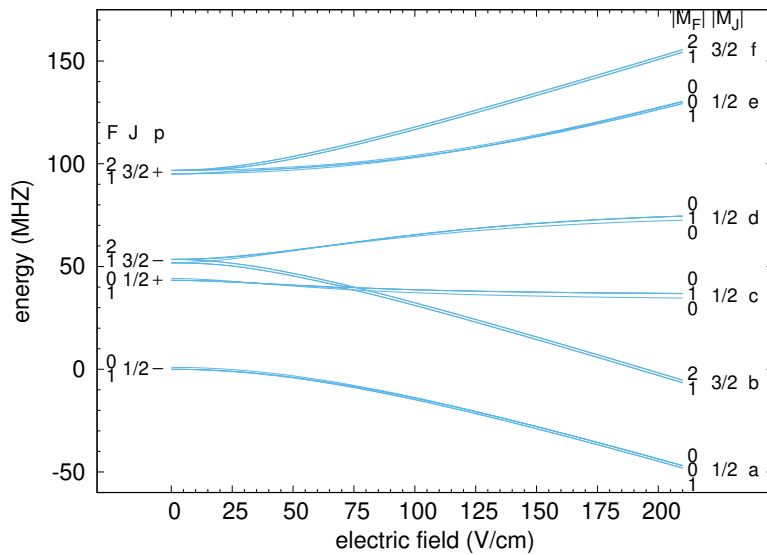


Figure 10: Adapted from Ref. Augustovičová and Bohn (2019): Stark effect in the $(0, 1^{l=1}, 0)$, $N = 1$ state of CaOH. At zero field, the states are labeled by the total electron-plus-rotation angular momentum J , the total spin F , and the parity p ; at larger electric field the states are labeled by the projections M_J and M_F of these angular momenta along the field axis. Each line is doubly degenerate in lM_F . As a shorthand, the fine structure manifold at high field are labeled by the indices $a - f$.

At ultralow collision energies, the molecular dynamics is dominated by the long-range forces. This includes a R^{-6} van der Waals

interaction, a centrifugal potential and electric dipole-dipole interaction between the two molecules

$$\begin{aligned} V_{\text{dd}}(\mathbf{R}) &= \frac{1}{4\pi\epsilon_0} \frac{\mathbf{d}_1 \cdot \mathbf{d}_2 - 3(\hat{\mathbf{R}} \cdot \mathbf{d}_1)(\hat{\mathbf{R}} \cdot \mathbf{d}_2)}{R^3} \\ &= -\frac{\sqrt{30}d^2}{4\pi\epsilon_0 R^3} \sum_{q, q_1, q_2} \begin{pmatrix} 2 & 1 & 1 \\ q & -q_1 & -q_2 \end{pmatrix} C_{2-q}(\theta\phi) C_{1q_1} C_{1q_2}, \end{aligned}$$

where the first-rank tensors as reduced spherical harmonics are functions of Euler angles giving orientation of molecular dipole vectors $\mathbf{d}_1, \mathbf{d}_2$, and $\mathbf{R} = (R, \theta, \phi)$ is the intermolecular vector. The matrix elements of the dipolar V_{dd} operator are evaluated in the two-molecule basis

$$|F_1, M_{F_1}; p_1\rangle |F_2, M_{F_2}; p_2\rangle |LM_L\rangle_S, \quad (17)$$

where the individual kets in the direct product space are one-molecule functions (15) or (16) depending on the molecular species, $|LM_L\rangle$ is a partial wave state satisfying the conservation of the total angular momentum projection on the Z-axis, and the subscript S denotes a symmetrized combination of two identical particles, fermions in the case of NO and bosons as for CaOH molecules.

The exact coupled-channel calculations for molecule-molecule scattering was performed employing the log-derivative propagator method (Johnson, 1973). Cross sections as functions of collision energy were computed from the S-matrix elements for processes in which both molecules remain unchanged (elastic) or at least one molecule converts its internal state to another (inelastic). The scattering rate coefficients K were then defined as $v_i \sigma$, where v_i is the incident collision velocity and σ is the collision cross section.

Evaporative cooling is not impossible to achieve for molecular radicals, as it was actually demonstrated in OH (Stuhl et al., 2012); the possibility of evaporative cooling was scarcely probed for only few other molecular species, partly due to technological limitations for experiments. Recently, I have investigated the situation for the $^2\Pi_{1/2}$ and $^2\Pi_{3/2}$ states of the important atmospheric radical NO (Augustovičová and Bohn, 2017; Augustovičová and Bohn, 2018b), which can be prepared for ultracold experiments by means of Stark decelerator (Vogels et al., 2015) or by other means (Bichsel et al., 2007; Elioff et al., 2003). Therefore, it was deemed to be worthwhile to study whether the ratio between elastic and inelastic collisional rates can be altered by an external electric (or magnetic) field. Example of the dependence of calculated elastic and inelastic rate coefficients for collision energy of 100 mK on electric field is plotted in Fig. 11. The NO molecules in this case are in the states with quantum numbers either $|F, M; p\rangle = |3/2, 1/2; +\rangle$ or $|3/2, 3/2; +\rangle$ before collisions.

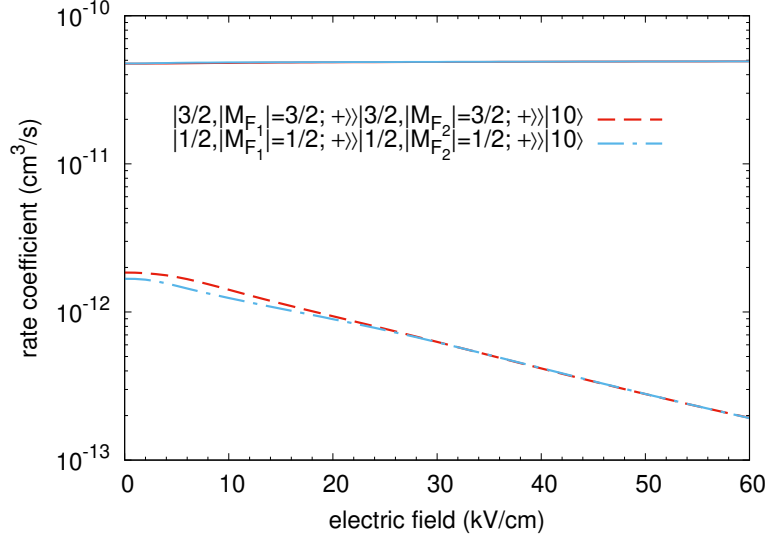


Figure 11: Adapted from Ref. Augustovičová and Bohn (2017): Rate coefficients for elastic (solid curves) and inelastic (dashed curves) scattering as a function of the electric field for the two incident channels $|F = 1/2, |M_{F_1}| = 1/2; +\rangle|F = 1/2, |M_{F_2}| = 1/2; +\rangle|L = 1, M_L = 0\rangle_S$ and $|F = 3/2, |M_{F_1}| = 3/2; +\rangle|F = 3/2, |M_{F_2}| = 3/2; +\rangle|L = 1, M_L = 0\rangle_S$ of NO molecules. The collision energy is fixed at the value $E_c = 100$ mK.

At all values of electric field the elastic rate coefficients remain high and constant, due to generically strong scattering of polarized dipoles. The elastic rate actually far exceeds the inelastic rate for low electric fields but their ratio is insufficient for the figure of merit of evaporation. After a threshold field of hundreds of V/cm, a new effect appears, namely, the value of the inelastic rate coefficients decrease with increasing electric field. Nevertheless, the suppression effect would require fields as large as 40 kV/cm to exceed 100 for the ratio of elastic to inelastic scattering, which is probably unrealistically high field in electrostatic traps as currently built.

The reasons behind this suppression of inelastic collisional rate coefficient at high electric fields are described in detail in (Augustovičová and Bohn, 2017; Augustovičová and Bohn, 2018b). A qualitative explanation of this high field dependence can be seen if the inelastic scattering of NO molecules is treated using Born approximation. In the field regime where the molecules are fully polarized the losses are controlled by the energy between incident and final thresholds released in the collision. As this energy gap gets larger with electric field the ultracold inelastic rate should scale as $\mathcal{E}^{-1/2}$. Another cause of suppression is due to the matrix elements of the dipole-dipole coupling V_{dd} in the dressed states of the molecules that depend strongly on electric field; the most probable inelastic process is the one that changes the sum of total angular momentum projec-

tion for both collision species by one while the molecular state parities p_1, p_2 are preferred to be changed.

The found non-trivial field dependence of the inelastic collisional rate coefficient is surprising given the conclusions of related studies (see e.g., Avdeenkov and Bohn, 2002 or Fig. 5 in Augustovičová and Bohn, 2019), so it is worth contemplating its applicability to other polar molecules. For the reasons outlined earlier in this section mainly in the context of designing efficient laser cooling schemes I have focused on ultracold collisions of CaOH with the main goal to investigate the possibility of evaporative cooling in an appropriate state. To this end, molecules in the b fine structure manifolds (in the notation of Fig. 10) were considered. Fig. 12 presents rate coefficients as a function of field strength at two different collision energies, 1 mK and 1 μ K, for incident channel built of the spin-stretched $|b, l = 1; M_F = 2\rangle$ molecular states.

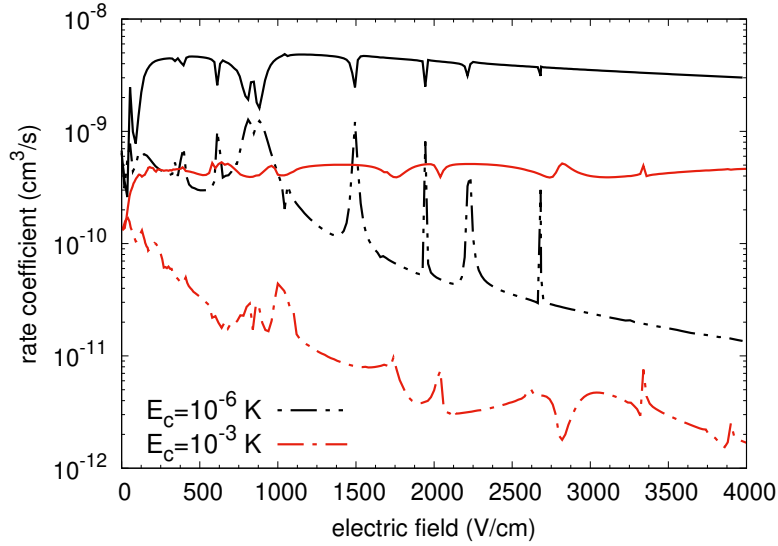


Figure 12: Adapted from Ref. Augustovičová and Bohn (2019): Rate coefficients for elastic (solid curves) and inelastic (dashed curves) scattering as a function of electric field. The collision is initiated in the states $|b, l = 1; M_F = 2\rangle$ of CaOH molecules at two different collision energies $E_c = 1 \mu\text{K}$ (black lines) and $E_c = 1 \text{ mK}$ (red lines).

In contrast to the case of NO molecular scattering the field dependence of inelastic collision rates is much more favorable for CaOH. Not only do collisions feature an overall decreasing trend of loss rates with applied electric field at both energies but they also decay faster, and thus the ratio of elastic to inelastic collisions above 10^2 , as a rule of thumb, occurs at experimentally reasonable field strengths. The obtained results indicate that for $E_c = 1 \text{ mK}$ such a field is $\mathcal{E} \sim 3500 \text{ V/cm}$ while for $E_c = 1 \mu\text{K}$ the critical field is $\mathcal{E} \sim 2500 \text{ V/cm}$.

The cause of this suppression of inelastic scattering is described in detail in Augustovičová and Bohn (2019), which estimates transition amplitudes in the Born approximation as was found useful in the explanation of the phenomenon found out for NO collisions. In a nutshell, for a large field, say $\mathcal{E} > 200$ V/cm, the dominant contribution to the total state-changing rate coefficient is from the final channel $|b, l = 1; M_F = 2\rangle|a, l = 1; M_F = 1\rangle|L = 2, M_L = 1\rangle$. The R-independent off-diagonal matrix elements $|C_{i,f}|$ of dipole-dipole interaction V_{dd} rapidly vanish with an increasing electric field as $\gamma/(d\mathcal{E} + \gamma)$, where γ is the spin-rotation constant, and the contribution to the total inelastic rate from such final channel decreases much faster, with the square of $C_{i,f}$. The weak coupling between a b-level and an a-level is related to the matrix elements of the Stark Hamiltonian H_S diagonal in M_N (the projection of the rotational angular momentum N along the field axis) perturbed by coupling terms that trigger the splitting of $M_N = 1$ energy levels due to spin-rotation interaction.

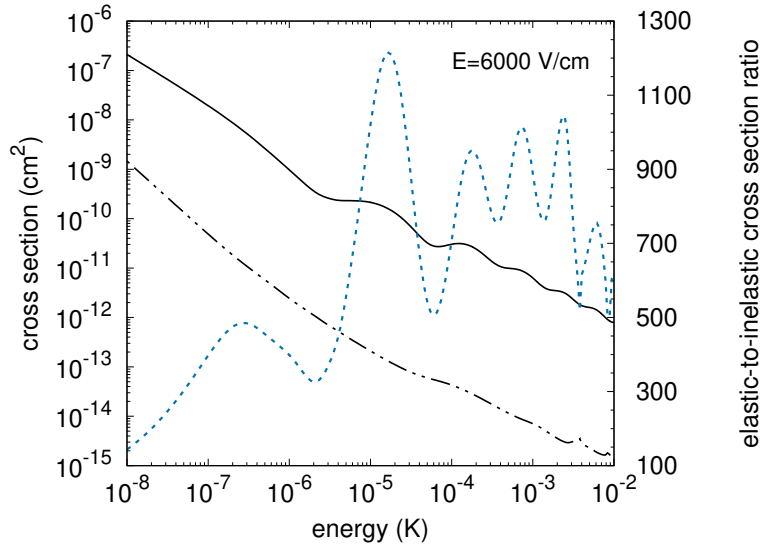


Figure 13: Adapted from Ref. Augustovičová and Bohn (2019): Cross sections for elastic (solid curve), inelastic (dash-dotted curve) scattering, and their ratio (dotted curve, right-hand axis) as a function of collision energy. The collision is initiated in the states $|b, l = 1, M_F = 2\rangle$ of CaOH molecules at an electric field of $\mathcal{E} = 6000$ V/cm.

It turns out that optically trapped CaOH molecules exposed to an electric field in the fine b state with $M_F = 2$ appear to be a suitable candidate for viability of further cooling down to ultracold domain driven by elastic collisions and evaporation. This optimistic message is supported by Fig. 13 showing the calculated elastic σ_{el} versus inelastic σ_{inel} cross sections (and their ratio) versus collision energy at a fixed value of electric field, $\mathcal{E} = 6000$ V/cm. On the whole studied range, from 10 mK down to 10 nK, the ratio $\sigma_{el}/\sigma_{inel}$ exceeds 2

orders of magnitude with a maximum at energies $\sim 10 \mu\text{K}$ evidencing that the ratio can be even 1000 or larger. This ratio plummets to zero with lower collision energies because of the Wigner threshold laws that govern elastic cross section to approach a constant while the state-changing cross section varies as $E_c^{-1/2}$.

In addition, it is predicted that by selecting molecules in the f -state, collisions can create newly described "field-linked" dimers by ramping the electric field across the resonance. Upon formation, the long range field-linked states can hold a molecular dimer $(\text{CaOH})_2$ in the lifetime of μs order (Augustovičová and Bohn, 2019), providing another degree of control by giving the experimenter time to further manipulate the molecules. Such ability could provide excellent tools for studying the reaction chemistry and molecular dynamics.

QUANTUM CHAOS EMERGING FROM COLLISIONS OF COLD MAGNETIC ATOMS

Random Matrix Theory developed by Wigner to describe the statistics of eigenvalues (and eigenfunctions) of quantum many body systems (Wigner, 1955) for heavy nuclei with a large number of degrees of freedom has seen application in various physical problems ranging from fluctuations in spectra of atomic nuclei or molecules (Guhr et al., 1998), through statistical fluctuations observed in scattering processes for these systems, to quantum optics and condensed matter physics (Beenakker, 2001).

Quantum systems manifesting chaotic properties can be classified based on the nearest-neighbor spacing distribution (NNSD) of their eigenvalues (or observed resonances). The distribution of the spacings can be used to characterize the spectral fluctuations and is closely connected with absence or presence of correlation between energy levels. In case of non-interacting energy levels, the NNSD is Poissonian:

$$P_P(s) = \exp(-s),$$

where s is the normalized nearest neighbor spacing. If the interaction between energy levels is very strong, the NNSD is best described by fully chaotic Wigner-Dyson statistics (Wigner surmise) (Podolskiy and Narimanov, 2007):

$$P_{WD}(s) = \frac{\pi}{2} s \exp\left(-\frac{\pi}{4} s^2\right),$$

where the strong repulsion between energy levels is reflected in $P_{WD}(0) = 0$. The intermediate, partially chaotic cases (Karremans et al., 1998; Sakhr and Nieminen, 2005), are best described by Brody distribution (Brody, 1973):

$$P_B(\nu, s) = (1 + \nu) \alpha s^\nu \exp(-\alpha s^{\nu+1}), \quad (18)$$

where $\alpha = [\Gamma((\nu + 2)/(\nu + 1))]^{\nu+1}$ and ν is the Brody parameter that serves as a measure of the chaos in the spectrum. Random, non-chaotic, Poisson spectrum corresponds to $\nu = 0$, while a fully chaotic spectrum, whose levels have characteristics of the eigenvalues of matrices from the Gaussian orthogonal ensemble (GOE), corresponds to the $\nu = 1$.

Theoretical calculations and corresponding experiments show emergence of chaos in complex triatomic systems such as Ar_3 (Leitner et al., 1989) or in reactive scattering of atoms and dimers (Croft et al., 2017). For diatomic molecules, the presence of chaotic behavior is less

obvious due to lesser complexity of these systems. Ultracold dipolar gases, due to inherent anisotropic interactions, have proved to be suitable systems for tests of exotic phenomena in few-body (Bohn et al., 2009; Wang et al., 2011; Mayle et al., 2012; Croft and Bohn, 2014) or many body physics (Ni et al., 2010; Baranov et al., 2012; Kadau et al., 2016), quantum computation (DeMille, 2002; Yelin et al., 2006; Carr et al., 2009) and ultracold chemistry (Quéméner and Julienne, 2012; Miranda et al., 2011; Pérez-Ríos et al., 2014). Recently, manifestations of quantum chaos were reported in collisions of ultracold dysprosium and erbium atoms (Maier et al., 2015b; Frisch et al., 2014; Maier et al., 2015a; Aikawa et al., 2012; Baumann et al., 2014). The nearest-neighbor spacings statistics applied on measured dense spectrum of Fano-Feshbach resonances was very close to Wigner-Dyson distribution (Frisch et al., 2014). In this case, the chaotic behavior of the measured spectra arises from the states that lie energetically just below the dissociation threshold of the dysprosium (or erbium) dimers. These experiments prompted Yang et al., 2017 to investigate the correspondence between classical and quantum chaos in ultracold collisions of dipolar molecules.

As my calculation were inspired by experiments on ultracold erbium and dysprosium atoms, I will briefly describe them. In a standard procedure found e.g. in Aikawa et al. (2012) and Frisch et al. (2014), the atoms are precooled in the magneto-optical trap and then loaded in an optical dipole trap, where the atoms are further cooled by evaporative cooling just slightly above the temperature needed for Bose-Einstein condensation. The trap then contains $\sim 10^5$ atoms with typical number densities of $\sim 10^{13} \text{ cm}^{-3}$ and temperature on the order of hundreds of nanoKelvin. The probing magnetic field is then ramped up to a desired value and after set time suddenly switched off. The number of atoms and the cloud size is then measured by absorption imaging. The typical atom loss spectra of Fano-Feshbach

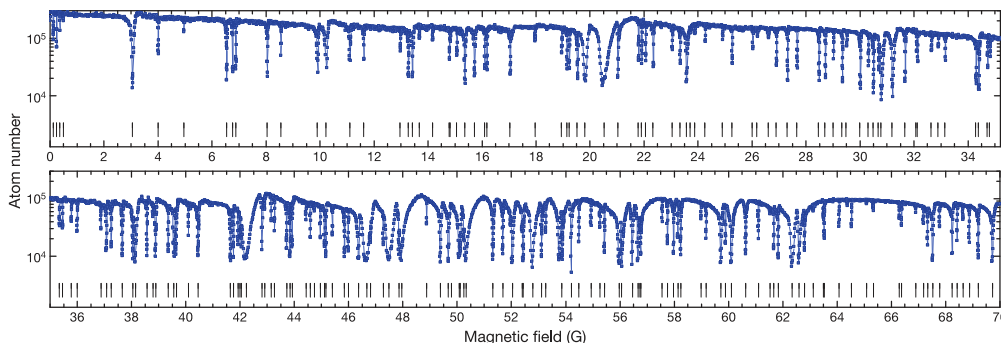


Figure 14: Fano-Feshbach spectrum of ^{166}Er in the energetically lowest Zeeman sublevel from 0 to 70 G as measured at temperature of 330 nK by Frisch et al. (2014) using trap-loss spectroscopy. The figure was adapted from the mentioned publication. Resonance positions are denoted by vertical lines.

resonances as measured by Frisch et al. (2014) are plotted in Fig. 14. At certain values of probing magnetic field some of the states of the dimer (see Fig. 15) are so close to the dissociation threshold so that the weakly bound dimer can be formed in collision of ultracold erbium (or dysprosium) atoms. This is accompanied by measured loss of the atoms in the trap.

We first used a simplified model for erbium and dysprosium dimers taking into account the features of about the right scale and quality. In our approximation the basic structure of rovibrational energy levels and spins is separated from the strong anisotropic couplings that are responsible for the emergence of chaos in the studied systems.

The model Hamilton operator describing a pair of ^{162}Dy atoms (in an external magnetic field) is taken to be

$$H = -\frac{\hbar^2}{2m_r} \left(\frac{d^2}{dR^2} - \frac{L^2}{R^2} \right) + H_1 + H_2 + V_{\text{int}} \equiv H_{\text{diag}} + V_{\text{int}}, \quad (19)$$

where m_r is the reduced mass of the atom pair, $\mathbf{R} = R\hat{\mathbf{R}}$ describes the orientation of and the distance between the two atoms in relative coordinates, L^2 is the squared partial wave angular momentum operator, V_{int} is regarded as interaction Hamiltonian that hold the molecule together and that engenders chaos in the spectra, and H_1 and H_2 are

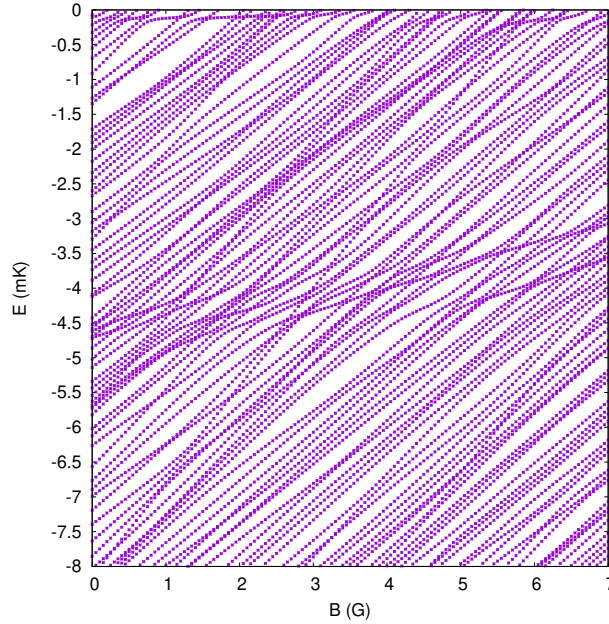


Figure 15: Adapted from Ref. Augustovičová and Bohn (2018a): Simulated spectrum of Dy_2 molecules, versus magnetic field, generated as described in the text. Each energy level at $B = 0$ evolves as the magnetic field is increased, eventually finding its way to zero energy, where it appears as a scattering resonance.

the internal Hamiltonians of the individual atoms, which depend in general on a magnetic field.

Specifically, the interaction term V_{int} is taken to include an isotropic contribution $V_{\text{iso}}(\mathbf{R})$ as well as anisotropic contributions, $V_{\text{dd}}(\mathbf{R})$ and $V_{\text{ad}}(\mathbf{R})$, that also depend on the orientation of the interatomic axis. The isotropic interaction describes an approximately correct long-range van der Waals interaction of Dy_2 with dispersion coefficient $C_6 = 2003$ au (Maier et al., 2015a). This potential is closed off at short range and it has an attractive well with depth 785.7 cm^{-1} (Petrov et al., 2012) to allow the calculation of rovibrational levels. The two total angular momenta $\mathbf{j}_1, \mathbf{j}_2$ of magnetic atoms interact via a long-range magnetic dipole-dipole interaction of the form

$$V_{\text{dd}}(\mathbf{R}) = \left(\frac{g\alpha}{2}\right)^2 \frac{\mathbf{j}_1 \cdot \mathbf{j}_2 - 3(\hat{\mathbf{R}} \cdot \mathbf{j}_1)(\hat{\mathbf{R}} \cdot \mathbf{j}_2)}{R^3}, \quad (20)$$

where α is the fine structure constant, g is the g -factor for the ground $^5\text{I}_8$ state of the Dy atom, whose value is $g = 1.2508$ (Judd and Lindgren, 1961), and $\mathbf{j}_1 = \mathbf{j}_2 = 8$. Furthermore, an anisotropic van der Waals interaction is an expansion in the dipole-dipole interaction given to first order by (Petrov et al., 2012)

$$V_{\text{ad}}(\mathbf{R}) = \frac{C_{\text{ad}}}{\sqrt{6}} \sum_{i=1}^2 \frac{\mathbf{j}_i \cdot \mathbf{j}_i - 3(\hat{\mathbf{R}} \cdot \mathbf{j}_i)(\hat{\mathbf{R}} \cdot \mathbf{j}_i)}{R^6}, \quad (21)$$

where the coefficient C_{ad} sets the strength of this anisotropic dispersion interaction. It has been observed previously that V_{dd} is primarily responsible for anisotropic coupling in Dy_2 , while V_{ad} is more important for Er_2 (Maier et al., 2015b; Yang et al., 2017).

The Hamiltonian matrix can be constructed and diagonalized for any desired value of magnetic field B . Fig. 15 shows the resulting map of molecular binding energies versus B . The intersections of the bound-state spectrum with the $E = 0$ axis indicate crossings of molecular levels with the threshold of two atoms in their lowest Zeeman sublevels $m_j = -8$ and correspond to the Fano-Feshbach resonance locations.

Given the resolution of the experiments (Frisch et al., 2014; Maier et al., 2015a) some of the very narrow Fano-Feshbach resonances could have been unobserved. In our theoretical calculations we are able to resolve all resonances and the Brody parameter is used solely as a measure of chaos. The histogram taken for calculated energy spectrum at zero magnetic field was best fitted with Brody parameter $\nu_E = 1_{-0.23}^{+0}$, while for the histogram drawn for magnetic field spectrum (i.e. Fano-Feshbach resonance spectrum) at $E = 0$ (dissociation threshold energy) we obtained Brody parameter $\nu_B = 0.93_{-0.28}^{+0.07}$ (see Figures 2a and 2b in Augustovičová and Bohn (2018a) for details). Both histograms of the NNS distributions were generated from 250 levels of the spectrum. The stated uncertainties are $1\text{-}\sigma$ uncertainties

arising from the fit of the data to the Brody functions (18), and are mainly given by the counting statistics of data in the histogram. Both spectra are chaotic to a high degree and the chaotic behavior is preserved in the mapping from energy to magnetic field spectra. It is necessary to note, that large statistical uncertainties of our calculations limit the quantitative precision of our results. Nevertheless, within these uncertainties, the obtained value of ν_B is almost consistent, albeit somewhat higher than the values of ~ 0.5 – 0.75 reported for the original ^{164}Dy data (Maier et al., 2015b).

Here it is important to note that the degree of chaos in the experimental data could have been underestimated due to difficulty to detect very narrow resonances. Mur-Petit and Molina (2015) made a new analysis of the original erbium data (Frisch et al., 2014) and concluded that the nearest neighbor spacing distribution is probably underestimating the chaoticity of the system if some of the levels were too narrow to be observed in the spectra. They found out that the data of Frisch et al. (2014) were consistent with a fraction of missing levels of 20–25% with minimum widths of the missing resonances of about 10 mG. Their result hinted that the spectrum was in indeed chaotic but the original analysis was marred by insufficient resolution.

A single statistical evaluation as described above results in relatively large error bars. In order to get more accurate estimates of the corresponding Brody parameters we employ the random matrix theory of Wigner (1955). In this approach, the nonzero matrix elements of V_{int} of a chaotic molecule are represented by random variables with normal distribution centered around zero with a variance of w_0 . In such simulation, a more general description of the molecule can be achieved using the matrix elements with a distribution given by the probability density function (Życzkowski et al., 1992)

$$\begin{aligned} P(w, V_{ii}) &= \frac{1}{\sqrt{2\pi w}} \exp\left(-\frac{V_{ii}^2}{2w^2}\right), \\ P(w, V_{ij}) &= \frac{1}{\sqrt{\pi w}} \exp\left(-\frac{V_{ij}^2}{w^2}\right), \quad i \neq j. \end{aligned} \quad (22)$$

The variance w_0 in this approximate model of Dy_2 molecule is determined from the root-mean-squared variances calculated from the exact non-zero matrix elements. For the $^{164}\text{Dy}_2$ molecule, the calculated width $w_0 = 24.7$ mK. To construct the interaction matrix, the elements that are not zero due to symmetry are filled with random variables described by the GOE distribution (22). The elements of diagonal matrix H_{diag} in Eq. (19) are treated in the same way as in the exact calculation. We then performed a statistical analysis of many generated realizations of models of Dy_2 molecule to obtain an ensemble of independent Brody parameters. This set is further averaged to reduce the uncertainty, while approximately 30 realizations are necessary to decrease the determined uncertainty below 5%. The obtained

Brody parameters were $\nu_E = 0.94 \pm 0.05$, and $\nu_B = 0.98 \pm 0.05$, respectively. This indicates that the approximate model of the Dy_2 molecule is fully chaotic both in energy and magnetic field (i.e. Fano-Feshbach resonance) spectra.

My numerical and semianalytic results have shown that molecule exhibiting partial chaos in its energy spectrum below dissociation threshold can exhibit a similar or even greater degree of chaos in its spectrum of Fano-Feshbach resonances. To sum it up, in the discussed models, the transition from the energies at zero magnetic field to the Fano-Feshbach resonance spectrum at threshold energy involves either a number of avoided crossings or magnetic moment fluctuations of the molecular states that are not trivial in their nature.

CONCLUDING REMARKS

From the above overview of the studied problems and the accompanying publications it follows that the author has achieved the original results in the following areas:

I have investigated the radiative depopulation of helium metastable states 2^3S and 2^1S in collisions with helium, hydrogen and lithium ions within a fully quantum framework. Contrary to general expectation that these processes are governed by dipole moment interactions, I have discovered that in case of He_2^+ formation the radiative association driven by quadrupole moment is as important as that driven by dipole moment. This is the first time such observation was done for this kind of interactions. The comprehensive results on radiative processes involving primordial species can help to improve understanding of chemical evolution of the early Universe and shed more insight on the formation of the first molecules.

Several promising molecular systems were investigated in the search for a possible cosmological variation of proton to electron mass ratio. Actual calculations performed for diatomic hydride radicals revealed that particular energy levels pairs of diatomic radicals can be tuned to degeneracy by means of strong magnetic fields that prevail in many stellar and protostellar objects and that are achievable in the laboratory as well. I have shown that Zeeman tuning allows for a dramatic enhancement of the mass sensitivity coefficients of the involved transitions and also for a substantial reduction of their spectral line broadenings. Moreover, the tuned transitions exhibit favorable intensities, and therefore are being eminently suitable for radioastronomy observations. These findings could possibly result in more stringent constraints on m_p/m_e variation. Currently, I am trying to extend the approach to handle a broader range of classes of molecular transitions.

I have found and explained an effect that a combination of electric and magnetic field greatly enhances the prospect of evaporative cooling for polar molecules colliding in an appropriate state. In case of CaOH molecule I have shown that utilization of this technique can lead to temperatures in nanoKelvin range. A group of scientists led by prof. Doyle at Harvard University is currently attempting to use this proposed procedure to prepare an ultracold sample of CaOH

molecules, which may in the future lead to the development of an extremely precise molecular spectroscopy technique or to the formation of a previously unseen molecular Bose-Einstein condensate. There are several molecules, such as CaOCH_3 that seem to be promising with respect to possibility of their evaporative cooling and the respective calculations are in progress.

I have shown that for ultracold magnetic lanthanide atoms the chaotic scattering emerges due to a combination of anisotropic interaction potentials and Zeeman coupling under an external magnetic field. Several unique features of colliding magnetic lanthanides that have not been observed in any other ultracold atomic system were also discussed. An interesting observation was that molecule exhibiting partial chaos in its energy spectrum below dissociation threshold can exhibit a similar or even greater degree of chaos in its spectrum of Fano-Feshbach resonances.

Finally, I would like to point out that the covered topics are far from exhausted and many outstanding questions remain. The ongoing research is pursued not only by me, my coworkers and students but also by several theoretical and experimental groups abroad. The nature of the studied phenomena is such that international cooperation is crucial for further progress in the field.

MOLECULAR DESCRIPTION AND THEORY
DETAILS: OH

A.1 MOLECULAR HAMILTONIAN IN THE ABSENCE OF FIELD

The zero-field Hamiltonian for the OH molecule in the $X^2\Pi$ electronic ground state can be written as (Brown et al., 1978)

$$H = H_0 + H_{\text{rot}} + H_{\text{fs}} + H_{\text{hfs}} \quad (23)$$

where H_0 denotes the nonrelativistic Hamiltonian of the nonrotating molecule, the nuclear rotational energy operator H_{rot} represents the angular momentum of the rigid nuclear framework, the term H_{fs} describes the fine structure interactions, and H_{hfs} contains terms associated with nuclear spin and nuclear moments known as hyperfine interactions. In the Born-Oppenheimer approximation the first term represents energy of vibrational levels E_{v_i} with vibrational wave functions $v_i(r)$. The explicit form of the other terms in a Hund's case (a) representation are the following:

$$H_{\text{rot}} = B(r)\mathbf{N}^2,$$

where $\mathbf{N} = \mathbf{J} - \mathbf{S}$ and $B(r) = \hbar^2/(2\mu r)$, μ is the reduced mass of the nuclei.

$$H_{\text{fs}} = A(r)T_{q=0}^1(\mathbf{L})T_{q=0}^1(\mathbf{S}) + \gamma(r)(\mathbf{J} - \mathbf{S}) \cdot \mathbf{S} \\ + \sum_{q=\pm 1} \exp(-2iq\phi) [-q_{\Lambda}(r)T_{2q}^2(\mathbf{J}, \mathbf{J}) + (p_{\Lambda}(r) + 2q_{\Lambda}(r))T_{2q}^2(\mathbf{J}, \mathbf{S})],$$

where $A(r)$ is the spin-orbit coupling function, $\gamma(r)$ is the spin-rotation coupling parameter, and $p_{\Lambda}(r)$, $q_{\Lambda}(r)$ are Λ -doubling parameters, ϕ is the electron orbital azimuthal angle.

$$H_{\text{hfs}} = a(r)T_{q=0}^1(\mathbf{I})T_{q=0}^1(\mathbf{L}) + b_F(r)\mathbf{I} \cdot \mathbf{S} + \sqrt{\frac{2}{3}}c(r)T_{q=0}^2(\mathbf{I}, \mathbf{S}) \\ + d(r) \sum_{q=\pm 1} \exp(-2iq\phi)T_{2q}^2(\mathbf{I}, \mathbf{S}),$$

Similarly as in the DUO approach (Yurchenko et al., 2016; Semenov et al., 2016), we treat the full Hamiltonian (23) variationally, so that the eigenstates of H_0 are vibronic states $|v(r), |\Lambda|, S\rangle$ and the effective Hamiltonian $H_{\text{eff}} = H - H_0$ is evaluated in this basis set getting

$$X_{v,v'} = \langle v_i(r)|X(r)|v'_j(r)\rangle \text{ for } X = A, B, \gamma, p_{\Lambda}, q_{\Lambda}, a, b_F, c, d, \quad (24)$$

where $i, j = 0, 1, \dots$

The vibrational basis set functions v_i were obtained by solving the Schrödinger equation for H_0 using the effective potential energy curve which was obtained by morphing the ab initio potential energy curve of (Loo and Groenenboom, 2007) within the framework of the reduced potential energy curve approach (see e.g., Špirko, 2016) by fitting the experimental vibrational energies (Abrams et al., 1994). The resulting vibrational energies are shown in Table S1 in the Supplementary Material of Ref. Augustovičová and Špirko, 2020.

The radial independent tensorial terms of Hamiltonian H_{eff} are set up in hyperfine-rotational uncoupled $|J, M_J, L, S, \Omega, \Sigma, \Lambda\rangle |IM_I\rangle$ Hund's case (a) basis set, where $L = 1, S = 1/2$; Λ, Σ are a projection of L, S onto the molecule's axis, respectively. The spin-orbit interaction splits the ${}^2\Pi$ electronic state into two components, which are characterized by the quantum number $|\Omega|$, where $\Omega = \Lambda + \Sigma$, while $|\Omega| = 3/2$ is the energetically lower component and $|\Omega| = 1/2$ is the upper one. The total angular momentum without nuclear spin $J \geq |\Omega|$, and $I = 1/2$ for ${}^16\text{OH}$. These states are combined into symmetrized eigenstates constructed from linear combinations of $|\pm|\Omega|\rangle$

$$\begin{aligned} & \| \Lambda, J, M_J, |\Omega|, I, M_I, \epsilon \rangle & (25) \\ & = \frac{1}{\sqrt{2}} \left(\| \Lambda, J, M_J, |\Omega|, I, M_I \rangle + \epsilon (-1)^{J-S} | -\Lambda, J, M_J, -|\Omega|, I, M_I \rangle \right) \end{aligned}$$

with the total parity under the inversion operation E^* for each rotational level. These functions can also be classified according to rotationless $p = e/f$ -symmetry, total parity exclusive of a $(-1)^{J-1/2}$ factor, i.e. total wave functions with well-defined p -parity can therefore be

$$\begin{aligned} & |v(r), \Lambda; J, M_J, |\Omega|, I, M_I, \epsilon\rangle \\ & = \frac{1}{\sqrt{2}} \left(|v(r), \Lambda; J, M_J, |\Omega|, I, M_I \rangle \pm |v(r), -\Lambda; J, M_J, -|\Omega|, I, M_I \rangle \right). \end{aligned}$$

The spectroscopic constants $X_{v,v'}$ in (24) entering the effective Hamiltonian H_{eff} (see Table S2 and S3 in the Supplementary Material of Ref. Augustovičová and Špirko, 2020) were obtained by morphing their $X(r)$ approximants expressed as rational functions and by a direct nonlinear fitting the measured line frequencies for Λ -type doubling hyperfine transitions (Amano, 1984; Meerts and Dymanus, 1975; Dousmanis et al., 1955; Radford, 1968; Ball et al., 1970; Coxon et al., 1979; Ter Meulen and Dymanus, 1972; Ter Meulen et al., 1976; Destombes and Marlière, 1975; Destombes et al., 1979; Kolbe et al., 1981) and hyperfine-resolved rotational transitions (Varberg and Evenson, 1993; Blake et al., 1986; Farhoomand et al., 1985). With an exception for $\gamma(r)$, the functional forms of the morphed approximants were deduced from the available ab initio data (Loo and Groenenboom, 2007; Langhoff and Partridge, 1984; Kristiansen and Veseth, 1986): $\gamma(r)$ was assumed to be a linear function in r . To allow for evaluation of the mass dependence of the molecular states, the mass

dependence of each of the Hamiltonian terms was respected explicitly.

A.2 ZEEMAN HAMILTONIAN

If a homogenous magnetic field is applied the molecular magnetic moment interacts with the field and as a result the energy levels are shifted due to the Zeeman effect, with the Zeeman interaction Hamiltonian operator $H_Z = -\boldsymbol{\mu}_s \cdot \mathbf{B}$, where $\boldsymbol{\mu}_s$ is the magnetic moment in the space-fixed reference frame. The magnetic moment of the $|\Omega| = 3/2$ state is large in contrast with the $|\Omega| = 1/2$ state for which the orbital and spin contribution to the molecular magnetic moment nearly cancel. Magnetic field \mathbf{B} is chosen along the space-fixed Z-axis.

The field-free Hamiltonian H is invariant under any rotation of the space fixed axis system, hence the total angular momentum including nuclear spin and its component relative to the space-fixed Z axis, F, M_F (in the coupling scheme $\mathbf{F} = \mathbf{J} + \mathbf{I}$, where the nuclear spin of the hydrogen nucleus \mathbf{J} is coupled with the rotational angular momentum \mathbf{J}) are good quantum numbers. The total parity ϵ as a good quantum label was mentioned earlier. The symmetries of the system are further reduced when an external magnetic field is applied. The term H_Z is not, however, totally symmetric in the group of spatial three-dimensional pure rotations but it is invariant under arbitrary rotation about the direction of \mathbf{B} . In other words the symmetries of H_Z includes precession about the Z axis and inversion of the spatial coordinates of all atoms in a molecule, thus M_F and ϵ remain good quantum numbers.

We adopted the Zeeman Hamiltonian for a diatomic molecule, which contains the isotropic electron spin Zeeman effect, the electron orbital Zeeman effect, the rotational Zeeman effect, the anisotropic electron spin Zeeman effect, the nuclear spin Zeeman effect, extended to the Λ -doubling Zeeman terms for Π molecules (Brown et al., 1978)

$$\begin{aligned} H_Z = \mu_0 B & \left[g_S T_{p=0}^1(\mathbf{S}) + g_L T_{p=0}^1(\mathbf{L}) - g_r(\tau) T_{p=0}^1(\mathbf{J} - \mathbf{L} - \mathbf{S}) \right. \\ & + g_t \sum_{q=\pm 1} D_{0q}^1(\omega)^* T_q^1(\mathbf{S}) \\ & - g'_t \sum_{q=\pm 1} e^{-2iq\phi} D_{0-q}^1(\omega)^* T_q^1(\mathbf{S}) \\ & \left. - g_r^{e'} \sum_{q=\pm 1} \sum_p e^{-2iq\phi} (-1)^p D_{-p-q}^1(\omega)^* T_q^1(\mathbf{J} - \mathbf{S}) \right] \\ & - \mu_N B g_N T_{p=0}^1(\mathbf{I}) - \frac{1}{2} T^2(\chi(r)) T^2(\mathbf{B}, \mathbf{B}), \end{aligned}$$

where μ_0 is the Bohr magneton, μ_N is the nuclear magneton, g_S is the electron spin g-factor, g_L is the electron orbital g-factor, g_r is the rotational g-factor, g_N is the nuclear spin g-factor, and χ is the magnetic susceptibility (Ramos and Bueno, 2006; Flygare, 1974). Note that

a reliable determination of the functions $g_r(r)$ and $\chi(r)$ for open-shell molecules appears as still infeasible. However, for fields weaker than $\sim 10^6$ Gauss, $g_r(r)$ can be treated as a constant and $\chi(r)$ safely neglected (Angel and Landstreet, 1974); in this study we rely on $g_s = 2.00152$, $g_L = 1.00107$, $g_r = -0.000633$, $g_l = 0.00400$, $g'_l = 0.006386$, $g'_r = 0.0020446$ (Brown et al., 1978), and $\chi=0$.

The sought energies of ^1OH in a homogenous magnetic field \mathbf{B} were obtained by diagonalizing the total Hamiltonian $H + H_Z$ as a matrix in the basis (25).

A.3 ESTIMATIONS OF TRANSITION INTENSITIES

The probability of an electric and magnetic dipole transitions from an initial state $|\psi\rangle$ to a final state $|\psi'\rangle$ is proportional to the square of the transition matrix element $\langle\psi|\mathbf{T}_p^1(\boldsymbol{\mu}_s^{\text{el/mag}})|\psi'\rangle$ times a cube of the transition frequency. The spherical irreducible tensor operator of the dipole moment transforms under rotation of the coordinate frame as

$$\mathbf{T}_p^1(\boldsymbol{\mu}_s^{\text{el/mag}}) = \sum_q \mathbf{D}_{pq}^1(\omega)^* \mathbf{T}_q^1(\boldsymbol{\mu}_m^{\text{el/mag}}),$$

where $\mathbf{D}_{pq}^1(\omega)$ are elements of Wigner rotation matrix, ω is a general symbol for a set of three Euler angles. Using a direct product wave function $|((J) \Omega, F, M_F)|v; \Lambda, S, \Sigma\rangle$, we can separate the rotational part involved only by the Wigner D-matrix and vibronic part involved only by $\mathbf{T}_q^1(\boldsymbol{\mu}_m^{\text{el/mag}})$. Employing the Wigner-Eckart theorem we can calculate the rotational matrix element as Brink and Satchler (1994)

$$\begin{aligned} & \langle((J) \Omega, F, M_F)|\mathbf{D}_{pq}^1(\omega)^*|(J') \Omega', F', M'_F\rangle \\ &= (-1)^{F+F'+\Omega+I-M_F+1} [F][F'][J][J'] \\ & \times \begin{pmatrix} F & 1 & F' \\ -M_F & p & M'_F \end{pmatrix} \begin{Bmatrix} F & F' & 1 \\ J' & J & I \end{Bmatrix} \begin{pmatrix} J & 1 & J' \\ -\Omega & q & \Omega' \end{pmatrix}, \end{aligned}$$

where $[F] = \sqrt{2F+1}$ etc. The vibrational transition moment $\langle v; \Lambda, S, \Sigma | \mathbf{T}_q^1(\boldsymbol{\mu}_m^{\text{el/mag}}) | v; \Lambda', S, \Sigma' \rangle \delta_{\Sigma'\Sigma} \delta_{\Lambda'\Lambda}$ for the ground electronic state varies with vibrational quantum number only weakly (Loo and Groenenboom, 2007), therefore we can assume a constant value taken as one for the purpose of the relative intensities determination:

$$I_{\text{rel}}^{\text{el/mag}} \propto |\langle J, M_J, |\Omega|, I, M_I, p | \mathbf{D}_{pq}^1(\omega)^* | J', M'_J, |\Omega'|, I, M'_I, p' \rangle|^2,$$

where the transformation from coupled to uncoupled representation is given as usual via Clebsch-Gordan coefficients

$$|J, M_J, \Omega, I, M_I\rangle = \sum_{F=|J-I|}^{J+I} \sum_{M_F=-F}^F |((J) \Omega, F, M_F)\langle F, M_F | J M_J I M_I \rangle.$$

BIBLIOGRAPHY

- Abrams, M. C., S. P. Davis, M. L. P. Rao, R. Engleman Jr., and J. W. Brault (1994). "High-resolution Fourier transform spectroscopy of the Meinel system of OH." In: *Astrophys. J. Suppl. Ser.* 93, pp. 351–395 (cit. on p. 54).
DOI: [10.1086/192058](https://doi.org/10.1086/192058).
- Aikawa, K., A. Frisch, M. Mark, S. Baier, A. Rietzler, R. Grimm, and F. Ferlaino (2012). "Bose-Einstein Condensation of Erbium." In: *Phys. Rev. Lett.* 108 (21), p. 210401 (cit. on p. 46).
DOI: [10.1103/PhysRevLett.108.210401](https://doi.org/10.1103/PhysRevLett.108.210401).
- Amano, T. (1984). "Difference frequency laser spectroscopy of OH and OD: Simultaneous fit of the infrared and microwave lines." In: *J. Mol. Spectrosc.* 103.2, pp. 436–454 (cit. on p. 54).
DOI: [https://doi.org/10.1016/0022-2852\(84\)90067-5](https://doi.org/10.1016/0022-2852(84)90067-5).
- Anderegg, L., B. L. Augenbraun, Y. Bao, S. Burchesky, L. W. Cheuk, W. Ketterle, and J. M. Doyle (2018). "Laser cooling of optically trapped molecules." In: *Nature Physics* 14.9, pp. 890–893 (cit. on p. 36).
DOI: [10.1038/s41567-018-0191-z](https://doi.org/10.1038/s41567-018-0191-z).
- Angel, J. R. P. and J. D. Landstreet (1974). "A Determination by the Zeeman Effect of the Magnetic Field Strength in the White Dwarf G99-37." In: *Astrophys. J.* 191, pp. 457–464 (cit. on p. 56).
DOI: [10.1086/152984](https://doi.org/10.1086/152984).
- Augenbraun, B. L., Z. D. Lasner, A. Frenett, H. Sawaoka, C. Miller, T. C. Steimle, and J. M. Doyle (2020). "Laser-cooled polyatomic molecules for improved electron electric dipole moment searches." In: *New Journal of Physics* 22.2, p. 022003 (cit. on p. 38).
DOI: [10.1088/1367-2630/ab687b](https://doi.org/10.1088/1367-2630/ab687b).
- Augustovičová, L. (2011). "Radiative association of atoms." MA thesis. Czech Technical University in Prague, Faculty of Nuclear Sciences and Physical Engineering (cit. on p. 15).
- Augustovičová, L. (2014). *Quantum dynamics of small molecules*. Dissertation thesis. Faculty of Mathematics and Physics, Charles University (cit. on p. 14).
- Augustovičová, L., W. P. Kraemer, and P. Soldán (2014a). "Depopulation of metastable helium by radiative association with hydrogen and lithium ions." In: *Astrophys. J.* 782, p. 46 (cit. on pp. 14, 17, 18, 20, 24, 25).
DOI: [10.1088/0004-637X/782/1/46](https://doi.org/10.1088/0004-637X/782/1/46).
- Augustovičová, L., W. P. Kraemer, and P. Soldán (2014b). "Depopulation of metastable helium He(2^1S) by radiative association with

- hydrogen and lithium cations." In: *J. Quant. Spec. Rad. Trans.*, 148. accepted, pp. 27–37 (cit. on pp. 14, 17–19, 24, 25).
DOI: [10.1016/j.jqsrt.2014.06.012](https://doi.org/10.1016/j.jqsrt.2014.06.012).
- Augustovičová, L., W. P. Kraemer, V. Špirko, and P. Soldán (2015a). "The role of molecular quadrupole transitions in the depopulation of metastable helium." In: *Mon. Not. R. Astron. Soc.* 446, pp. 2738–2743 (cit. on pp. 14, 18, 21–24).
DOI: [10.1093/mnras/stu2317](https://doi.org/10.1093/mnras/stu2317).
- Augustovičová, L., P. Soldán, W. P. Kraemer, and V. Špirko (2014c). "Potential microwave probes of the proton-to-electron mass ratio at very high redshifts." In: *Mon. Not. R. Astron. Soc.* 439, pp. 1136–1139 (cit. on pp. 12, 29–31).
DOI: [10.1093/mnras/stu060](https://doi.org/10.1093/mnras/stu060).
- Augustovičová, L., P. Soldán, and V. Špirko (2016). "Effective hyperfine structure functions of ammonia." In: *The Astrophysical Journal* 824, p. 147 (cit. on pp. 28, 31).
DOI: [10.3847/0004-637x/824/2/147](https://doi.org/10.3847/0004-637x/824/2/147).
- Augustovičová, L., V. Špirko, W. P. Kraemer, and P. Soldán (2012). "Radiative association of LiHe^+ ." In: *Chem. Phys. Lett.* 531, pp. 59–63 (cit. on pp. 14, 16, 20, 24, 25).
DOI: [10.1016/j.cplett.2012.02.038](https://doi.org/10.1016/j.cplett.2012.02.038).
- Augustovičová, L., V. Špirko, W. P. Kraemer, and P. Soldán (2013a). "Radiative association of He_2^+ revisited." In: *Astron. Astrophys.* 553, A42 (cit. on pp. 14, 16).
DOI: [10.1088/0004-637X/749/1/22](https://doi.org/10.1088/0004-637X/749/1/22).
- Augustovičová, L., V. Špirko, W. P. Kraemer, and P. Soldán (2013b). "Radiative association of He_2^+ : the role of quartet states." In: *Mon. Not. R. Astron. Soc.* 435, pp. 1541–1546 (cit. on pp. 14, 17).
DOI: [10.1093/mnras/stt1395](https://doi.org/10.1093/mnras/stt1395).
- Augustovičová, L. D. and J. L. Bohn (2017). "No evaporative cooling of nitric oxide in its ground state." In: *Phys. Rev. A* 96, p. 042712 (cit. on pp. 40, 41).
DOI: [10.1103/PhysRevA.96.042712](https://doi.org/10.1103/PhysRevA.96.042712).
- Augustovičová, L. D. and J. L. Bohn (2018a). "Manifestation of quantum chaos in Fano-Feshbach resonances." In: *Physical Review A* 98, p. 023419 (cit. on pp. 47, 48).
DOI: [10.1103/PhysRevA.98.023419](https://doi.org/10.1103/PhysRevA.98.023419).
- Augustovičová, L. D. and J. L. Bohn (2018b). "NO evaporative cooling in the $^2\Pi_{3/2}$ state." In: *Phys. Rev. A* 97, p. 062703 (cit. on pp. 40, 41).
DOI: [10.1103/PhysRevA.97.062703](https://doi.org/10.1103/PhysRevA.97.062703).
- Augustovičová, L. D. and J. L. Bohn (2019). "Ultracold collisions of polyatomic molecules: CaOH ." In: *New Journal of Physics* 21.10, p. 103022 (cit. on pp. 38, 39, 42–44).
DOI: [10.1088/1367-2630/ab4720](https://doi.org/10.1088/1367-2630/ab4720).

- Augustovičová, L. D. and V. Špirko (2020). “Zeeman molecular probe for tests of fundamental physical constants.” In: *Monthly Notices of the Royal Astronomical Society* 494.2, pp. 1675–1680 (cit. on pp. 33, 34, 54).
DOI: [10.1093/mnras/staa792](https://doi.org/10.1093/mnras/staa792).
- Augustovičová, L., M. Zámečnicková, W. P. Kraemer, and P. Soldán (2015b). “Radiative association of He(2^3P) with lithium cations.” In: *Chemical Physics* 462. Inelastic Processes in Atomic, Molecular and Chemical Physics, pp. 65–70 (cit. on pp. 14, 17, 18).
DOI: [10.1016/j.chemphys.2015.07.003](https://doi.org/10.1016/j.chemphys.2015.07.003).
- Avdeenkov, A. V. and J. L. Bohn (2002). “Collisional dynamics of ultracold OH molecules in an electrostatic field.” In: *Phys. Rev. A* 66 (5), p. 052718 (cit. on p. 42).
DOI: [10.1103/PhysRevA.66.052718](https://doi.org/10.1103/PhysRevA.66.052718).
- Babb, J. F. and A. Dalgarno (1995). “Radiative association and inverse predissociation of oxygen atoms.” In: *Phys. Rev. A* 51, pp. 3021–3026 (cit. on p. 13).
DOI: [10.1103/PhysRevA.51.3021](https://doi.org/10.1103/PhysRevA.51.3021).
- Bacchus-Montabonel, M.-C. and D. Talbi (1999). “A theoretical treatment of the LiH and BeH formation through radiative association.” In: *J. Mol. Struct. (Theochem)* 463, pp. 91–97 (cit. on p. 14).
DOI: [10.1016/S0166-1280\(98\)00397-2](https://doi.org/10.1016/S0166-1280(98)00397-2).
- Bagdonaite, J., M. Daprà, P. Jansen, H. L. Bethlem, W. Ubachs, S. Muller, C. Henkel, and K. M. Menten (2013a). “Robust Constraint on a Drifting Proton-to-Electron Mass Ratio at $z=0.89$ from Methanol Observation at Three Radio Telescopes.” In: *Phys. Rev. Lett.* 111, p. 231101 (cit. on p. 28).
DOI: [10.1103/PhysRevLett.111.231101](https://doi.org/10.1103/PhysRevLett.111.231101).
- Bagdonaite, J., P. Jansen, C. Henkel, H. L. Bethlem, K. M. Menten, and W. Ubachs (2013b). “A stringent limit on a drifting proton-to-electron mass ratio from alcohol in the early Universe.” In: *Science* 339, pp. 46–48 (cit. on p. 28).
DOI: [10.1126/science.1224898](https://doi.org/10.1126/science.1224898).
- Ball, J. A., D. F. Dickinson, C. A. Gottlieb, and H. E. Radford (1970). “The 3.8-cm Spectrum of OH: Laboratory Measurement and Low-Noise Search in W₃ (OH).” In: *The Astronomical Journal* 75, p. 762 (cit. on p. 54).
DOI: [10.1086/111022](https://doi.org/10.1086/111022).
- Baranov, M. A., M. Dalmonte, G. Pupillo, and P. Zoller (2012). “Condensed Matter Theory of Dipolar Quantum Gases.” In: 112.9, pp. 5012–5061 (cit. on p. 46).
DOI: [10.1021/cr2003568](https://doi.org/10.1021/cr2003568).
- Barry, J. F., D. J. McCarron, E. B. Norrgard, M. H. Steinecker, D. DeMille, J. F. Barry, D. J. McCarron, E. B. Norrgard, et al. (2014).

- “Magneto-optical trapping of a diatomic molecule.” In: *Nature* 512, pp. 286–289 (cit. on p. 36).
DOI: [10.1038/nature13634](https://doi.org/10.1038/nature13634).
- Bates, D. R. (1951). “Rate of formation of molecules by radiative association.” In: *Mon. Not. R. Astron. Soc.* 111, pp. 303–314 (cit. on p. 13).
DOI: [10.1093/mnras/111.3.303](https://doi.org/10.1093/mnras/111.3.303).
- Bates, D. R. and L. Spitzer (1951). “The density of molecules in interstellar space.” In: *Astrophys. J.* 113, pp. 414–463 (cit. on p. 13).
DOI: [10.1086/145415](https://doi.org/10.1086/145415).
- Baumann, K., N. Q. Burdick, M. Lu, and B. L. Lev (2014). “Observation of low-field Fano-Feshbach resonances in ultracold gases of dysprosium.” In: *Phys. Rev. A* 89 (2), p. 020701 (cit. on p. 46).
DOI: [10.1103/PhysRevA.89.020701](https://doi.org/10.1103/PhysRevA.89.020701).
- Beenakker, C. W. J. (2001). *The Oxford Handbook of Random Matrix Theory*. Ed. by P. D. F. G. Akemann J. Baik. Oxford: Oxford University Press, pp. 723–758 (cit. on p. 45).
- Belov, S., Š. Urban, and G. Winnewisser (1998). “Hyperfine Structure of Rotation-Inversion Levels in the Excited v_2 State of Ammonia.” In: *Journal of Molecular Spectroscopy* 189.1, pp. 1–7 (cit. on p. 31).
DOI: <https://doi.org/10.1006/jmsp.1997.7516>.
- Beloy, K., A. Borschevsky, P. Schwerdtfeger, and V. V. Flambaum (2010). “Enhanced sensitivity to the time variation of the fine-structure constant and m_p/m_e in diatomic molecules: A closer examination of silicon monobromide.” In: *Phys. Rev. A* 82 (2), p. 022106 (cit. on p. 27).
DOI: [10.1103/PhysRevA.82.022106](https://doi.org/10.1103/PhysRevA.82.022106).
- Belyaev, A. K., L. Augustovičová, P. Soldán, and W. P. Kraemer (2014). “Non-radiative inelastic processes in lithium-helium ion-atom collisions.” In: *Astron. Astrophys.* 565, A106 (cit. on pp. 19, 24, 25).
DOI: [10.1051/0004-6361/201423578](https://doi.org/10.1051/0004-6361/201423578).
- Belyaev, A. K., D. S. Rodionov, L. Augustovičová, P. Soldán, and W. P. Kraemer (2015). “Full quantum study of non-radiative inelastic processes in lithium–helium ion–atom collisions.” In: *Mon. Not. R. Astron. Soc.* 449, pp. 3323–3332 (cit. on pp. 17, 24, 25).
DOI: [10.1093/mnras/stv391](https://doi.org/10.1093/mnras/stv391).
- Bennett, O. J., A. S. Dickinson, T. Leininger, and F. X. Gadéa (2003). “Radiative association in Li+H revisited: the role of quasi-bound states.” In: *Mon. Not. R. Astron. Soc.* 341, pp. 361–368 (cit. on p. 14).
DOI: [10.1111/j.1365-2966.2008.12586.x](https://doi.org/10.1111/j.1365-2966.2008.12586.x).
- Bernath, P. F. (2005). *Spectra of Atoms and Molecules*. 2nd. New York: Oxford University Press (cit. on pp. 16, 17).
- Bertone, G. (2013). *Particle Dark Matter: Observations, Models and Searches*. Cambridge, UK: Cambridge University Press (cit. on p. 26).

- Beyer, M. and F. Merkt (2018). "Half-Collision Approach to Cold Chemistry: Shape Resonances, Elastic Scattering, and Radiative Association in the $H^+ + H$ and $D^+ + D$ Collision Systems." In: *Phys. Rev. X* 8, p. 031085 (cit. on p. 13).
DOI: [10.1103/PhysRevX.8.031085](https://doi.org/10.1103/PhysRevX.8.031085).
- Bichsel, B. J., M. A. Morrison, N. Shafer-Ray, and E. R. I. Abraham (2007). "Experimental and theoretical investigation of the Stark effect for manipulating cold molecules: Application to nitric oxide." In: *Phys. Rev. A* 75, p. 023410 (cit. on p. 40).
DOI: [10.1103/PhysRevA.75.023410](https://doi.org/10.1103/PhysRevA.75.023410).
- Blake, G. A., J. Farhoomand, and H. M. Pickett (1986). "The far-infrared rotational spectrum of $X^2\Pi$ OH." In: *J. Mol. Spectrosc.* 115.1, pp. 226–228 (cit. on p. 54).
DOI: [https://doi.org/10.1016/0022-2852\(86\)90289-4](https://doi.org/10.1016/0022-2852(86)90289-4).
- Bohn, J. L., M. Cavagnero, and C. Ticknor (2009). "Quasi-universal dipolar scattering in cold and ultracold gases." In: *New Journal of Physics* 11.5, p. 055039 (cit. on p. 46).
DOI: [10.1088/1367-2630/11/5/055039](https://doi.org/10.1088/1367-2630/11/5/055039).
- Bohn, J. L. and D. S. Jin (Feb. 2014). "Differential scattering and rethermalization in ultracold dipolar gases." In: *Phys. Rev. A* 89 (2), p. 022702 (cit. on p. 36).
DOI: [10.1103/PhysRevA.89.022702](https://doi.org/10.1103/PhysRevA.89.022702).
- Bohn, J. L., A. M. Rey, and J. Ye (2017). "Cold molecules: Progress in quantum engineering of chemistry and quantum matter." In: *Science* 357.6355, pp. 1002–1010 (cit. on p. 36).
DOI: [10.1126/science.aam6299](https://doi.org/10.1126/science.aam6299).
- Bovino, S., M. Tacconi, and F. A. Gianturco (2011). "Photon-induced evolutionary rates of $LiHe^+$ ($^1\Sigma^+$) in early Universe from accurate quantum computations." In: *Astrophys. J.* 740, p. 101 (cit. on p. 14).
DOI: [10.1088/0004-637X/740/2/101](https://doi.org/10.1088/0004-637X/740/2/101).
- Brink, D. M. and G. R. Satchler (1994). *Angular Momentum*. 3rd. Oxford: Clarendon Press (cit. on p. 56).
- Brody, T. A. (1973). "A statistical measure for the repulsion of energy levels." In: *Lett. Nuovo Cimento* 7.12, pp. 482–484 (cit. on p. 45).
DOI: [10.1007/BF02727859](https://doi.org/10.1007/BF02727859).
- Brown, J., M. Kaise, C. Kerr, and D. Milton (1978). "A determination of fundamental Zeeman parameters for the OH radical." In: *Mol. Phys.* 36.2, pp. 553–582 (cit. on pp. 53, 55, 56).
DOI: [10.1080/00268977800101761](https://doi.org/10.1080/00268977800101761).
- Cahn, S. B., J. Ammon, E. Kirilov, Y. V. Gurevich, D. Murphree, R. Paolino, D. A. Rahmlow, M. G. Kozlov, et al. (2014). "Zeeman-Tuned Rotational Level-Crossing Spectroscopy in a Diatomic Free Radical." In: *Phys. Rev. Lett.* 112 (16), p. 163002 (cit. on p. 33).
DOI: [10.1103/PhysRevLett.112.163002](https://doi.org/10.1103/PhysRevLett.112.163002).

- Carr, L. D., D. DeMille, R. V. Krems, and J. Ye (2009). "Cold and ultracold molecules: science, technology and applications." In: *New Journal of Physics* 11.5, p. 055049 (cit. on p. 46).
DOI: [10.1088/1367-2630/11/5/055049](https://doi.org/10.1088/1367-2630/11/5/055049).
- Carrington, A. (1996). "Microwave spectroscopy at the dissociation limit." In: *Science* 274, pp. 1327–1331 (cit. on p. 30).
DOI: [10.1126/science.274.5291.1327](https://doi.org/10.1126/science.274.5291.1327).
- Carrington, A., A. M. Shaw, and S. M. Taylor (1995). "Ion-beam spectroscopy of long-range complexes." In: *J. Chem. Soc. Faraday Trans.* 91, pp. 3725–3740 (cit. on p. 30).
DOI: [10.1039/ft9959103725](https://doi.org/10.1039/ft9959103725).
- Chae, E., L. Anderegg, B. L. Augenbraun, A. Ravi, B. Hemmerling, N. R. Hutzler, A. L. Collopy, J. Ye, et al. (2017). "One-dimensional magneto-optical compression of a cold CaF molecular beam." In: *New Journal of Physics* 19, p. 033035 (cit. on p. 36).
DOI: [10.1088/1367-2630/aa6470](https://doi.org/10.1088/1367-2630/aa6470).
- Cheuk, L. W., L. Anderegg, B. L. Augenbraun, Y. Bao, S. Burchesky, W. Ketterle, and J. M. Doyle (Aug. 2018). "~-Enhanced Imaging of Molecules in an Optical Trap." In: *Phys. Rev. Lett.* 121 (8), p. 083201 (cit. on p. 36).
DOI: [10.1103/PhysRevLett.121.083201](https://doi.org/10.1103/PhysRevLett.121.083201).
- Chin, C., V. V. Flambaum, and M. G. Kozlov (2009). "Ultracold molecules: new probes on the variation of fundamental constants." In: *New Journal of Physics* 11.5, p. 055048 (cit. on p. 27).
DOI: [10.1088/1367-2630/11/5/055048](https://doi.org/10.1088/1367-2630/11/5/055048).
- Chin, C. and V. V. Flambaum (2006). "Enhanced Sensitivity to Fundamental Constants In Ultracold Atomic and Molecular Systems near Feshbach Resonances." In: *Phys. Rev. Lett.* 96 (23), p. 230801 (cit. on p. 27).
DOI: [10.1103/PhysRevLett.96.230801](https://doi.org/10.1103/PhysRevLett.96.230801).
- Cooley, J. W. (1961). "An improved eigenvalue corrector formula for solving the Schrödinger equation for central fields." In: *Math. Comput.* 15, pp. 363–374 (cit. on p. 15).
DOI: [10.1090/S0025-5718-1961-0129566-X](https://doi.org/10.1090/S0025-5718-1961-0129566-X).
- Coxon, J. A., K. V. L. N. Sastry, J. A. Austin, and D. H. Levy (1979). "The microwave spectrum of the OH X²Π radical in the ground and vibrationally-excited ($v \leq 6$) levels." In: *Canadian Journal of Physics* 57.5, pp. 619–634 (cit. on p. 54).
DOI: [10.1139/p79-089](https://doi.org/10.1139/p79-089).
- Croft, J. F. E., C. Makrides, M. Li, A. Petrov, B. K. Kendrick, N. Balakrishnan, and S. Kotochigova (2017). "Universality and chaoticity in ultracold K plus KRb chemical reactions." In: *Nature Communications* 8, p. 15897 (cit. on p. 45).
DOI: [10.1038/ncomms15897](https://doi.org/10.1038/ncomms15897).

- Croft, J. F. E. and J. L. Bohn (2014). "Long-lived complexes and chaos in ultracold molecular collisions." In: *Phys. Rev. A* 89 (1), p. 012714 (cit. on p. 46).
DOI: [10.1103/PhysRevA.89.012714](https://doi.org/10.1103/PhysRevA.89.012714).
- Crutcher, R. M. (1999). "Magnetic Fields in Molecular Clouds: Observations Confront Theory." In: *The Astrophysical Journal* 520.2, pp. 706–713 (cit. on p. 33).
DOI: [10.1086/307483](https://doi.org/10.1086/307483).
- Crutcher, R. M. (2012). "Magnetic Fields in Molecular Clouds." In: *Annual Review of Astronomy and Astrophysics* 50.1, pp. 29–63 (cit. on p. 33).
DOI: [10.1146/annurev-astro-081811-125514](https://doi.org/10.1146/annurev-astro-081811-125514).
- Dalgarno, A., K. Kirby, and P. C. Stancil (1996). "The radiative association of Li^+ and H, Li and H^+ , and Li and H." In: *Astrophys. J.* 458, pp. 397–400 (cit. on p. 13).
DOI: [10.1086/176823](https://doi.org/10.1086/176823).
- DeMille, D. (2002). "Quantum Computation with Trapped Polar Molecules." In: *Phys. Rev. Lett.* 88 (6), p. 067901 (cit. on p. 46).
DOI: [10.1103/PhysRevLett.88.067901](https://doi.org/10.1103/PhysRevLett.88.067901).
- Destombes, J., B. Lemoine, and C. Marlière-Demuynck (1979). "Microwave spectrum of the hydroxyl radical in the $v = 1 \ ^2\Pi_{3/2}$ state." In: *Chem. Phys. Lett.* 60.3, pp. 493–495 (cit. on p. 54).
DOI: [https://doi.org/10.1016/0009-2614\(79\)80619-3](https://doi.org/10.1016/0009-2614(79)80619-3).
- Destombes, J. and C. Marlière (1975). "Measurement of hyperfine splitting in the OH radical by a radio-frequency microwave double resonance method." In: *Chem. Phys. Lett.* 34.3, pp. 532–536 (cit. on p. 54).
DOI: [https://doi.org/10.1016/0009-2614\(75\)85556-4](https://doi.org/10.1016/0009-2614(75)85556-4).
- Dickinson, A. S. (2005). "Radiative association of H and D." In: *J. Phys. B* 38, pp. 4329–4334 (cit. on p. 14).
DOI: [10.1088/0953-4075/38/23/014](https://doi.org/10.1088/0953-4075/38/23/014).
- Dine, M. and A. Kusenko (2003). "Origin of the matter-antimatter asymmetry." In: *Rev. Mod. Phys.* 76 (1), pp. 1–30 (cit. on p. 26).
DOI: [10.1103/RevModPhys.76.1](https://doi.org/10.1103/RevModPhys.76.1).
- Dousmanis, G. C., T. M. Sanders, and C. H. Townes (1955). "Microwave Spectra of the Free Radicals OH and OD." In: *Phys. Rev.* 100 (6), pp. 1735–1754 (cit. on p. 54).
DOI: [10.1103/PhysRev.100.1735](https://doi.org/10.1103/PhysRev.100.1735).
- Drake, G. W. F. (1971). "Theory of relativistic magnetic dipole transitions: lifetime of the metastable 2^3S state of the heliumlike ions." In: *Phys. Rev. A* 3, pp. 908–915 (cit. on p. 13).
DOI: [10.1103/PhysRevA.3.908](https://doi.org/10.1103/PhysRevA.3.908).
- Elioff, M. S., J. J. Valentini, and D. W. Chandler (2003). "Subkelvin Cooling NO Molecules via "Billiard-like" Collisions with Argon." In: 302, pp. 1940–1943 (cit. on p. 40).
DOI: [10.1126/science.1090679](https://doi.org/10.1126/science.1090679).

- Farhoomand, J., H. M. Pickett, and G. A. Blake (1985). "Direct measurement of the fundamental rotational transitions of the OH radical by laser sideband spectroscopy." In: *Astrophys. J. Lett.* 291, pp. L19–L22 (cit. on p. 54).
DOI: [10.1086/184450](https://doi.org/10.1086/184450).
- Flambaum, V. V. (2006). "Enhanced Effect of Temporal Variation of the Fine Structure Constant and the Strong Interaction in ^{229}Th ." In: *Phys. Rev. Lett.* 97 (9), p. 092502 (cit. on p. 27).
DOI: [10.1103/PhysRevLett.97.092502](https://doi.org/10.1103/PhysRevLett.97.092502).
- Flambaum, V. V. and M. G. Kozlov (2007). "Enhanced Sensitivity to the Time Variation of the Fine-Structure Constant and m_p/m_e in Diatomic Molecules." In: *Phys. Rev. Lett.* 99 (15), p. 150801 (cit. on pp. 27, 28).
DOI: [10.1103/PhysRevLett.99.150801](https://doi.org/10.1103/PhysRevLett.99.150801).
- Flygare, W. H. (1974). "Magnetic interactions in molecules and an analysis of molecular electronic charge distribution from magnetic parameters." In: *Chemical Reviews* 74, pp. 653–687 (cit. on p. 55).
DOI: [10.1021/cr60292a003](https://doi.org/10.1021/cr60292a003).
- Frisch, A., M. Mark, K. Aikawa, F. Ferlaino, J. L. Bohn, C. Makrides, A. Petrov, and S. Kotochigova (2014). "Quantum chaos in ultracold collisions of gas-phase erbium atoms." In: *Nature* 507 (7493), p. 475 (cit. on pp. 46–49).
DOI: [10.1038/nature13137](https://doi.org/10.1038/nature13137).
- Gacesa, M. and R. Côté (2014). "Photoassociation of ultracold molecules near a Feshbach resonance as a probe of the electron–proton mass ratio variation." In: *J. Mol. Spectrosc.* 300. Spectroscopic Tests of Fundamental Physics, pp. 124–130 (cit. on p. 27).
DOI: <https://doi.org/10.1016/j.jms.2014.03.005>.
- Gerlich, D. and S. Horning (1992). "Experimental investigation of radiative association processes as related to interstellar chemistry." In: *Chem. Rev.* 92, pp. 1509–1539 (cit. on p. 13).
DOI: [10.1021/cr00015a003](https://doi.org/10.1021/cr00015a003).
- Gerlich, D., P. Jusko, S. Roucka, I. Zymak, R. Plasil, and J. Glosik (2012). "Ion Trap Studies of $\text{H}^- + \text{H} \rightarrow \text{H}_2 + \text{e}^-$ Between 10 and 135 K." In: *Astrophys. J.* 749.1, 22, p. 22 (cit. on p. 12).
DOI: [10.1088/0004-637X/749/1/22](https://doi.org/10.1088/0004-637X/749/1/22).
- Gianturco, F. A. and P. G. Giorgi (1996). "Radiative association of LiH ($X^1\Sigma^+$) from electronically excited lithium atoms." In: *Phys. Rev. A* 54, pp. 4073–4077 (cit. on p. 14).
DOI: [10.1103/PhysRevA.54.4073](https://doi.org/10.1103/PhysRevA.54.4073).
- Gianturco, F. A. and P. G. Giorgi (1997). "Radiative association rates and structure of resonances for Li and Li^+ colliding with H and H^+ ." In: *Astrophys. J.* 479, pp. 560–567 (cit. on p. 14).
DOI: [10.1086/303902](https://doi.org/10.1086/303902).

- Godun, R. M., P. B. R. Nisbet-Jones, J. M. Jones, S. A. King, L. A. M. Johnson, H. S. Margolis, K. Szymaniec, S. N. Lea, et al. (2014). "Frequency Ratio of Two Optical Clock Transitions in $^{171}\text{Yb}^+$ and Constraints on the Time Variation of Fundamental Constants." In: *Phys. Rev. Lett.* 113, p. 210801 (cit. on pp. 26, 28).
DOI: [10.1103/PhysRevLett.113.210801](https://doi.org/10.1103/PhysRevLett.113.210801).
- Guhr, T., A. Müller-Groeling, and H. A. Weidenmüller (1998). "Random-matrix theories in quantum physics: common concepts." In: *Physics Reports* 299.4, pp. 189–425 (cit. on p. 45).
DOI: [https://doi.org/10.1016/S0370-1573\(97\)00088-4](https://doi.org/10.1016/S0370-1573(97)00088-4).
- Güsten, R., H. Wiesemeyer, D. Neufeld, K. M. Menten, U. U. Graf, K. Jacobs, B. Klein, O. Ricken, et al. (2019). "Astrophysical detection of the helium hydride ion HeH^+ ." In: *Nature* 568.7752, pp. 357–359 (cit. on p. 12).
DOI: [10.1038/s41586-019-1090-x](https://doi.org/10.1038/s41586-019-1090-x).
- Henkel, C., Braatz, J. A., Menten, K. M., and Ott, J. (2008). "The kinetic temperature of a molecular cloud at redshift 0.9: ammonia in the gravitational lens PKS0-211." In: *A&A* 485, pp. 451–456 (cit. on p. 32).
DOI: [10.1051/0004-6361:20079140](https://doi.org/10.1051/0004-6361:20079140).
- Henkel, C., Jethava, N., Kraus, A., Menten, K. M., Carilli, C. L., Grasshoff, M., Lubowich, D., and Reid, M. J. (2005). "The kinetic temperature of a molecular cloud at redshift 0.7: ammonia in the gravitational lens B0218+357." In: *A&A* 440, pp. 893–899 (cit. on p. 32).
DOI: [10.1051/0004-6361:20052816](https://doi.org/10.1051/0004-6361:20052816).
- Henkel, C., Menten, K. M., Murphy, M. T., Jethava, N., Flambaum, V. V., Braatz, J. A., Muller, S., Ott, J., et al. (2009). "The density, the cosmic microwave background, and the proton-to-electron mass ratio in a cloud at redshift 0.9." In: *A&A* 500, pp. 725–734 (cit. on p. 28).
DOI: [10.1051/0004-6361/200811475](https://doi.org/10.1051/0004-6361/200811475).
- Hodgman, S. S., R. G. Dall, L. J. Byron, K. G. H. Baldwin, S. J. Buckman, and A. G. Truscott (2009). "Metastable helium: a new determination of the longest atomic excited-state lifetime." In: *Phys. Rev. Lett.* 103, 053002 (cit. on p. 13).
DOI: [10.1103/PhysRevLett.103.053002](https://doi.org/10.1103/PhysRevLett.103.053002).
- Huntemann, N., B. Lipphardt, C. Tamm, V. Gerginov, S. Weyers, and E. Peik (2014). "Improved Limit on a Temporal Variation of m_p/m_e from Comparisons of Yb^+ and Cs Atomic Clocks." In: *Phys. Rev. Lett.* 113, p. 210802 (cit. on pp. 26, 28).
DOI: [10.1103/PhysRevLett.113.210802](https://doi.org/10.1103/PhysRevLett.113.210802).
- Hutzler, N. R., H.-I. Lu, and J. M. Doyle (2012). "The Buffer Gas Beam: An Intense, Cold, and Slow Source for Atoms and Molecules." In: *Chemical Reviews* 112.9, pp. 4803–4827 (cit. on p. 36).
DOI: [10.1021/cr200362u](https://doi.org/10.1021/cr200362u).

- Isaev, T. A. and R. Berger (2016). "Polyatomic Candidates for Cooling of Molecules with Lasers from Simple Theoretical Concepts." In: *Phys. Rev. Lett.* 116 (6), p. 063006 (cit. on p. 38).
DOI: [10.1103/PhysRevLett.116.063006](https://doi.org/10.1103/PhysRevLett.116.063006).
- Jansen, P., H. L. Bethlem, and W. Ubachs (2014). "Perspective: Tipping the scales: Search for drifting constants from molecular spectra." In: *J. Chem. Phys.* 140, 010901 (cit. on pp. 28, 29).
DOI: [10.1063/1.4853735](https://doi.org/10.1063/1.4853735).
- Jansen, P., I. Kleiner, C. Meng, R. M. Lees, M. H. Janssen, W. Ubachs, and H. L. Bethlem (2013). "Prospects for high-resolution microwave spectroscopy of methanol in a Stark-deflected molecular beam." In: *Molecular Physics* 111.12-13, pp. 1923–1930 (cit. on p. 27).
DOI: [10.1080/00268976.2013.802819](https://doi.org/10.1080/00268976.2013.802819).
- Jenč, F. (1983). "The Reduced Potential Curve Method for Diatomic Molecules and Its Applications." In: *Advances in Atomic and Molecular Physics* 19. Ed. by D. Bates and B. Bederson, pp. 265–307 (cit. on p. 30).
DOI: [https://doi.org/10.1016/S0065-2199\(08\)60255-9](https://doi.org/10.1016/S0065-2199(08)60255-9).
- Jenč, F., B. A. Brandt, V. Špirko, and O. Bludský (1993). "Estimation of the ground-state potentials of alkali-metal diatomic molecules with the use of the multiparameter generalized reduced-potential-curve method." In: *Phys. Rev. A* 48, pp. 1319–1327 (cit. on p. 30).
DOI: [10.1103/PhysRevA.48.1319](https://doi.org/10.1103/PhysRevA.48.1319).
- Johnson, B. R. (1973). "The multichannel log-derivative method for scattering calculations." In: *Journal of Computational Physics* 13.3, pp. 445–449 (cit. on p. 40).
DOI: [http://dx.doi.org/10.1016/0021-9991\(73\)90049-1](http://dx.doi.org/10.1016/0021-9991(73)90049-1).
- Judd, B. R. and I. Lindgren (June 1961). "Theory of Zeeman Effect in the Ground Multiplets of Rare-Earth Atoms." In: *Phys. Rev.* 122 (6), pp. 1802–1812 (cit. on p. 48).
DOI: [10.1103/PhysRev.122.1802](https://doi.org/10.1103/PhysRev.122.1802).
- Juřek, M., V. Špirko, and W. P. Kraemer (1995). "Ab-initio determination of the rate coefficients for radiative association of He(¹S)+H⁺." In: *Chem. Phys.* 193, pp. 287–296 (cit. on p. 14).
DOI: [10.1016/0301-0104\(94\)00428-D](https://doi.org/10.1016/0301-0104(94)00428-D).
- Kadau, H., M. Schmitt, M. Wenzel, C. Wink, T. Maier, I. Ferrier-Barbut, and T. Pfau (2016). "Observing the Rosensweig instability of a quantum ferrofluid." In: *Nature* 530.7589, pp. 194–197 (cit. on p. 46).
DOI: [10.1038/nature16485](https://doi.org/10.1038/nature16485).
- Kanekar, N. (2011). "Constraining changes in the proton-electron mass ratio with inversion and rotational lines." In: *The Astrophysical Journal* 728, p. L12 (cit. on p. 28).
DOI: [10.1088/2041-8205/728/1/L12](https://doi.org/10.1088/2041-8205/728/1/L12).

- Karremans, K., W. Vassen, and W. Hogervorst (1998). "Observation of the Transition to Chaos in the Level Statistics of Diamagnetic Helium." In: *Phys. Rev. Lett.* 81 (22), pp. 4843–4846 (cit. on p. 45).
DOI: [10.1103/PhysRevLett.81.4843](https://doi.org/10.1103/PhysRevLett.81.4843).
- Ketterle, W. and N. V. Druten (1996). "Evaporative Cooling of Trapped Atoms." In: *Advances In Atomic, Molecular, and Optical Physics* 37, pp. 181–236 (cit. on p. 37).
DOI: [http://dx.doi.org/10.1016/S1049-250X\(08\)60101-9](http://dx.doi.org/10.1016/S1049-250X(08)60101-9).
- Koester, D. and G. Chanmugam (1990). "Physics of white dwarf stars." In: *Rep. Prog. Phys.* 837, p. 53 (cit. on p. 12).
DOI: [10.1088/0034-4885/53/7/001](https://doi.org/10.1088/0034-4885/53/7/001).
- Kolbe, W. F., W. Zollner, and B. Leskovar (1981). "Microwave spectrometer for the detection of transient gaseous species." In: *Rev. Sci. Instrum.* 52.4, pp. 523–532 (cit. on p. 54).
DOI: [10.1063/1.1136633](https://doi.org/10.1063/1.1136633).
- Kozlov, M. G. and S. A. Levshakov (2013). "Microwave and submillimeter molecular transitions and their dependence on fundamental constants." In: *Annalen der Physik* 525.7, pp. 452–471 (cit. on p. 28).
DOI: [10.1002/andp.201300010](https://doi.org/10.1002/andp.201300010).
- Kozyryev, I., L. Baum, K. Matsuda, B. L. Augenbraun, L. Anderegg, A. P. Sedlack, and J. M. Doyle (2017). "Sisyphus Laser Cooling of a Polyatomic Molecule." In: *Phys. Rev. Lett.* 118 (17), p. 173201 (cit. on p. 38).
DOI: [10.1103/PhysRevLett.118.173201](https://doi.org/10.1103/PhysRevLett.118.173201).
- Kozyryev, I., L. Baum, K. Matsuda, and J. M. Doyle (2016). "Proposal for Laser Cooling of Complex Polyatomic Molecules." In: *Chem. Phys. Chem* 17, pp. 3641–3648 (cit. on p. 36).
DOI: [10.1002/cphc.201601051](https://doi.org/10.1002/cphc.201601051).
- Kreckel, H., H. Bruhns, M. Čížek, S. C. O. Glover, K. A. Miller, X. Urbain, and D. W. Savin (2010). "Experimental Results for H₂ Formation from H⁻ and H and Implications for First Star Formation." In: *Science* 329.5987, pp. 69–71 (cit. on p. 12).
DOI: [10.1126/science.1187191](https://doi.org/10.1126/science.1187191).
- Krems, R. V. (2019). *Molecules in Electromagnetic Fields*. Hoboken, NJ: John Wiley and Sons, p. 483 (cit. on p. 36).
- Kristiansen, P. and L. Veseth (1986). "Many-body calculations of hyperfine constants in diatomic molecules. II. First-row hydrides." In: *J. Chem. Phys.* 84.11, pp. 6336–6344 (cit. on p. 54).
DOI: [10.1063/1.450726](https://doi.org/10.1063/1.450726).
- Langhoff, S. R. and H. Partridge (1984). "Theoretical study of the Λ -doubling parameters for X² Π OH." In: *J. Mol. Spectrosc.* 105.2, pp. 261–275 (cit. on p. 54).
DOI: [10.1016/0022-2852\(84\)90217-0](https://doi.org/10.1016/0022-2852(84)90217-0).

- Leitner, D. M., R. S. Berry, and R. M. Whitnell (1989). "Quantum chaos of Ar₃: Statistics of eigenvalues." In: *The Journal of Chemical Physics* 91, pp. 3470–3476 (cit. on p. 45).
DOI: [10.1063/1.456876](https://doi.org/10.1063/1.456876).
- Lemarchand, C., M. Triki, B. Darquié, C. J. Bordé, C. Chardonnet, and C. Daussey (2011). "Progress towards an accurate determination of the Boltzmann constant by Doppler spectroscopy." In: *New Journal of Physics* 13.7, p. 073028 (cit. on p. 32).
DOI: [10.1088/1367-2630/13/7/073028](https://doi.org/10.1088/1367-2630/13/7/073028).
- Lepp, S., P. C. Stancil, and A. Dalgarno (2002). "Atomic and molecular processes in the early Universe." In: *J. Phys. B: At. Mol. Opt. Phys.* 35, R57–R80 (cit. on p. 12).
DOI: [10.1088/0953-4075/35/10/201](https://doi.org/10.1088/0953-4075/35/10/201).
- Loo, M. P. J. van der and G. C. Groenenboom (2007). "Theoretical transition probabilities for the OH Meinel system." In: *J. Chem. Phys.* 126.11, p. 114314 (cit. on pp. 54, 56).
DOI: [10.1063/1.2646859](https://doi.org/10.1063/1.2646859).
- Maier, T., I. Ferrier-Barbut, H. Kadau, M. Schmitt, M. Wenzel, C. Wink, T. Pfau, K. Jachymski, et al. (2015a). "Broad universal Feshbach resonances in the chaotic spectrum of dysprosium atoms." In: *Phys. Rev. A* 92 (6), p. 060702 (cit. on pp. 46, 48).
DOI: [10.1103/PhysRevA.92.060702](https://doi.org/10.1103/PhysRevA.92.060702).
- Maier, T., H. Kadau, M. Schmitt, M. Wenzel, I. Ferrier-Barbut, T. Pfau, A. Frisch, S. Baier, et al. (2015b). "Emergence of Chaotic Scattering in Ultracold Er and Dy." In: *Phys. Rev. X* 5 (4), p. 041029 (cit. on pp. 46, 48, 49).
DOI: [10.1103/PhysRevX.5.041029](https://doi.org/10.1103/PhysRevX.5.041029).
- Martí-Vidal, I., Muller, S., Combes, F., Aalto, S., Beelen, A., Darling, J., Guélin, M., Henkel, C., et al. (2013). "Probing the jet base of the blazar PKS0-211 from the chromatic variability of its lensed images - Serendipitous ALMA observations of a strong gamma-ray flare." In: *A&A* 558, A123 (cit. on p. 29).
DOI: [10.1051/0004-6361/201322131](https://doi.org/10.1051/0004-6361/201322131).
- Mayle, M., B. P. Ruzic, and J. L. Bohn (2012). "Statistical aspects of ultracold resonant scattering." In: *Phys. Rev. A* 85 (6), p. 062712 (cit. on p. 46).
DOI: [10.1103/PhysRevA.85.062712](https://doi.org/10.1103/PhysRevA.85.062712).
- McCarron, D. J., M. H. Steinecker, Y. Zhu, and D. DeMille (2018a). "Magnetic Trapping of an Ultracold Gas of Polar Molecules." In: *Phys. Rev. Lett.* 121 (1), p. 013202 (cit. on p. 36).
DOI: [10.1103/PhysRevLett.121.013202](https://doi.org/10.1103/PhysRevLett.121.013202).
- McCarron, D. J., M. H. Steinecker, Y. Zhu, and D. DeMille (2018b). "Magnetic Trapping of an Ultracold Gas of Polar Molecules." In: *Phys. Rev. Lett.* 121 (1), p. 013202 (cit. on p. 36).
DOI: [10.1103/PhysRevLett.121.013202](https://doi.org/10.1103/PhysRevLett.121.013202).

- Meerts, W. L. and A. Dymanus (1975). "A Molecular Beam Electric Resonance Study of the Hyperfine Λ Doubling Spectrum of OH, OD, SH, and SD." In: *Canadian Journal of Physics* 53.19, pp. 2123–2141 (cit. on p. 54).
DOI: [10.1139/p75-261](https://doi.org/10.1139/p75-261).
- Miranda, M. H. G. de, A. Chotia, B. Neyenhuis, D. Wang, G. Quéméner, S. Ospelkaus, J. L. Bohn, J. Ye, et al. (2011). "Controlling the quantum stereodynamics of ultracold bimolecular reactions." In: *Nature Physics* 7.6, pp. 502–507 (cit. on p. 46).
DOI: [10.1038/nphys1939](https://doi.org/10.1038/nphys1939).
- Monroe, C. R., E. A. Cornell, C. A. Sackett, C. J. Myatt, and C. E. Wieman (Jan. 1993). "Measurement of Cs-Cs elastic scattering at $T=30\ \mu\text{K}$." In: *Phys. Rev. Lett.* 70, pp. 414–417 (cit. on p. 37).
DOI: [10.1103/PhysRevLett.70.414](https://doi.org/10.1103/PhysRevLett.70.414).
- Mrugała, F. and W. P. Kraemer (2005). "Radiative association of He^+ with H_2 at temperatures below 100 K." In: *J. Chem. Phys.* 122, 224321 (cit. on p. 14).
DOI: [10.1063/1.1924453](https://doi.org/10.1063/1.1924453).
- Mrugała, F., V. Špirko, and W. P. Kraemer (2003). "Radiative association of HeH_2^+ ." In: *J. Chem. Phys.* 118, pp. 10547–10560 (cit. on p. 14).
DOI: [10.1063/1.1573184](https://doi.org/10.1063/1.1573184).
- Mur-Petit, J. and R. A. Molina (Oct. 2015). "Spectral statistics of molecular resonances in erbium isotopes: How chaotic are they?" In: *Phys. Rev. E* 92 (4), p. 042906 (cit. on p. 49).
DOI: [10.1103/PhysRevE.92.042906](https://doi.org/10.1103/PhysRevE.92.042906).
- Murphy, M. T., V. V. Flambaum, S. Muller, and C. Henkel (2008). "Strong Limit on a Variable Proton-to-Electron Mass Ratio from Molecules in the Distant Universe." In: *Science* 320, pp. 1611–1613 (cit. on p. 28).
DOI: [10.1126/science.1156352](https://doi.org/10.1126/science.1156352).
- Ni, K. -.-K., S. Ospelkaus, D. Wang, G. Quéméner, B. Neyenhuis, M. H. G. de Miranda, J. L. Bohn, J. Ye, et al. (2010). "Dipolar collisions of polar molecules in the quantum regime." In: *Nature* 464.7293, pp. 1324–1328 (cit. on p. 46).
DOI: [10.1038/nature08953](https://doi.org/10.1038/nature08953).
- Numerov, B. V. (1923). "Méthode nouvelle de la détermination des orbites et le calcul des éphémérides en tenant compte des perturbations." In: *Trudy Glavnoï rossiiskoi astrofizicheskoi observatorii* 2, pp. 188–14 (cit. on p. 15).
- Owens, A., S. N. Yurchenko, O. L. Polyansky, R. I. Ovsyannikov, W. Thiel, and V. Špirko (2015). "Accurate prediction of H_3O^+ and D_3O^+ sensitivity coefficients to probe a variable proton-to-electron mass ratio." In: *Monthly Notices of the Royal Astronomical Society* 454.3, pp. 2292–2298 (cit. on p. 28).
DOI: [10.1093/mnras/stv2023](https://doi.org/10.1093/mnras/stv2023).

- Owens, A., S. N. Yurchenko, and V. Špirko (2018). “Anomalous phosphine sensitivity coefficients as probes for a possible variation of the proton-to-electron mass ratio.” In: *Monthly Notices of the Royal Astronomical Society* 473, pp. 4986–4992 (cit. on p. 28).
DOI: [10.1093/mnras/stx2696](https://doi.org/10.1093/mnras/stx2696).
- Owens, A., S. N. Yurchenko, W. Thiel, and V. Špirko (2016). “Enhanced sensitivity to a possible variation of the proton-to-electron mass ratio in ammonia.” In: *Phys. Rev. A* 93, p. 052506 (cit. on p. 28).
DOI: [10.1103/PhysRevA.93.052506](https://doi.org/10.1103/PhysRevA.93.052506).
- Patkowski, K., V. Špirko, and K. Szalewicz (2009). “On the Elusive Twelfth Vibrational State of Beryllium Dimer.” In: 326.5958, pp. 1382–1384 (cit. on p. 30).
DOI: [10.1126/science.1181017](https://doi.org/10.1126/science.1181017).
- Patrignani C. et al. (Particle Data Group) (2016). “Review of Particle Physics.” In: *Chinese Physics C* 40.10, p. 100001 (cit. on p. 26).
DOI: [10.1088/1674-1137/40/10/100001](https://doi.org/10.1088/1674-1137/40/10/100001).
- Pérez-Ríos, J. and A. S. Sanz (2013). “How does a magnetic trap work?” In: *American Journal of Physics* 81, pp. 836–843 (cit. on p. 37).
DOI: [10.1119/1.4819167](https://doi.org/10.1119/1.4819167).
- Pérez-Ríos, J., M. Lepers, R. Vexiau, N. Bouloufa-Maafa, and O. Dulieu (2014). “Progress toward ultracold chemistry: ultracold atomic and photonic collisions.” In: *Journal of Physics: Conference Series* 488.1, p. 012031 (cit. on p. 46).
DOI: [10.1088/1742-6596/488/1/012031](https://doi.org/10.1088/1742-6596/488/1/012031).
- Perlmutter, S. (2012). “Nobel Lecture: Measuring the acceleration of the cosmic expansion using supernovae.” In: *Rev. Mod. Phys.* 84 (3), pp. 1127–1149 (cit. on p. 26).
DOI: [10.1103/RevModPhys.84.1127](https://doi.org/10.1103/RevModPhys.84.1127).
- Petrov, A., E. Tiesinga, and S. Kotochigova (2012). “Anisotropy-Induced Feshbach Resonances in a Quantum Dipolar Gas of Highly Magnetic Atoms.” In: *Phys. Rev. Lett.* 109 (10), p. 103002 (cit. on p. 48).
DOI: [10.1103/PhysRevLett.109.103002](https://doi.org/10.1103/PhysRevLett.109.103002).
- Podolskiy, V. A. and E. E. Narimanov (2007). “Level spacing distribution in systems with partially chaotic classical dynamics.” In: *Physics Letters A* 362.5, pp. 412–416 (cit. on p. 45).
DOI: [10.1016/j.physleta.2006.10.065](https://doi.org/10.1016/j.physleta.2006.10.065).
- Quémener, G. and P. S. Julienne (2012). “Ultracold Molecules under Control!” In: *Chem. Rev.* 112.9, pp. 4949–5011 (cit. on p. 46).
DOI: [10.1021/cr300092g](https://doi.org/10.1021/cr300092g).
- Quintero-Pérez, M., T. E. Wall, S. Hoekstra, and H. L. Bethlem (2014). “Preparation of an ultra-cold sample of ammonia molecules for precision measurements.” In: *Journal of Molecular Spectroscopy* 300.

- Spectroscopic Tests of Fundamental Physics, pp. 112–115 (cit. on p. 27).
 DOI: <https://doi.org/10.1016/j.jms.2014.03.018>.
- Radford, H. E. (1968). “Scanning Microwave Echo Box Spectrometer.” In: *Rev. Sci. Instrum.* 39.11, pp. 1687–1691 (cit. on p. 54).
 DOI: [10.1063/1.1683203](https://doi.org/10.1063/1.1683203).
- Ramos, A. A. and J. T. Bueno (2006). “Theory and Modeling of the Zeeman and Paschen-Back Effects in Molecular Lines.” In: *The Astrophysical Journal* 636, pp. 548–563 (cit. on p. 55).
 DOI: [10.1086/497892](https://doi.org/10.1086/497892).
- Rothman, L. S., C. P. Rinsland, A. Goldman, S. T. Massie, D. P. Edwards, J.-M. Flaud, A. Perrin, C. Camy-Peyret, et al. (1998). “The HITRAN 2004 molecular spectroscopic database.” In: *J. Quant. Spectrosc. Radiat. Transfer* 60, pp. 665–710 (cit. on p. 18).
 DOI: [10.1016/S0022-4073\(98\)00078-8](https://doi.org/10.1016/S0022-4073(98)00078-8).
- Safronova, M. S., D. Budker, D. DeMille, D. F. J. Kimball, A. Derevianko, and C. W. Clark (2018). “Search for new physics with atoms and molecules.” In: *Rev. Mod. Phys.* 90 (2), p. 025008 (cit. on p. 26).
 DOI: [10.1103/RevModPhys.90.025008](https://doi.org/10.1103/RevModPhys.90.025008).
- Sakhr, J. and J. M. Nieminen (2005). “Poisson-to-Wigner crossover transition in the nearest-neighbor statistics of random points on fractals.” In: *Phys. Rev. E* 72 (4), p. 045204 (cit. on p. 45).
 DOI: [10.1103/PhysRevE.72.045204](https://doi.org/10.1103/PhysRevE.72.045204).
- Semenov, M., S. N. Yurchenko, and J. Tennyson (2016). “Predicted Landé g-factors for open shell diatomic molecules.” In: *J. Mol. Spectrosc.* 330. Potentiology and Spectroscopy in Honor of Robert Le Roy, pp. 57–62 (cit. on p. 53).
 DOI: <https://doi.org/10.1016/j.jms.2016.11.004>.
- Shelkovnikov, A., R. J. Butcher, C. Chardonnet, and A. Amy-Klein (2008). “Stability of the Proton-to-Electron Mass Ratio.” In: *Phys. Rev. Lett.* 100 (15), p. 150801 (cit. on p. 27).
 DOI: [10.1103/PhysRevLett.100.150801](https://doi.org/10.1103/PhysRevLett.100.150801).
- Shuman, E. S., J. F. Barry, and D. DeMille (2010). “Laser cooling of a diatomic molecule.” In: *Nature* 467, pp. 820–823 (cit. on p. 36).
 DOI: [10.1038/nature09443](https://doi.org/10.1038/nature09443).
- Soldán, P. and W. P. Kraemer (2012). “Molecular ion LiHe⁺: *ab initio* study.” In: *Chem. Phys.* 393, pp. 135–139 (cit. on p. 16).
 DOI: [10.1016/j.chemphys.2011.11.040](https://doi.org/10.1016/j.chemphys.2011.11.040).
- Spilker, J. S., M. Aravena, M. Béthermin, S. C. Chapman, C.-C. Chen, D. J. M. Cunningham, C. De Breuck, C. Dong, et al. (2018). “Fast molecular outflow from a dusty star-forming galaxy in the early Universe.” In: 361.6406, pp. 1016–1019 (cit. on p. 33).
 DOI: [10.1126/science.aap8900](https://doi.org/10.1126/science.aap8900).

- Špirko, V. (2014). “Highly Sensitive Ammonia Probes of a Variable Proton-to-Electron Mass Ratio.” In: *J. Phys. Chem. Lett.* 5, pp. 919–923 (cit. on p. 28).
DOI: [10.1021/jz500163j](https://doi.org/10.1021/jz500163j).
- Špirko, V. (2016). “Morphing ab initio potential energy curve of beryllium monohydride.” In: *Journal of Molecular Spectroscopy* 330. Potentiology and Spectroscopy in Honor of Robert Le Roy, pp. 89–95 (cit. on pp. 30, 54).
DOI: <https://doi.org/10.1016/j.jms.2016.08.009>.
- Stancil, P. C., J. F. Babb, and A. Dalgarno (1993). “The radiative association of He^+ and He and H^+ and H.” In: *Astrophys. J.* 414, pp. 672–675 (cit. on p. 13).
DOI: [10.1086/173113](https://doi.org/10.1086/173113).
- Stancil, P. C. and A. Dalgarno (1997). “Stimulated radiative association of Li and H in the early Universe.” In: *Astrophys. J.* 479, pp. 543–546 (cit. on pp. 15, 16).
DOI: [10.1086/303920](https://doi.org/10.1086/303920).
- Stuhl, B. K., M. T. Hummon, M. Yeo, G. Quémener, J. L. Bohn, and J. Ye (2012). “Evaporative cooling of the dipolar hydroxyl radical.” In: *Nature* 492, pp. 396–400 (cit. on p. 40).
DOI: [10.1038/nature11718](https://doi.org/10.1038/nature11718).
- Swings, P. (1942). “Considerations regarding cometary and interstellar molecules.” In: *Astrophys. J.* 95, pp. 270–280 (cit. on p. 13).
DOI: [10.1086/144393](https://doi.org/10.1086/144393).
- Talbi, D. and M.-C. Bacchus-Montabonel (2007). “Formation of HF through radiative association in the early universe.” In: *Chem. Phys. Lett.* 443, pp. 40–42 (cit. on p. 14).
DOI: [10.1016/j.cpllett.2007.06.071](https://doi.org/10.1016/j.cpllett.2007.06.071).
- Ter Meulen, J. J. and A. Dymanus (1972). “Beam-Maser Measurements of the Ground-State Transition Frequencies of OH.” In: *Astrophys. J. Lett.* 172, p. L21 (cit. on p. 54).
DOI: [10.1086/180882](https://doi.org/10.1086/180882).
- Ter Meulen, J. J., W. L. Meerts, G. W. M. van Mierlo, and A. Dymanus (1976). “Observations of Population Inversion between the Λ -Doublet States of OH.” In: *Phys. Rev. Lett.* 36 (17), pp. 1031–1034 (cit. on p. 54).
DOI: [10.1103/PhysRevLett.36.1031](https://doi.org/10.1103/PhysRevLett.36.1031).
- Tielens, A. G. G. M. (2013). “The molecular universe.” In: *Rev. Mod. Phys.* 85, pp. 1021–1081 (cit. on p. 12).
DOI: [10.1103/RevModPhys.85.1021](https://doi.org/10.1103/RevModPhys.85.1021).
- Ubachs, W., J. Bagdonaite, E. J. Salumbides, M. T. Murphy, and L. Kaper (2016). “Colloquium: Search for a drifting proton-electron mass ratio from H_2 .” In: *Rev. Mod. Phys.* 88, p. 021003 (cit. on p. 28).
DOI: [10.1103/RevModPhys.88.021003](https://doi.org/10.1103/RevModPhys.88.021003).

- Uzan, J.-P. (2011). "Varying Constants, Gravitation and Cosmology." In: *Living Reviews in Relativity* 14.1, p. 2 (cit. on p. 26).
DOI: [10.12942/lrr-2011-2](https://doi.org/10.12942/lrr-2011-2).
- Varberg, T. and K. Evenson (1993). "The Rotational Spectrum of OH in the $v = 0 - 3$ Levels of Its Ground State." In: *J. Mol. Spectrosc.* 157.1, pp. 55-67 (cit. on p. 54).
DOI: <https://doi.org/10.1006/jmsp.1993.1005>.
- Varberg, T. D., F. Stroh, and K. M. Evenson (1999). "Far-Infrared Rotational and Fine-Structure Transition Frequencies and Molecular Constants of ^{14}NO and ^{15}NO in the $X^2\Pi$ ($v = 0$) State." In: *Journal of Molecular Spectroscopy* 196.1, pp. 5-13 (cit. on p. 38).
DOI: <http://dx.doi.org/10.1006/jmsp.1999.7850>.
- Vogels, S. N., J. Onvlee, S. Chefdeville, A. van der Avoird, G. C. Groenenboom, and S. Y. T. van de Meerakker (2015). "Imaging resonances in low-energy NO-He inelastic collisions." In: *Science* 350, p. 787 (cit. on p. 40).
DOI: [10.1126/science.aad2356](https://doi.org/10.1126/science.aad2356).
- Wang, Y., J. P. D'Incao, and C. H. Greene (2011). "Universal Three-Body Physics for Fermionic Dipoles." In: *Phys. Rev. Lett.* 107 (23), p. 233201 (cit. on p. 46).
DOI: [10.1103/PhysRevLett.107.233201](https://doi.org/10.1103/PhysRevLett.107.233201).
- Wigner, E. P. (1955). "Characteristic Vectors of Bordered Matrices With Infinite Dimensions." In: *Annals of Mathematics* 62.3, pp. 548-564 (cit. on pp. 45, 49).
DOI: [10.2307/1970079](https://doi.org/10.2307/1970079).
- Williams, H. J., L. Caldwell, N. J. Fitch, S. Truppe, J. Rodewald, E. A. Hinds, B. E. Sauer, and M. R. Tarbutt (2018). "Magnetic Trapping and Coherent Control of Laser-Cooled Molecules." In: *Phys. Rev. Lett.* 120 (16), p. 163201 (cit. on p. 36).
DOI: [10.1103/PhysRevLett.120.163201](https://doi.org/10.1103/PhysRevLett.120.163201).
- Yang, B. C., J. Pérez-Ríos, and F. Robicheaux (Apr. 2017). "Classical Fractals and Quantum Chaos in Ultracold Dipolar Collisions." In: *Phys. Rev. Lett.* 118 (15), p. 154101 (cit. on pp. 46, 48).
DOI: [10.1103/PhysRevLett.118.154101](https://doi.org/10.1103/PhysRevLett.118.154101).
- Yelin, S. F., K. Kirby, and R. Côté (2006). "Schemes for robust quantum computation with polar molecules." In: *Phys. Rev. A* 74 (5), p. 050301 (cit. on p. 46).
DOI: [10.1103/PhysRevA.74.050301](https://doi.org/10.1103/PhysRevA.74.050301).
- Yeo, M., M. T. Hummon, A. L. Collopy, B. Yan, B. Hemmerling, E. Chae, J. M. Doyle, and J. Ye (2015). "Rotational State Microwave Mixing for Laser Cooling of Complex Diatomic Molecules." In: *Phys. Rev. Lett.* 114, p. 223003 (cit. on p. 36).
DOI: [10.1103/PhysRevLett.114.223003](https://doi.org/10.1103/PhysRevLett.114.223003).
- Yurchenko, S. N., L. Lodi, J. Tennyson, and A. V. Stolyarov (2016). "Duo: A general program for calculating spectra of diatomic

- molecules." In: *Computer Physics Communications* 202, pp. 262–275 (cit. on p. 53).
DOI: <https://doi.org/10.1016/j.cpc.2015.12.021>.
- Zámečníková, M., L. Augustovičová, W. P. Kraemer, and P. Soldán (2015). "Formation of molecular ion LiHe^+ by radiative association of metastable helium $\text{He}(2^3\text{P})$ with lithium ions." In: *Journal of Physics: Conference Series* 635, p. 022038 (cit. on p. 14).
DOI: [10.1088/1742-6596/635/2/022038](https://doi.org/10.1088/1742-6596/635/2/022038).
- Życzkowski, K., M. Lewenstein, M. Kuś, and F. Izrailev (1992). "Eigenvector statistics of random band matrices." In: *Phys. Rev. A* 45 (2), pp. 811–815 (cit. on p. 49).
DOI: [11.1103/PhysRevA.45.811](https://doi.org/10.1103/PhysRevA.45.811).
- Zygelman, B. and A. Dalgarno (1990). "The radiative association of He^+ and H." In: *Astrophys. J.* 365, pp. 239–240 (cit. on pp. 14, 16).
DOI: [10.1086/169475](https://doi.org/10.1086/169475).
- Zygelman, B., A. Dalgarno, M. Kimura, and N. F. Lane (1989). "Radiative and nonradiative charge transfer in $\text{He}^+ + \text{H}$ collisions at low energy." In: *Phys. Rev. A* 40, pp. 2340–2345 (cit. on p. 19).
DOI: [10.1103/PhysRevA.40.2340](https://doi.org/10.1103/PhysRevA.40.2340).
- Zygelman, B., P. C. Stancil, and A. Dalgarno (1998). "Stimulated radiative association of He and H^+ ." In: *Astrophys. J.* 508, pp. 151–156 (cit. on p. 14).
DOI: [10.1086/306399](https://doi.org/10.1086/306399).

ATTACHED PUBLICATIONS

DEPOPULATION OF METASTABLE HELIUM BY
RADIATIVE ASSOCIATION WITH HYDROGEN AND
LITHIUM IONS

Bibliographic record of the attached publication:

Augustovičová, L., W. P. Kraemer, and P. Soldán (2014). “Depopulation of metastable helium by radiative association with hydrogen and lithium ions.” In: *The Astrophysical Journal* 782, 46.
DOI: [10.1088/0004-637X/782/1/46](https://doi.org/10.1088/0004-637X/782/1/46).

DEPOPULATION OF METASTABLE HELIUM BY RADIATIVE ASSOCIATION WITH HYDROGEN AND LITHIUM IONS

L. AUGUSTOVIČOVÁ¹, W. P. KRAEMER², AND P. SOLDÁN¹

¹ Charles University in Prague, Faculty of Mathematics and Physics, Department of Chemical Physics and Optics, Ke Karlovu 3, CZ-12116 Prague 2, Czech Republic; pavel.soldan@mff.cuni.cz

² Max-Planck Institute of Astrophysics, Postfach 1371, D-85741 Garching, Germany

Received 2013 September 11; accepted 2013 December 19; published 2014 January 24

ABSTRACT

Depopulation of metastable He(2^3S) by radiative association with hydrogen and lithium ions is investigated using a fully quantal approach. Rate coefficients for spontaneous and stimulated radiative association of the HeH⁺, HeD⁺, and LiHe⁺ molecular ions on the spin-triplet manifold are presented as functions of temperature considering the association to rotational-vibrational states of the lowest triplet electronic states $a^3\Sigma^+$ and $b^3\Sigma^+$ from the continuum states of the $b^3\Sigma^+$ electronic state. Evaluation of the rate coefficients is based on highly accurate quantum calculations, taking into account all possible state-to-state transitions at thermal energies (for spontaneous association) or at higher background energies (stimulated association). As expected, calculations show that the rate coefficients for radiative association to the a state are several orders of magnitude larger than the one for the b state formation. A noticeable effect by blackbody background radiation on the radiative association is only obtained for the $b \rightarrow b$ process. Aspects of the formation and abundance of the metastable HeH⁺($a^3\Sigma^+$) in astrophysical environments are briefly discussed.

Key words: atomic data – atomic processes – molecular data – molecular processes

Online-only material: color figures

1. INTRODUCTION

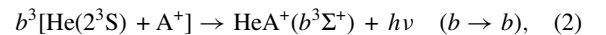
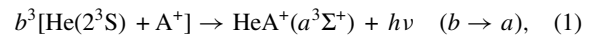
Metastable helium 2^3S with its electronic configuration ($1s2s$) lying as much as 19.75 eV above the helium 1^1S_0 ground state has been found to have an unusually long lifetime of about two hours (Drake 1971; Hodgman et al. 2009). This extreme metastable life time arises from the fact that the direct photon decay to the ground state is doubly forbidden by quantum mechanical selection rules.

In view of the relatively large abundance of helium in the interstellar space, astrophysical consequences of the possible formation of its metastable levels were discussed early (Struve et al. 1939). It was then postulated that the excited (2^3S) state can be populated either by recombination from the ionized state or by collisional excitations from the neutral ground state by thermal electrons (Zeldovich et al. 1966). These processes can only produce a significant population of the metastable state if the gas temperature is high enough—such as, for instance, in planetary nebulae (Rees et al. 1968). Using a simple reaction network in which cosmic ray ionized helium recombines with electrons to form the metastable helium triplet and relying on the fact that spontaneous emission to the ground state level is forbidden, Scherb (1968) and Rees et al. (1968) suggested that interstellar metastable helium should be observable. However, whereas in these earlier studies two-photon emission from the metastable triplet was thought to be the dominant depopulation process (see also Robbins 1968), depopulations through excitations to higher excited helium levels are now considered to be most effective in energetic environments.

Especially due to its long lifetime, the He(2^3S) can act as an efficient base for the He I* λ 10830 ($2s \rightarrow 2p$) and He I* λ 3889 ($2s \rightarrow 3p$) absorption lines, which are suitable for measuring the He⁺ fraction and column density in the outflows of active galaxies (Indriolo et al. 2009; Leighly et al. 2012). Observations of the λ 10830 absorption line are reported for the Orion nebula (Boyce & Ford 1966) and BALQSO (Leighly et al. 2011),

the λ 3889 line toward ζ Ophiuchi (Galazutdinov & Krelowski 2012), and the λ 3889 and λ 3188 (due to $2s \rightarrow 4p$) lines from the Scorpii SN 2007 (Naito et al. 2013). Apart from these excitations to higher levels, depopulation of the 2^3S state in more dense plasmas can occur via collisions in the photoionized gas.

In this context, the depopulation of He(2^3S) by collisions with He⁺ ions was investigated in previous studies: via radiative association (RA), these collisions can lead to the formation of helium ion dimer either in its electronic ground state ($X^2\Sigma_u^+$; Augustovičová et al. 2013a) or in the lowest excited quartet state ($b^4\Sigma_u^+$; Augustovičová et al. 2013b). In the present study, the corresponding RA processes of the He(2^3S) metastable with highly abundant protons as well as with Li⁺ ions are investigated. The corresponding processes induced by dipole-moment continuum-bound transitions are described as



where $^3[. . .]$ means a triplet submanifold of the corresponding collisional continuum and A is H, D, or Li. According to this scheme, reactions (1) and (2) start from collisions of helium in the metastable state 2^3S with hydrogen or lithium ions, and then proceed via resonance and continuum states of the $b^3\Sigma^+$ potential of the collisional complex to form (under spontaneous photon emission) the molecular ion in the triplet states $a^3\Sigma^+$ or $b^3\Sigma^+$. These processes are characterized as $b \rightarrow a$ and $b \rightarrow b$ in the following text. Apart from spontaneous emission, the corresponding processes stimulated by the background radiation (Stancil & Dalgarno 1997; Zygelman et al. 1998) are also considered.

2. METHODS

Our attempt to investigate RA is based on the approach of Zygelman & Dalgarno (1990) and Stancil & Dalgarno

(1997) and has been used in our previous work (Augustovičová et al. 2012, 2013a, 2013b). Including the possibility of dipole-moment transitions in the presence of the blackbody radiation field characterized by temperature T_b , the individual cross section for the transition between a continuum state with a positive energy E and orbital angular momentum J' to bound rovibrational states with vibrational quantum number v'' and orbital angular momentum J'' can be expressed as

$$\sigma_{J',v'',J''}(E; T_b) = \frac{1}{4\pi\epsilon_0} \frac{64}{3} \frac{\pi^5}{c^3 k^2} p v_{E;v'',J''}^3 S_{J',J''} M_{E,J',v'',J''}^2 \times \left[\frac{1}{1 - \exp(-hv_{E;v'',J''}/k_B T_b)} \right], \quad (3)$$

where c is the speed of light in a vacuum, $k^2 = 2\mu E/\hbar^2$, μ is the “charge-modified reduced mass” (Watson 1980) of the molecular ion ($\mu = 1467.778424$ a.u. for ${}^4\text{HeH}^+$, $\mu = 2442.670838$ a.u. for ${}^4\text{HeD}^+$, and $\mu = 4646.087837$ a.u. for ${}^4\text{He}^7\text{Li}^+$), p is the probability of approach in the initial electronic state ($p = 1$ for both $b \rightarrow a$ and $b \rightarrow b$), and $v_{E;v'',J''}$ is the emitted photon frequency, $hv_{E;v'',J''} = E + \Delta E - E_{v'',J''}$, where $\Delta E_{b \rightarrow b} = 0$ eV, $\Delta E_{b \rightarrow a} = 8.8306602$ eV for HeH^+ and HeD^+ , and $\Delta E_{b \rightarrow a} = 0.62394103$ eV for LiHe^+ (Kramida et al. 2011). $M_{E,J',v'',J''}$ is the matrix element of the transition dipole moment function between the initial continuum radial wave function and the final bound-state radial wave function. For dipole moment transitions of a heteronuclear diatomic molecule within the Hund’s case (a) spinless approximation (Hansson & Watson 2005), the only non-zero Hönl-London coefficients are $S_{J',J'+1} = J' + 1$ and $S_{J',J'-1} = J'$.

The radial wave functions are determined by numerical integration of the corresponding Schrödinger equations using the Numerov–Cooley method (Numerov 1933; Cooley 1961). Resonance positions and tunneling widths were calculated employing the computer program LEVEL 7.7 (Le Roy 2005) and making use of the Airy-function boundary condition at the outermost classical turning point (Le Roy & Liu 1978) and the uniform semiclassical method (Connor & Smith 1981; Huang & Le Roy 2003).

For evaluation of the radial wave functions and the dipole-moment matrix elements, the potential energy and dipole-moment functions were represented numerically by a one-dimensional reciprocal-power reproducing kernel Hilbert space (RP-RKHS) interpolation method (Ho & Rabitz 1996), which allows for qualitatively correct extrapolation in the long-range region and it also allows for using predetermined values of long-range coefficients Ho & Rabitz (2000). In the case of potential energy curves, the interpolation was done with respect to r^2 (Soldán & Hutson 2000) using RP-RKHS parameters $m = 1$ and $n = 2$, and the coefficient D_4 , which is equal to $\alpha_d(A)/2$, was kept fixed to the values given by static dipole polarizabilities ($\alpha_d[\text{He}(2^3\text{S})] = 315.631468$ a.u., Yan & Babb 1998; $\alpha_d[\text{H}(1^2\text{S})] = 4.5$ a.u., Sewell 1949; and $\alpha_d[\text{Li}(2^2\text{S})] = 162.87$ a.u., Wansbeek et al. 2008).

Ab initio interaction energies for the $a^3\Sigma^+$ and $b^3\Sigma^+$ electronic states of HeH^+ , and the corresponding dipole-moment values were calculated within the Born–Oppenheimer approximation. The aug-cc-pV6Z basis sets augmented by sets of $(1s, 2p, 1d, 1f)$ even-tempered diffuse functions were used for He and H; in order to increase the basis-set flexibility, a set of $(4s, 4p)$ mid-bond functions was also added. A multi-reference configuration interaction (MRCI) method with single and double excitations (Werner & Knowles 1988; Knowles & Werner 1988), as

implemented in MOLPRO (Werner & Knowles 2010), was employed with the active space formed by $14\sigma^+$ and 5π orbitals (the actual calculations were performed within the C_{2v} point-group symmetry using $14a_1$, $5b_1$, and $5b_2$ orbitals). The MRCI calculations were preceded by complete active space self-consistent field calculations (Werner & Knowles 1985; Knowles & Werner 1985) with the active space formed by $11\sigma^+$ and 3π orbitals ($11a_1$, $4b_1$, and $4b_2$ orbitals in the C_{2v} point-group symmetry). All interaction energies were calculated in the supermolecular manner and no counterpoise correction was applied to the MRCI interaction energies. The transition dipole-moment function was calculated with respect to the center of mass of the molecular ion (the position of the center of mass was determined using the standard atomic weights). The same Born–Oppenheimer potential energy curves and dipole moments were used for HeD^+ . In the case of LiHe^+ , the corresponding highly accurate potential energy curves and dipole moments obtained recently by Soldán & Kraemer (2012) were used.

The rate coefficient for formation of a molecule by (spontaneous and stimulated) RA at temperature T is defined by

$$k(T; T_b) = \left(\frac{8}{\mu\pi} \right)^{1/2} \left(\frac{1}{k_B T} \right)^{3/2} \int_0^\infty E \sigma(E; T_b) e^{-E/k_B T} dE, \quad (4)$$

where $\sigma(E; T_b)$ is the total cross section for RA, i.e., the sum of individual cross sections presented in Equation (3) over all allowed transitions. When evaluating this integral, we followed the approach of Augustovičová et al. (2012), where contributions from wide and narrow resonances are treated separately from the background contribution. It is often convenient to use some simple analytical form to represent the numerical values of the rate coefficients. In the present study, we use the Arrhenius-type function

$$f(T) = \alpha \left(\frac{T}{300} \right)^\beta e^{-\gamma/T}, \quad (5)$$

where α , β , and γ are the fitting parameters. In order to keep the maximum relative error below 10%, the temperature range is divided into several intervals.

3. RESULTS AND DISCUSSION

Potential energy curves for HeH^+ calculated in this work (shown together with the corresponding transition dipole moment in Figure 1) can be compared with the results obtained previously by others. For the $a^3\Sigma^+$ state, our equilibrium distance $R_e = 4.452 a_0$ and dissociation energy relative to the potential minimum $D_e = 851.9 \text{ cm}^{-1}$ compare very well with the results of Kolos (1976; $R_e = 4.455 a_0$ and $D_e = 850.0 \text{ cm}^{-1}$) and those of Kraemer et al. (1995; $R_e = 4.452 a_0$ and $D_e = 840.6 \text{ cm}^{-1}$), whereas the much smaller dissociation energy value obtained in the early calculations by Michels (1966; $D_e = 656.5 \text{ cm}^{-1}$ at $R_e = 4.452 a_0$) turns out to be close to the present $D_0 = 666.9 \text{ cm}^{-1}$, i.e., the dissociation energy relative to the ground vibrational level. For the $b^3\Sigma^+$ state, our equilibrium distance $R_e = 7.720 a_0$ and dissociation energy $D_e = 5848.1 \text{ cm}^{-1}$ are in reasonable agreement with the values obtained earlier by Michels (1966; $R_e = 7.754 a_0$ and $D_e = 5907.2 \text{ cm}^{-1}$). The numbers of vibrational and rovibrational levels supported by these potentials are given in Table 1 for the two isotopologues HeH^+ and HeD^+ as well as for LiHe^+ . For HeH^+ and HeD^+ they are in perfect agreement

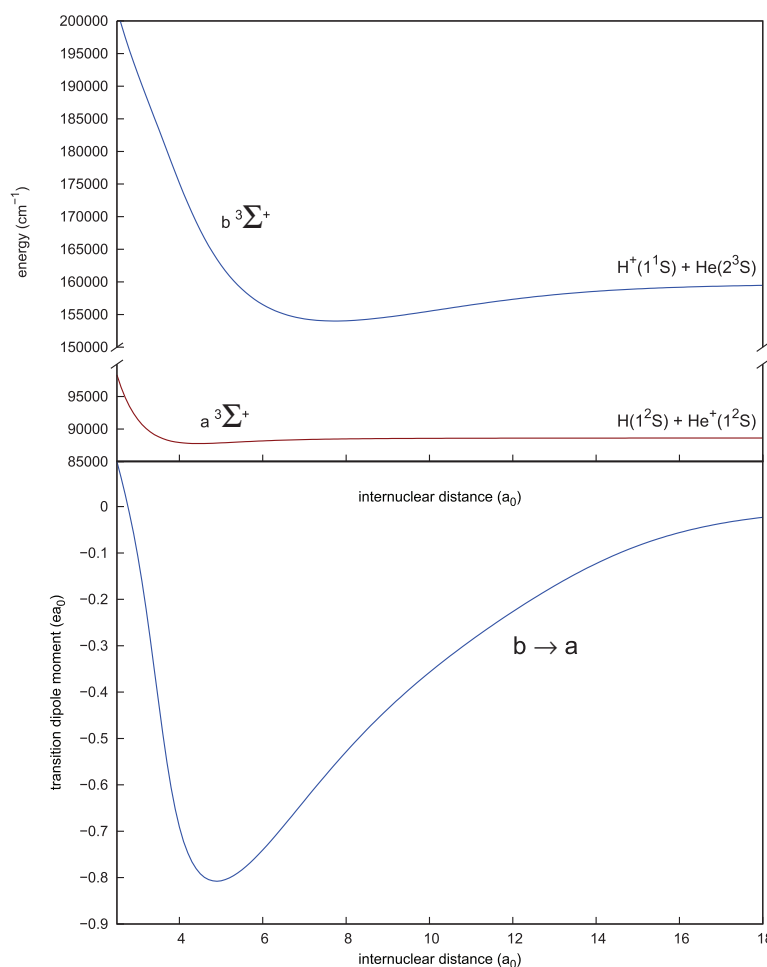


Figure 1. Potential energy curves and the transition dipole moment of HeH^+ . The energy scale zero is set to the $\text{H}^+(1^1\text{S}) + \text{He}(1^1\text{S})$ dissociation limit. (A color version of this figure is available in the online journal.)

Table 1
Process Characteristics for Radiative Association of $\text{He}(2^3\text{S})$ with Hydrogen and Lithium Ions

System	Process	n_{tot}	n_r	n_w	n_n	\mathcal{D}_0 (cm^{-1})	n_v	n_{rv}
HeH^+	$b \rightarrow a$	214	6	5	1	666.9	6	51
	$b \rightarrow b$	214	162	86	76	5652.4	35	1325
HeD^+	$b \rightarrow a$	353	7	7	0	706.4	8	85
	$b \rightarrow b$	353	266	122	144	5696.2	45	2209
$\text{LiHe}^{+\text{a}}$	$b \rightarrow a$	214	214	122	92	8181.1	61	4172
	$b \rightarrow b$	214	168	92	76	829.5	33	1289

Notes. Using the formalism of Augustovičová et al. (2012), n_{tot} is the total number of orbital resonances supported by the initial electronic states, from which n_r is the number of symmetry-allowed resonances, n_w is the number of wide resonances, and n_n is the number of narrow resonances; \mathcal{D}_0 is the dissociation energy of the target electronic state from the ground ($v'' = 0, J'' = 0$) rovibrational state, n_v is the number of bound vibrational ($J'' = 0$) states of the target electronic state, and n_{rv} is the total number of bound rovibrational states of the target electronic state.

^a From Soldán & Kraemer (2012), the CCSD(T) potential energy curve is used for the $a^3\Sigma^+$ state and the MRCI potential energy curve is used for the $b^3\Sigma^+$ state.

with results of Yousif et al. (1994) and Chibisov et al. (1996). In the case of the $a^3\Sigma^+$ state, the last supported vibrational levels are $E_{v=5} = 1.082 \text{ cm}^{-1}$ and $E_{v=7} = 0.323 \text{ cm}^{-1}$ for HeH^+ and HeD^+ , respectively. In the case of the much deeper $b^3\Sigma^+$ state potential, the highest bound vibrational levels are $E_{v=34} = 9.59 \times 10^{-4} \text{ cm}^{-1}$ and $E_{v=44} = 1.142 \times 10^{-4} \text{ cm}^{-1}$

for HeH^+ and HeD^+ , respectively. Compared to HeH^+ and HeD^+ , the situation is reversed for LiHe^+ : the $a^3\Sigma^+$ electronic state is much stronger bound than the $b^3\Sigma^+$ electronic state (Soldán & Kraemer 2012).

Cross sections for spontaneous ($T_b = 0 \text{ K}$) RA of the $b \rightarrow a$ and $b \rightarrow b$ processes in the three dimer systems

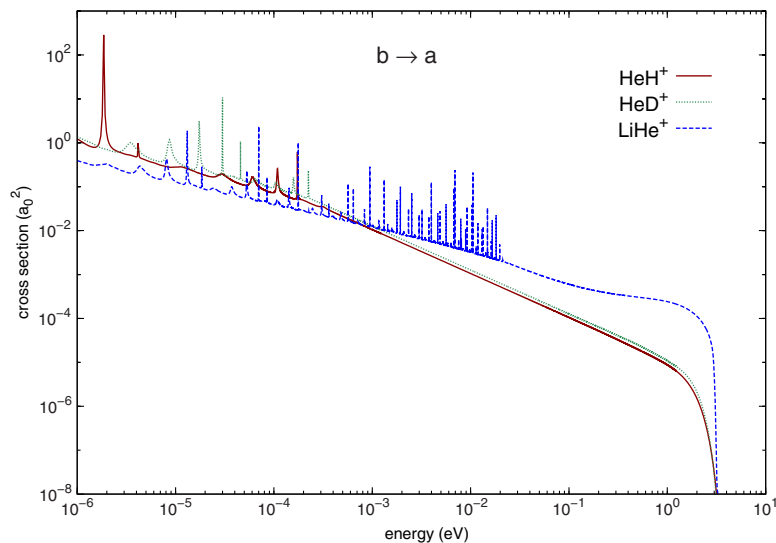


Figure 2. Cross sections for spontaneous ($T_b = 0$ K) radiative association process $b \rightarrow a$. Only the contribution of resonances wider than 0.01 cm^{-1} is shown. (A color version of this figure is available in the online journal.)

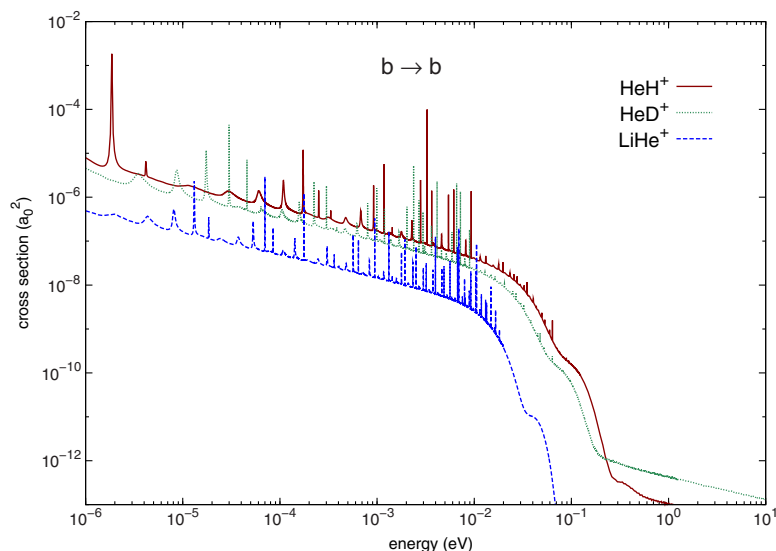


Figure 3. Cross sections for spontaneous ($T_b = 0$ K) radiative association process $b \rightarrow b$. Only the contribution of resonances wider than 0.01 cm^{-1} is shown. (A color version of this figure is available in the online journal.)

considered here (HeH^+ , HeD^+ , LiHe^+) are displayed in Figures 2 and 3, respectively. As expected the results obtained for the associations of $\text{He}(2^3\text{S})$ with H^+ or D^+ differ only marginally from each other. For the $b \rightarrow a$ processes, at least at lower energies, the cross section curves of the three association processes are very close to each other, whereas for $b \rightarrow b$ there is a substantial difference of about one order of magnitude between the cross section curve for the association with Li^+ compared to the others. The drop-off of the cross section curves for the $b \rightarrow a$ processes occurs at higher energies compared to $b \rightarrow b$.

The low-energy resonance structure of the RA cross sections, which is created by the quasi-bound states trapped behind the centrifugal barrier, is practically identical for the $b \rightarrow a$ and $b \rightarrow b$ processes in each of the three dimers. It seems that the fact that for each of the two processes the initial complex

formation takes place on their respective b -state potentials is predominant for the cross section structure in this very low energy region. For the Li^+ association an obvious increase of the density of resonance lines in the medium energy region is observed. Especially for the $b \rightarrow a$ process, this should be due to the deep potential well of the $\text{LiHe}^+(a^3\Sigma^+)$ state potential with the larger number of bound rovibrational states in this target electronic state (see Table 1). For comparison, the number of the corresponding bound rovibrational states on the $\text{HeH}^+(a^3\Sigma^+)$ state potential curve is substantially smaller. On the other hand, as shown in Table 1, for the H^+ and D^+ associations the number of the bound rovibrational states in the $\text{HeH}^+(b^3\Sigma^+)$ target state potential is larger, leading to a denser resonance structure for the $b \rightarrow b$ processes in the medium energy region in Figure 3.

The corresponding rate coefficients for the spontaneous ($T_b = 0$ K) RA $b \rightarrow a$ process are plotted in Figure 4, and numerical

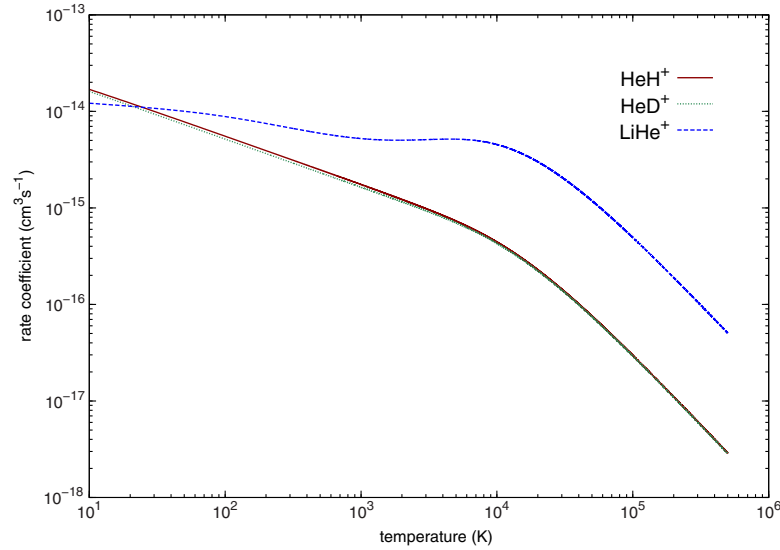


Figure 4. Rate coefficients for spontaneous ($T_b = 0$ K) radiative association $b \rightarrow a$ of $\text{He}(2^3\text{S})$ with hydrogen and lithium ions. (A color version of this figure is available in the online journal.)

Table 2
Values of the Rate Coefficients (in $\text{cm}^3 \text{s}^{-1}$) for Radiative Association of $\text{He}(2^3\text{S})$ with Hydrogen and Lithium Ions^a

T (K)	HeH^+			HeD^+			LiHe^+		
	$b \rightarrow a^b$	$b \rightarrow b^b$	$b \rightarrow b^c$	$b \rightarrow a^b$	$b \rightarrow b^b$	$b \rightarrow b^c$	$b \rightarrow a^b$	$b \rightarrow b^b$	$b \rightarrow b^c$
10	1.69(-14)	3.71(-19)	1.94(-17)	1.61(-14)	1.64(-19)	1.03(-17)	1.22(-14)	1.45(-20)	1.36(-18)
20	1.22(-14)	3.54(-19)	1.67(-17)	1.15(-14)	1.43(-19)	8.28(-18)	1.13(-14)	1.30(-20)	1.13(-18)
30	1.00(-14)	3.30(-19)	1.47(-17)	9.39(-15)	1.31(-19)	7.19(-18)	1.08(-14)	1.19(-20)	9.83(-19)
50	7.79(-15)	2.87(-19)	1.19(-17)	7.29(-15)	1.14(-19)	5.81(-18)	1.00(-14)	9.93(-21)	7.65(-19)
100	5.53(-15)	2.18(-19)	8.10(-18)	5.16(-15)	8.56(-20)	3.90(-18)	8.84(-15)	6.60(-21)	4.63(-19)
200	3.92(-15)	1.43(-19)	4.76(-18)	3.65(-15)	5.41(-20)	2.21(-18)	7.50(-15)	3.54(-21)	2.32(-19)
500	2.48(-15)	6.21(-20)	1.85(-18)	2.31(-15)	2.22(-20)	8.14(-19)	5.94(-15)	1.21(-21)	7.49(-20)
1000	1.75(-15)	2.78(-20)	7.78(-19)	1.64(-15)	9.60(-21)	3.34(-19)	5.23(-15)	4.76(-22)	2.90(-20)
2000	1.22(-15)	1.13(-20)	3.03(-19)	1.16(-15)	3.82(-21)	1.28(-19)	5.03(-15)	1.78(-22)	1.07(-20)
2500	1.09(-15)	8.30(-21)	2.22(-19)	1.03(-15)	2.80(-21)	9.32(-20)	5.06(-15)	1.29(-22)	7.75(-21)
3000	9.85(-16)	6.44(-21)	1.71(-19)	9.36(-16)	2.17(-21)	7.17(-20)	5.10(-15)	9.88(-23)	5.93(-21)
4000	8.36(-16)	4.29(-21)	1.13(-19)	7.99(-16)	1.44(-21)	4.73(-20)	5.16(-15)	6.48(-23)	3.88(-21)
6000	6.49(-16)	2.40(-21)	6.26(-20)	6.24(-16)	8.09(-22)	2.61(-20)	5.10(-15)	3.56(-23)	2.13(-21)
8000	5.29(-16)	1.58(-21)	4.10(-20)	5.10(-16)	5.36(-22)	1.71(-20)	4.86(-15)	2.33(-23)	1.39(-21)
10000	4.43(-16)	1.14(-21)	2.95(-20)	4.29(-16)	3.90(-22)	1.23(-20)	4.54(-15)	1.67(-23)	9.97(-22)
16000	2.88(-16)	5.73(-22)	1.47(-20)	2.80(-16)	2.02(-22)	6.12(-21)	3.54(-15)	8.30(-24)	4.94(-22)
20000	2.28(-16)	4.13(-22)	1.06(-20)	2.23(-16)	1.49(-22)	4.40(-21)	3.00(-15)	5.95(-24)	3.54(-22)
25000	1.78(-16)	2.98(-22)	7.57(-21)	1.74(-16)	1.11(-22)	3.16(-21)	2.48(-15)	4.27(-24)	2.54(-22)
32000	1.33(-16)	2.07(-22)	5.24(-21)	1.30(-16)	8.09(-23)	2.19(-21)	1.95(-15)	2.95(-24)	1.75(-22)
50000	7.59(-17)	1.09(-22)	2.69(-21)	7.45(-17)	4.80(-23)	1.13(-21)	1.19(-15)	1.52(-24)	8.98(-23)
64000	5.47(-17)	7.63(-23)	1.86(-21)	5.38(-17)	3.69(-23)	7.84(-22)	8.79(-16)	1.05(-24)	6.21(-23)
100000	2.97(-17)	4.05(-23)	9.55(-22)	2.92(-17)	2.34(-23)	4.06(-22)	4.93(-16)	5.44(-25)	3.18(-23)
200000	1.11(-17)	1.53(-23)	3.39(-22)	1.09(-17)	1.12(-23)	1.47(-22)	1.90(-16)	1.95(-25)	1.13(-23)
500000	2.89(-18)	4.13(-24)	8.61(-23)	2.85(-18)	3.65(-24)	3.79(-23)	5.04(-17)	5.00(-26)	2.85(-24)

Notes.

^a $x(-y) \equiv x \times 10^{-y}$.

^b Spontaneous process ($T_b = 0$ K).

^c Stimulated process ($T_b = 10,000$ K).

values for the $b \rightarrow a$ and $b \rightarrow b$ processes, evaluated at selected temperatures, are provided in Table 2. In Table 3, the values of the fitted parameters from the Arrhenius-type function (5) are presented for the dominant $b \rightarrow a$ process. As expected, the rate coefficients for the $b \rightarrow b$ RA processes are very small because of $\Delta E_{b \rightarrow b} = 0$. For the $b \rightarrow a$ processes the rates at very low temperatures between 10 and 100 K are rather similar

for the three dimer systems considered here (in the range of $10^{-14} \text{ cm}^3 \text{ s}^{-1}$). However, whereas the rate curves for HeH^+ and HeD^+ show the typical temperature fall off, the rate constant for the LiHe^+ association stays almost constant up to a temperature of about $T = 10,000$ K. The difference between the HeH^+ and the LiHe^+ curves at this temperature becomes about one order of magnitude ($4.4 \times 10^{-16} \text{ cm}^3 \text{ s}^{-1}$ versus $4.9 \times 10^{-15} \text{ cm}^3 \text{ s}^{-1}$).

Table 3
Values of the Arrhenius-function Parameters Representing the Rate Coefficients for the Spontaneous Radiative Association $b \rightarrow a$ of $\text{He}(2^3\text{S})$ with Hydrogen and Lithium Ions^a

System	Process	T (K)	α ($\text{cm}^3 \text{s}^{-1}$)	β	γ (K)
HeH ⁺	$b \rightarrow a$	1–1000	3.1998(–15)	–0.4994	0.2514
		1000–15000	8.7121(–15)	–0.8337	698.8793
		15000–500000	1.7782(–13)	–1.4829	8624.2387
HeD ⁺	$b \rightarrow a$	1–1000	2.9880(–15)	–0.4993	0.1525
		1000–15000	8.0080(–15)	–0.8190	698.3095
		15000–500000	1.7504(–13)	–1.4826	8818.9643
LiHe ⁺	$b \rightarrow a$	1–200	7.2229(–15)	–0.1733	0.2822
		200–5000	4.2584(–15)	0.0581	–136.5920
		5000–15000	1.7184(–13)	–0.8943	5014.2119
		15000–500000	3.0222(–12)	–1.4771	14201.5149

Note. ^a $x(-y) \equiv x \times 10^{-y}$.

This higher LiHe⁺ association rate corresponds to the finding that the cross sections for the $b \rightarrow a$ process for LiHe⁺ are larger at higher energies.

Our results for the spontaneous RA $b \rightarrow a$ of HeH⁺ can be compared with the very recent theoretical study dedicated to the formation of HeH⁺ in the metastable triplet state $a^3\Sigma^+$ (Loreau et al. 2013). At lower temperatures, our rate coefficients for this process are almost an order of magnitude larger than those of Loreau et al. (2013). Apart from using slightly different potential energy curves for the $a^3\Sigma^+$ and $b^3\Sigma^+$ states and different methods for the cross section calculations (the time-dependent wave packet method in the diabatic representation in Loreau et al. 2013 versus the time-independent method in the Born–Oppenheimer approximation in the present study), which leads overall to different cross sections in these two studies, the discrepancy is also caused by the inclusion of the low-energy RA cross sections into our rate-coefficient calculations. Furthermore, several shape resonances in this low-energy region (up to 10^{-3} eV, see Figure 2 and Table 1) contribute to the corresponding rate coefficient at lower temperatures as well.

Stimulated RA is relevant only for processes with very small ΔE , where it can lead to an increase of the rate coefficients by up to two orders of magnitude (for moderate background temperatures up to $T_b = 10,000$ K). That is why in our study the stimulation of RA by background blackbody radiation concerns only the $b \rightarrow b$ process. The calculated increase at $T_b = 10,000$ K in the rate coefficients is indeed two orders of magnitude (see Table 2), similar to He₂⁺ (Augustovičová et al. 2013a, 2013b). Even then, it results in the values of the corresponding rate coefficients of the order of (10^{-17} $\text{cm}^3 \text{s}^{-1}$) at low temperatures. This is still much smaller than the rate coefficients of the spontaneous $b \rightarrow a$ process.

In previous studies, the depopulation of He(2^3S) via RA reactions with the He⁺ ions was investigated leading to the formation of He₂⁺ either in its electronic ground state ($X^2\Sigma_u^+$; Augustovičová et al. 2013a) or in the lowest excited quartet state ($b^4\Sigma_u^+$; Augustovičová et al. 2013b). Comparison of the rate coefficients obtained in these calculations with the present results shows that at very low temperatures between 10 and 100 K only the rate for the He₂⁺ ground state formation has a magnitude comparable to the present rates, whereas the rate obtained for the quartet state formation is about two orders of magnitude smaller. At high temperatures, $T = 10,000$ K, magnitudes of the rates for the both helium-dimer ion formations

are similar to the HeH⁺ or HeD⁺ association rates (in the range of 10^{-16} $\text{cm}^3 \text{s}^{-1}$) with LiHe⁺ association being about one order of magnitude higher.

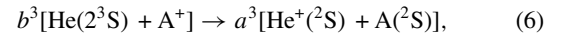
4. CONCLUSION

RA processes between the very long-lived He(2^3S) metastable atom and the atomic ions H⁺, D⁺, and Li⁺ producing the HeH⁺, HeD⁺, or LiHe⁺ dimers in their $a^3\Sigma^+$ and $b^3\Sigma^+$ excited triplet states are investigated in this study. The dynamic calculations are based on highly accurate state-of-the-art ab initio calculations of the $a^3\Sigma^+$ and $b^3\Sigma^+$ state interaction potentials of HeH⁺ and LiHe⁺ and the associated transition dipole-moment functions. Characteristics of these states such as equilibrium bond distances R_e and \mathcal{D}_e are in the case of HeH⁺ in excellent agreement with the benchmark calculations of Kolos (1976). In the case of LiHe⁺, the corresponding highly accurate potential energy curves and dipole moments obtained recently by Soldán & Kraemer (2012) are used.

Cross sections for the spontaneous ($T_b = 0$ K) RA for the $b \rightarrow a$ and $b \rightarrow b$ RA processes are calculated as functions of collision energy. The corresponding rate coefficients characterizing the efficiency of the formation of the dimer ions in their $a^3\Sigma^+$ and $b^3\Sigma^+$ triplet states are obtained as functions over a wide range of temperatures. Due to the large differences between the ionization energies of He and Li or He and H, the two-state $b \rightarrow a$ processes are as expected by far the most efficient ones compared to the one-state $b \rightarrow b$ processes. With exception for the LiHe⁺ formation reaction, the rates for the two other formation reactions are steadily decreasing with increasing reaction temperatures. The rate for the LiHe⁺ formation reaction, however, remains more or less constant up to a temperature of about $T = 10,000$ K. Compared to previously studied depopulation reactions of the metastable He(2^3S) atom by collisions with He⁺ ions the processes considered in the present study are more efficient in the low temperature region, and in the case of LiHe⁺ formation even over a wider temperature range.

Collisional reactions of He(2^3S) with ions provide significant cooling in nebulae with low heavy-element abundances (Clegg 1987). The $a^3\Sigma^+$ state of HeH⁺ thus formed according to the processes described here is metastable with a lifetime of 150 s (Loreau et al. 2010) because the direct radiative transition to the singlet ground state is spin-forbidden. In low density plasmas, photodissociation processes are then the dominant depopulation reactions rather than collisional destructions (Loreau et al. 2013). Assuming equilibrium conditions between radiative associative formation and photodissociative destruction of the HeH⁺($a^3\Sigma^+$) and using information about the abundance of metastable helium in nebulae as a function of the He⁺ and electron densities (Clegg 1987), Loreau et al. (2013) derived a number density for the metastable HeH⁺ triplet state $n = 3 \times 10^{-10}$ cm^{-3} , a value which should be about an order of magnitude larger using the association rates obtained in this study. Although much less abundant than the ground state singlet species, it has been argued that the RA process forming the triplet could nonetheless be of importance in primordial chemistry (Lepp et al. 2002).

In competition with the two-state $b \rightarrow a$ RA processes studied here, radiative charge transfer (RCT) reactions become an important alternative for the heteroatomic dimers. Using the notation of the association processes listed above, the relevant RCT reactions can be described as



where A substitutes for H, D, or Li. In contrast to RA, in the RCT reaction, transitions under spontaneous photon emission take place from the initial resonance/continuum levels on the *b*-state potential to the resonance/continuum levels on the target *a*-state potential leading to immediate dissociation. For dimer systems the energy of the higher continuum levels is simply converted into kinetic energy of the dissociation partners. Previous accurate state-to-state calculations have shown that the rate constants for these RCT reactions can be orders of magnitude larger than the rates for the associated RA processes. Work is in progress to investigate differences in the efficiencies of the two reaction types.

L.A. and P.S. appreciate support from the Charles University in Prague. L.A. acknowledges funding from the Grant Agency of the Charles University in Prague (GAUK grant No. 550112).

REFERENCES

- Augustovičová, L., Špirko, V., Kraemer, W. P., & Soldán, P. 2012, *CPL*, **531**, 59
 Augustovičová, L., Špirko, V., Kraemer, W. P., & Soldán, P. 2013a, *A&A*, **553**, A42
 Augustovičová, L., Špirko, V., Kraemer, W. P., & Soldán, P. 2013b, *MNRAS*, **435**, 1541
 Boyce, P. B., & W. K. Ford, J. 1966, *PASP*, **78**, 163
 Chibisov, M. I., Yousif, F. B., Van der Donk, P. J. T., & Mitchell, J. B. A. 1996, *PhRvA*, **54**, 4997
 Clegg, R. 1987, *MNRAS*, **229**, 31
 Connor, J. N. L., & Smith, A. D. 1981, *MolPh*, **43**, 397
 Cooley, J. W. 1961, *MaCom*, **15**, 363
 Drake, G. W. F. 1971, *PhRvA*, **3**, 908
 Galazutdinov, G. A., & Krelowski, J. 2012, *MNRAS*, **422**, 3457
 Hansson, A., & Watson, J. K. G. 2005, *JMoSp*, **233**, 169
 Ho, T. S., & Rabitz, H. 1996, *JChPh*, **104**, 2584
 Ho, T. S., & Rabitz, H. 2000, *JChPh*, **113**, 3960
 Hodgman, S. S., Dall, R. G., Byron, L. J., et al. 2009, *PhRvL*, **103**, 053002
 Huang, Y., & Le Roy, R. J. 2003, *JChPh*, **119**, 7398
 Indriolo, N., Hobbs, L., Hinkle, K. H., & McCall, B. J. 2009, *ApJ*, **703**, 2131
 Knowles, P. J., & Werner, H.-J. 1985, *CPL*, **115**, 259
 Knowles, P. J., & Werner, H.-J. 1988, *CPL*, **145**, 514
 Kolos, W. 1976, *IJQC*, **10**, 217
 Kraemer, W. P., Špirko, V., & Juřek, M. 1995, *CPL*, **236**, 177
 Kramida, A., Ralchenko, Y., Reader, J., et al. 2011, NIST Atomic Spectra Database (version 5.0). See <http://physics.nist.gov/asd3>
 Le Roy, R. J. 2005, LEVEL 7.7: A Computer Program for Solving the Radial Schrödinger Equation CPRR-661 (Ontario: University of Waterloo)
 Le Roy, R. J., & Liu, W. K. 1978, *JChPh*, **69**, 3622
 Leighly, K. M., Dietrich, M., & Barber, S. 2011, *ApJ*, **728**, 94
 Leighly, K. M., Lucy, A. B., Dietrich, M., Temdrup, D., & Gallagher, S. C. 2012, in ASP Conf. Ser. 460, AGN Winds in Charleston, ed. G. Chartas, F. Hamann, & K. M. Leighly (San Francisco, CA: ASP), 72
 Lepp, S., Stancil, P. C., & Dalgarno, A. 2002, *JPhB*, **35**, R57
 Loreau, J., Liévin, J., & Vaeck, N. 2010, *JChPh*, **133**, 114302
 Loreau, J., Vranckx, S., Desouter-Lecomte, M., Vaeck, N., & Dalgarno, A. 2013, *JPCA*, **117**, 9486
 Michels, H. H. 1966, *JChPh*, **44**, 3834
 Naito, H., Tajitsu, A., Arai, A., & Sadakane, K. 2013, *PASJ*, **65**, 37
 Numerov, B. 1933, *MaCom*, **2**, 188
 Rees, M. J., Sciama, D. W., & Stobbs, S. 1968, *ApL*, **2**, 243
 Robbins, R. R. 1968, *ApJL*, **151**, L35
 Scherb, F. 1968, *ApJL*, **153**, L55
 Sewell, G. L. 1949, *PCPS*, **45**, 678
 Soldán, P., & Hutson, J. M. 2000, *JChPh*, **112**, 4415
 Soldán, P., & Kraemer, W. P. 2012, *CP*, **393**, 135
 Stancil, P. C., & Dalgarno, A. 1997, *ApJ*, **479**, 543
 Struve, O., Wurm, K., & Henyey, L. 1939, *PNAS*, **25**, 67
 Wansbeek, L. W., Sahoo, B. K., Timmermans, R. G. E., Das, B. P., & Mukherjee, D. 2008, *PhRvA*, **78**, 012515
 Watson, J. K. G. 1980, *JMoSp*, **80**, 411
 Werner, H.-J., & Knowles, P. J. 1985, *JChPh*, **82**, 5053
 Werner, H.-J., & Knowles, P. J. 1988, *JChPh*, **89**, 5803
 Werner, H.-J., & Knowles, P. J. 2010, MOLPRO, version 2010.2: A Package of Ab Initio Quantum-chemistry Programs, See <http://www.molpro.net>
 Yan, Z.-C., & Babb, J. F. 1998, *PhRvA*, **58**, 1247
 Yousif, F. B., Mitchell, J. B. A., Rogelstad, M., et al. 1994, *PhRvA*, **49**, 4610
 Zeldovich, Y. B., Novikov, I. D., & Sunyaev, R. A. 1966, *Astron. Circ. U.S.S.R.*, No. 371
 Zygelman, B., & Dalgarno, A. 1990, *ApJ*, **365**, 239
 Zygelman, B., Stancil, P. C., & Dalgarno, A. 1998, *ApJ*, **508**, 151

DEPOPULATION OF METASTABLE HELIUM $\text{He}(2^1\text{S})$
BY RADIATIVE ASSOCIATION WITH HYDROGEN
AND LITHIUM CATIONS

Bibliographic record of the attached publication:

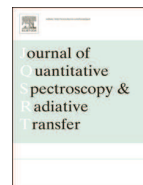
Augustovičová, L., W. P. Kraemer, and P. Soldán (2014). “Depopulation of metastable helium $\text{He}(2^1\text{S})$ by radiative association with hydrogen and lithium cations.” In: *Journal of Quantitative Spectroscopy and Radiative Transfer*, 148, pp. 27–37.

DOI: [10.1016/j.jqsrt.2014.06.012](https://doi.org/10.1016/j.jqsrt.2014.06.012).



Contents lists available at ScienceDirect

Journal of Quantitative Spectroscopy & Radiative Transfer

journal homepage: www.elsevier.com/locate/jqsrt

Depopulation of metastable helium He(2^1S) by radiative association with hydrogen and lithium cations

Lucie Augustovičová^a, Wolfgang P. Kraemer^b, Pavel Soldán^{a,*}^a Charles University in Prague, Faculty of Mathematics and Physics, Department of Chemical Physics and Optics, Ke Karlovu 3, CZ-12116 Prague 2, Czech Republic^b Max-Planck-Institute of Astrophysics, Postfach 1371, D-85741 Garching, Germany

ARTICLE INFO

Article history:

Received 29 April 2014

Received in revised form

10 June 2014

Accepted 18 June 2014

Available online 26 June 2014

Keywords:

Radiative association

Metastable helium

Rates of formation

Molecular ions

ABSTRACT

Depopulation of metastable He(2^1S) by radiative association with hydrogen and lithium ions resulting in the formation of the HeH⁺ and HeLi⁺ molecular ions is investigated. Energy dependent cross-sections for spontaneous and stimulated processes on the spin-singlet manifold are calculated using a fully quantal approach and considering the association to rotational–vibrational states of the lowest singlet electronic states $X^1\Sigma^+$, $A^1\Sigma^+$, and $B^1\Sigma^+$ from the continuum states of the $B^1\Sigma^+$ electronic state. Evaluation of the cross-sections is based on highly accurate quantum calculations taking into account all possible state-to-state transitions at thermal energies (for spontaneous association) or at higher background temperatures (stimulated association). The corresponding rate coefficients are then presented as functions of temperature. As expected calculations show that the rate coefficients for radiative association to the X and A states are several orders of magnitude larger than the one for the B state formation. On the other hand, stimulation of the radiative association by black-body background radiation has a noticeable effect only on the $B \rightarrow B$ process.

© 2014 Elsevier Ltd. All rights reserved.

1. Introduction

In view of the relatively large abundance of helium in the interstellar space astrophysical consequences of the possible formation of its metastable levels were discussed as early as in 1939 [1]. Whereas depopulation of atomic metastable states was initially thought to occur entirely through collisions, absorption of radiation, or perturbation by external fields, it was later found [2] that secondary decay mechanisms (i.e., through second-order multipole radiation such as electric quadrupole or magnetic dipole rather than only electric dipole radiation) could be equally

efficient depending on the lifetime of the metastable state and the reaction conditions. In this context, the theory of multiple quanta radiation was outlined by Goepfert-Mayer [3].

Radiation due to spontaneous as well as collisional depopulation is of high astrophysical interest because metastable states of atoms provide much of the light emitted from planetary nebulae. Measurements of the intensity of the relevant radiation lines yield information about densities, temperatures, chemical compositions, or other properties of these non-terrestrial features.

In the case of metastable He(2^1S) the key characteristic is its lifetime. The first estimate by Dalgarno [4] of 22 ms was later corrected to 20 ms [5]. The most reliable recent theoretical [6] and experimental [7,8] lifetime values are $\tau(2^1S) = 19.7 \pm 0.1$ ms. After the first estimate by Dalgarno, Breit and Teller [9] have pointed out that the 2^1S state of

* Corresponding author.

E-mail addresses: lucie.augustovicova@mff.cuni.cz (L. Augustovičová), wpk@mpa-garching.mpg.de (W.P. Kraemer), pavel.soldan@mff.cuni.cz (P. Soldán).

<http://dx.doi.org/10.1016/j.jqsrt.2014.06.012>

0022-4073/© 2014 Elsevier Ltd. All rights reserved.

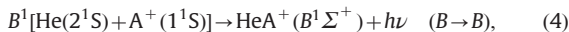
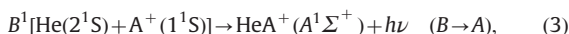
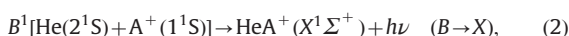
helium should decay predominantly by two-photon electric dipole emission. In their proposed scheme initial quenching of the metastable helium occurs by resonant absorption to the intermediate 2^1P_1 -state which almost immediately decays to the 1^1S ground state. At higher matter densities this spontaneous process is in competition with depopulation via collisions with positive ions, especially with protons.

In 1963 Allison and Dalgarno [10] investigated deactivation of metastable helium by proton impact at temperatures up to 16,000 K. The metastable state considered there was $\text{He}(2^1S)$, and its deactivation by proton impact leading to the atomic ground state $\text{He}(1^1S)$



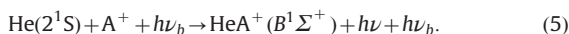
was studied on a semiempirical level of theory. This reaction represents the direct deactivation of metastable $\text{He}(2^1S)$ to the $\text{He}(1^1S)$ ground state via an inelastic collision with a proton (the initial and final states are the continuum states supported by the corresponding potential curves).

In the present study, collisional depopulations of the $\text{He}(2^1S)$ metastable state via radiative association with highly abundant protons as well as with Li^+ ions are investigated. The corresponding processes induced by dipole-moment continuum-bound transitions are



where $^1[\dots]$ describes the singlet manifold of the corresponding collisional continuum and A stands for H or Li. According to this scheme the reactions start from collisions of helium in the 2^1S metastable state with H^+ or Li^+ ions, and proceed via resonance and continuum states of the $B^1\Sigma^+$ potential of the collisional complex to form (under spontaneous photon emission) the molecular ions in one of the $X^1\Sigma^+$, $A^1\Sigma^+$, and $B^1\Sigma^+$ electronic states. In the following text these processes are denoted as $B \rightarrow X$, $B \rightarrow A$, and $B \rightarrow B$, respectively. The $B \rightarrow X$ process starts from the same reactant channel on the $B^1\Sigma^+$ state potential as the reaction (1), but proceeds under spontaneous photon emission to bound rovibrational levels of the ground state.

Apart from the spontaneous emission, the corresponding radiative association processes stimulated by background radiation are also considered [11,12]. Since this stimulated radiative association is relevant only for processes with very small photon energies (see for instance Ref. [13]), the background radiation effect is only determined for the $B \rightarrow B$ processes:



Background temperatures up to 10^4 K are taken into account.

2. Methods

The theory of formation of diatomic bound species via radiative association has been reviewed by Dalgarno and

coworkers [14,11], and this approach has been implemented in our computer program suite [15]. The radiative association treatment is based on the calculations of cross-sections at various collision energies and rate coefficients over various temperatures.

The rate coefficients for formation of a molecule by (spontaneous or stimulated) radiative association at a given temperature T are obtained by averaging the corresponding cross-sections σ over a Maxwellian velocity distribution of the collisional continuum

$$\alpha(T; T_b) = \left(\frac{8}{\mu\pi}\right)^{1/2} \left(\frac{1}{k_B T}\right)^{3/2} \int_0^\infty E \sigma(E; T_b) e^{-E/k_B T} dE, \quad (6)$$

where T_b is the brightness temperature.

Given that the numbers of shape resonances in some studied processes (see Table 2) are not negligible, they have to be taken into account in order to evaluate this integral as accurately as possible. The contributions from wide and narrow resonances to the radiative association rate coefficients are treated in a separate calculation following the approach of Ref. [15]. They enhance the background contribution to the rate coefficients up to 15%. It is also convenient to use a simple analytical form to represent the numerical values of the rate coefficients. In the present study, we use the Arrhenius-type function

$$f(T) = \alpha \left(\frac{T}{300}\right)^\beta e^{-\gamma/T}, \quad (7)$$

where α , β , and γ are the fitting parameters. In order to keep the maximum relative error below 10%, the temperature range is divided into several intervals.

The quantum-mechanical radiative association cross sections $\sigma(E; T_b)$ in the field of black-body radiation (characterized by T_b) are a sum of individual cross-sections corresponding to allowed transitions from a continuum state (with a positive energy E and orbital angular momentum J') to bound rovibrational states (with vibrational and rotational quantum numbers v'' and J'' , respectively):

$$\sigma(E; T_b) = \sum_{J', v'', J''} \sigma_{J', v'', J''}(E; T_b). \quad (8)$$

The individual cross-sections, in the case of dipole moment transitions, can be expressed as

$$\sigma_{J', v'', J''}(E; T_b) = \frac{1}{4\pi\epsilon_0} \frac{64}{3} \frac{\pi^5}{c^3 k^2} p \nu_{E; v'', J''}^3 S_{J' J''} M_{E; J', v'', J''}^2 \times \left[\frac{1}{1 - \exp(-h\nu_{E; v'', J''}/k_B T_b)} \right], \quad (9)$$

where c is the speed of light in vacuum, $k^2 = 2\mu E/\hbar^2$, μ is the “charge-modified reduced mass” [16] of the molecular ion ($\mu = 1467.778424$ a.u. for $^4\text{HeH}^+$ and $\mu = 4646.087837$ a.u. for $^4\text{He}^7\text{Li}^+$), p is the probability of approach in the initial electronic state ($p = 1$ for all three processes) and $\nu_{E; v'', J''}$ is the emitted photon frequency, $h\nu_{E; v'', J''} = E + \Delta E - E_{v'', J''}$, where $\Delta E_{B \rightarrow B} = 0$ eV and $\Delta E_{B \rightarrow X} = 20.6153$ eV for both species, $\Delta E_{B \rightarrow A} = 9.6266$ eV for HeH^+ and $\Delta E_{B \rightarrow A} = 1.4201$ eV for HeLi^+ [17]. For dipole moment transitions of a heteronuclear diatomic molecule within the Hund’s case (a) spin-less approximation [18] the final rotational level J'' is governed by the rotational selection rule $\Delta J = J' - J'' = \mp 1$. Thus there are only two branches and the only non-zero Hönl–London

coefficients are $S_{J',J'+1} = J' + 1$ and $S_{J',J'-1} = J'$, respectively. $M_{EJ',v',J'}$ is the matrix element of the transition dipole moment function $d_z(R)$ between the energy-normalized continuum radial wave function $\chi_{J'}(E, R)$ for the partial wave J' and the normalized bound-state radial wave function $\psi_{v',J'}(R)$. The radial wave functions are determined by numerical integration of the corresponding Schrödinger equations including a centrifugal term and potential energy functions supporting the initial continuum state E , J' and the final bound state v' , J' , respectively [19,20]. Positions and tunneling widths of resonances were calculated employing the computer program LEVEL 7.7 [21] and making use of the Airy-function boundary condition at the outermost classical turning point [22] and the uniform semiclassical method [23,24].

We choose numerical representation of the potential energy and dipole moment functions by one-dimensional reciprocal-power reproducing kernel Hilbert space (RP-RKHS) interpolation method [25]. This method allows not only for qualitatively correct extrapolation in the long-range region of the $A + B^+$ interaction potential but it also allows for the use of predetermined values of long-range coefficients [26]. In the case of potential energy curves the interpolation was done with respect to R^2 [27] using RP-RKHS parameters $m=1$ and $n=2$ and the leading long-range coefficient D_4 , which is equal to $\alpha_d/2$, was kept fixed to the values given by static dipole polarizabilities ($\alpha_d[\text{He}(1^1\text{S})] = 1.383191$ a.u. [28], $\alpha_d[\text{H}(1^2\text{S})] = 4.5$ a.u. [29], $\alpha_d[\text{He}(2^1\text{S})] = 800.31633$ a.u. [30] and $\alpha_d[\text{Li}(2^2\text{S})] = 162.87$ a.u. [31]). *Ab initio* interaction energies for the $X^1\Sigma^+$, $A^1\Sigma^+$, and $B^1\Sigma^+$ electronic states of HeH^+ and the corresponding transition dipole moment values were calculated by us employing multireference configuration interaction method (combined with a very large electron basis set) as implemented in the quantum chemistry program suit MOLPRO [32]. In the case of HeLi^+ , the corresponding

highly accurate potential energy curves and dipole moments obtained recently [33] were used.

3. Results and discussion

Potential energy curves calculated in this study for the three lowest $^1\Sigma^+$ states of HeH^+ and the corresponding transition dipole moment functions (for the $B \rightarrow X$ and $B \rightarrow A$ processes) together with the electric dipole moment curve (for the $B \rightarrow B$ process) are shown in Figs. 1 and 2, respectively. A few molecular characteristics of these potentials as well as of those calculated previously for the corresponding lowest $^1\Sigma^+$ states of HeLi^+ [33] are summarized in Table 1.

For the HeH^+ ion the results are in good agreement with the best literature data: position and well depth of the $X^1\Sigma^+$ potential agree within a few per mille with previous highly accurate results of the benchmark calculations of Kołos and Peek [34] or the calculations of Bishop and Cheung [35] in which adiabatic corrections are also included. For the $A^1\Sigma^+$ excited state equilibrium bond distance R_e and potential minimum \mathcal{D}_e also agree perfectly with the values calculated previously by Kołos [36] ($R_e = 5.522 a_0$, $\mathcal{D}_e = 380.802 \text{ cm}^{-1}$). Early comprehensive calculations by Michels [37] covering as many as 14 excited states of the HeH^+ ion are in surprisingly reasonable agreement with the present results. It should be noted however that the potential minimum energies in Ref. [37] appear to be more close to the present \mathcal{D}_0 values, i.e. to the dissociation energies relative to the ground vibrational level.

The numbers of vibrational and rovibrational levels supported by the different HeH^+ and HeLi^+ potentials and participating in the radiative association processes are collected in Table 2. In the case of the $A^1\Sigma^+$ state of HeH^+ the number of bound vibrational levels $n_v = 5$ is slightly

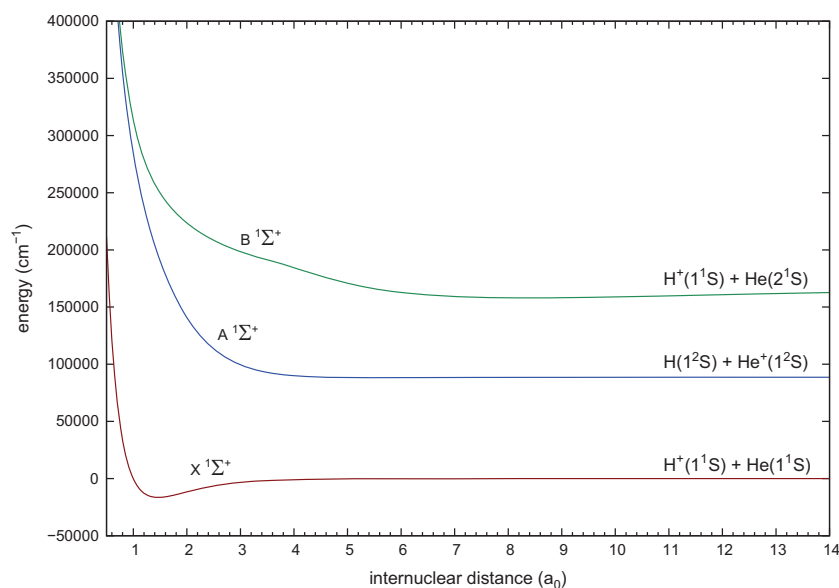


Fig. 1. Born–Oppenheimer potential energy curves of the relevant singlet states of HeH^+ with their dissociation limits.

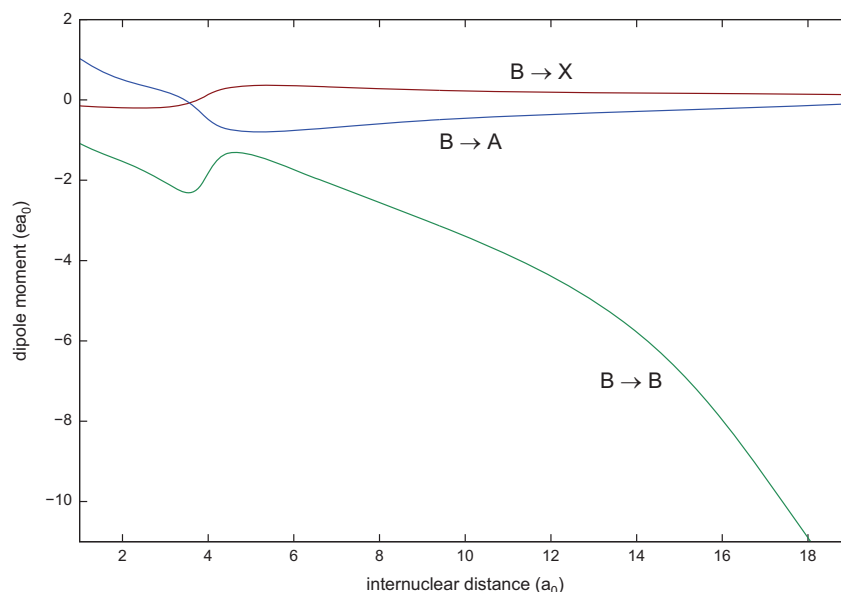


Fig. 2. Dipole-moment and transition dipole-moment functions between the relevant HeH^+ singlet electronic states.

Table 1

Molecular characteristics of the potential energy curves used in the cross-section calculations of the HeH^+ and HeLi^+ radiative association.

System	State	R_e (a_0)	D_e (cm^{-1})	D_0 (cm^{-1})	$\Delta\epsilon^a$ (eV)
HeH^+	$X^1\Sigma^+$	1.463	16,463.147	14,887.390	0
	$A^1\Sigma^+$	5.520	382.999	270.567	10.9887
	$B^1\Sigma^+$	8.381	8270.574	8086.961	20.6153
HeLi^+	$X^1\Sigma^+$	3.579	653.566	523.831	0
	$A^1\Sigma^+$	6.907	5384.068	5261.331	19.1952
	$B^1\Sigma^+$	12.049	2805.473	2744.611	20.6153

^a The energy difference of the corresponding dissociation limits from the ground state dissociation limit; experimental values from Ref. [17] were used for $\Delta\epsilon$.

Table 2

Resonance situation overview and target states characteristics for the three studied processes of the HeH^+ and HeLi^+ radiative associations^a.

System	Process	n_{tot}	n_r	n_w	n_n	n_v	n_{rv}	ΔE (eV)
HeH^+	$B \rightarrow X$	410	15	12	3	12	162	20.6153
	$B \rightarrow A$	410	3	3	0	5	33	9.6266
	$B \rightarrow B$	410	308	135	173	50	2621	0
HeLi^+	$B \rightarrow X$	656	8	8	0	8	73	20.6153
	$B \rightarrow A$	656	332	143	189	51	2948	1.4201
	$B \rightarrow B$	656	504	190	314	61	4124	0

^a Using formalism of Ref. [15]: n_{tot} is the total number of orbital resonances supported by the initial electronic state; n_r is the number of symmetry-allowed resonances, i.e. the number of resonances which have a bound partner in the corresponding target electronic state allowed by the dipole-moment selection rules; n_w is the number of symmetry-allowed wide resonances supported by the initial electronic state; n_n is the number of symmetry-allowed narrow resonances; n_v is the number of bound vibrational ($J''=0$) states of the target electronic state; n_{rv} is the number of bound rovibrational states of the target electronic state.

larger than the one given by Yousif et al. [38]. This is due to the fact that the vibrational levels in their study were determined from the potential calculations of Ref. [37]. The large difference between our n_v values for the $X^1\Sigma^+$ and $B^1\Sigma^+$ states of HeH^+ is due to the fact that the narrow (although rather deep) ground state potential can hold much less vibrational levels compared to the wide (less deep) potential of the B -state. The n_v values for the two excited states of HeLi^+ are rather large for the same reason, i.e. their potentials are fairly wide compared to the ground state.

Cross sections for spontaneous ($T_b=0$) radiative associations of the three processes for the HeH^+ and HeLi^+ dimers are displayed in Figs. 3 and 4, respectively. The cross section curves are generally decreasing with increasing collision energy and have a rapid drop-off in the energy range between 10^{-1} and 10^1 eV which is typical for radiative collision processes (e.g. [39,40]). As expected, because of much smaller photon energies the cross sections for the $B \rightarrow B$ single-state processes are orders of magnitude smaller compared to the two-state processes. The absolute magnitudes of the cross sections for the $B \rightarrow X$ and $B \rightarrow A$ processes are very comparable for both molecular ions. In the case of HeH^+ the cross sections for both the $B \rightarrow X$ and $B \rightarrow A$ processes are almost identical at low collision energies although the energy gain in $B \rightarrow X$ is twice as big. However, the corresponding factor 8 (arising from the third power of the emitted photon frequency in Eq. (8)), by which the $B \rightarrow X$ cross sections should be larger than the $B \rightarrow A$ cross sections, is easily compensated by much more favorable Franck-Condon conditions for the $B \rightarrow A$ transitions. In the case of HeLi^+ the cross sections for the $B \rightarrow A$ process are even larger than those for the $B \rightarrow X$ process at energies up to one eV despite of the fact that the energy gain in $B \rightarrow X$ is much larger. In this case, the compensation is caused by much larger $B \rightarrow A$ transition

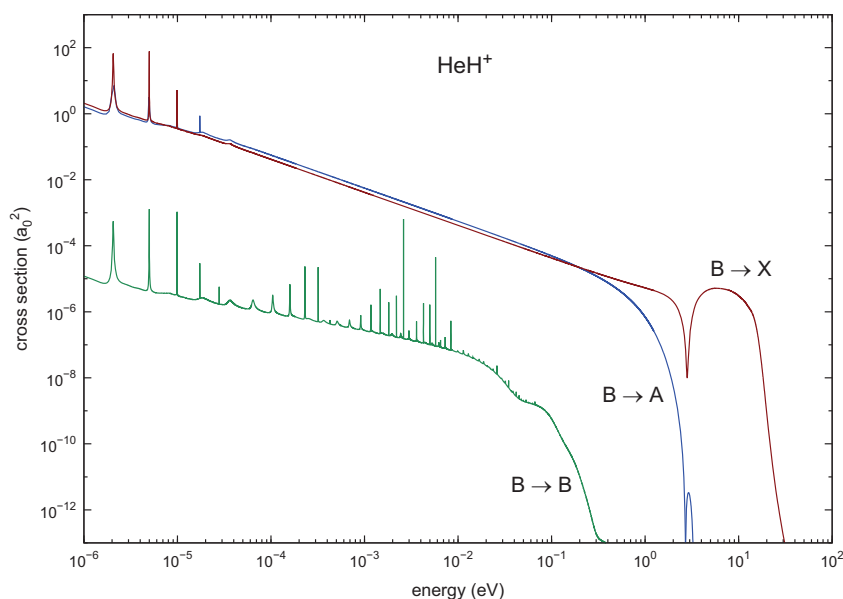


Fig. 3. Cross sections for spontaneous ($T_b = 0$ K) radiative association of HeH^+ . Only the contribution of resonances wider than 0.1 cm^{-1} is shown.

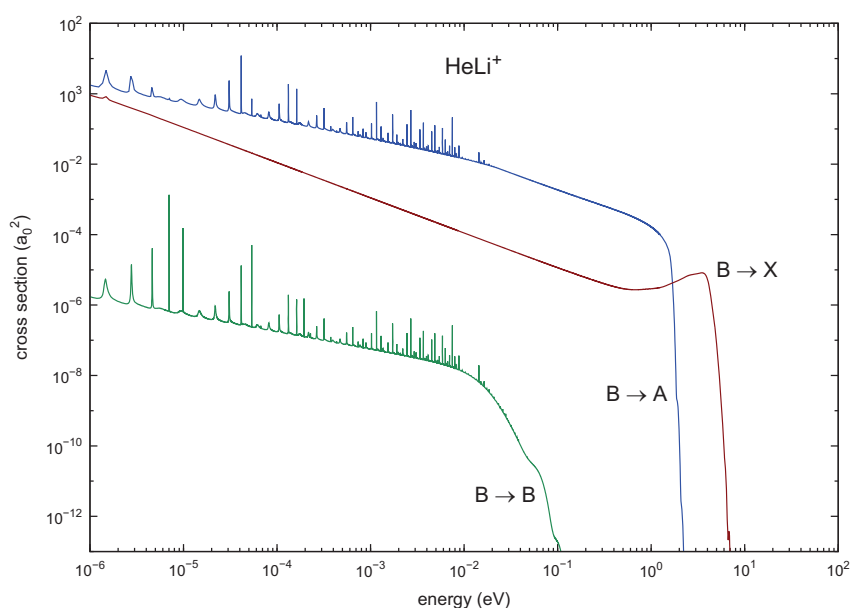


Fig. 4. Cross sections for spontaneous ($T_b = 0$ K) radiative association of HeLi^+ . Only the contribution of resonances wider than 0.1 cm^{-1} is shown.

dipole moment (see Fig. 5) combined with greater number of rovibrational states in the target $A^1\Sigma^+$ electronic state (i.e. many more terms in the sum in Eq. (8)) and more favourable Franck–Condon conditions for the $B \rightarrow A$ transitions. Samples of radiative association spectra at selected off-resonance collisional energies are depicted for two-state processes in Fig. 6 (only dominating lines are shown). In the case of the $B \rightarrow X$ process for both molecular species and also in the case of the HeH^+ $B \rightarrow A$ process, the large

values of ΔE have caused the compression of spectral lines into relatively small ultraviolet intervals. Dense visible/near-infrared spectrum of the HeLi^+ $B \rightarrow A$ process reflects the great number of target rovibrational bound states (see Table 2).

Low-energy resonance structure in the radiative association cross section curves, which is created by quasi-bound states trapped behind centrifugal barriers in the reactant channel, is practically missing for the $B \rightarrow X$

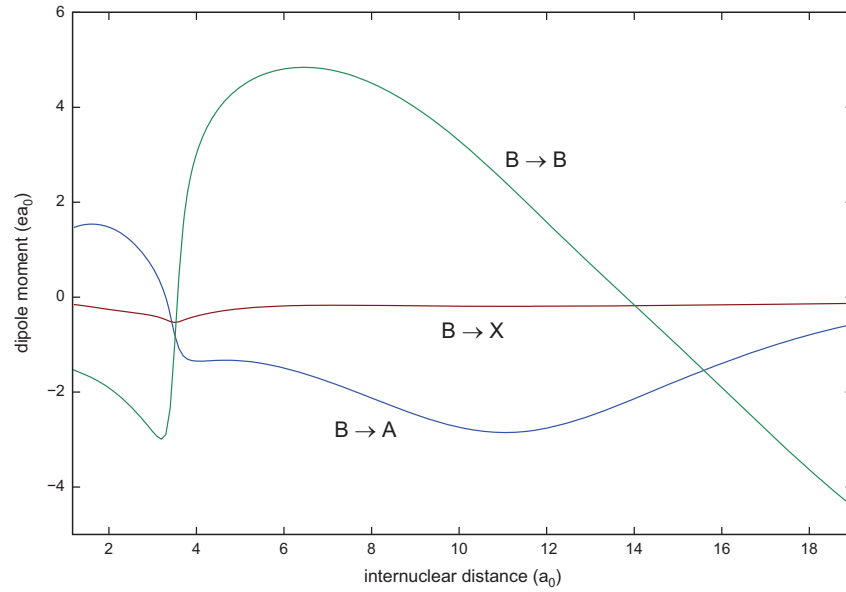


Fig. 5. Dipole-moment and transition dipole-moment functions between the relevant HeLi^+ singlet electronic states.

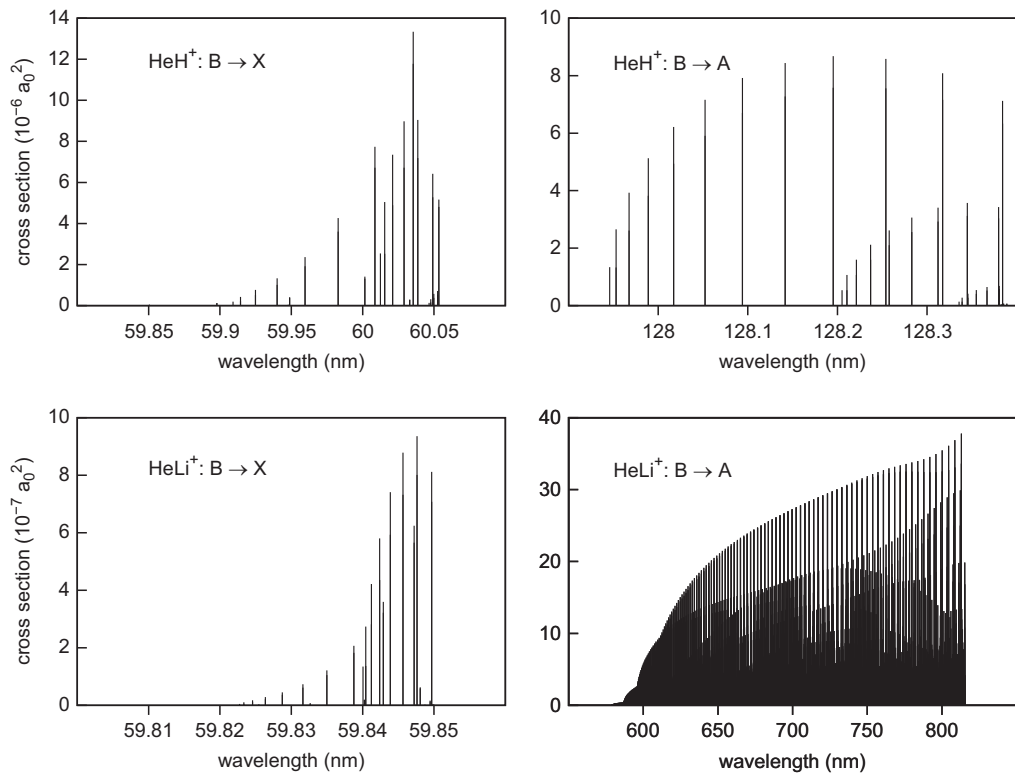


Fig. 6. Spontaneous radiative association spectra of HeH^+ at collision energy of 30 meV and of HeLi^+ at collision energy of 100 meV.

processes of the two ions and is most pronounced for $B \rightarrow B$ in both cases. In our previous study, the depopulation of metastable $\text{He}(2^3\text{S})$ by radiative association with H^+ and Li^+ ions leading to the formation of HeH^+ and HeLi^+ in

their $a^3\Sigma^+$ or $b^3\Sigma^+$ electronic states was investigated applying the same quantal approach used here [13]. The gross character of the cross sections for spontaneous radiative association obtained there appears to be very

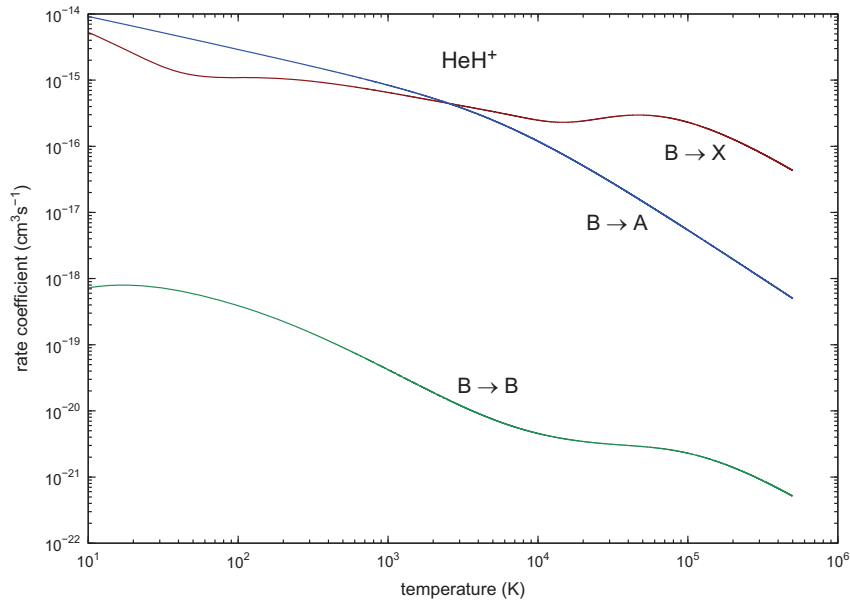


Fig. 7. Rate coefficients for spontaneous ($T_b = 0$ K) radiative association of HeH^+ .

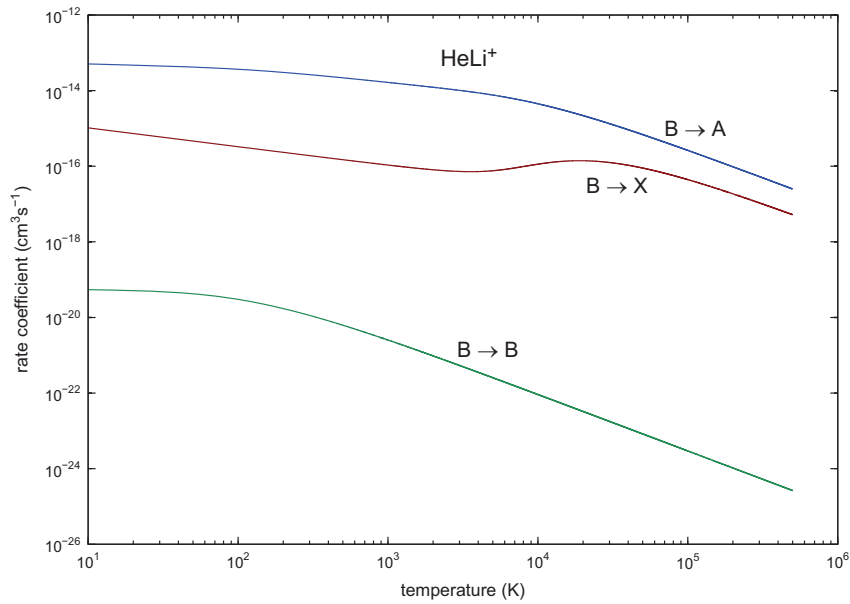


Fig. 8. Rate coefficients for spontaneous ($T_b = 0$ K) radiative association of HeLi^+ .

similar to the curves in Figs. 3 and 4. The maximum values of the cross sections at low collision energies are almost identical and the energy-dependent decrease agrees very well with the present cross section curves.

Rate coefficients for spontaneous ($T_b = 0$) radiative association of HeH^+ and HeLi^+ calculated from the cross sections are displayed in Figs. 7 and 8 for the temperature range between 10 and 10^6 K. Numerical values, evaluated at selected temperatures, are collected in Table 3 and the parameter values of the fitted Arrhenius-type function (see

Eq. (7)) are given in Table 4. As in most radiative inelastic collision processes the rate coefficients for the radiative association reactions considered here reach their maximum values at very low temperatures and decrease steadily with increasing temperatures. As expected, they are very small for the single-state $B \rightarrow B$ processes. For the $B \rightarrow X$ processes the HeH^+ radiative association rate coefficients are slightly larger compared to the corresponding results for HeLi^+ over the entire temperature range considered here. The situation is reversed for radiative

Table 3Values of the rate coefficients (in $\text{cm}^3 \text{s}^{-1}$) for radiative association of $\text{He}(2^1\text{S})$ with hydrogen and lithium cations^a.

T (K)	HeH^+				HeLi^+			
	$B \rightarrow X^b$	$B \rightarrow A^b$	$B \rightarrow B^b$	$B \rightarrow B^c$	$B \rightarrow X^b$	$B \rightarrow A^b$	$B \rightarrow B^b$	$B \rightarrow B^c$
10	5.28(−15)	9.20(−15)	7.28(−19)	4.34(−17)	1.04(−15)	5.08(−14)	5.45(−20)	4.79(−18)
20	2.54(−15)	6.53(−15)	7.93(−19)	4.45(−17)	7.34(−16)	4.72(−14)	5.13(−20)	4.20(−18)
30	1.66(−15)	5.34(−15)	7.30(−19)	3.97(−17)	5.99(−16)	4.50(−14)	4.83(−20)	3.75(−18)
50	1.19(−15)	4.13(−15)	5.91(−19)	3.06(−17)	4.64(−16)	4.20(−14)	4.23(−20)	3.04(−18)
100	1.10(−15)	2.91(−15)	3.90(−19)	1.85(−17)	3.29(−16)	3.68(−14)	3.01(−20)	1.94(−18)
200	1.05(−15)	2.04(−15)	2.25(−19)	9.58(−18)	2.33(−16)	3.04(−14)	1.72(−20)	1.02(−18)
500	8.39(−16)	1.25(−15)	9.10(−20)	3.33(−18)	1.49(−16)	2.18(−14)	6.23(−21)	3.41(−19)
1000	6.51(−16)	8.39(−16)	4.20(−20)	1.36(−18)	1.07(−16)	1.65(−14)	2.53(−21)	1.34(−19)
2000	4.91(−16)	5.31(−16)	1.90(−20)	5.25(−19)	8.07(−17)	1.23(−14)	9.60(−22)	5.01(−20)
2500	4.48(−16)	4.50(−16)	1.48(−20)	3.84(−19)	7.55(−17)	1.11(−14)	6.98(−22)	3.62(−20)
3000	4.16(−16)	3.90(−16)	1.22(−20)	2.98(−19)	7.28(−17)	1.02(−14)	5.36(−22)	2.78(−20)
4000	3.69(−16)	3.05(−16)	9.15(−21)	1.98(−19)	7.23(−17)	8.74(−15)	3.53(−22)	1.82(−20)
6000	3.09(−16)	2.07(−16)	6.42(−21)	1.12(−19)	8.24(−17)	6.78(−15)	1.94(−22)	1.00(−20)
8000	2.72(−16)	1.53(−16)	5.21(−21)	7.48(−20)	9.83(−17)	5.45(−15)	1.27(−22)	6.53(−21)
10,000	2.48(−16)	1.19(−16)	4.56(−21)	5.49(−20)	1.13(−16)	4.49(−15)	9.13(−23)	4.69(−21)
16,000	2.31(−16)	6.76(−17)	3.70(−21)	2.90(−20)	1.38(−16)	2.81(−15)	4.54(−23)	2.33(−21)
20,000	2.41(−16)	5.08(−17)	3.45(−21)	2.17(−20)	1.40(−16)	2.19(−15)	3.26(−23)	1.67(−21)
25,000	2.59(−16)	3.79(−17)	3.26(−21)	1.64(−20)	1.35(−16)	1.68(−15)	2.33(−23)	1.19(−21)
32,000	2.81(−16)	2.72(−17)	3.11(−21)	1.23(−20)	1.22(−16)	1.23(−15)	1.61(−23)	8.25(−22)
50,000	2.96(−16)	1.46(−17)	2.89(−21)	7.62(−21)	8.95(−17)	6.87(−16)	8.28(−24)	4.23(−22)
64,000	2.84(−16)	1.03(−17)	2.73(−21)	6.01(−21)	7.15(−17)	4.90(−16)	5.72(−24)	2.92(−22)
100,000	2.31(−16)	5.40(−18)	2.29(−21)	3.98(−21)	4.43(−17)	2.62(−16)	2.93(−24)	1.50(−22)
200,000	1.28(−16)	1.95(−18)	1.40(−21)	2.00(−21)	1.86(−17)	9.64(−17)	1.04(−24)	5.30(−23)
500,000	4.31(−17)	5.01(−19)	5.14(−22)	6.67(−22)	5.22(−18)	2.50(−17)	2.63(−25)	1.34(−23)

^a $x(-y) = x \times 10^{-y}$.^b Spontaneous process ($T_b = 0$ K).^c Stimulated process ($T_b = 10,000$ K).**Table 4**Values of the Arrhenius-function parameters representing the rate coefficients for the spontaneous radiative association of $\text{He}(2^1\text{S})$ with hydrogen and lithium cations^a.

System	Process	T (K)	α ($\text{cm}^3 \text{s}^{-1}$)	β	γ (K)
HeH^+	$B \rightarrow X$	10–55	3.9397(−16)	−0.4918	−10.0215
		55–15,000	1.0974(−15)	−0.4163	40.7415
		15,000–50,000	2.3033(−16)	7.2942(−2)	4876.2037
	$B \rightarrow A$	50,000–500,000	1.4873(−12)	−1.3867	71,877.0270
		10–1000	1.6271(−15)	−0.5308	0.3098
		1000–15,000	8.7591(−15)	−1.1994	994.5077
	$B \rightarrow B$	15,000–500,000	3.3244(−14)	−1.4950	4083.6086
		10–250	1.7205(−19)	−0.8776	16.4225
		250–15,000	2.9494(−19)	−1.4641	209.3461
		15,000–500,000	3.0709(−19)	−1.4785	99.6248
HeLi^+	$B \rightarrow X$	10–1500	1.9083(−16)	−0.4762	−1.1647
		1500–15,000	3.8555(−18)	0.8789	−2701.5979
		15,000–50,000	2.7231(−13)	−1.4521	29,491.0745
	$B \rightarrow A$	10–250	2.7828(−14)	−0.2791	4.1283
		250–5000	1.6304(−12)	−1.4918	6987.5637
		5000–15,000	3.2678(−14)	−0.5021	68.7217
		15,000–50,000	5.3376(−13)	−1.2638	3474.7564
	$B \rightarrow B$	10–100	1.8874(−20)	−0.5296	8.0894
		100–15,000	1.7097(−20)	−1.4886	117.1636
		15,000–500,000	1.7836(−20)	−1.4995	171.7953

^a $x(-y) = x \times 10^{-y}$.

association via the $B \rightarrow A$ processes. In this case the rate coefficients for the formation of HeLi^+ in the $A^1\Sigma^+$ state are larger compared to HeH^+ formation, especially at higher temperatures the difference can be more than one order of magnitude. Whereas maximum values for radiative-association rate coefficients in single-state processes for

weakly bound diatomics like HeH^+ and HeLi^+ are extremely small, of the order of roughly $10^{-20} \text{cm}^3 \text{s}^{-1}$ and even smaller, two-state processes have larger rate coefficients by orders of magnitudes (depending on the size of the excitation energy ΔE). In the previous studies of the radiative associations ($\text{He}^+ + \text{H}$) and ($\text{He}^+ + \text{Li}$) (i.e., $A \rightarrow X$ two-state

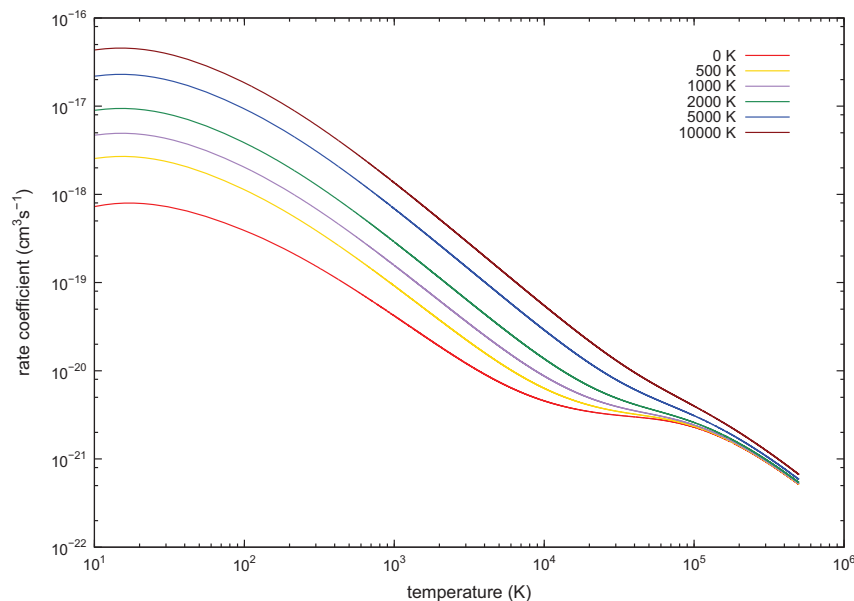


Fig. 9. Rate coefficients for the stimulated plus spontaneous radiative association of H^+ and He ($B \rightarrow B$ process) for different background temperatures.

processes according to the notation used here) maximum values for the rate coefficients at very low temperatures were obtained, which are of the same order of magnitude as the present $B \rightarrow X$ processes: about $5 \times 10^{-15} \text{ cm}^3 \text{ s}^{-1}$ [14,41,15].

Stimulated radiative association is relevant only for processes with very small ΔE where it can lead to a considerable increase of the rate coefficients. A study of the background blackbody radiation effect is therefore performed here only for the $B \rightarrow B$ processes. For HeH^+ the rate coefficients for the stimulated plus spontaneous radiative association via the $B \rightarrow B$ process at different background temperatures are plotted in Fig. 9 and numerical values for both ions are provided in Table 3. The calculated increase at $T_b = 10^4 \text{ K}$ in the rate coefficients is about one order of magnitude for HeH^+ and slightly larger for HeLi^+ , and can reach about two orders of magnitude at very low temperatures. But even with this increase the rate coefficients for the stimulated radiative association are much smaller than those for the two-state spontaneous processes.

4. Conclusion

Radiative association processes between the metastable $\text{He}(2^1S)$ and the H^+ and Li^+ ions producing HeH^+ and HeLi^+ molecular ions in the $X^1\Sigma^+$ ground states and the $A^1\Sigma^+$ and $B^1\Sigma^+$ lowest excited singlet states have been investigated in this study. The quantum-dynamics calculations have been performed based on highly accurate state-of-the-art quantum-chemistry *ab initio* calculations of the relevant interaction potentials and transition moments.

Cross sections for the three spontaneous processes $B \rightarrow X$, $B \rightarrow A$ and $B \rightarrow B$ have been calculated. The corresponding rate coefficients characterizing the efficiencies of the molecular-ion formation in the $X^1\Sigma^+$, $A^1\Sigma^+$ and

$B^1\Sigma^+$ electronic states have been obtained as functions of temperature. Due to the large differences in the ionization energies of He and H or He and Li, the two-state processes have been shown to be by far more efficient than the single-state ones.

Finally, a comparison of the results obtained here for the $B \rightarrow X$ process in HeH^+ with the radiative deactivation reaction (1) of Ref. [10] can be of interest. It was pointed out previously that both reactions start from the same initial conditions: the collision of $\text{He}(2^1S)$ with H^+ and the formation a temporary collision complex on the $B^1\Sigma^+$ potential of HeH^+ . Whereas from there in $B \rightarrow X$ radiative association via continuum-to-bound-state transitions takes place, the deactivation process described in the form of reaction (1) proceeds via radiative continuum-continuum transitions. Allison and Dalgarno [10] summarized their results by the statement that within a wide temperature range up to 16,000 K their calculated rate coefficients are rather constant with values between $(2 \text{ and } 4) \times 10^{-11} \text{ cm}^3 \text{ s}^{-1}$. Present results for the rate coefficients of the $B \rightarrow X$ process in HeH^+ show that the decrease in the temperature interval between 10 and 16,000 K is also fairly modest. The large difference in the absolute values of the rate coefficients must be attributed to the different efficiencies of the respective radiative transitions. However, a final definite conclusion of this aspect requires an accurate quantum-mechanical state-to-state treatment of reaction (1) using state-of-the-art *ab initio* data.

Apart from radiative association studied here, which is based on dipole-moment induced continuum-bound transitions, radiative and non-radiative charge transfer or deactivation processes taking place via continuum-continuum transitions are known to play a major role in astrophysical environments [42]. Comparison of radiative association with radiative charge transfer shows that the continuum-continuum processes are generally faster.

For instance, in the simple two-atomic $\text{Li}(2^1\text{S}) + \text{H}^+$ system it was found that the rate coefficient for the radiative charge transfer process is about two orders of magnitude larger compared to the corresponding radiative association over a wide temperature range up to 5000 K [43,44]. A similar finding applies for example to the three-atomic system $\text{He}^+ + \text{H}_2$, where the difference is smaller, but it is still about one order of magnitude in the low-temperature regime up to 100 K [45,46]. Finally, comparing efficiencies of radiative and non-radiative processes in this context, it was shown that radiative charge transfer dominates over the non-radiative one at low collision energies and vice-versa at high energies, where the non-radiative reaction is dominating. This has important consequences for modeling stellar atmospheres [39,40].

Our approach to radiative association, in which we strictly consider only continuum-bound transitions, differs from the approach of Bennett et al. [47], who also included transitions to the low-lying quasibound states, which have sufficiently long tunneling lifetimes for radiative decay to bound states.

Acknowledgments

L.A. acknowledges funding from the Grant Agency of the Charles University in Prague – GAUK (Grant no. 550112).

References

- [1] Struve O, Wurm K, Henyey L. Astrophysical consequences of metastable levels in hydrogen and helium. *Proc Natl Acad Sci USA* 1939;25:67–73. <http://dx.doi.org/10.1073/pnas.25.2.67>.
- [2] Bowen IS. The origin of nebular lines and the structure of planetary nebulae. *Astrophys J* 1928;67:1–15. <http://dx.doi.org/10.1086/143091>.
- [3] Goepfert-Mayer M. Über Elementarakte mit zwei Quantenspringen. *Ann Phys* 1931;9:273–81. <http://dx.doi.org/10.1002/andp.19314010303>.
- [4] Dalgarno A. Two-photon decay of singlet metastable helium. *Mon Not R Astron Soc* 1966;131:311–5.
- [5] Victor GA. Two-quantum processes in the coupled Hartree–Fock approximation. *Proc Phys Soc (London)* 1967;91:825–30. <http://dx.doi.org/10.1088/0370-1328/91/4/308>.
- [6] Jacobs V. Two-photon decay rate of the 2^1S_0 metastable state of helium. *Phys Rev A* 1971;4:939–45. <http://dx.doi.org/10.1103/PhysRevA.4.939>.
- [7] Dyck RSV, Johnson CE, Shugart HA. Radiative lifetime of the 2^1S_0 metastable state of helium. *Phys Rev A* 1971;4:1327–37. <http://dx.doi.org/10.1103/PhysRevA.4.1327>.
- [8] Baklanov EV, Denisov AV. Methods of high-resolution laser spectroscopy of helium. *Laser Phys* 1999;9:259–65.
- [9] Breit G, Teller E. Metastability of hydrogen and helium levels. *Astrophys J* 1940;91:215–20. <http://dx.doi.org/10.1086/144158>.
- [10] Allison DCS, Dalgarno A. Deactivation of metastable helium by proton impact. *Proc Phys Soc* 1963;81:23–8. <http://dx.doi.org/10.1088/0370-1328/81/1/306>.
- [11] Stancil PC, Dalgarno A. Stimulated radiative association of Li and H in the Early Universe. *Astrophys J* 1997;479:543–9. <http://dx.doi.org/10.1086/303920>.
- [12] Zygelman B, Stancil PC, Dalgarno A. Stimulated radiative association of He and H^+ . *Astrophys J* 1998;508:151–7. <http://dx.doi.org/10.1086/306399>.
- [13] Augustovičová L, Kraemer WP, Soldán P. Depopulation of metastable helium by radiative association with hydrogen or lithium ions. *Astrophys J* 2014;46:782–9. <http://dx.doi.org/10.1088/0004-637X/782/1/46>.
- [14] Zygelman B, Dalgarno A. The radiative association of He^+ and H. *Astrophys J* 1990;365:239–41. <http://dx.doi.org/10.1086/169475>.
- [15] Augustovičová L, Špirko V, Kraemer WP, Soldán P. Radiative association of LiHe^+ . *Chem Phys Lett* 2012;531:59–64. <http://dx.doi.org/10.1016/j.cpllett.2012.02.038>.
- [16] Watson JKG. The isotope dependence of diatomic dunham coefficients. *J Mol Spectrosc* 1980;80:411–21. [http://dx.doi.org/10.1016/0022-2852\(80\)90152-6](http://dx.doi.org/10.1016/0022-2852(80)90152-6).
- [17] Račchenko Y, Kramida AE, Reader J, Team, NA. Nist Atomic Spectra Database (version 3.1.5); 2010. See (<http://physics.nist.gov/asd3>).
- [18] Hansson A, Watson JKG. A comment on Hönl–London factors. *J Mol Spectrosc* 2005;233:169–74. <http://dx.doi.org/10.1016/j.jms.2005.06.009>.
- [19] Numerov BV. Méthode nouvelle de la détermination des orbites et le calcul des éphémérides en tenant compte des perturbations. *Trudy Glavn Rossijskoi astrofiz obs* 1923;2:188–202.
- [20] Cooley JW. An improved eigenvalue corrector formula for solving the Schrödinger equation for central fields. *Math Comput* 1961;15:363–74. <http://dx.doi.org/10.1090/S0025-5718-1961-0129566-X>.
- [21] Le Roy RJ. Level 7.7: a computer program for solving the radial Schrödinger equation CRR-661; 2005.
- [22] Le Roy RJ, Liu W. Energies and widths of quasibound levels (orbiting resonances) for spherical potentials. *J Chem Phys* 1978;69:3622–32. <http://dx.doi.org/10.1063/1.437070>.
- [23] Connor JNL, Smith AD. Uniform semiclassical calculation of resonance energies and widths near a barrier maximum. *Mol Phys* 1981;43:397–415. <http://dx.doi.org/10.1080/00268978100101411>.
- [24] Huang Y, Le Roy RJ. Potential energy, λ doubling and Born–Oppenheimer breakdown functions for the $b^1\pi_u$ barrier state of Li_2 . *J Chem Phys* 2003;119:7398–7417. doi: 10.1063/1.1607313; Erratum. *J Chem Phys* 2007;126:169904. doi: 10.1063/1.2723739.
- [25] Ho TS, Rabitz H. A general method for constructing multidimensional molecular potential energy surfaces from ab initio calculations. *J Chem Phys* 1996;104(7):2584–681. <http://dx.doi.org/10.1063/1.470984>.
- [26] Ho TS, Rabitz H. Proper construction of ab initio global potential surfaces with accurate long-range interactions. *J Chem Phys* 2000;113(10):3960–8. <http://dx.doi.org/10.1063/1.1288268>.
- [27] Soldán P, Hutson JM. On the long-range and short-range behavior of potentials from reproducing kernel Hilbert space interpolation. *J Chem Phys* 2000;112(9):4415–21. <http://dx.doi.org/10.1063/1.480988>.
- [28] Pachucki K, Sapirstein J. Relativistic and QED corrections to the polarizability of helium. *Phys Rev A* 2000;63:012504–9. <http://dx.doi.org/10.1103/PhysRevA.63.012504>.
- [29] Sewell GL. Stark effect for a hydrogen atom in its ground state. *Proc Camb Philos Soc* 1949;45:678–86. <http://dx.doi.org/10.1017/S0305004100025378>.
- [30] Yan Z, Babb JF. Long-range interactions of metastable helium atoms. *Phys Rev A* 1998;58:1247–51. <http://dx.doi.org/10.1103/PhysRevA.58.1247>.
- [31] Wansbeek LW, Sahoo BK, Timmermans RGE, Das BP, Mukherjee D. Ab initio determination of polarizabilities and van der Waals coefficients of Li atoms using the relativistic coupled-cluster method. *Phys Rev A* 2008;78:012515–21. <http://dx.doi.org/10.1103/PhysRevA.78.012515>.
- [32] Werner HJ, Knowles PJ, et al. MOLPRO, version 2010.2: a package of ab initio programs; 2010. See (<http://www.molpro.net>).
- [33] Soldán P, Kraemer WP. Molecular ion LiHe^+ : ab initio study. *Chem Phys* 2012;393:135–44. <http://dx.doi.org/10.1016/j.chemphys.2011.11.040>.
- [34] Kolos W, Peek JM. New ab initio potential curve and quasibound states of HeH^+ . *Chem Phys* 1976;12:381–6. [http://dx.doi.org/10.1016/0301-0104\(76\)87076-0](http://dx.doi.org/10.1016/0301-0104(76)87076-0).
- [35] Bishop DM, Cheung LM. A theoretical investigation of HeH^+ . *J Mol Spectrom* 1979;75:462–73. [http://dx.doi.org/10.1016/0022-2852\(79\)90090-0](http://dx.doi.org/10.1016/0022-2852(79)90090-0).
- [36] Kolos W. Long- and intermediate-range interaction in three lowest sigma states of the HeH^+ ion. *Int J Quantum Chem* 1976;10:217–24. <http://dx.doi.org/10.1002/qua.560100203>.
- [37] Michels FH. Molecular orbital studies of the ground and low-lying excited states of the HeH^+ molecular ion. *J Chem Phys* 1966;44:3834–61. <http://dx.doi.org/10.1063/1.1726541>.
- [38] Yousif FB, Mitchell JBA, Rogelstad M, Paddelec AL, Canosa A, Chibisov MI. Dissociative recombination of heh^+ : a reexamination. *Phys Rev A* 1994;49:4610–5. <http://dx.doi.org/10.1103/PhysRevA.49.4610>.
- [39] Zygelman B, Dalgarno A, Kimura M, Lane NF. Radiative and non-radiative charge transfer in $\text{He}^+ + \text{H}$ collisions at low energy. *Phys Rev A* 1989;40:2340–6. <http://dx.doi.org/10.1103/PhysRevA.40.2340>.
- [40] Belyaev AK, Augustovičová L, Soldán P, Kraemer WP. Non-radiative inelastic processes in lithium–helium ion–atom collisions. *Astron Astrophys* 2014;565:A106–11. <http://dx.doi.org/10.1051/0004-6361/201423578>.

- [41] Kraemer WP, Špirko V, Juřek M. Formation of HeH^+ by radiative association of $\text{He}^+ + \text{H}$. An advanced ab initio study. *Chem Phys Lett* 1995;236:177–84. [http://dx.doi.org/10.1016/0009-2614\(95\)00187-9](http://dx.doi.org/10.1016/0009-2614(95)00187-9).
- [42] Stancil PC. Charge transfer calculations for astrophysical modeling. *ASP Conf Ser* 2001;247:3–14.
- [43] Dalgarno A, Kirby K, Stancil P. The radiative association of Li^+ and H , Li and H^+ , and Li and H . *Astrophys J* 1996;458:397–401. <http://dx.doi.org/10.1086/176823>.
- [44] Stancil PC, Zygelman B. Radiative charge transfer in collisions of Li with H^+ . *Astrophys J* 1996;472:102–8. <http://dx.doi.org/10.1086/178044>.
- [45] Mrugała F, Špirko V, Kraemer W. Radiative association of HeH_2^+ . *J Chem Phys* 2003;118:10547–59. <http://dx.doi.org/10.1063/1.1573184>.
- [46] Mrugała F, Kraemer W. Radiative charge transfer in $\text{He}^+ + \text{H}^2$ collisions in the milli- to nano-electron-volt range: a theoretical study within state-to-state and optical potential approaches. *J Chem Phys* 2013;138:104315–43. <http://dx.doi.org/10.1063/1.4793986>.
- [47] Bennett OJ, Dickinson AS, Leininger T, Gadéa FX. Radiative association in $\text{Li}+\text{H}$ revisited: the role of quasi-bound states. *Mon Not R Astron Soc* 2003;341:361–8. <http://dx.doi.org/10.1046/j.1365-8711.2003.06422.x>.

THE ROLE OF MOLECULAR QUADRUPOLE
TRANSITIONS IN THE DEPOPULATION OF
METASTABLE HELIUM

Bibliographic record of the attached publication:

Augustovičová, L., W. P. Kraemer, V. Špirko, and P. Soldán (2015).

“The role of molecular quadrupole transitions in the depopulation of metastable helium.” In: *Monthly Notices of the Royal Astronomical Society* 446, pp. 2738–2743.

DOI: [10.1093/mnras/stu2317](https://doi.org/10.1093/mnras/stu2317).

The role of molecular quadrupole transitions in the depopulation of metastable helium

L. Augustovičová,¹ W. P. Kraemer,² V. Špirko³ and P. Soldán^{1*}

¹Department of Chemical Physics and Optics, Faculty of Mathematics and Physics, Charles University in Prague, Ke Karlovu 3, CZ-12116 Prague 2, Czech Republic

²Max-Planck-Institute of Astrophysics, Postfach 1371, D-85741 Garching, Germany

³Institute of Organic Chemistry and Biochemistry, Academy of Sciences of the Czech Republic, Flemingovo nám. 2, CZ-16010 Prague 6, Czech Republic

Accepted 2014 October 27. Received 2014 October 27; in original form 2014 July 30

ABSTRACT

Depopulation of metastable He(2^3S) and He(2^1S) by radiative association with helium ions resulting in the formation of the He $_2^+$ molecular ions is investigated. Rate coefficients for spontaneous radiative association of the He $_2^+$ molecular ion on the spin-doublet manifold are presented as functions of temperature from 10 up to 500 000 K considering the association to rotational-vibrational bound states of the lowest doublet electronic states $X^2\Sigma_u^+$ and $A^2\Sigma_g^+$ from the continuum states of the excited doublet electronic states $B^2\Sigma_u^+$ and $D^2\Sigma_u^+$. The dipole-driven processes $B \rightarrow A$ and $D \rightarrow A$ are compared to the quadrupole-driven processes $B \rightarrow X$ and $D \rightarrow X$. For all considered temperatures, the dipole-driven process $D \rightarrow A$ dominates over the other processes. The rate coefficient for the quadrupole-driven process $B \rightarrow X$ is at least three orders of magnitude larger than the rate coefficient of the dipole-driven process $B \rightarrow A$.

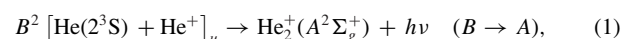
Key words: atomic processes – molecular data – molecular processes.

1 INTRODUCTION

It has been suggested already some time ago that the molecular ions H $_2^+$ and He $_2^+$ should be significantly abundant in the atmospheres of cool white dwarfs (Gaur et al. 1988). Extensive efforts were undertaken since then to determine the influence of photoionization and collisional absorption charge exchange reactions on the opacity of DB white dwarf atmospheres (Stancil 1994a, 1994b; Ignjatovic et al. 2009). In these calculations and especially in studies of radiative molecular formation processes in the primordial gas and in other astrophysical environments, it is generally assumed that these processes are mediated by dipole transitions. For instance, the dipole-driven photodissociation reaction in He $_2^+$ proceeding from bound states of the ground electronic state $X^2\Sigma_u^+$ to the continuum states of the first excited state $A^2\Sigma_g^+$ was studied (Stancil 1994b; Ignjatovic et al. 2009); the dipole-driven radiative-association reactions resulting in formation of H $_2^+$ or He $_2^+$ were investigated between the g and u manifolds for both the doublet and quartet states (Stancil, Babb & Dalgarno 1993; Augustovičová et al. 2013a, 2013b); very recently, the Carrington rovibronic microwave spectra of H $_2^+$, D $_2^+$, and He $_2^+$ (Carrington, Shaw & Taylor 1995a; Carrington, Pyne & Knowles 1995b; Carrington 1996) were proposed as a potentially sensitive probe for detection of a variable proton-to-electron mass ratio (Augustovičová et al. 2014).

However, unlike in heteronuclear molecules, in homonuclear molecules such as H $_2^+$ and He $_2^+$ the extra symmetry classification of gerade (g ; even parity) and ungerade (u ; odd parity) introduces new selection rules for radiative transitions. The $g \leftrightarrow g$ or $u \leftrightarrow u$ dipole-induced transitions are forbidden because all dipole moment components exhibit the u symmetry. On the other hand, some of the quadrupole moment components transform according to the g symmetry. The corresponding quadrupole-induced transitions are therefore allowed.

In our previous study (Augustovičová et al. 2013b), we investigated the depopulation of the metastable helium states $^4\text{He}(2^3S)$ and $^4\text{He}(2^1S)$ by collisions with $^4\text{He}^+$ ions taking place in the continuum of the $C^2\Sigma_g^+$ or the $E^2\Sigma_g^+$ electronic states of He $_2^+$, respectively, leading via dipole-driven radiative association to the formation of He $_2^+$ in the $X^2\Sigma_u^+$ electronic ground state. The present study considers the depopulation of these two metastable helium states occurring in the continuum of the $B^2\Sigma_u^+$ and $D^2\Sigma_u^+$ electronic states, which are the ungerade counterparts of the above-mentioned C and E states. In this case, radiative association to the lowest doublet states can proceed either via dipole-induced transitions to the bound levels of the first excited electronic state $A^2\Sigma_g^+$, or via quadrupole-induced transitions to the bound levels of the $X^2\Sigma_u^+$ ground electronic state. The processes induced by dipole continuum-bound transitions considered here are



*E-mail: pavel.soldan@mff.cuni.cz

$$D^2 [\text{He}(2^1\text{S}) + \text{He}^+]_u \rightarrow \text{He}_2^+(A^2\Sigma_g^+) + h\nu \quad (D \rightarrow A). \quad (2)$$

These are compared to the following processes induced by quadrupole continuum-bound transitions:

$$B^2 [\text{He}(2^3\text{S}) + \text{He}^+]_u \rightarrow \text{He}_2^+(X^2\Sigma_u^+) + h\nu \quad (B \rightarrow X), \quad (3)$$

$$D^2 [\text{He}(2^1\text{S}) + \text{He}^+]_u \rightarrow \text{He}_2^+(X^2\Sigma_u^+) + h\nu \quad (D \rightarrow X). \quad (4)$$

The $2^2[\dots]_u$ symbol designates a doublet u submanifold of the corresponding collisional continuum. According to this scheme, reactions (1)–(4) start by collisions of He in one of the two lowest metastable atomic levels (2^3S , 2^1S) with He^+ ions, and then proceed via resonance and continuum states of the $B^2\Sigma_u^+$ and $D^2\Sigma_u^+$ potentials of the collisional complex to form (under spontaneous photon emission) the molecular ion in the lowest doublet states $X^2\Sigma_u^+$ or $A^2\Sigma_g^+$. These processes are labelled as $B \rightarrow A$, $D \rightarrow A$, $B \rightarrow X$, or $D \rightarrow X$ in the above scheme.

Normally one would expect that the cross-sections for quadrupole-induced transitions should be at least four orders of magnitude smaller compared to those for dipole-induced transitions (c^5 compared to c^3 in the denominator of the respective cross-section formulae). However, there are several factors contributing to the corresponding cross-sections that could change this situation. The major factors include: first, the number of target states, i.e. the number of accessible rovibrational bound states supported by the target electronic states; secondly, the size of the corresponding transition moments; thirdly, the Franck–Condon overlap conditions between the initial and target electronic states.

The understanding of the development of population densities in vibrationally excited homonuclear diatomic molecular systems H_2/H_2^+ , C_2/C_2^+ , O_2/O_2^+ is also the key problem in studies of planetary evolutions (Glinski, Schulz & Nuth 1997). Quadrupole-allowed bound-bound vibrational transitions in homonuclear diatomics were studied intensively in the past (Dalgarno 1995; Leach & Moss 1995; Glinski et al. 1997). To our knowledge, this study presents for the first time a direct comparison between molecular formations of homonuclear diatomic ions driven by electric quadrupole transitions with those driven by electric dipole transitions. The efficiencies of the quadrupole-driven reactions (3) and (4) and the dipole-driven reactions (1) and (2) are studied here based on highly accurate state-of-the-art potential energies and transition moment calculations.

2 METHODS

In quantum mechanics, the total cross-sections for spontaneous radiative association of a diatomic molecule can be expressed as a sum over allowed transitions from a continuum state with a positive energy E and orbital angular momentum N' to bound rovibrational states characterized by vibrational quantum number v'' and orbital angular momentum N'' (Zygelman & Dalgarno 1990)

$$\sigma(E) = \sum_{N', v'', N''} \sigma_{N', v'', N''}(E). \quad (5)$$

In the case of the dipole-induced transitions, the individual cross-sections can be expressed as

$$\sigma_{N', v'', N''}^{\text{dip}}(E) = \frac{1}{4\pi\epsilon_0} \frac{64}{3} \frac{\pi^5}{c^3 k^2} p v_{E; v'', N''}^3 S_{N', N''} M_{E, N'; v'', N''}^2, \quad (6)$$

while for the quadrupole-induced transitions they are given by formula

$$\sigma_{N', v'', N''}^{\text{quad}}(E) = \frac{1}{4\pi\epsilon_0} \frac{32}{5} \frac{\pi^7}{c^5 k^2} p v_{E; v'', N''}^5 S_{N', N''} M_{E, N'; v'', N''}^2, \quad (7)$$

where c is the speed of light in vacuum, $k^2 = 2\mu E/\hbar^2$, μ is the ‘reduced mass’ of the molecular ion ($\mu = 3647.89986 m_e$ for ${}^4\text{He}_2^+$), p is the probability of approach in the initial electronic state ($p = 1/6$ for $B \rightarrow A$ and $B \rightarrow X$ and $p = 1/2$ for $D \rightarrow A$ and $D \rightarrow X$) and $v_{E; v'', N''}$ is the emitted photon frequency, $h\nu_{E; v'', N''} = E + E - E_{v'', N''}$, where $\Delta E = 19.8196$ eV for $B \rightarrow A$ and $B \rightarrow X$, $\Delta E = 20.6158$ eV for $D \rightarrow A$ and $D \rightarrow X$ (Kramida et al. 2014),

$$M_{E, N'; v'', N''} = \int_0^\infty \chi_{N'}(E, R) T^l(R) \psi_{v'', N''}(R) dR \quad (8)$$

is the matrix element of the transition dipole moment function $T^1 = d_z$ or quadrupole moment function $T^2 = Q_{zz}$ between the initial continuum radial wavefunction $\chi_{N'}(E, R)$ and the final bound-state radial wavefunction $\psi_{v'', N''}(R)$.

In the case of a homonuclear diatomic molecule with zero nuclear spin (such as ${}^4\text{He}_2^+$ considered here), symmetry requires that only even N and only odd N rotational levels are populated in the Σ_g and Σ_u electronic states, respectively. Within the Hund case (a) spin-less approximation, the dipole-induced transitions between Σ_g and Σ_u states of a homonuclear diatomic molecule are governed by the rotational selection rules $\Delta N = N' - N'' = \mp 1$. The only non-zero Hönl–London coefficients are $S_{N', N'+1} = N' + 1$ and $S_{N', N'-1} = N'$ and thus only P and R branches are present. Dipole transitions between Σ_u states of a homonuclear diatomic molecule are symmetry forbidden, but the quadrupole-induced transitions are allowed. In the case of ${}^4\text{He}_2^+$ the corresponding selection rules have the form $\Delta N = N' - N'' = 0, \mp 2$. The non-zero Hönl–London coefficients are

$$S_{N', N'+2} = \frac{3}{2} \frac{(N'+1)(N'+2)}{2N'+3}, \quad S_{N', N'-2} = \frac{3}{2} \frac{N'(N'-1)}{2N'-1},$$

$$S_{N', N'} = \frac{(2N'+1)N'(N'+1)}{(2N'-1)(2N'+3)},$$

and there are O , S , and Q branches present, respectively.¹

The wave functions $\chi_{N'}(E, R)$ and $\psi_{v'', N''}(R)$ were calculated by numerical integration of the corresponding radial Schrödinger equations using the Numerov–Cooley method (Numerov 1923; Cooley 1961). Resonance positions and tunnelling widths were calculated employing the computer program LEVEL 7.7 (Le Roy 2005) and making use of the Airy-function boundary condition at the outermost classical turning point (Le Roy & Liu 1978) and the uniform semiclassical method (Connor & Smith 1981; Huang & Le Roy 2003).

Potential energy and transition moment functions were represented numerically by one-dimensional reciprocal-power reproducing kernel Hilbert space (RP-RKHS) interpolation method (Ho & Rabitz 1996). In the case of potential energy curves the interpolation was done with respect to r^2 (Soldán & Hutson 2000) using RP-RKHS parameters $m = 1$ and $n = 2$ and the leading long-range term $\alpha_d/2R^4$ with fixed values of the static dipole polarizabilities in atomic units: $\alpha_d[\text{He}(1^1\text{S})] = 1.383191$ (Pachucki & Sapirstein 2000), $\alpha_d[\text{He}(2^3\text{S})] = 315.631468$, and $\alpha_d[\text{He}(2^1\text{S})] = 800.31633$

¹ Notice that here the P and R branches are missing solely because of the zero nuclear spin of ${}^4\text{He}$; they would be present if isotopologues with ${}^3\text{He}$ were also considered.

(Yan & Babb 1998). Previously calculated accurate interaction energies of the ground $X^2\Sigma_u^+$ state (Tung, Pavanello & Adamowicz 2012) and of the lowest excited $A^2\Sigma_g^+$ state (Augustovičová et al. 2013b) were exploited as known data points for the interpolation. Ab initio interaction energies for the excited states $B^2\Sigma_u^+$ and $D^2\Sigma_g^+$ and the corresponding transition dipole and quadrupole moments were calculated by us following the same multireference approach as in Augustovičová et al. (2013a). All ab initio calculations were performed employing the quantum chemistry program suit MOLPRO (Werner et al. 2010).

The rate coefficients for formation of a molecule by spontaneous radiative association at temperature T is then derived from the total cross-sections (5) as

$$k(T) = \left(\frac{8}{\mu\pi}\right)^{1/2} \left(\frac{1}{k_B T}\right)^{3/2} \int_0^\infty E \sigma(E) e^{-E/k_B T} dE. \quad (9)$$

Evaluation of this integral was done following the method which was successfully used for recent calculations of radiative-association rate coefficients of the molecular ion LiHe^+ (Augustovičová et al. 2012).

3 RESULTS AND DISCUSSION

Potential energy curves used in this study for the ground electronic state and its gerade counterpart together with the two lowest excited $^2\Sigma_u^+$ states of He_2^+ are shown in Fig. 1 and the corresponding transition dipole moments for $B \rightarrow A$ and $D \rightarrow A$ and the transition quadrupole moments for $B \rightarrow X$ and $D \rightarrow X$ are displayed in the upper and lower panels of Fig. 2, respectively.

The two lowest excited states of Σ_u^+ symmetry represent relatively weakly bound direct associates of metastable $\text{He}(2^3\text{S})$ or

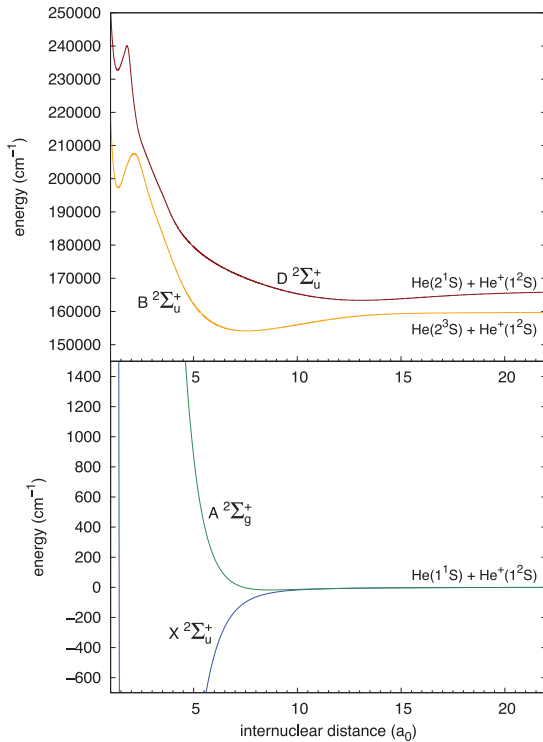


Figure 1. Potential energy curves of the relevant He_2^+ doublet electronic states.

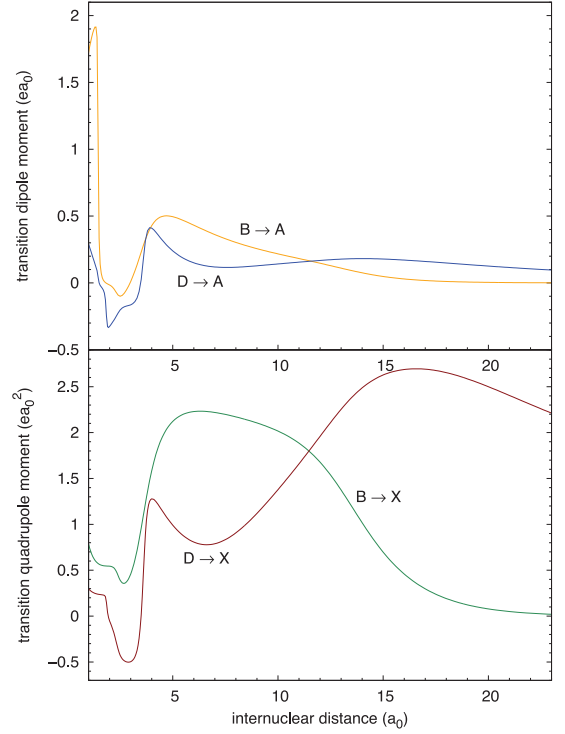


Figure 2. Transition dipole-moment and quadrupole moment functions between the relevant He_2^+ doublet electronic states.

Table 1. Molecular characteristics of the potential energy curves used in the cross-section calculations of the He_2^+ radiative association.

State	R_e (a_0)	\mathcal{D}_e (cm^{-1})	\mathcal{D}_0 (cm^{-1})	n_v	n_{rv}
$X^2\Sigma_u^+$	2.042 ^a	19 954.583 ^a	19 099.776 ^{a, b}	24	409
$A^2\Sigma_g^+$	8.718 ^c	17.516 ^c	8.185 ^c	3	6
$B^2\Sigma_u^+$	7.559	5699.412	5568.248 ^b	49	1395
$D^2\Sigma_u^+$	13.100	2912.274	2841.091 ^b	51	1694

R_e is the position of the global minimum (equilibrium distance), \mathcal{D}_e is the dissociation energy from the potential global minimum, \mathcal{D}_0 is the dissociation energy from the lowest rovibrational state, n_v is the number of pure bound vibrational states of the electronic state, and n_{rv} is the number of bound rovibrational states of the electronic state.

^aThe Born–Oppenheimer potential energy curve from Tung et al. (2012) was used for the $X^2\Sigma_u^+$ state.

^bIn the electronic state of u symmetry the rovibrational ground state refers to the $v = 0, J = 1$ state.

^cPotential energy curve from Augustovičová et al. (2013b) was used for the $A^2\Sigma_g^+$ state.

$\text{He}(2^1\text{S})$ with He^+ . Their wide potential wells can support much larger numbers of bound rovibrational levels compared to the more deep but narrow potential well of the electronic ground state (see Table 1). The essentially repulsive $A^2\Sigma_g^+$ state can support only a maximum of six rovibrational levels which could affect the efficiency of radiative processes with the A state as the target state. In Table 1, basic data characterizing the electronic state potentials are summarized. Some of these data can be compared to the results obtained previously by Metropoulos & Nicolaides (1991): whereas their equilibrium distances for the X and B states and their well depth

for the X state seem to be in good agreement with the present data, the well depths for the B and D states and the equilibrium distance for the D state cannot be compared because the corresponding interaction energies at longer distances ($>10 a_0$) were not presented. Numbers of orbital resonances in the initial association potentials are provided in Table 2.

Cross-sections for spontaneous radiative association for the four processes investigated here are displayed in Fig. 3. Considering the difference in the power of c in the denominator of equations (6) and (7), it is surprising to notice in Fig. 3 that the cross-sections of the quadrupole-induced transitions are fairly comparable to those of the dipole-induced transitions. A couple of reasons can be named which may explain this result. First, it is the large difference in the numbers of rovibrational levels in the target X and A states (409 rovibrational states in X compared to 6 rovibrational states in A). Moreover, examining the Hönl–London coefficients in ${}^4\text{He}_2^+$, the dipole-induced transitions offer only two branches (P and R) in comparison to the three branches (O , Q , and S) offered by the quadrupole-induced transitions. These facts imply that the quadrupole-driven radiative association processes $B \rightarrow X$ and $D \rightarrow X$ have many more (approximately factor of 100) contributions to the summation in equation

Table 2. Resonance situation overview of the four radiative association processes studied.

Process	n_{tot}	n_r	n_w	n_n	ΔE (eV)
$B \rightarrow A$	254	0	0	0	19.8196
$D \rightarrow A$	322	0	0	0	20.6158
$B \rightarrow X$	254	44	25	19	19.8196
$D \rightarrow X$	322	41	25	16	20.6158

Using formalism of Augustovičová et al. (2012): n_{tot} is the total number of orbital resonances supported by the initial electronic states, n_r is the number of symmetry-allowed resonances, i.e. the number of resonances which have a bound partner in the corresponding target electronic state allowed by the dipole-moment or quadrupole-moment selection rules, n_w is the number of wide resonances, and n_n is the number of narrow resonances, ΔE is the energy difference between the corresponding dissociation limits.

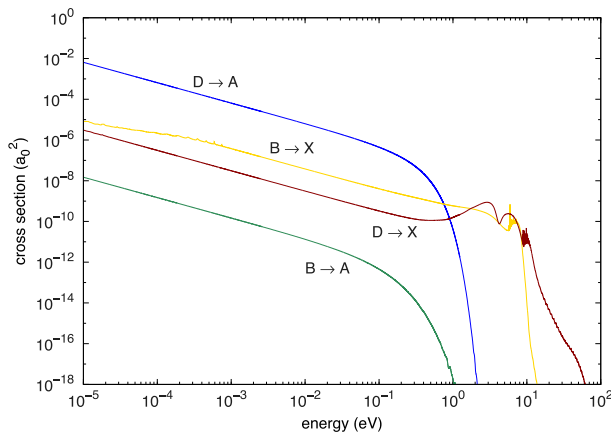


Figure 3. Cross-sections for spontaneous radiative association of He_2^+ . Only the contribution of resonances wider than 0.01 cm^{-1} is shown.

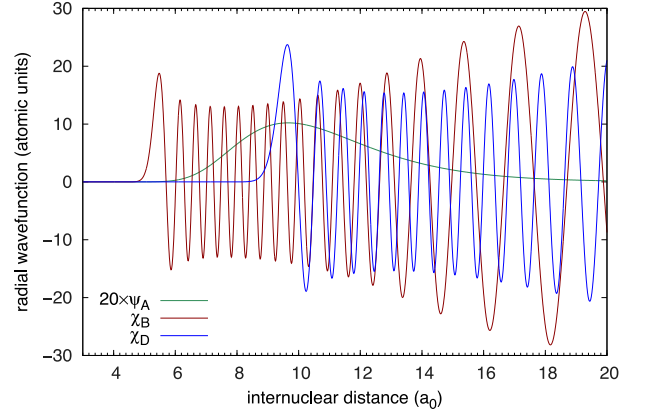


Figure 4. Schematic figure of wavefunctions for the ($v'' = 0$, $J'' = 0$) final bound state of the A electronic state and ($E = 1 \text{ cm}^{-1}$, $J' = 1$) initial continuum state of the B and D electronic states. For better visibility, the L^2 -normalized bound-state wavefunction ψ_A is multiplied by a factor of 20.

(5) compared to the dipole-driven processes $B \rightarrow A$ and $D \rightarrow A$.² Secondly, Fig. 2 shows that the absolute values of the quadrupole transition moments are larger compared to the corresponding dipole transition moments over the entire distance range.

At collisional energies up to 1 eV the cross-sections for the dipole-driven $B \rightarrow A$ and $D \rightarrow A$ processes differ by six orders of magnitude from each other. The large difference in the efficiency of the two association reactions should be due to the different Franck–Condon conditions as indicated in Fig. 4, which result in the integrand in equation (8) being much larger for the $D \rightarrow A$ process than for the $B \rightarrow A$ process.

Interesting feature in the cross-section graphs is the onset of the usual sharp drop-off in the cross-sections for radiative association: in the case of the dipole-driven processes $B \rightarrow A$ and $D \rightarrow A$ it occurs around 1 eV, while for the quadrupole-driven processes $B \rightarrow X$ and $D \rightarrow X$ it happens around 10 eV, which is very similar to the dipole-driven processes having the same target electronic state, $C \rightarrow X$ and $E \rightarrow X$, studied earlier by Augustovičová et al. (2013b).

Rate coefficients for spontaneous radiative association of the He_2^+ states considered here are calculated from the cross-sections according to equation (9) and their temperature dependence is shown in Fig. 5 for the temperature range between 10 and 5×10^5 K. Numerical values are tabulated at selected temperatures in Table 3. Reflecting the behaviour of the corresponding cross-sections the rate coefficients have their maximum values at very low temperatures. The dipole-driven $D \rightarrow A$ process is by far the dominating one at the low temperatures, whereas the corresponding $B \rightarrow A$ is almost negligible for the reasons given above. The rate-coefficient curves of the quadrupole-driven $B \rightarrow X$ and $D \rightarrow X$ processes are rather close to each other, and due to a slight increase at temperatures beyond 10^4 K, which mimics the corresponding cross-section behaviour, they almost reach the $D \rightarrow A$ rate-coefficient curve at temperatures exceeding 10^5 K.

For modelling purposes of chemical network systems it is convenient to parametrize the temperature dependence of reaction rates of the association processes of the present study in terms of the Arrhenius-type formula $k(T) = \alpha(T/300)^\beta e^{-\gamma/T}$, where the

² Consequently, quadrupole-induced transitions conserving $g \leftrightarrow g$ symmetry can be expected to have much smaller cross-sections because the number of rovibrational levels in the $A^2\Sigma_g^+$ target state is very small.

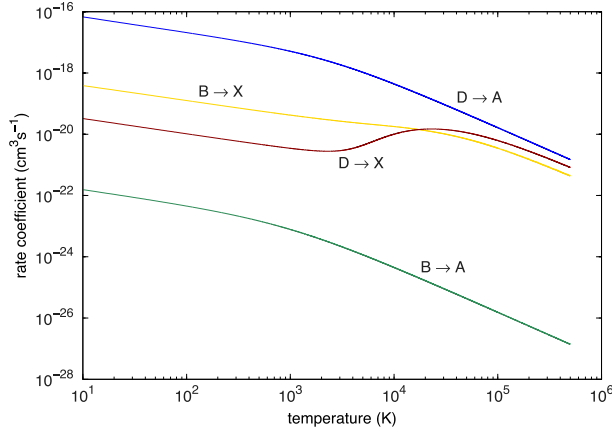


Figure 5. Rate coefficients for spontaneous radiative association of He_2^+ .

temperature of 300 K is used as a reference temperature, and α , β , and γ are the fitting parameters. In order to keep the maximum relative error below 10 per cent, the whole temperature range is usually divided into several temperature intervals. The parameter values of the fitted Arrhenius-type function are given in Table 4.

4 CONCLUSION

Depopulation processes of metastable $\text{He}(^3\text{S})$ and $\text{He}(^1\text{S})$ in collisions with He^+ leading via quadrupole-induced radiative transitions to the $X^2\Sigma_u^+$ ground electronic state of He_2^+ or via dipole-induced radiative transitions to the $A^2\Sigma_g^+$ first excited electronic state were investigated in this study. The quantum-mechanical calculations were performed based on highly accurate state-of-the-art quantum-

Table 4. Values of the Arrhenius-function parameters representing the rate coefficients for the spontaneous radiative association of He_2^+ .

Process	T (K)	α (cm^3s^{-1})	β	γ (K)
$B \rightarrow A$	10–400	$2.2370\text{e}-23$	-0.6747	4.4907
	400–5000	$5.3916\text{e}-23$	-1.3388	310.8314
	5000–500 000	$9.3598\text{e}-23$	-1.4985	900.8113
$D \rightarrow A$	10–400	$1.1440\text{e}-17$	-0.5549	1.4501
	400–5000	$2.9663\text{e}-17$	-1.1545	348.2106
	5000–500 000	$9.8798\text{e}-17$	-1.4957	1726.3553
$B \rightarrow X$	10–1000	$7.3806\text{e}-20$	-0.4743	-0.7267
	1000–20 000	$6.3192\text{e}-20$	-0.3651	1.8363
	20 000–500 000	$1.1961\text{e}-17$	-1.3647	22 638.5880
$D \rightarrow X$	10–1000	$6.0492\text{e}-21$	-0.4726	-1.1200
	1000–4000	$2.0436\text{e}-22$	0.9001	-1816.3976
	4000–20 000	$1.5508\text{e}-22$	1.1986	103.0550
	20 000–500 000	$3.0480\text{e}-17$	-1.4030	35 747.7314

chemical ab initio calculations of the relevant interaction potentials and transition moments.

Cross-sections for the spontaneous processes (1–4), i.e. the dipole-driven reactions $B \rightarrow A$ and $D \rightarrow A$ as well as the quadrupole-driven reactions $B \rightarrow X$ and $D \rightarrow X$, were calculated. The corresponding rate coefficients characterizing the efficiencies of the A - and X -state formations via these two different reaction path-ways were obtained as functions of temperature.

While for the two dipole-driven processes $B \rightarrow A$ and $D \rightarrow A$ the reaction conditions seem to be rather comparable, their cross-sections and consequently their rate-coefficient values obtained in the calculations differ nevertheless by several orders of magnitude. It is shown here that this large difference can be rationalized to be mostly due to different Franck–Condon overlaps of the respective wavefunctions.

Table 3. Values of the total rate coefficients (in cm^3s^{-1}) for the four spontaneous processes of the He_2^+ radiative association.

T (K)	$D \rightarrow A$	$B \rightarrow A$	$B \rightarrow X$	$D \rightarrow X$
10	6.79×10^{-17}	1.55×10^{-22}	3.87×10^{-19}	3.25×10^{-20}
20	4.74×10^{-17}	1.09×10^{-22}	2.77×10^{-19}	2.30×10^{-20}
30	3.85×10^{-17}	8.81×10^{-23}	2.27×10^{-19}	1.88×10^{-20}
50	2.97×10^{-17}	6.70×10^{-23}	1.77×10^{-19}	1.46×10^{-20}
100	2.08×10^{-17}	4.52×10^{-23}	1.26×10^{-19}	1.03×10^{-20}
200	1.43×10^{-17}	2.92×10^{-23}	8.96×10^{-20}	7.36×10^{-21}
500	8.32×10^{-18}	1.47×10^{-23}	5.78×10^{-20}	4.73×10^{-21}
1000	5.11×10^{-18}	7.79×10^{-24}	4.21×10^{-20}	3.48×10^{-21}
2000	2.82×10^{-18}	3.66×10^{-24}	3.14×10^{-20}	2.81×10^{-21}
2500	2.26×10^{-18}	2.81×10^{-24}	2.87×10^{-20}	2.80×10^{-21}
3000	1.87×10^{-18}	2.24×10^{-24}	2.68×10^{-20}	2.91×10^{-21}
4000	1.36×10^{-18}	1.55×10^{-24}	2.41×10^{-20}	3.47×10^{-21}
6000	8.42×10^{-19}	9.06×10^{-25}	2.11×10^{-20}	5.50×10^{-21}
8000	5.86×10^{-19}	6.10×10^{-25}	1.93×10^{-20}	7.91×10^{-21}
10 000	4.38×10^{-19}	4.46×10^{-25}	1.79×10^{-20}	1.01×10^{-20}
16 000	2.31×10^{-19}	2.28×10^{-25}	1.48×10^{-20}	1.39×10^{-20}
20 000	1.69×10^{-19}	1.65×10^{-25}	1.32×10^{-20}	1.47×10^{-20}
25 000	1.23×10^{-19}	1.19×10^{-25}	1.16×10^{-20}	1.48×10^{-20}
32 000	8.67×10^{-20}	8.32×10^{-26}	9.91×10^{-21}	1.41×10^{-20}
50 000	4.54×10^{-20}	4.31×10^{-26}	6.99×10^{-21}	1.13×10^{-20}
64 000	3.16×10^{-20}	2.99×10^{-26}	5.57×10^{-21}	9.42×10^{-21}
100 000	1.64×10^{-20}	1.54×10^{-26}	3.49×10^{-21}	6.22×10^{-21}
200 000	5.84×10^{-21}	5.46×10^{-27}	1.51×10^{-21}	2.80×10^{-21}
500 000	1.49×10^{-21}	1.39×10^{-27}	4.33×10^{-22}	8.22×10^{-22}

However, the most interesting result of this study is the finding that the efficiencies of the quadrupole-driven processes are surprisingly high. Whereas the rate coefficient of the dipole reaction $D \rightarrow A$ at lower temperatures exceeds the values of the quadrupole-driven processes $B \rightarrow X$ and $D \rightarrow X$ by about two orders of magnitude, the rate coefficient curves of these three processes get fairly close to each other at temperatures above 10^5 K. This could have implications for radiative processes in high-temperature helium-rich astrophysical environments.

A comparison could be of interest here between the present rate-coefficient results and those obtained previously by Augustovičová et al. (2013b) for the depopulation of the metastable helium states $\text{He}(2^3\text{S})$ and $\text{He}(2^1\text{S})$ taking place in collisions with the He^+ ions in the continuum of the $C^2\Sigma_g^+$ or $E^2\Sigma_g^+$ states of He_2^+ , respectively. The rates of these dipole-driven depopulations are about four orders of magnitude larger compared to the present quadrupole-induced transition reactions $B \rightarrow X$ and $D \rightarrow X$ over the entire temperature range shown in Fig. 5. The shapes of the temperature curves of the corresponding pairs of rate-coefficient functions are rather similar, especially for the $\text{He}(2^1\text{S})$ depopulations $E \rightarrow X$ in Augustovičová et al. (2013b) and $D \rightarrow X$ in the present study. In this case, after the usual initial decrease with increasing temperature at lower temperatures both rate-coefficient curves have maxima at high temperatures in the region close to 50 000 K. Another depopulation reaction of the metastable $\text{He}(2^3\text{S})$ in collisions with He^+ ions was recently studied by Augustovičová et al. (2013a). It takes place in the continuum of the $c^4\Sigma_g^+$ state of He_2^+ and leads via radiative dipole transition to the $b^4\Sigma_u^+$ state. The rate coefficient for this process is comparable to the present dipole-driven reaction $D \rightarrow A$.

The two metastable helium states $\text{He}(2^3\text{S})$ and $\text{He}(2^1\text{S})$ with their long lifetimes (van Dyck, Johnson & Shugart 1971; Hodgman et al. 2009) are also known since long as origins of nebular lines in planetary nebulae (Bowen 1928), and consequences of their formation in various astrophysical environments are widely discussed (Struve, Wurm & Henyey 1939; Osterbrock 1974; Roberge & Dalgarno 1982). Preferred formation of the two metastables is assumed to occur via recombination of He^+ ions with electrons both in primordial helium plasmas (Kholupenko, Ivanchik & Varshalovich 2007, 2008; Chluba & Sunyaev 2008) or in planetary nebulae (Mathis 1957; Piacentini 1977). Whereas in the early cosmological epoch at high redshifts (≈ 1000 – 3000) the recombination of primordial plasmas affects significantly the growth of gravitational instability and the formation of cosmic microwave background spectral distortions and anisotropy (Dubrovich 1975), in diffuse clouds or in quasi-stellar objects the absorption in the metastable $\text{He}(2^3\text{S})$ through its $\lambda 10\,830$ or $\lambda 3889$ absorption lines is used as a probe for determination of the cosmic ray ionization rate (Indriolo et al. 2009) or for measurements of the He^+ column density (Leighly et al. 2012). Collisional ionization of the metastable $\text{He}(2^3\text{S})$ is also important for high-temperature planetary nebulae providing significant cooling in these objects (Clegg 1987). The present investigations of collisional depopulations of the two metastable helium states through radiative association with the helium ions are assumed to complement the possible reaction network of the corresponding excited helium atoms.

ACKNOWLEDGEMENTS

LA acknowledges funding from the Grant Agency of the Charles University in Prague - GAUK (Grant no. 550112). LA and VŠ also appreciate support of the Czech Science Foundation - GAČR (Grant no. P208/11/0436).

REFERENCES

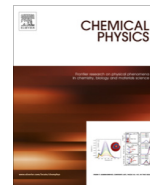
- Augustovičová L., Špirko V., Kraemer W. P., Soldán P., 2012, *Chem. Phys. Lett.*, 531, 59
- Augustovičová L., Špirko V., Kraemer W. P., Soldán P., 2013a, *MNRAS*, 435, 1541
- Augustovičová L., Špirko V., Kraemer W. P., Soldán P., 2013b, *A&A*, 553, A42
- Augustovičová L., Soldán P., Kraemer W. P., Špirko V., 2014, *MNRAS*, 439, 1136
- Bowen I. S., 1928, *ApJ*, 67, 1
- Carrington A., 1996, *Science*, 274, 1327
- Carrington A., Shaw A. M., Taylor S. M., 1995a, *J. Chem. Soc. Faraday Trans.*, 91, 3725
- Carrington A., Pyne C. H., Knowles P. J., 1995b, *J. Chem. Phys.*, 102, 5979
- Chluba J., Sunyaev R. A., 2008, *A&A*, 478, L27
- Clegg R. E. S., 1987, *MNRAS*, 229, 31
- Connor J. N. L., Smith A. D., 1981, *Mol. Phys.*, 43, 397
- Cooley J. W., 1961, *Math. Comput.*, 15, 363
- Dalgarno A., 1995, in Ferrara A., McKee C. F., Heiles C., Shapiro P. R., eds, *ASP Conf. Ser. Vol. 80, The Physics of the Interstellar Medium and Intergalactic Medium*. Astron. Soc. Pac., San Francisco, p. 37
- Dubrovich V. K., 1975, *Sov. Astron. Lett.*, 1, 1
- Gaur V. P., Tripathi B. M., Joshi G. C., Pande M. C., 1988, *Ap&SS*, 147, 107
- Gliniski R. J., Schulz S. A., Nuth J. A., III, 1997, *MNRAS*, 288, 286
- Ho T. S., Rabitz H., 1996, *J. Chem. Phys.*, 104, 2584
- Hodgman S. S., Dall R. G., Byron L. J., Baldwin K. G. H., Buckman S. J., Truscott I. A. G., 2009, *Phys. Rev. Lett.*, 103, 053002
- Huang Y., Le Roy R. J., 2003, *J. Chem. Phys.*, 119, 7398
- Ignjatovic L. M., Mihajlov A. A., Sakan N. M., Dimitrijevic M. S., Metropoulos A., 2009, *MNRAS*, 396, 2201
- Indriolo N., Hobbs L., Hinkle K., McCall B., 2009, *ApJ*, 703, 2131
- Kholupenko E., Ivanchik A., Varshalovich D., 2007, *MNRAS*, 378, L39
- Kholupenko E., Ivanchik A., Varshalovich D., 2008, *Astron. Lett.*, 34, 725
- Kramida A., Ralchenko Y., Reader J., NIST ASD Team, 2014, *NIST Atomic Spectra Database (version 5.2)*. National Institute of Standards and Technology, Gaithersburg, MD. Available at: <http://physics.nist.gov/asd>
- Le Roy R. J., 2005, *LEVEL 7.7: A Computer Program for Solving the Radial Schrödinger Equation CPRR-661*
- Le Roy R. J., Liu W., 1978, *J. Chem. Phys.*, 69, 3622
- Leach C. A., Moss R. E., 1995, *Ann. Rev. Phys. Chem.*, 55, 46
- Leighly K., Lucy A., Dietrich M., Terndrup D., Gallagher S., 2012, in Chartas G., Hamann F., Leighly K. M., eds, *ASP Conf. Ser. Vol. 460, AGN Winds in Charleston*. Astron. Soc. Pac., San Francisco, p. 72
- Mathis J. S., 1957, *ApJ*, 126, 493
- Metropoulos A., Nicolaidis C. A., 1991, *Chem. Phys. Lett.*, 187, 487
- Numerov B. V., 1923, *Tr. Gl. Ross. Astrofiz. Obs.*, 2, 188
- Osterbrock D., 1974, *Astrophysics of Gaseous Nebulae*. Freeman & Co., San Francisco
- Pachucki K., Sapirstein J., 2000, *Phys. Rev. A*, 63, 012504
- Piacentini R. D., 1977, *J. Phys. B*, 10, L159
- Roberge W., Dalgarno A., 1982, *ApJ*, 255, 489
- Soldán P., Hutson J. M., 2000, *J. Chem. Phys.*, 112, 4415
- Stancil P. C., 1994a, *J. Quant. Spectrosc. Radiat. Transfer*, 51, 655
- Stancil P. C., 1994b, *ApJ*, 430, 360
- Stancil P. C., Babb J. F., Dalgarno A., 1993, *ApJ*, 414, 672
- Struve O., Wurm K., Henyey L. G., 1939, *Ap. J.*, 25, 67
- Tung W., Pavanello M., Adamowicz L., 2012, *J. Chem. Phys.*, 136, 104309
- van Dyck R. S., Johnson C. E., Shugart H. A., 1971, *Phys. Rev. A*, 4, 1327
- Werner H.-J., Knowles P. J. et al., 2010, *MOLPRO*, Version 2010.2: A Package of Ab Initio Quantum-Chemistry Programs. Available at: <http://www.molpro.net/>
- Yan Z., Babb J. F., 1998, *Phys. Rev. A*, 58, 1247
- Zygelman B., Dalgarno A., 1990, *ApJ*, 365, 239

This paper has been typeset from a $\text{\TeX}/\text{\LaTeX}$ file prepared by the author.

RADIATIVE ASSOCIATION OF HE(2^3P) WITH
LITHIUM CATIONS

Bibliographic record of the attached publication:

Augustovičová, L., M. Zámečnicková, W. P. Kraemer, and P. Soldán
(2015). "Radiative association of He(2^3P) with lithium cations."
In: *Chemical Physics* 462. Inelastic Processes in Atomic, Molecular
and Chemical Physics, pp. 65–70.
DOI: [10.1016/j.chemphys.2015.07.003](https://doi.org/10.1016/j.chemphys.2015.07.003).

Radiative association of He(2^3P) with lithium cationsLucie Augustovičová^a, Martina Zámečníková^a, Wolfgang P. Kraemer^b, Pavel Soldán^{a,*}^a Charles University in Prague, Faculty of Mathematics and Physics, Department of Chemical Physics and Optics, Ke Karlovu 3, CZ-12116 Prague 2, Czech Republic^b Max-Planck-Institute of Astrophysics, Postfach 1371, D-85741 Garching, Germany

ARTICLE INFO

Article history:
Available online 7 July 2015

Keywords:
Radiative association
Metastable helium
Rates of formation
Molecular ions

ABSTRACT

Formation of HeLi⁺ molecular ion by radiative association of metastable helium atoms with lithium ions is investigated on the triplet-Sigma manifold. Energy dependent cross-sections are calculated for He(2^3P) colliding with Li⁺ in the continuum of the $c^3\Sigma^+$ electronic state and undergoing radiative transition into one of the rotational-vibrational states of the lower electronic states $a^3\Sigma^+$, $b^3\Sigma^+$, or $c^3\Sigma^+$ of HeLi⁺. Evaluation of the cross-sections is based on the fully quantal approach taking into account all possible state-to-state transitions at thermal energies (spontaneous association) or at higher background temperatures (stimulated association). The corresponding rate coefficients are presented as functions of temperature. Calculations show that the rate coefficients for two-state processes $c \rightarrow a$ and $c \rightarrow b$ are several orders of magnitude larger than the rate coefficient for the c -state formation. The rate coefficient for the $c \rightarrow a$ radiative association reaches $10^{-15} \text{ cm}^3 \text{ s}^{-1}$ at low temperatures. As expected stimulation of the radiative association by black-body background radiation has a noticeable effect only on the one-state $c \rightarrow c$ process.

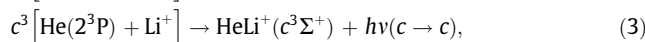
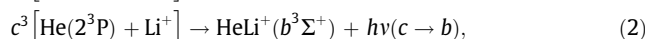
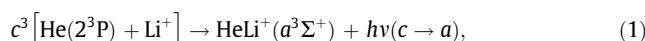
© 2015 Published by Elsevier B.V.

1. Introduction

Helium with its metastable excited states provides interesting aspects and useful information in different fields of atomic physics and also for diagnostics in astrophysical environments. Due to its extremely long lifetime [1], metastable He(2^3S) can effectively be viewed as “ground state” species for many atomic optics phenomena and Bose–Einstein condensation experiments [2–4]. It also acts as a base for excitations to the 2^3P state, which can be achieved using 1083 nm laser radiation corresponding to the energy difference of 1.1445 eV between the two lowest triplet-state levels [5]. Rather good agreement was obtained between different lifetime measurements [6–9] and an early theoretical lifetime prediction of $\tau \sim 98 \text{ ns}$ for metastable He(2^3P) from transition probability calculations [10]. This quite short lifetime originates from the spin-allowed $2^3P_1 \rightarrow 2^3S_1$ transition. However, single-photon transitions from the 2^3P manifold directly to the true ground state He(1^1S_0) can only occur for the 2^3P_1 and 2^3P_2 states with a small decay probability either via spin-forbidden electric dipole transitions ($2^3P_1 \rightarrow 1^1S_0$ with $\tau \sim 5.7 \text{ ms}$ [1]) or via spin-forbidden magnetic

quadrupole transitions ($2^3P_2 \rightarrow 1^1S_0$ with $\tau \sim 3.1 \text{ s}$ [11]), whereas for the 2^3P_0 state the direct decay is strictly forbidden to all orders in multipole expansion.

Recently, we have explored intensively the depopulation of metastable helium He(2^3S) and He(2^1S) in collisions with hydrogen, helium, and lithium ions by radiative association [12–16] and also by non-radiative inelastic processes [17,18]. The depopulation of metastable He(2^3P) by collisions with hydrogen or helium ions was also considered in previous studies: via radiative association these collisions can lead to the formation of HeH⁺ [19] or He₂⁺ [13], respectively. In this paper, we investigate three radiative-association processes originating in the triplet-Sigma continuum of the collisional system He(2^3P) + Li⁺. The considered processes induced by dipole-moment continuum-bound transitions are described as:



where $c^3[\dots]$ means the corresponding collisional continuum of the $c^3\Sigma^+$ electronic states of HeLi⁺.

In this scheme, reaction (3) is just a direct one-state radiative association while the other two reactions describe two-state

* Corresponding author.

E-mail addresses: lucie.augustovicova@mff.cuni.cz (L. Augustovičová), martina.zamecnikova@mff.cuni.cz (M. Zámečníková), wpk@mpa-garching.mpg.de (W.P. Kraemer), pavel.soldan@mff.cuni.cz (P. Soldán).

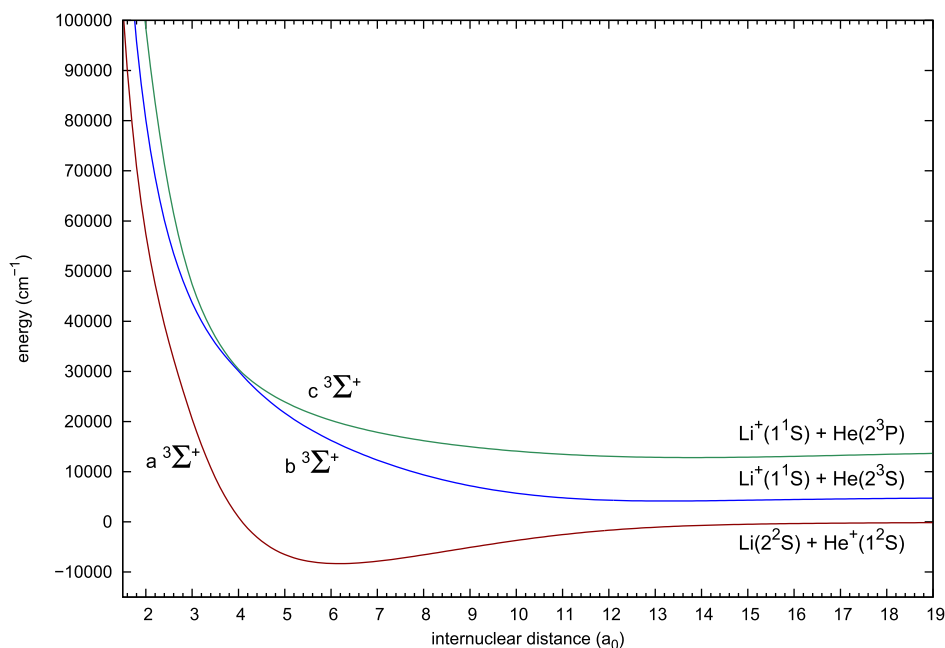


Fig. 1. Potential energy curves of the $a^3\Sigma^+$, $b^3\Sigma^+$, and $c^3\Sigma^+$ states of HeLi^+ .

processes. According to general experience these are expected to have larger efficiencies compared to (3) due to the larger energy gain by the spontaneous photon emissions in the transitions $c \rightarrow a$ and $c \rightarrow b$. Reaction (1) connects the initial $\text{Li}^+(1^1\text{S}) + \text{He}(2^3\text{P})$ reaction channel with the lowest molecular triplet state $a^3\Sigma^+$ of HeLi^+ , which dissociates to $\text{Li}(1^2\text{S}) + \text{He}^+(1^2\text{S})$. It can thus be viewed as the continuum-bound analogue of a charge transfer process. In reaction (2), the same initial $\text{Li}^+(1^1\text{S}) + \text{He}(2^3\text{P})$ reaction channel is connected to the intermediate molecular triplet state $b^3\Sigma^+$ which dissociates to $\text{Li}^+(1^1\text{S}) + \text{He}(2^3\text{S})$. Reaction (2)

would effectively correspond to the de-excitation of helium $\text{He}(2^3\text{P})$ to $\text{He}(2^3\text{S})$.

2. Methods

In our approach the full quantum dynamics calculations were performed using potential energy curves of the $a^3\Sigma^+$, $b^3\Sigma^+$, and $c^3\Sigma^+$ electronic states of HeLi^+ , the dipole moment of the c state, and the transition dipole moments between the c and a or b states. The corresponding ab initio interaction energies and moment-

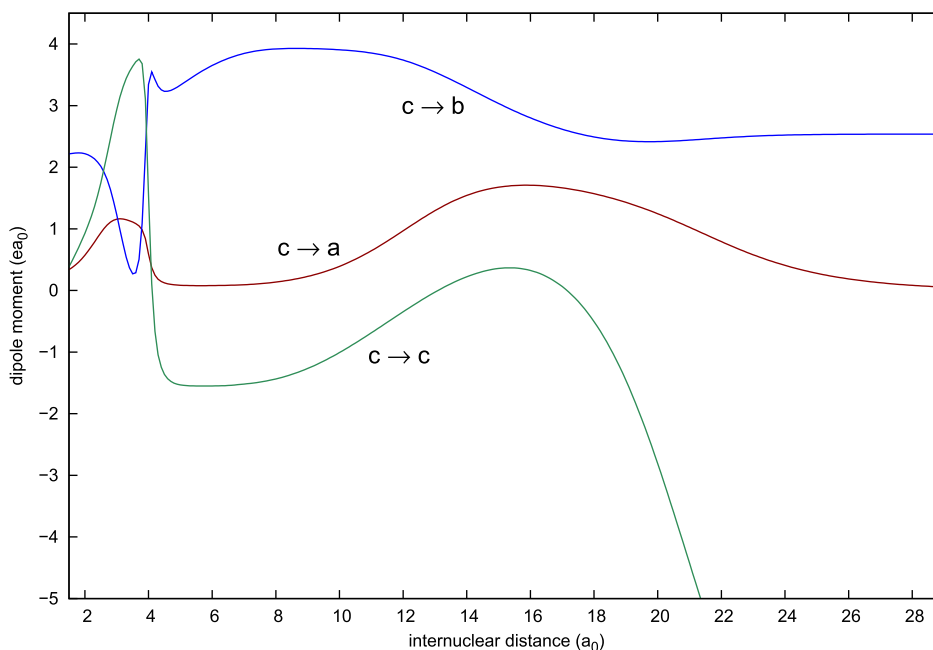


Fig. 2. Transition dipole moments for the $c \rightarrow a$ and $c \rightarrow b$ processes and the dipole moment of the $c^3\Sigma^+$ state of HeLi^+ .

Table 1

Process characteristics for radiative association of He(2^3P) with lithium cations (D_0 and ΔE are in cm^{-1}).^a

Process	n_{tot}	n_r	n_w	n_n	D_0	n_v	n_{rv}	ΔE
$c \rightarrow a$	458	416	193	223	8183.0	61	4172	14,263
$c \rightarrow b$	458	133	76	57	829.5	33	1289	9231
$c \rightarrow c$	458	301	140	161	1399.5	54	2727	0

^a The MRCI potential energy curves of [20] are used for all the electronic states. According to the definitions of [26]: n_{tot} is the total number of orbital resonances supported by the initial electronic state, from which n_r is the number of symmetry-allowed resonances, i.e. the number of resonances which have a bound partner in the corresponding target electronic state allowed by the dipole-moment selection rules, n_w is the number of wide resonances, and n_n is the number of narrow resonances; D_0 is the dissociation energy of the target electronic state from the ground ($v''=0, J''=0$) ro-vibrational state, n_v is the number of bound vibrational ($J''=0$) states of the target electronic state, n_{rv} is the total number of bound ro-vibrational states of the target electronic state, and ΔE is the energy difference between the dissociation levels of the potentials.

function values were taken from Soldán and Kraemer [20]. For numerical representation of the potential energy curves and moment functions we used one-dimensional reproducing kernel Hilbert space (RKHS) interpolation method [21–23]. In the case of the potential energy curves of the a and b states we employed the same reciprocal-power reproducing kernel Hilbert space (RP-RKHS) representation as in [14]. The RP-RKHS interpolation was also used for the c -state potential energy curve; because of the charge-quadrupole interaction between the Li^+ and $\text{He}(2^3P)$ the leading long-range term is $-C_3/R^3$, and thus the interpolation was done with respect to R using RP-RKHS parameters $m=2$ and $n=2$.

Our radiative-association treatment is based on calculation of cross-sections at various collision energies and rate coefficients over various temperatures. The corresponding theory for formation of diatomic bound species via radiative association was reviewed by Dalgarno and coworkers [24,25], and this approach was implemented in our computer-program suite [26].

The radiative-association cross-section $\sigma(E; T_b)$ at collision energy E in the field of black-body radiation (characterized by

temperature T_b) is a sum of individual cross-sections, which correspond to allowed transitions from a continuum state (characterized by E and orbital angular momentum J') to bound ro-vibrational states (labeled by quantum numbers v'' and J''). In the case of dipole-moment transitions, the individual cross-sections can be expressed as

$$\sigma_{J',v'';J''}^{J',v'';J''}(E; T_b) = \frac{1}{4\pi\epsilon_0} \frac{64}{3} \frac{\pi^5}{c^3 k^2} p v_{E,v'';J''}^3 S_{J',J''}^2 M_{E,J',v'';J''}^2 \times \left[\frac{1}{1 - \exp(-h\nu_{E,v'';J''}/k_B T_b)} \right], \quad (4)$$

where c is the speed of light in vacuum, $k^2 = 2\mu E/\hbar^2$, μ is the “charge-modified reduced mass” [27] of the molecular ion ($\mu = 4646.087837$ a.u. for $^4\text{He}^7\text{Li}^+$), p is the probability of approach in the initial electronic state ($p=1/3$ for all three processes) and $\nu_{E,v'';J''}$ is the emitted photon frequency, $h\nu_{E,v'';J''} = E + \Delta E - E_{v'';J''}$, where $\Delta E_{c-c} = 0$ eV, $\Delta E_{c-b} = 1.1444818$ eV, and $\Delta E_{c-a} = 1.7684229$ eV [28]. Within the Hund’s case (a) spin-less approximation [29] the dipole-moment transitions of a heteronuclear diatomic molecule are governed by the rotational selection rule $\Delta J = J' - J'' = \mp 1$. There are just two branches, and the only non-zero Hönl-London coefficients are $S_{J',J'+1} = J' + 1$ and $S_{J',J'-1} = J'$, respectively. $M_{E,J',v'';J''}$ is the matrix element of the transition dipole moment function $d_z(R)$ between the energy-normalized continuum radial wave function $\chi_{J'}(E, R)$ for the partial wave J' and the normalized bound-state radial wave function $\psi_{v'';J''}(R)$. The radial wave functions $\chi_{J'}(E, R)$ and $\psi_{v'';J''}(R)$ are determined by numerical integration [30,31] of the corresponding Schrödinger equations

$$\left[-\frac{\hbar^2}{2\mu} \frac{d^2}{dR^2} + \frac{\hbar^2 J'(J'+1)}{2\mu R^2} + U_c(R) \right] \chi_{J'}(E, R) = E \chi_{J'}(E, R), \quad (5)$$

$$\left[-\frac{\hbar^2}{2\mu} \frac{d^2}{dR^2} + \frac{\hbar^2 J''(J''+1)}{2\mu R^2} + U_b(R) \right] \psi_{v'';J''}(R) = E_{v'';J''} \psi_{v'';J''}(R), \quad (6)$$

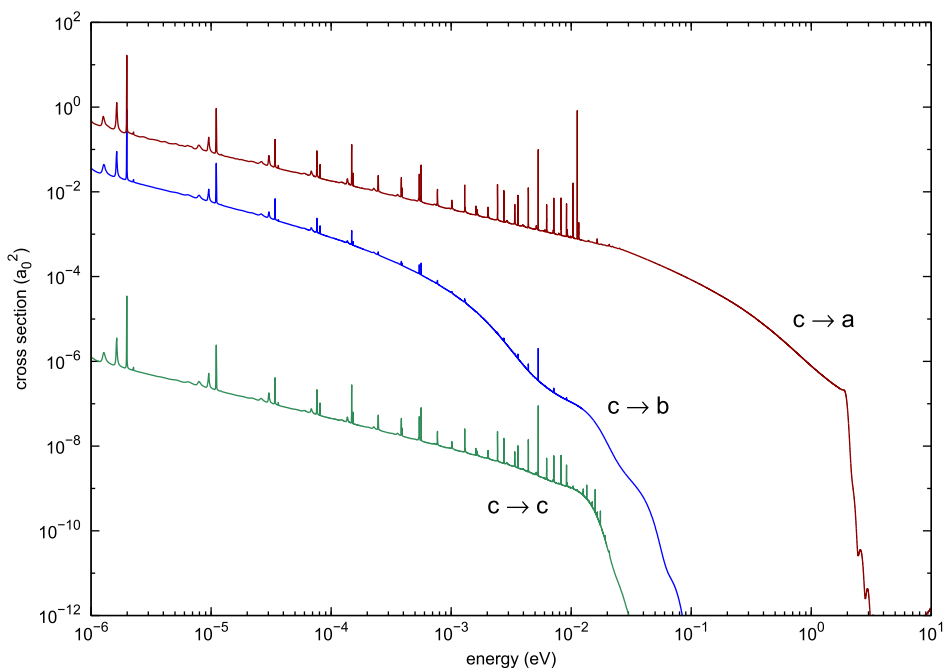


Fig. 3. Cross sections for radiative association of Li^+He . Of the resonances, only those with a tunneling width larger than 0.1 cm^{-1} are shown.

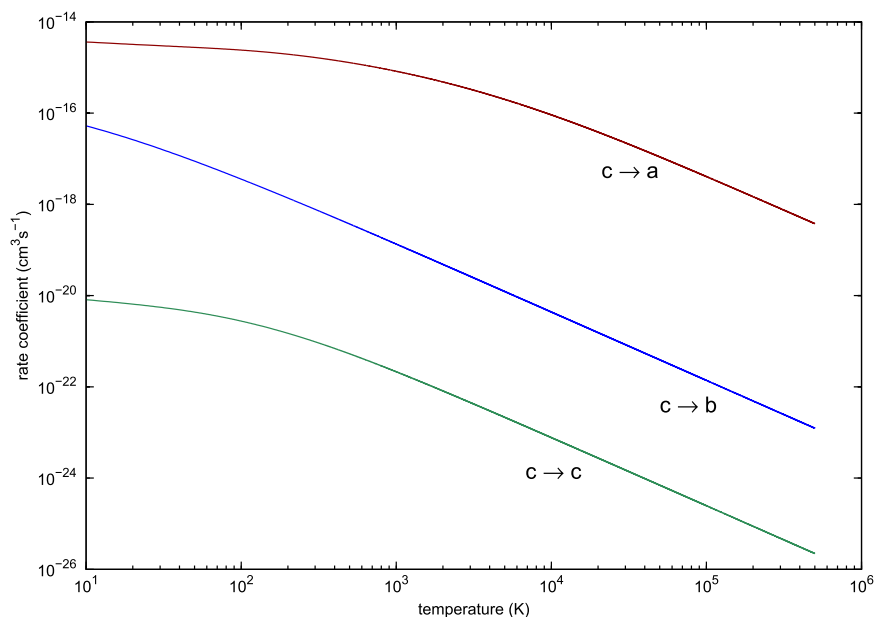


Fig. 4. Rate coefficients for radiative association of HeLi⁺.

which include potential energy functions $U_c(R)$ and $U_b(R)$ supporting the initial continuum state E, J' and the final bound state v'', J'' , respectively. Positions and tunneling widths of resonances were calculated employing the computer program LEVEL 7.7 [32] and making use of the Airy-function boundary condition at the outermost classical turning point [33] and the uniform semiclassical method [34,35].

The rate coefficients for formation of a molecule by (spontaneous, $T_b = 0$ K, or stimulated, $T_b > 0$ K) radiative association at a given temperature T are obtained by averaging the corresponding cross-sections $\sigma(E; T_b)$ over a Maxwellian velocity distribution of the collisional continuum

$$\alpha(T; T_b) = \left(\frac{8}{\mu\pi}\right)^{1/2} \left(\frac{1}{k_B T}\right)^{3/2} \int_0^\infty E \sigma(E; T_b) e^{-E/k_B T} dE, \quad (7)$$

where T_b is the background temperature. For the numerical evaluation of integral (7) the approach outlined in Ref. [26] is followed. In order to represent analytically the rate coefficients it is often convenient to use the Kooij function

$$f(T) = \alpha \left(\frac{T}{300}\right)^\beta e^{-\gamma/T} \quad (8)$$

where α , β , and γ are fitting parameters. For fitting purposes the corresponding temperature range was divided into several intervals in order to keep the maximum relative error below 10%.

Table 2

Values of the total rate coefficients ($\text{cm}^3 \text{s}^{-1}$) for the three radiative-association processes of the HeLi⁺ molecular ion.^a

T (K)	$c \rightarrow a$	$c \rightarrow b$	$c \rightarrow c$
10	3.63(−15)	5.27(−17)	8.13(−21)
20	3.22(−15)	2.62(−17)	6.52(−21)
30	3.01(−15)	1.66(−17)	5.57(−21)
50	2.77(−15)	8.86(−18)	4.36(−21)
100	2.41(−15)	3.58(−18)	2.77(−21)
200	1.96(−15)	1.38(−18)	1.49(−21)
500	1.28(−15)	3.72(−19)	5.30(−22)
1000	8.29(−16)	1.35(−19)	2.14(−22)
2000	4.83(−16)	4.83(−20)	8.14(−23)
2500	3.97(−16)	3.47(−20)	5.91(−23)
3000	3.35(−16)	2.64(−20)	4.54(−23)
4000	2.53(−16)	1.72(−20)	2.99(−23)
6000	1.65(−16)	9.39(−21)	1.65(−23)
8000	1.19(−16)	6.10(−21)	1.08(−23)
10,000	9.17(−17)	4.37(−21)	7.73(−24)
16,000	5.13(−17)	2.16(−21)	3.84(−24)
20,000	3.85(−17)	1.55(−21)	2.75(−24)
25,000	2.86(−17)	1.11(−21)	1.97(−24)
32,000	2.05(−17)	7.65(−22)	1.36(−24)
50,000	1.10(−17)	3.92(−22)	7.00(−25)
64,000	7.75(−18)	2.71(−22)	4.84(−25)
100,000	4.07(−18)	1.39(−22)	2.48(−25)
200,000	1.47(−18)	4.90(−23)	8.77(−26)
500,000	3.78(−19)	1.24(−23)	2.22(−26)

^a $x(-y) \equiv x \times 10^{-y}$.

3. Results and discussion

Potential energy curves for the three lowest $3^3\Sigma^+$ states of HeLi⁺ used in our study are shown in Fig. 1. The corresponding transition dipole-moment functions for the $c \rightarrow a$ and $c \rightarrow b$ processes together with the c -state dipole-moment function are displayed in Fig. 2.

The potential well of the lowest state $a^3\Sigma^+$ is quite deep ($D_e = 8328 \text{ cm}^{-1}$), which reflects the interaction between two open-shell atoms He⁺(1^2S) and Li(1^2S). As a result, it supports more

Table 3

Values of the Kooij-function parameters representing the rate coefficients for the spontaneous radiative association of He(2^3P) with lithium cations.^a

Process	T (K)	α ($\text{cm}^3 \text{s}^{-1}$)	β	γ (K)
$c \rightarrow a$	10–300	1.7461(−15)	−0.3183	4.4846
	300–4000	3.4109(−15)	−0.9751	233.3678
	4000–500,000	2.1088(−14)	−1.4676	2749.5471
$c \rightarrow b$	10–100	8.3954(−19)	−1.3752	5.5286
	100–500,000	8.4152(−19)	−1.4996	22.5182
$c \rightarrow c$	10–150	1.2535(−21)	−0.7919	9.1688
	150–500,000	1.4932(−21)	−1.4979	127.3372

^a $x(-y) \equiv x \times 10^{-y}$.

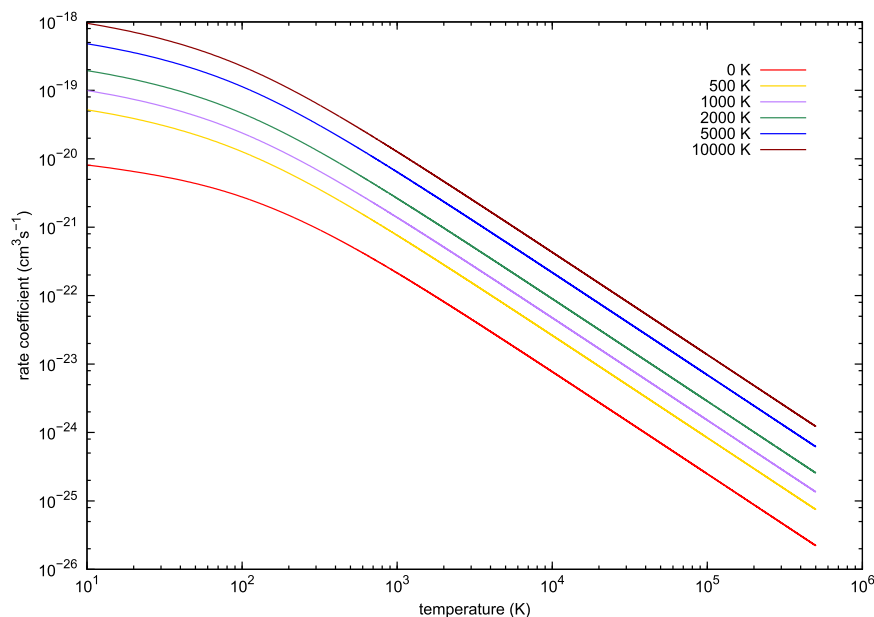


Fig. 5. $c \rightarrow c$ rate coefficients at different background temperatures for the stimulated radiative association of HeLi^+ .

than four thousand ro-vibrational states. In contrast, the two higher $b^3\Sigma^+$ and $c^3\Sigma^+$ states are relatively weakly bound ($D_e = 872 \text{ cm}^{-1}$ and 1439 cm^{-1} , respectively). Nevertheless, they can also accommodate well over thousand ro-vibrational states each, because their potentials are rather wide as a result of their long-range properties. In these potentials the interactions of metastable $\text{He}(2^3\text{S})$ or $\text{He}(2^3\text{P})$ with effectively closed-shell $\text{Li}^+(1^1\text{S})$ include major contributions from induction forces (in the latter case also from an electrostatic charge-quadrupole interaction), and these are slowly varying with the internuclear distance.

In Table 1 some basic data are collected specifying the numbers of bound and quasi-bound states, which are supported by the electronic states considered here.

Cross-sections for spontaneous radiative-association processes $c \rightarrow a$, $c \rightarrow b$, and $c \rightarrow c$ are displayed as functions of collision energy in Fig. 3. The curves have the characteristic behavior for radiative processes with an attractive barrier-less initial electronic state: maximum values at the lowest energies, decreasing values with increasing collision energy, and a rapid drop-off at higher energies. As expected, the values of the cross-sections of the two-state processes are orders of magnitude larger compared to the one-state reaction. At lower energies the curves exhibit some resonance structure, which is created by the quasi-bound states trapped behind the centrifugal barrier of the initial $c^3\Sigma^+$ state. Actually, up to an energy of about 10^{-3} eV this resonance structure is identical for all the three processes, with differences only in the heights of the resonance peaks (the $c \rightarrow b$ resonance peaks are generally smaller). Apparently, in this low-energy region the initial complex formation taking place on the c -state potential is predominant for all these processes. In the energy interval between 10^{-3} to 10^{-2} eV the $c \rightarrow b$ cross-section curve has practically no resonances, whereas a rich resonance structure appears especially for $c \rightarrow a$. This is partly due to the fact that there are fewer symmetry-allowed resonances¹ for the $c \rightarrow b$ process than for the other two processes (see Table 1).

¹ Symmetry-allowed resonances are the quasi-bound states in the initial electronic state from which there exists at least one dipole-moment allowed transition to a ro-vibrational state in the corresponding target electronic state.

The corresponding rate coefficients for the spontaneous radiative associations determined from the cross-sections are shown in Fig. 4 as functions of temperature. Numerical values evaluated at selected temperatures are provided in Table 2 and the fitted parameters of Kooij function (8) are given in Table 3. Rate constants of the most efficient $c \rightarrow a$ process are six orders of magnitude larger compared to $c \rightarrow c$. The curves are steadily decreasing with increasing temperature, which is characteristic for the radiative processes studied here and is in contrast to typical temperature dependencies observed in many non-radiative inelastic collision processes [17,18,36,37]. As already indicated by the similar shapes and similar structures of the cross-section curves of reactions $c \rightarrow a$ and $c \rightarrow c$ in Fig. 3, the corresponding rate constant curves in Fig. 4 are practically parallel, whereas the $c \rightarrow b$ curve has a different shape.

It was shown previously that the stimulation of the radiative association by the background radiation is relevant only for one-state processes [12] (or more generally, for processes with zero ΔE), and the situation is not different in this study. The rate coefficient for the stimulated radiative-association $c \rightarrow c$ process is shown graphically for different black-body radiation temperatures T_b in Fig. 5. The difference in rate coefficients between the limit cases ($T_b = 0 \text{ K}$ and $T_b = 10,000 \text{ K}$) does not wash out up to 500,000 K, instead it keeps almost constant at two orders of magnitude in favor of the stimulated process. This is qualitatively different behavior compared to the stimulated radiative association of He_2^+ , where the difference was decreasing rapidly with increasing temperature until it almost became negligible at temperatures around $T = 10,000 \text{ K}$ [12,13].

4. Conclusion

Radiative-association processes originating in the triplet-Sigma continuum of the $\text{He}(2^3\text{P}) + \text{Li}^+$ collisional system are investigated in this study. The dynamic calculations are based on highly accurate state-of-the-art ab initio calculations of the three lowest $^3\Sigma^+$ states of HeLi^+ and the associated transition dipole moment functions obtained previously by Soldán and Kraemer [20]. Cross-sections for the spontaneous and stimulated radiative-association

processes are calculated as functions of collision energy. The corresponding rate coefficients characterizing the efficiency of the formation of the molecular ion in its $a^3\Sigma^+$, $b^3\Sigma^+$, and $c^3\Sigma^+$ states are obtained over a wide range of temperatures. Due to the large difference between the ionization energies of He and Li, the two-state process $c \rightarrow a$ is by far the most efficient one with a rate coefficient value of about $3.6 \times 10^{-15} \text{ cm}^3 \text{ s}^{-1}$ at a temperature of 10 K.

The radiative-association reactions of this study can also be viewed as radiative depopulation processes of metastable He(2^3P) in collisions with Li^+ ions, restricting the processes to $^3\Sigma^+$ symmetry. In this context, the present results can be directly compared with those of the recent study of radiative depopulation of He(2^3S) in collisions with Li^+ ions [14]. In that study, the formation of the $a^3\Sigma^+$ state (following the $\text{He}(2^3S) + \text{Li}^+ \rightarrow \text{HeLi}^+(a^3\Sigma^+) + h\nu$ reaction) appears to be slightly more efficient with a rate coefficient value of about $1.2 \times 10^{-14} \text{ cm}^3 \text{ s}^{-1}$ at $T = 10 \text{ K}$. The cross-sections and rate coefficients for this depopulation process (Figs. 2 and 4 in Ref. [14]) turn out to be different from the present results. Particularly, the rate coefficient as a function of temperature stays almost constant at its initial value at 10 K up to a temperature of about $T = 10,000 \text{ K}$, before it decreases for higher temperatures. However, the whole picture of the metastable He(2^3P) depopulation by radiative association will be obtained only when the results for radiative-association processes involving the $1^3\Pi$ state will become available. This will be included in one of our future studies.

5. Conflict of interest

The authors declare no conflict of interest.

Acknowledgements

LA, MZ, and PS acknowledge funding from the Czech Science Foundation – GAČR (Grant No. P209/15-10267S). MZ is grateful for support from the Grant Agency of the Charles University in Prague – GAUK (Grant No. 366115).

References

- [1] S.S. Hodgman, R.G. Dall, L.J. Byron, K.G.H. Baldwin, S.J. Buckman, A.G. Truscott, *Phys. Rev. Lett.* 103 (2009) 053002, <http://dx.doi.org/10.1103/PhysRevLett.103.053002>.
- [2] A. Robert, O. Sirjean, A. Browaeys, J. Poupard, S. Nowak, D. Boiron, et al., *Science* 292 (2001) 461, <http://dx.doi.org/10.1126/science.1060622>.
- [3] F. Pereira Dos Santos, J. Léonard, J. Wang, C.J. Barrelet, F. Perales, E. Rasel, et al., *Phys. Rev. Lett.* 86 (2001) 3459, <http://dx.doi.org/10.1103/PhysRevLett.86.3459>.
- [4] J. Léonard, M. Walhout, A.P. Mosk, T. Müller, M. Leduc, C. Cohen-Tannoudji, *Phys. Rev. Lett.* 91 (2003) 073203, <http://dx.doi.org/10.1103/PhysRevLett.91.073203>.
- [5] W. Martin, *J. Phys. Chem. Ref. Data* 2 (1973) 257, <http://dx.doi.org/10.1063/1.3253119>.
- [6] R. Thompson, *J. Quant. Spectrosc. Radiat. Transfer* 14 (1974) 1179, [http://dx.doi.org/10.1016/0022-4073\(74\)90034-X](http://dx.doi.org/10.1016/0022-4073(74)90034-X).
- [7] W. Bennett, P. Kindlmann, G. Mercer, *Chem. Lasers: Appl. Opt. Suppl.* 2 (1965) 34.
- [8] J. Lifshitz, R. Sands, *Bull. Am. Phys. Soc.* 10 (1965) 1214.
- [9] D. Landman, *Phys. Rev.* 173 (1968) 33, <http://dx.doi.org/10.1103/PhysRev.173.33>.
- [10] B. Schiff, C. Pekeris, *Phys. Rev.* 134 (1964) A638, <http://dx.doi.org/10.1103/PhysRev.134.A638>.
- [11] S.S. Hodgman, R.G. Dall, K.G.H. Baldwin, A.G. Truscott, *Phys. Rev. A* 80 (2009) 044501, <http://dx.doi.org/10.1103/PhysRevA.80.044501>.
- [12] L. Augustovičová, V. Špirko, W.P. Kraemer, P. Soldán, *Astron. Astrophys.* 553 (2013) A42, <http://dx.doi.org/10.1051/0004-6361/201220957>.
- [13] L. Augustovičová, V. Špirko, W.P. Kraemer, P. Soldán, *Mon. Not. R. Astron. Soc.* 435 (2013) 1541, <http://dx.doi.org/10.1093/mnras/stt1395>.
- [14] L. Augustovičová, W.P. Kraemer, P. Soldán, *Astron. Astrophys. J.* 782 (2014) 46, <http://dx.doi.org/10.1088/0004-637X/782/1/46>.
- [15] L. Augustovičová, W.P. Kraemer, P. Soldán, *J. Quant. Spectrosc. Radiat. Transfer* 148 (2014) 27, <http://dx.doi.org/10.1016/j.jqsrt.2014.06.012>.
- [16] L. Augustovičová, V. Špirko, W.P. Kraemer, P. Soldán, *Mon. Not. R. Astron. Soc.* 446 (2015) 2738, <http://dx.doi.org/10.1093/mnras/stu2317>.
- [17] A.K. Belyaev, L. Augustovičová, P. Soldán, W.P. Kraemer, *Astron. Astrophys.* 565 (2014) A106, <http://dx.doi.org/10.1051/0004-6361/201423578>.
- [18] A.K. Belyaev, D.S. Rodionov, L. Augustovičová, P. Soldán, W.P. Kraemer, *Mon. Not. R. Astron. Soc.* 449 (2015) 3323, <http://dx.doi.org/10.1093/mnras/stv391>.
- [19] J. Loreau, S. Vranckx, M. Desouter-Lecomte, N. Vaeck, A. Dalgarno, *J. Phys. Chem. A* 117 (2013) 9486, <http://dx.doi.org/10.1021/jp312007q>.
- [20] P. Soldán, W.P. Kraemer, *Chem. Phys.* 393 (2012) 135, <http://dx.doi.org/10.1016/j.chemphys.2011.11.040>.
- [21] T.S. Ho, H. Rabitz, *J. Chem. Phys.* 104 (7) (1996) 2584, <http://dx.doi.org/10.1063/1.470984>.
- [22] T.S. Ho, H. Rabitz, *J. Chem. Phys.* 113 (10) (2000) 3960, <http://dx.doi.org/10.1063/1.1288268>.
- [23] P. Soldán, J.M. Hutson, *J. Chem. Phys.* 112 (9) (2000) 4415, <http://dx.doi.org/10.1063/1.480988>.
- [24] B. Zygelman, A. Dalgarno, *Astron. Astrophys. J.* 365 (1990) 239, <http://dx.doi.org/10.1086/169475>.
- [25] P.C. Stancil, A. Dalgarno, *Astron. Astrophys. J.* 479 (1997) 543, <http://dx.doi.org/10.1086/303920>.
- [26] L. Augustovičová, V. Špirko, W.P. Kraemer, P. Soldán, *Chem. Phys. Lett.* 531 (2012) 59, <http://dx.doi.org/10.1016/j.cplett.2012.02.038>.
- [27] J.K.G. Watson, *J. Mol. Spectrosc.* 80 (1980) 411, [http://dx.doi.org/10.1016/0022-2852\(80\)90152-6](http://dx.doi.org/10.1016/0022-2852(80)90152-6).
- [28] Y. Ralchenko, A.E. Kramida, J. Reader, N.A. Team, Nist Atomic Spectra Database (version 3.1.5), 2010. See <<http://physics.nist.gov/asd3>>
- [29] A. Hansson, J.K.G. Watson, *J. Mol. Spectrosc.* 233 (2005) 169, <http://dx.doi.org/10.1016/j.jms.2005.06.009>.
- [30] B.V. Numerov, *Trudy Glavnoi rossiiskoi astrofizicheskoi observatorii* 2 (1923) 188.
- [31] J.W. Cooley, *Math. Comput.* 15 (1961) 363, <http://dx.doi.org/10.1090/S0025-5718-1961-0129566-X>.
- [32] R.J. Le Roy, Level 7.7: A computer program for solving the radial Schrödinger equation CRR-661, 2005.
- [33] R.J. Le Roy, W. Liu, *J. Chem. Phys.* 69 (1978) 3622, <http://dx.doi.org/10.1063/1.437070>.
- [34] J.N.L. Connor, A.D. Smith, *Mol. Phys.* 43 (1981) 397, <http://dx.doi.org/10.1080/00268978100101411>.
- [35] Y. Huang, R.J. Le Roy, *J. Chem. Phys.* 2003 (119) (2007) 7398, <http://dx.doi.org/10.1063/1.2723739>.
- [36] B. Zygelman, A. Dalgarno, M. Kimura, N.F. Lane, *Phys. Rev. A* 40 (1989) 2340, <http://dx.doi.org/10.1103/PhysRevA.40.2340>.
- [37] P.C. Stancil, C.C. Havener, P.S. Krstić, D.R. Schultz, M. Kimura, J.P. Gu, et al., *Astron. Astrophys. J.* 502 (1998) 1006, <http://dx.doi.org/10.1086/305937>.

NON-RADIATIVE INELASTIC PROCESSES IN
LITHIUM-HELIUM ION-ATOM COLLISIONS

Bibliographic record of the attached publication:

Belyaev, A. K., L. Augustovičová, P. Soldán, and W. P. Kraemer (2014).
“Non-radiative inelastic processes in lithium-helium ion-atom collisions.” In: *Astronomy & Astrophysics* 565, A106.
DOI: [10.1051/0004-6361/201423578](https://doi.org/10.1051/0004-6361/201423578).

Non-radiative inelastic processes in lithium-helium ion-atom collisions

Andrey K. Belyaev¹, Lucie Augustovičová², Pavel Soldán², and Wolfgang P. Kraemer³

¹ Department of Theoretical Physics and Astronomy, Herzen University, St. Petersburg 191186, Russia and Max-Planck Institute for Astrophysics, Postfach 1371, 85741 Garching, Germany

e-mail: andrey.k.belyaev@gmail.com

² Charles University in Prague, Faculty of Mathematics and Physics, Department of Chemical Physics and Optics, Ke Karlovu 3, 12116 Prague 2, Czech Republic

³ Max-Planck Institute for Astrophysics, Postfach 1371, 85741 Garching, Germany

Received 5 February 2014 / Accepted 12 March 2014

ABSTRACT

Aims. The aims are to estimate efficiencies of non-radiative inelastic processes in lithium-helium ion-atom collisions and to compare them to those for radiative processes.

Methods. Non-radiative inelastic cross-sections and rate coefficients for different lithium-helium ion-atom collisions are estimated by means of the recently proposed branching probability current method, which is based on the accurate ab initio adiabatic Born-Oppenheimer potentials that have been recently calculated for the low-lying $1,3\Sigma^+$ and $1,3\Pi$ states of the LiHe^+ ion.

Results. It is shown that at low temperatures the radiative depopulation in $\text{Li}^+ + \text{He}$ and $\text{Li} + \text{He}^+$ collisions dominates over the non-radiative processes, while in $\text{Li}^+ + \text{He}(2s\ ^3S)$ collisions the non-radiative processes dominate over the radiative association at temperatures above 3000 K, which can be expected to have some influence on depopulations of metastable He in high temperature astrophysical environments.

Key words. atomic data – molecular data – scattering

1. Introduction

Studies of non-adiabatic effects in the interactions between $(\text{Li}^+ + \text{He})$ and $(\text{Li} + \text{He}^+)$ collisional complexes on different excitation levels can contribute to a better understanding of primordial and interstellar lithium chemistry, especially when the efficiencies of radiative and non-radiative processes at different temperatures are compared.

According to the Big Bang nucleosynthesis theory, lithium is the heaviest stable element produced in this event (Burles et al. 2001). After the initial period, when in the rapidly expanding Universe matter and radiation were in close thermal contact, the Universe became transparent and temperature was sufficiently lowered to allow the initially formed fully stripped atomic nuclei (H^+ , D^+ , He^{2+} , Li^{3+}) to recombine with electrons to form finally neutral atoms. In the case of lithium, the recombination process proceeded sequentially in the order of its ionization potentials: beginning with Li^{3+} , ending with both Li atoms and remaining Li^+ ions, which could not readily recombine due to a lack of free electrons by the end of the recombination era. Intensive studies were performed to investigate the primordial lithium chemistry (Stancil & Zygelman 1996; Stancil & Dalgarno 1997; Galli & Palla 1998, 2013) and to analyze the effect of neutral lithium on the cosmic microwave background anisotropies (Palla et al. 1995; Loeb 2001). At the time when the fractional abundances of Li and Li^+ became comparable at a $z \approx 100$ redshift (Stancil et al. 2002), the abundance of He^+ ions dropped by several orders of magnitude (Stancil et al. 1998). At smaller redshifts, reactions of neutral Li atoms with He^+ ions are therefore rather improbable. They are, however, included in this study because $(\text{Li} + \text{He}^+)$ collision pairs are obtained here via charge transfer

processes in $(\text{Li}^+ + \text{He})$ collisions. In addition, even if lithium is rather rare compared to the other primordial elements synthesized in the early Universe, inelastic collisional processes of neutral lithium with hydrogen and other atomic or ionic species are of high interest in modeling stellar atmospheres (Carlsson et al. 1994; Barklem et al. 2003; Belyaev & Barklem 2003).

To get a first overview of the possible non-adiabatic effects in lithium-helium ion-atom interactions at different excitation levels, a model approach (Belyaev & Lebedev 2011; Belyaev 2013a) is applied here to estimate the cross-sections and rate coefficients in the corresponding non-radiative inelastic collisions.

2. Nonadiabatic nuclear dynamics

The theoretical treatment is performed within the standard adiabatic Born-Oppenheimer (BO) approach, which considers a collision problem in two steps: (i) electronic structure calculations and (ii) a study of the non-adiabatic nuclear dynamics.

Adiabatic BO potentials and electric dipole moment functions for several low-lying excited $1,3\Sigma^+$ and $1,3\Pi$ states of the LiHe^+ ion were recently determined on a high-accuracy level of ab initio theory (Soldán & Kraemer 2012). For the $X^1\Sigma^+$ ground state, the calculated characteristic spectroscopic data were found to be in perfect agreement with the best obtained results available from the literature in the past (Senff & Burton 1986; Elford et al. 1999). For the ground state (X-state) and the first excited $1,3\Sigma^+$ states (A- and a-states), radiative association processes were investigated in detail (Augustovičová et al. 2012; Bovino et al. 2011). In addition, depopulation of metastable $\text{He}(2^3S)$

Table 1. Parameters of the non-adiabatic regions for LiHe⁺.

Collision channel j	Molecular state j	Collision channel k	Molecular state k	Center R_c (au)	Minimal splitting Z_{jk} (au)	LZ parameter ξ_{jk} (au)
¹ Σ^+ symmetry						
Li ⁺ + He(1s ² ¹ S)	X ¹ Σ^+	Li(2s) + He ⁺	A ¹ Σ^+	6.940	6.812(-1)	1.157(1)
Li(2s) + He ⁺	A ¹ Σ^+	Li ⁺ + He(2s ¹ S)	B ¹ Σ^+	13.376	4.403(-2)	4.137(-1)
Li(2s) + He ⁺	A ¹ Σ^+	Li ⁺ + He(2s ¹ S)	B ¹ Σ^+	2.728	9.589(-2)	2.084(-1)
Li ⁺ + He(2s ¹ S)	B ¹ Σ^+	Li(2p) + He ⁺	C ¹ Σ^+	3.503	6.310(-3)	2.040(-3)
Li(2p) + He ⁺	C ¹ Σ^+	Li ⁺ + He(2p ¹ P)	D ¹ Σ^+	1.194	6.916(-3)	6.387(-4)
³ Σ^+ symmetry						
Li(2s) + He ⁺	a ³ Σ^+	Li ⁺ + He(2s ³ S)	b ³ Σ^+	15.511	2.180(-2)	3.131(-1)
Li(2s) + He ⁺	a ³ Σ^+	Li ⁺ + He(2s ³ S)	b ³ Σ^+	2.448	9.488(-2)	1.570(-1)
Li ⁺ + He(2s ³ S)	b ³ Σ^+	Li ⁺ + He(2p ³ P)	c ³ Σ^+	15.089	3.913(-2)	6.858(-1)
Li ⁺ + He(2s ³ S)	b ³ Σ^+	Li ⁺ + He(2p ³ P)	c ³ Σ^+	3.962	1.728(-3)	4.326(-4)
Li ⁺ + He(2p ³ P)	c ³ Σ^+	Li(2p) + He ⁺	d ³ Σ^+	24.753	2.633(-3)	3.709(-2)
Li ⁺ + He(2p ³ P)	c ³ Σ^+	Li(2p) + He ⁺	d ³ Σ^+	1.201	1.010(-2)	3.041(-3)
³ Π symmetry						
Li ⁺ + He(2p ³ P)	1 ³ Π	Li(2p) + He ⁺	2 ³ Π	22.898	2.913(-3)	1.899(-1)

Notes. $x(y) \equiv x \times 10^y$.

by radiative association processes was most recently studied (Augustovičová et al. 2014).

The excited-states adiabatic BO potentials calculated by Soldán & Kraemer (2012) are used here as a basis for the present model calculations.

In general, in order to study non-adiabatic nuclear dynamics entirely by means of quantum mechanical methods one needs to know not only adiabatic BO potentials, but also non-adiabatic couplings. On the other hand, non-adiabatic transition probabilities, inelastic cross-sections, and rate coefficients can be estimated within a model approach, especially when complete quantum-chemical information is not available. Such a model approach, the so-called branching probability current method, that requires information only about adiabatic potentials, has been recently proposed (Belyaev 2013a) and applied to inelastic aluminium-hydrogen collisions (Belyaev 2013a,b). The main assumption of the approach is that non-adiabatic transition probabilities can be estimated within the framework of the Landau-Zener (LZ) model (Landau 1932a,b; Zener 1932). The bottleneck of the LZ-model application is twofold: (i) the conventional LZ formula requires the knowledge of diabatic parameters though a diabaticization procedure is not uniquely defined; and (ii) usually, there are several non-adiabatic regions that determine the non-adiabatic nuclear dynamics without a particular order. The branching probability current method handles the latter by branching all incoming and outgoing probability currents after each traverse of the non-adiabatic regions in any order they appear during a collision. The method is similar to the branching classical trajectory method (Belyaev & Lebedev 2011), which is based on classical trajectories and determines LZ parameters along each trajectory. The branching probability current method determines LZ parameters beforehand and then varies an internuclear distance R without calculating any classical trajectories (see Belyaev 2013a).

The key point of the branching probability current method is a novel formula for a non-adiabatic transition probability within the LZ model, the so-called adiabatic-potential-based formula (Belyaev & Lebedev 2011; Belyaev 2013a). Positions of non-adiabatic regions R_c are determined by minima of adiabatic splittings $Z_{jk} = |U_j - U_k|$ between adjacent adiabatic states with $U_{j,k}(R)$ being adiabatic potentials. In these regions,

the LZ parameters are determined by the following formula (Belyaev & Lebedev 2011; Belyaev 2013a):

$$\xi_{jk} = \frac{\pi}{2\hbar} \sqrt{\frac{Z_{jk}^3}{Z'_{jk}}} \Big|_{R=R_c}. \quad (1)$$

Primed quantities are referred to derivatives with respect to the internuclear distance R . Equation (1) expresses the LZ parameter only in terms of the adiabatic splitting Z_{jk} and its second distance derivative at R_c . Finally, a non-adiabatic transition probability p_{jk}^{LZ} after a single traverse of a non-adiabatic region is written in the usual form,

$$p_{jk}^{LZ} = \exp(-\xi_{jk}/v), \quad (2)$$

where v is a radial velocity of colliding atoms. All values are evaluated at the centers of the non-adiabatic regions.

Thus, Eqs. (1) and (2) allow one to calculate non-adiabatic transition probabilities in each non-adiabatic region based on the information about adiabatic potentials only. Then branching of incoming and outgoing currents allows one to compute probabilities for transitions between a given initial state and a given final state, and finally inelastic cross-sections and rate coefficients.

3. Results of calculations

3.1. Nonadiabatic regions

In the present paper, we treat non-adiabatic transitions separately between the low-lying ¹ Σ^+ states, between the low-lying ³ Σ^+ states, and between the pair of the lowest excited ³ Π states. The adiabatic BO potentials for these symmetries are taken from Soldán & Kraemer (2012). For the lowest excited pair of ¹ Π states, the form and relative separation of their potentials (Soldán & Kraemer 2012) indicate that non-adiabatic coupling between them is negligible. It is therefore not considered here. Transitions between states of different symmetries are also not considered in the present estimates.

The parameters of the non-adiabatic regions for the ¹ Σ^+ , ³ Σ^+ and ³ Π symmetries of LiHe⁺ are collected in Table 1. The centers R_c of these regions are determined by the local minima of

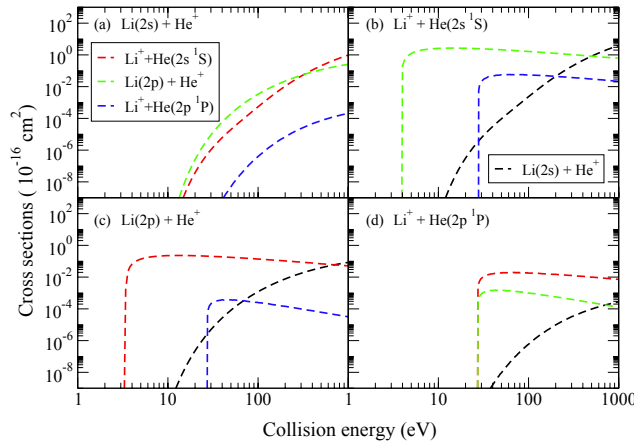


Fig. 1. Inelastic cross-sections within the $^1\Sigma^+$ system. The initial collision channel is indicated in each panel. The key for final channels is common to all panels and is shown in panels **a**) and **b**). The statistical probability factors for the initial channels are taken into account in the cross-sections.

the corresponding adiabatic splittings Z_{jk} . The LZ parameters ξ_{jk} are then calculated in each region by means of Eq. (1). There are five non-adiabatic regions within the $^1\Sigma^+$ symmetry, six regions within the $^3\Sigma^+$ symmetry, and one region within the $^3\Pi$ symmetry. Table 1 also shows that within the $^1\Sigma^+$ and $^3\Sigma^+$ symmetries, several non-adiabatic regions can exist for certain pairs of adjacent potentials, which makes the non-adiabatic nuclear dynamics more complicated. Actually, the branching probability current method applied here takes this situation automatically into account. The calculated LZ parameters allow us to estimate inelastic cross-sections and rate coefficients.

3.2. Inelastic cross-sections

According to the data for non-adiabatic transitions within the $^1\Sigma^+$ symmetry, that are listed in Table 1, a non-adiabatic region around $R_c = 6.94$ au is indicated by the present model calculations for the adiabatic potentials of the ground state ($X^1\Sigma^+$) and the first excited state ($A^1\Sigma^+$). The energy gap, however, between these two potentials is very big (see Table 1 for the minimum of the adiabatic splitting Z_{jk}), resulting in the large LZ parameter ξ_{jk} and making the probabilities for non-adiabatic transitions from and to the ground molecular state extremely small. Inelastic non-radiative collision processes involving the $\text{Li}^+ + \text{He}(1s^2 \ ^1S)$ channel (both as the initial and as the final channels) have, thus, negligible inelastic cross-sections and rate coefficients and are therefore disregarded here.

The inelastic cross-sections for the other transitions within the $^1\Sigma^+$ symmetry are shown in Fig. 1 as a function of the collision energy E . The initial collision channel is specified in the top of each panel, whereas the final collision channels, which are labeled by colors, are defined in the insets of panels (a) and (b). The definitions of the color labels are common for all figures in the present paper.

Figure 1 shows that practically all partial cross-sections have large energy thresholds, reaching from 3.4 eV up to about 28 eV. These large thresholds are due to the fact that most non-adiabatic regions within the $^1\Sigma^+$ symmetry are located at short internuclear distances in the repulsive part of the adiabatic potentials with $R_c < 3.5$ au. For non-adiabatic transitions to occur, the collision system has therefore to have enough kinetic energy. For

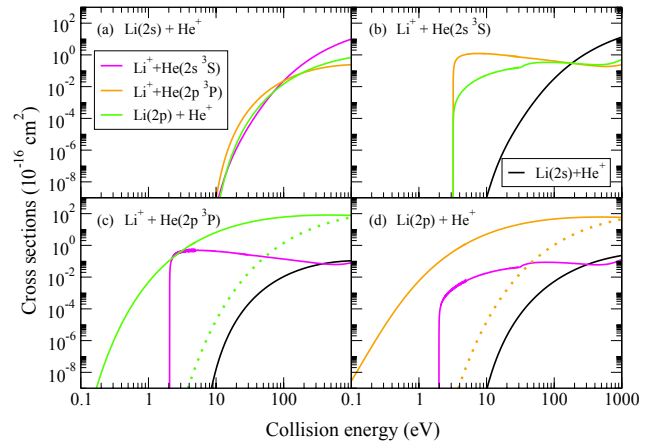


Fig. 2. Inelastic cross-sections within the $^3\Sigma^+$ system (solid lines) and within the $^3\Pi$ system (dotted lines). The initial collisional channel is indicated in each panel. The key for final channels is common to all panels and is shown in panels **a**) and **b**). The statistical probability factors for the initial channels are taken into account in the cross-sections.

the charge transfer reaction $\text{Li}(2s) + \text{He}^+ \rightleftharpoons \text{Li}^+ + \text{He}(2s \ ^1S)$, however, there exists a second non-adiabatic region at large internuclear distance ($R_c = 13.376$ au). The LZ parameter here is relatively large and the non-adiabatic transition probabilities get remarkable values at rather high collision energies.

At low collision energies, most partial cross-sections have rather small values in Fig. 1. An exception here is the $\text{Li}^+ + \text{He}(2s \ ^1S) \rightleftharpoons \text{Li}(2p) + \text{He}^+$ charge transfer into excited state processes. For this endothermic process, the cross-section increases rapidly right above the threshold and reaches its maximum value of 2.7 \AA^2 at a collision energy of $E = 14$ eV. Similar large cross-sections are obtained for other processes only at higher collision energies.

The calculated partial inelastic cross-sections within the $^3\Sigma^+$ system and within the $^3\Pi$ system are shown in Fig. 2 by solid and dotted lines, respectively. Initial and final collisional channels are specified here in the same way as in Fig. 1. Obviously many partial cross-sections have also relatively large energy thresholds for the same reasons discussed before for the $^1\Sigma^+$ system. The cross-sections for the $\text{Li}^+ + \text{He}(2p \ ^3P) \rightleftharpoons \text{Li}(2p) + \text{He}^+$ charge transfer into excited state processes, on the other hand, have a small energy threshold (actually, 0.08 eV for the endothermic process and practically no energy threshold for the exothermic process). This occurs because the second non-adiabatic region at large internuclear distance with $R_c = 24.753$ au is located between the $c \ ^3\Sigma^+$ and $d \ ^3\Sigma^+$ molecular states with the closely lying potentials in this region (Soldán & Kraemer 2012). For the $^3\Pi$ system the non-adiabatic region also occurs at a long distance, $R_c = 22.898$ au. However, the LZ parameter obtained in this region appears to be large, given the effect that the non-adiabatic transitions with observable probabilities and larger inelastic cross-sections occur only at higher energies (indicated by the dotted lines in Fig. 2).

Cross-sections obtained here for the $^3\Sigma^+$ system have typically larger values compared to those for the $^1\Sigma^+$ system. The values range from a few Å^2 at low collision energies to $5\text{--}7 \text{ \AA}^2$ at $E = 10$ eV and up to 80 \AA^2 at high energies for the $\text{Li}^+ + \text{He}(2p \ ^3P) \rightleftharpoons \text{Li}(2p) + \text{He}^+$ charge transfer processes. For these processes, the transitions mainly take place in the non-adiabatic region around $R = 24.753$ au, that is, at large internuclear distances. In addition, the excitation/de-excitation

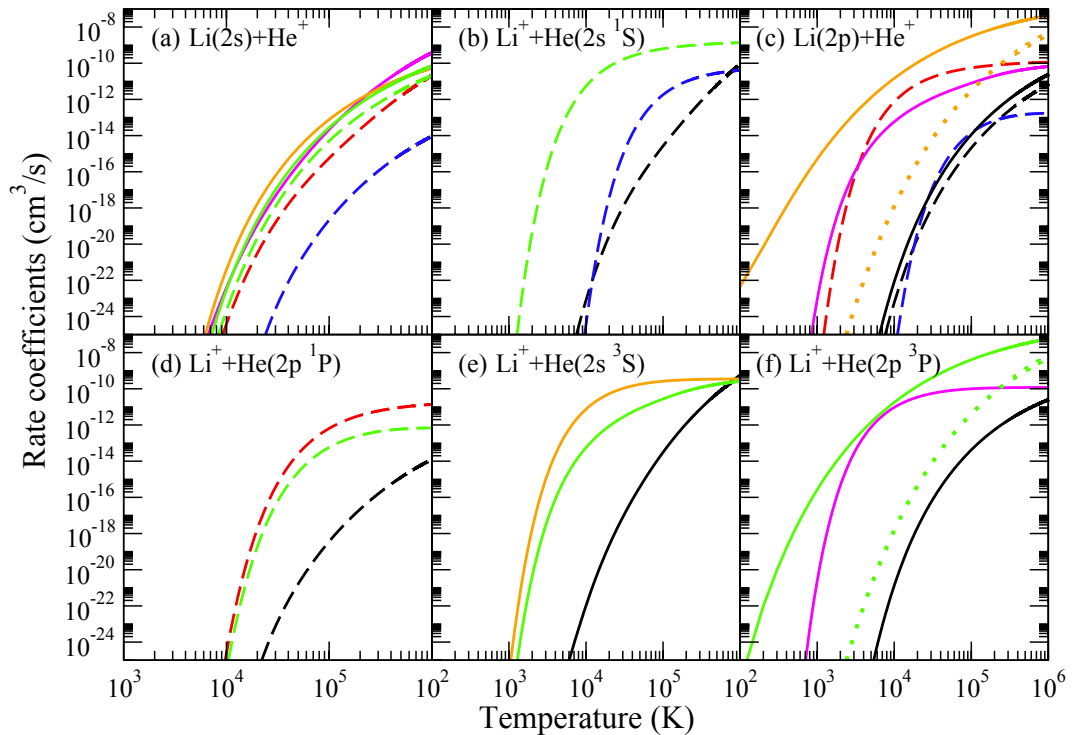


Fig. 3. Inelastic rate coefficients within the $^1\Sigma^+$ (dashed lines), $^3\Sigma^+$ (solid lines), and $^3\Pi$ (dotted lines) systems. The initial collisional channel is indicated in each panel. The key for final channels is common to all panels and is labeled by colors: black lines correspond to $\text{Li}(2s) + \text{He}^+$; red lines to $\text{Li}^+ + \text{He}(2s \ ^1S)$; green to $\text{Li}(2p) + \text{He}^+$; blue to $\text{Li}^+ + \text{He}(2p \ ^1P)$; magenta to $\text{Li}^+ + \text{He}(2s \ ^3S)$; and orange to $\text{Li}^+ + \text{He}(2p \ ^3P)$.

processes $\text{Li}^+ + \text{He}(2s \ ^3S) \rightleftharpoons \text{Li}^+ + \text{He}(2p \ ^3P)$ also have large cross-section values reaching 1.2 \AA^2 as a maximum.

Apart from the processes discussed here, other partial processes can occur via non-adiabatic transitions within different molecular symmetries. The $\text{Li}^+ + \text{He}(2p \ ^3P) \rightleftharpoons \text{Li}(2p) + \text{He}^+$ charge transfer processes, for example, involve transitions within the $^3\Sigma^+$ and $^3\Pi$ systems and the $\text{Li}(2s) + \text{He}^+ \rightleftharpoons \text{Li}(2p) + \text{He}^+$ excitation/de-excitation processes are based on non-adiabatic transitions within the $^1\Sigma^+$ and $^3\Sigma^+$ systems.

Finally, it should be emphasized that the LZ model might provide less accurate transition probabilities for non-adiabatic regions with large adiabatic splittings or for cases when other quantum effects, such as tunneling, are substantial. In those situations the model estimates have larger uncertainties for small transition probabilities and, hence, low cross-sections. A fully quantum-mechanical treatment of the tunneling effect at short internuclear distances in the repulsive part of the potentials, for instance, could increase some non-adiabatic transition probabilities and lower the energy threshold. This would eventually increase the rate coefficients, whereas the model provides smaller estimates. However, for cases with substantial transition probabilities, the model applied here has been found to provide reliable estimates of the dominant cross-sections and rate coefficients (Belyaev 2013a).

3.3. Rate coefficients

The calculated inelastic rate coefficients are presented in Fig. 3 as a function of the temperature T in the range between 10^3 to 10^6 K. The initial collision channels are again specified in the top of each panel and the same color labels are used for the final collision channels as in Figs. 1 and 2.

The gross behavior of the rate coefficients reflects the characteristics of the corresponding cross-sections. The rate coefficients increase from very low values at low temperatures up to roughly $6 \times 10^{-8} \text{ cm}^3/\text{s}$ at high temperatures. Low rate coefficients for the partial processes at low temperatures are partly due to the large energy thresholds for the partial cross-sections and partly to low values of the low-energy cross-sections, as discussed above. The high temperature increase of the rate coefficients corresponds to the increase of the cross-sections at high collision energies.

It is seen from Fig. 3 that depopulation of the $\text{Li}(2s) + \text{He}^+$ channel is inefficient at low temperatures that are below 10^4 K. The partial rate coefficients are smaller than $4 \times 10^{-22} \text{ cm}^3/\text{s}$, and all depopulation processes are endothermic, since the cross-section for the only exothermic channel, $\text{Li}^+ + \text{He}(1s^2 \ ^1S)$, is negligible. At high temperatures, depopulation of the $\text{Li}(2s) + \text{He}^+$ channel can occur due to several processes, which are mostly due to charge transfer and excitation. The rate coefficients can reach the values up to $5 \times 10^{-10} \text{ cm}^3/\text{s}$, which are mainly due to transitions into the $\text{Li}^+ + \text{He}(2s \ ^3S)$ final channel. Depopulation of the $\text{Li}^+ + \text{He}(2p \ ^1P)$ channel is much less efficient than that for the $\text{Li}(2s) + \text{He}^+$ channel. Actually it is the least efficient among the treated collision channels. Depopulation of the $\text{Li}^+ + \text{He}(2s \ ^1S)$ channel is more efficient even at low temperatures mainly because of the $\text{Li}^+ + \text{He}(2s \ ^1S) \rightarrow \text{Li}(2p) + \text{He}^+$ charge transfer into excited state process. The corresponding rate coefficient is equal to $5.4 \times 10^{-12} \text{ cm}^3/\text{s}$ at $T = 10^4$ K and increases up to $1.4 \times 10^{-9} \text{ cm}^3/\text{s}$ at $T = 10^6$ K. The efficiency of decay of the $\text{Li}^+ + \text{He}(2s \ ^3S)$ channel is comparable to that of the $\text{Li}^+ + \text{He}(2s \ ^1S)$. The rate coefficient equals $7.5 \times 10^{-12} \text{ cm}^3/\text{s}$ for the $\text{Li}^+ + \text{He}(2s \ ^3S) \rightarrow \text{Li}^+ + \text{He}(2p \ ^3P)$ excitation process

at $T = 10^4$ K and is 5.2×10^{-10} cm³/s, 3.5×10^{-10} cm³/s, and 2.6×10^{-10} cm³/s for the Li(2s) + He⁺, the Li⁺ + He(2p ³P), and the Li(2p) + He⁺ final channels, respectively, at $T = 10^6$ K. The largest values for the rate coefficients correspond to the Li⁺ + He(2p ³P) \rightleftharpoons Li(2p) + He⁺ charge transfer processes. They are equal to 1.8×10^{-11} cm³/s and 1.5×10^{-11} cm³/s for the direct and the inverse processes, respectively, at $T = 10^4$ K, and to 5.8×10^{-8} cm³/s and 4.4×10^{-8} cm³/s for direct and inverse processes, respectively, at $T = 10^6$ K. The rate coefficients for these charge transfer processes in the ³Π symmetry also reach values at $T = 10^6$ K, which are almost exactly one order of magnitude smaller than those for the ³Σ system, as shown by the dotted curves in Fig. 3. At relatively low temperatures, the Li⁺ + He(2p ³P) \rightarrow Li⁺ + He(2s ³S) de-excitation process also contributes noticeably into decay of He(2p ³P) in collisions with Li⁺: the corresponding rate coefficient equals 9.4×10^{-12} cm³/s at $T = 10^4$ K.

All partial inelastic rate coefficients decrease rapidly with decreasing the temperature below 10^4 K. The only noticeable rate coefficient remaining at low temperatures is that for the exothermic charge transfer process Li(2p) + He⁺ \rightarrow Li⁺ + He(2p ³P).

4. Discussion and conclusion

The non-radiative cross-sections and rate coefficients estimated in the present paper can be compared to the radiative association cross-sections and rate coefficients calculated by Augustovičová et al. (2012, 2014) for the same collision systems. The comparison shows that there are a couple of basic differences some of which are listed below.

First of all, the radiative association treatment provides noticeable cross-sections and rate coefficients from and to the ground molecular state LiHe⁺(X ¹Σ⁺), for which the present model study estimates negligible non-radiative cross-sections and rate coefficients. The non-radiative processes, thus, do not change depopulation of the Li⁺ + He(1s² ¹S) channel.

Second, the energy dependence of the cross-sections and the temperature dependence of the rate coefficients for radiative and non-radiative processes are totally different. The radiative cross-sections and rate coefficients generally decrease with increasing collision energy and temperature in the low-energy regime. In contrast to this, an increase of the cross-sections and rate coefficients with increasing energy and temperature is observed for non-radiative processes. A general conclusion from this controversial behavior would be that radiative processes are expected to be dominant over non-radiative ones at low energies. This finding actually agrees with the results of the treatment of radiative and non-radiative processes in He⁺ + H collisions (Zygelman et al. 1989), as well as in cold and ultra-cold Yb⁺ + Rb collisions (Sayfutyarova et al. 2013).

Third, depopulation of the Li(2s) + He⁺ collision system due to the radiative association into both the ¹Σ⁺ and the ³Σ⁺ symmetries, i.e., depopulation of the A and a molecular states (see Table 1), was recently studied by Augustovičová et al. (2012). It is shown there that the dominant channel corresponds to the A \rightarrow X transitions with a rate coefficient varying from 10^{-14} cm³/s at 0.1 K down to 10^{-16} cm³/s at 10^4 K. In this temperature range the present estimates show that the non-radiative depopulation of the same states has a maximum total rate coefficient of 4.4×10^{-22} cm³/s at 10^4 K due to transitions a \rightarrow c, b, d within ³Σ⁺ symmetry, whereas the rate coefficients for depopulation of the A state within the ¹Σ⁺ symmetry are much smaller than in the ³Σ⁺ symmetry (see Fig. 3). This leads to the conclusion

that the radiative depopulation of the Li(2s) + He⁺ collision system dominates over the non-radiative depopulation in the low-temperature range (below 10^4 K).

Fourth, most recently, depopulation of the Li⁺ + He(2s ³S) collision system due to radiative association in the ³Σ⁺ symmetry, i.e. depopulation of the b molecular state, was studied by Augustovičová et al. (2014). The dominant transition here is b \rightarrow a with the corresponding rate coefficient of 4.54×10^{-15} cm³/s at 10^4 K. For the same transition, the non-radiative rate coefficient is much smaller, 10^{-21} cm³/s at 10^4 K. On the other hand, according to Fig. 3, the rate coefficients for depopulation of the b state into other channels are much larger: 7.5×10^{-12} cm³/s at 10^4 K for the b \rightarrow c transition (i.e., the Li⁺ + He(2s ³S) \rightarrow Li⁺ + He(2p ³P) excitation process), and 5.6×10^{-14} cm³/s at 10^4 K for the b \rightarrow d transition (i.e., the Li⁺ + He(2s ³S) \rightarrow Li(2p) + He⁺ charge transfer process). Comparison of the temperature dependence of the rate coefficients for the radiative and non-radiative depopulation shows that the non-radiative depopulation dominates over the radiative one for the Li⁺ + He(2s ³S) collision channel at $T > 3000$ K.

Based on these results, it can be concluded that at relatively high temperatures a non-radiative decay (due to non-adiabatic transitions) is expected to dominate over a radiative decay for higher-lying excited states. A critical temperature has to be determined in each particular case. More generally, it appears that radiative and non-radiative processes apply to different areas in interstellar environments when studying atomic or molecular astrophysical questions. For example, non-radiative collision processes can, therefore, be expected to be dominant in stellar atmospheres.

Acknowledgements. A.K.B. gratefully acknowledges support from the Russian Foundation for Basic Research (Grant No. 13-03-00163-a) and from the Max-Planck Institute for Astrophysics at Garching (Germany). L.A. acknowledges funding from the Grant Agency of the Charles University in Prague – GAUK (Grant No. 550112).

References

- Augustovičová, L., Špirko, V., Kraemer, W. P., & Soldán, P. 2012, Chem. Phys. Lett., 531, 59
- Augustovičová, L., Kraemer, W. P., & Soldán, P. 2014, ApJ, 782, 46
- Barklem, P. S., Belyaev, A. K., & Asplund, M. 2003, A&A, 409, L1
- Belyaev, A. K. 2013a, Phys. Rev. A, 88, 2704
- Belyaev, A. K. 2013b, A&A, 560, A60
- Belyaev, A. K., & Barklem, P. S. 2003, Phys. Rev. A, 68, 2703
- Belyaev, A. K., & Lebedev, O. V. 2011, Phys. Rev. A, 84, 4701
- Bovino, S., Tacconi, M., & Gianturco, F. A. 2011, ApJ, 740, 101, erratum 2012, ApJ, 748, 150
- Burles, S., Nollett, K. M., & Turner, M. S. 2001, ApJ, 552, L1
- Carlsson, M., Rutten, R. J., Bruls, J. H. M. J., & Shchukina, N. G. 1994, A&A, 288, 860
- Elford, M. T., Røeggen, I., & Skullerud, H. R. 1999, J. Phys. B At. Mol. Phys., 32, 1873
- Galli, D., & Palla, F. 1998, A&A, 335, 403
- Galli, D., & Palla, F. 2013, ARA&A, 51, 163
- Landau, L. D. 1932a, Phys. Z. Sowjetunion, 1, 88
- Landau, L. D. 1932b, Phys. Z. Sowjetunion, 2, 46
- Loeb, A. 2001, ApJ, 555, L1
- Palla, F., Galli, D., & Silk, J. 1995, ApJ, 451, 44
- Sayfutyarova, E. R., Buchachenko, A. A., Yakovleva, S. A., & Belyaev, A. K. 2013, Phys. Rev. A, 87, 2717
- Senff, U. E., & Burton, P. G. 1986, Mol. Phys., 58, 637
- Soldán, P., & Kraemer, W. P. 2012, Chem. Phys., 393, 135
- Stancil, P. C., & Dalgarno, A. 1997, ApJ, 490, 76
- Stancil, P. C., & Zygelman, B. 1996, ApJ, 472, 102
- Stancil, P. C., Lepp, S., & Dalgarno, A. 1998, ApJ, 509, 1
- Stancil, P. C., Loeb, A., Zaldarriaga, M., Dalgarno, A., & Lepp, S. 2002, ApJ, 580, 29
- Zener, C. 1932, Proc. Roy. Soc. A, 137, 696
- Zygelman, B., Dalgarno, A., Kimura, M., & Lane, N. F. 1989, Phys. Rev. A, 40, 2340

FULL QUANTUM STUDY OF NON-RADIATIVE
INELASTIC PROCESSES IN LITHIUM–HELIUM
ION–ATOM COLLISIONS

Bibliographic record of the attached publication:

Belyaev, A. K., D. S. Rodionov, L. Augustovičová, P. Soldán, and W. P. Kraemer (2015). “Full quantum study of non-radiative inelastic processes in lithium-helium ion-atom collisions.” In: *Monthly Notices of the Royal Astronomical Society* 449, pp. 3323–3332.
DOI: [10.1093/mnras/stv391](https://doi.org/10.1093/mnras/stv391).

Full quantum study of non-radiative inelastic processes in lithium–helium ion–atom collisions[★]

A. K. Belyaev,^{1,2†} D. S. Rodionov,¹ L. Augustovičová,³ P. Soldán^{3†}
and W. P. Kraemer²

¹*Department of Theoretical Physics and Astronomy, Herzen University, St. Petersburg 191186, Russia*

²*Max-Planck Institute for Astrophysics, Postfach 1371, D-85741 Garching, Germany*

³*Charles University in Prague, Faculty of Mathematics and Physics, Department of Chemical Physics and Optics, Ke Karlovu 3, CZ-12116 Prague 2, Czech Republic*

Accepted 2015 February 20. Received 2015 February 2; in original form 2014 December 17

ABSTRACT

A full quantum study of non-radiative inelastic processes in lithium–helium ion–atom collisions is presented. The study uses the 13 lowest-lying electronic molecular states of LiHe⁺ of the ¹Σ⁺, ³Σ⁺, ¹Π, and ³Π symmetries. Radial non-adiabatic coupling matrix elements between states of the same symmetry are calculated. Quantum non-adiabatic nuclear dynamics is studied by the reprojection method, which takes into account all non-adiabatic couplings, including those that exhibit non-vanishing asymptotic values. The energy dependence of the cross-sections and temperature dependence of the rate coefficients for all partial processes between the scattering channels is determined. It is shown that the temperature dependence of rate coefficients for the non-radiative and the radiative processes behave differently: the non-radiative rate coefficients increase with increasing temperature, while the radiative rate coefficients decrease. Consequently, in the depopulation of the same scattering channel the non-radiative processes dominate in high-temperature environments, whereas at low temperature, such as in interstellar molecular clouds, the radiative processes are typically more efficient.

Key words: atomic data – atomic processes – molecular data – molecular processes.

1 INTRODUCTION

Lithium is considered to be a key element in various astrophysical theories ranging from cosmological development schemes to galactic chemical evolution studies as well as in stellar models (Signore et al. 1994; Asplund et al. 2006). According to standard big bang nucleosynthesis (BBN) theory, lithium is produced as the heaviest stable element in this event and can be observed in various stellar objects with abundances of the order of $({}^7\text{Li}/\text{H})_{\text{prim}} \sim 10^{-10}$ (Reeves 1998; González-Hernández et al. 2009). Actually, there is a discrepancy between the predicted BBN abundance of ⁷Li and the value measured in Population II stars or metal-poor halo dwarf stars (Audouze & Silk 1989; Mathews, Alcock & Fuller 1990; Iocco et al. 2009), which gives rise to the so-called lithium problem (Israelian 2012). However, the recent measurement of ⁷Li abundance in the

interstellar matter of the Small Magellanic Cloud by Howk et al. (2012) arrived at an abundance almost equal to the BBN predictions, and it appears that the lithium problem posed by stellar measurements may not be representative for the primordial value. In this context, nuclei such as ⁷Li or ⁹Be have recently gained considerable importance because their abundances may provide possible tests of BBN theories. In particular, a molecule such as LiH with its large dipole moment and low ionization potential can be expected to induce distortions in the cosmic microwave background radiation and might thus be used to determine the degree of inhomogeneity in the Universe (Dubrovich 1993; Maoli, Melciorri & Tosti 1994; Puy & Signore 1996, 1998).

The properties of primordial LiH and its ionic species have already been investigated extensively. Of particular importance are the detailed calculations of the rate constants for the formation of LiH via radiative association under primordial conditions (Dalgarno, Kirby & Stancil 1996; Stancil & Dalgarno 1997; Gianturco & Gori-Giorgi 1997; Bovino et al. 2011) and the corresponding collisional or photo destruction processes (Dalgarno et al. 1996; Bovino, Stoecklin & Gianturco 2010). More recently, detailed studies of radiative association processes in lithium–helium ion–atom collisions initiated by excited metastable states of He

*Tables 2 and 3 are only available in electronic form at the CDS via anonymous ftp to cdsarc.u-strasbg.fr (130.79.128.5) or via <http://cdsweb.u-strasbg.fr/cgi-bin/qcat?J/MNRAS/449/3323>

†E-mail: andrey.k.belyaev@gmail.com (AKB); pavel.soldan@mff.cuni.cz (PS)

Table 1. Lithium–helium ion–atom scattering channels, the corresponding molecular states, and the calculated and experimental asymptotic energies.

Channel number	Scattering channels	Molecular states		Asymptotic energies (eV)			
				Calculation ^a	Experiment ^b		
1	Li+(¹ S) + He(¹ S)	$X^1\Sigma^+$		0.000 00	0.000 00		
2	Li(² S) + He+(² S)	$A^1\Sigma^+$	$a^3\Sigma^+$	19.195 39	19.195 67		
3	Li+(¹ S) + He(² S)		$b^3\Sigma^+$	19.819 33	19.819 61		
4	Li+(¹ S) + He(² 1S)	$B^1\Sigma^+$		20.615 48	20.615 77		
5	Li+(¹ S) + He(² 3P)		$c^3\Sigma^+$	$1^3\Pi$	20.963 81	20.964 10	
6	Li(² 2P) + He+(² S)	$C^1\Sigma^+$	$d^3\Sigma^+$	$1^1\Pi$	$2^3\Pi$	21.043 20	21.043 52
7	Li+(¹ S) + He(² 1P)	$D^1\Sigma^+$		$2^1\Pi$		21.217 72	21.218 02

Notes. ^aSoldán & Kraemer (2012); ^bNIST (Kramida et al. 2014) weighted average values.

have been undertaken (Augustovičová et al. 2012; Augustovičová, Kraemer & Soldán 2014a,b).

To get an overview of possible non-adiabatic effects in lithium–helium ion–atom collisions at different excitation levels, a model approach has been applied (Belyaev et al. 2014) to calculate collisional cross-sections and rate coefficients, to compare with the corresponding radiative association reactions. It was shown that for certain collision channels, the non-radiative process dominates over the radiative one at higher temperatures. This underlines its importance in stellar atmospheres. Whereas in previous approaches, the transition probabilities were estimated by means of the Landau–Zener model, the present study uses instead a full quantum description of the non-radiative inelastic processes in lithium–helium ion–atom collisions employing *ab initio* calculated non-adiabatic couplings between the different excited electronic states. The direct comparison between the quantum results and those obtained previously using the semi-classical model approach can provide a useful basis on which the reliability of the model results may be judged. This could be helpful for future studies of larger collision systems, where rigorous quantum calculations become too complex and well beyond realistic computational limits.

In addition, the de-excitation of excited helium atomic states due to collision processes with lithium ions is of particular astrophysical importance (see below). Inclusion of the inelastic non-radiative collisions of excited helium atoms with lithium ions treated in the present study can open new perspectives in modelling stellar atmospheres and the interstellar medium.

2 METHODS

In the present work, a full quantum treatment of inelastic collision processes is employed within the formalism of the standard adiabatic Born–Oppenheimer approach. The problem is handled in two stages: (i) electronic structure calculations of the adiabatic Born–Oppenheimer molecular state potentials and the corresponding non-adiabatic couplings are performed, (ii) followed by a quantum treatment of the non-adiabatic nuclear dynamics.

2.1 Electronic structure

Electronic structure calculations provide fixed-nuclei adiabatic Born–Oppenheimer potential energies, transition dipole moments, and non-adiabatic couplings as functions of the internuclear distance.

However, the electronic structure calculations described in this subsection do not include the spin–orbit operators, the matrix el-

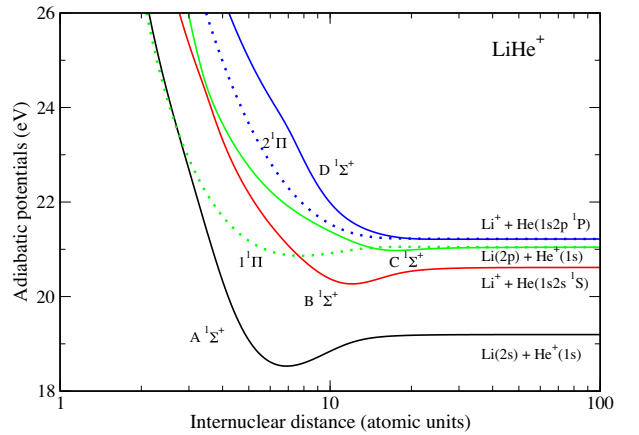


Figure 1. Adiabatic potentials of LiHe^+ for the $^1\Sigma^+$ (solid lines) and $^1\Pi$ (dotted lines) molecular symmetries. The zero-energy potential level corresponds to the asymptotic value of the $\text{LiHe}^+(X^1\Sigma^+)$ state, which is nearly 20 eV below the lowest-excited-state potential and is not shown in the figure.

ements of which are small for the lithium–helium interaction. For this reason, LiHe^+ molecular states are described by the S - Λ symmetries. Since spin–orbit couplings are neglected, we treat non-adiabatic transitions separately between molecular states of each S - Λ symmetry; transitions between states of different symmetries are not considered in the present paper.

For the lithium–helium ion–atom interaction system, 13 electronic molecular states correlating with the seven lowest dissociation limits were previously determined (Soldán & Kraemer 2012; see Table 1). The corresponding adiabatic potentials obtained in previous calculations are plotted here in Figs 1 and 2 using an extended scale to indicate possible coupling areas between the potentials.

The values of non-adiabatic coupling elements $T_{jk}(R) = \langle \varphi_j(r; R) | \partial / \partial R | \varphi_k(r; R) \rangle_r$ between molecular electronic states j and k were calculated employing the finite-difference algorithm implemented in the quantum chemistry program suit MOLPRO (Werner et al. 2010). To calculate the corresponding molecular electronic wavefunctions φ_j and φ_k , we used the multi-reference configuration interaction (MRCI) method with single and double excitations as implemented in MOLPRO (Werner & Knowles 1988; Knowles & Werner 1988). The active space was formed by 12σ , 6π , and 2δ orbitals (the actual calculations were performed within the C_{2v} point-group symmetry, i.e. using the corresponding $14a_1$, $6b_1$, $6b_2$, and

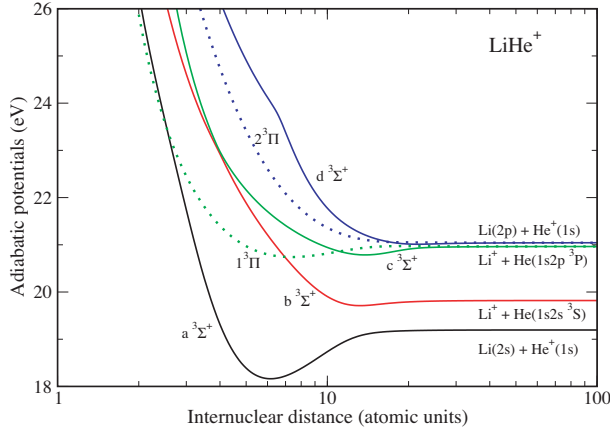


Figure 2. Adiabatic potentials of LiHe^+ for the $^3\Sigma^+$ (solid lines) and $^3\Pi$ (dotted lines) molecular symmetries.

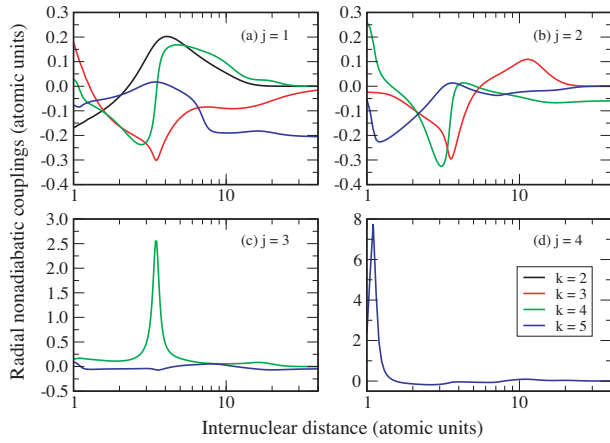


Figure 3. Radial non-adiabatic couplings $T_{jk}(R)$ ($k > j$) for the $^1\Sigma^+$ molecular symmetry as a function of the internuclear distance. The index j is indicated in each panel; the key for the index k is by colour and indicated in the right-hand bottom panel (d). The index 1 corresponds to the $X^1\Sigma^+$ state; 2 to $A^1\Sigma^+$, 3 to $B^1\Sigma^+$, 4 to $C^1\Sigma^+$, and 5 to $D^1\Sigma^+$.

$2a_2$ orbitals). Within these calculations, all electrons were correlated and the $1s$ orbital of lithium was always kept doubly occupied. The initial optimization of molecular orbitals was done with complete active space self-consistent field calculations (Werner & Knowles 1985; Knowles & Werner 1985) with the same active space. The molecular orbitals were expanded in the basis set, which consisted of the helium and lithium atomic basis sets. These contained many Gaussian basis functions optimized for each atom. For helium, the uncontracted valence basis set aug-cc-pCV6Z of van Mourik, Wilson & Dunning (1999) was used without the g and h functions; to increase the basis flexibility for the description of the excited states it was augmented by a set of (4s, 4p, 4d) even-tempered diffuse functions resulting in the (15s, 10p, 9d, 4f) basis set. For lithium, the uncontracted core-valence basis set cc-pCV5Z of Iron, Oren & Martin (2003) was employed without h functions; it was augmented by a set of (5s, 5p, 5d, 5f, 1g) even-tempered diffuse functions resulting in the (19s, 14p, 12d, 10f, 4g) basis set. The resulting curves of the non-adiabatic coupling elements between the singlet Sigma states, triplet Sigma states, and Pi states of LiHe^+ are displayed in Figs 3 and 4, respectively.

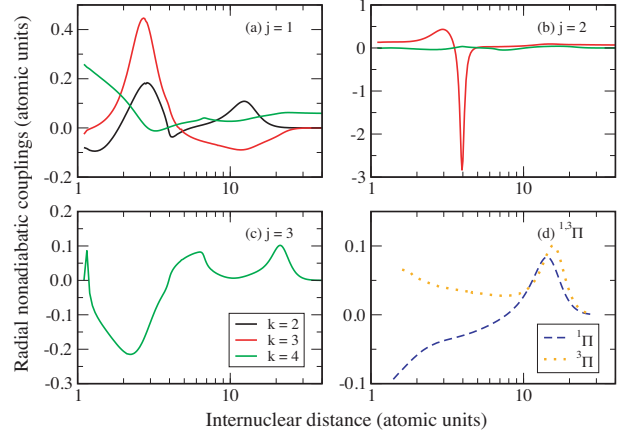


Figure 4. Radial non-adiabatic couplings $T_{jk}(R)$ ($k > j$) for the $^3\Sigma^+$ (solid lines), $^1\Pi$ (dashed lines), and $^3\Pi$ (dotted lines) molecular symmetries as a function of the internuclear distance. The index j is indicated in each panel; the key for the index k is by colour and indicated in the left-hand bottom panel (c). For the molecular states with $^3\Sigma^+$ symmetry the index 1 corresponds to $a^3\Sigma^+$, 2 to $b^3\Sigma^+$, 3 to $c^3\Sigma^+$, and 4 to $d^3\Sigma^+$. The couplings $T_{12}(R)$ within the $^1\Pi$ and $^3\Pi$ symmetries are plotted in the right-hand bottom panel (d).

There are a couple of obvious features in these figures that can be immediately interpreted here before treating the non-adiabatic dynamics calculations. The sharp peaks in some of the plots are clear indications of strong couplings between adjacent potentials. In panel (c) of Fig. 3, the peak at a distance of $\sim 4.5 a_0$ represents apparently the non-adiabatic avoided-crossing region between the $B^1\Sigma^+$ and $C^1\Sigma^+$ states as can be seen in Fig. 1.¹ This should hold also for the peak in panel (d) of the same figure, which occurs at a very short distance just slightly larger than $1 a_0$, actually outside the range shown in Fig. 1. It indicates the extent of the coupling between the $C^1\Sigma^+$ and $D^1\Sigma^+$ states in this short distance range. The corresponding explanation applies for the peak in panel (b) of Fig. 4, indicating a strong coupling between $b^3\Sigma^+$ and $c^3\Sigma^+$ states at a distance around $4 a_0$. Finally, the broad peaks in panel (d) of Fig. 4 identify the couplings between the Π states in Figs 1 and 2.

2.2 Non-adiabatic nuclear dynamics

The non-adiabatic nuclear dynamics is studied quantum mechanically by means of the multi-electron reprojection method (Belyaev 2010) within the standard adiabatic Born–Oppenheimer approach based on the molecular state representation (see e.g. Mott & Massey 1949; Macías & Riera 1982; Bransden & McDowell 1992).

As is well known, the form of the dynamical equations in this approach is different for different electron coordinate origins (Belyaev, Dalgarno & McCarroll 2002). To reach the simplest and the standard form of the coupled channel equations (Grosser, Menzel & Belyaev 1999; Belyaev et al. 2001, 2002; Belyaev 2010) the electronic structure calculations described above have been carried out with the electron coordinate origin at the centre of nuclear mass. In this case, according to the fundamental rules of the standard adiabatic approach, the asymptotic values of the non-adiabatic radial couplings are (Macías & Riera 1982; Grosser et al. 1999; Belyaev

¹ 1 atomic unit of length $\equiv 1 \text{ au} \equiv 1 a_0 = 5.291 772 1092 \times 10^{-11} \text{ m}$.

et al. 2001, 2002; Belyaev 2010):

$$T_{jk}(\infty) \equiv \left\langle j \left| \frac{\partial}{\partial R} \right| k \right\rangle (\infty) = \gamma_k \frac{m}{\hbar^2} [U_j(\infty) - U_k(\infty)] \langle j | d_z^{at} | k \rangle, \quad (1)$$

$\langle j | d_z^{at} | k \rangle$ being the atomic transition dipole moment, m the electron–nuclei reduced mass, and $U_j(R)$ an adiabatic potential for a molecular state j . The scalar factors γ_k depend on which nucleus an active electron is bound on to in the asymptotic region; in the present case, they are

$$\gamma_k = -\frac{M_{\text{He}}}{M_{\text{Li}} + M_{\text{He}}}, \quad (2)$$

if excitation takes place on Li, and

$$\gamma_k = -\frac{M_{\text{Li}}}{M_{\text{Li}} + M_{\text{He}}}, \quad (3)$$

if excitation takes place on He; M_{Li} and M_{He} being the masses for Li and He, respectively.

It is seen from equation (1) that some non-adiabatic radial coupling matrix elements calculated with the electron origin at the centre of nuclear mass have non-zero asymptotic values. The electronic structure calculations described in the previous subsection clearly show non-zero asymptotic non-adiabatic couplings.

As discussed in many papers (see e.g. Macías & Riera 1982; Grosser et al. 1999; Belyaev et al. 2001, 2002; Belyaev 2010, and references therein), non-vanishing asymptotic couplings are a fundamental feature of the Born–Oppenheimer approach. Choosing another electron origin does not remove non-zero asymptotic terms coupling different channels in the nuclear dynamical equations due to additional mixed-derivative terms in the total Hamiltonian, see Belyaev et al. (2002), and thus the centre of nuclear mass is the most natural choice for the electron origin.

For the five $\text{LiHe}^+(^1\Sigma^+)$ molecular states treated, there are three non-zero asymptotic non-adiabatic radial couplings; see Fig. 3. These are the couplings between molecular states that asymptotically correspond to transitions between atomic states with non-zero transition dipole moments (optically allowed transitions), for example, the coupling between $A^1\Sigma^+$ and $C^1\Sigma^+$ molecular states that asymptotically correspond to the $\text{Li}(2^2\text{S}) + \text{He}^+(2^2\text{S})$ and $\text{Li}(2^2\text{P}) + \text{He}^+(2^2\text{S})$ interactions. Between the four $^3\Sigma^+$ molecular states treated, there are two non-zero asymptotic couplings; see Fig. 4. The asymptotic couplings are relatively small, between 0.05 and 0.2 au by absolute value, but even small non-vanishing asymptotic couplings provide non-adiabatic transitions between molecular states at arbitrarily large internuclear separations and at any total angular momentum quantum numbers. This creates a problem that is twofold: (i) convergence with respect to the upper limit for numerical integration of the coupled-channel equations cannot be reached and a non-adiabatic transition probability is calculated with some uncertainty, which can be much larger than the probability itself, and (ii) calculations of inelastic cross-sections do not converge because a cross-section is calculated as a sum over an infinite number of partial waves, so a cross-section calculation may even result in an unphysical infinite value (Belyaev 2010). Thus, special care must be taken for non-zero asymptotic couplings.

In fact, the problem of non-vanishing asymptotic non-adiabatic couplings is part of a more general problem, the so-called molecular-state problem (Belyaev 2010). In other words, the molecular Jacobi

coordinates, used for a fixed-nuclei molecular-state representation, are not suitable for description of the free motion of atomic particles in the asymptotic region. The result is that a single molecular-state wavefunction (a function of the internuclear distance) does not properly describe a single asymptotic incoming or outgoing wavefunction, which is a function of interatomic distance. Thus, additional care must be taken regarding asymptotic wavefunctions.

The present study uses the reprojection method (Belyaev 2010), which takes account of about both non-zero asymptotic couplings and correct asymptotic wavefunctions. The reprojection method allows one to treat collisions with an arbitrary number of electrons and does not require any additional quantum chemical calculations; only adiabatic potentials and non-adiabatic couplings with the electron coordinate origin at the centre of nuclear mass are needed, which come from quantum chemical calculations. Within the reprojection method, the scattering matrix, S -matrix, is defined on the exact asymptotic incoming and outgoing wavefunctions and determined from numerical solutions of coupled channel equations with non-zero asymptotic non-adiabatic couplings by means of projecting correct asymptotic scattering wavefunctions on the molecular-state wavefunctions in the asymptotic region; non-zero asymptotic non-adiabatic couplings determine the coefficients of such projection (Grosser et al. 1999; Belyaev et al. 2001; Belyaev 2010). Non-adiabatic transitions between molecular states are kept in the asymptotic region, but the reprojection procedure removes transitions between scattering (atomic) states at large distances. Finally, the reprojection method leads to convergence of both (i) non-adiabatic transition probabilities with respect to the upper limit for integration of the coupled-channel equations and (ii) inelastic cross-sections with respect to the number of partial waves treated (Belyaev 2010).

The central point of the reprojection method is a determination of a correct S -matrix defined on exact asymptotic wavefunctions. Having the S -matrix known, an inelastic cross-section $\sigma_{if}(E)$ for a transition $i \rightarrow f$ is calculated as usual as a sum over a total angular momentum quantum number J ,

$$\sigma_{if}(E) = \frac{\pi \hbar^2 p_i^{\text{stat}}}{2\mu E} \sum_{J=0}^{\infty} |S_{if}(J, E)|^2 (2J+1), \quad (4)$$

where p_i^{stat} is the statistical probability for the population of the initial molecular state i , E is a collision energy, and μ a reduced nuclear mass.

3 RESULTS AND DISCUSSIONS

3.1 Non-radiative inelastic cross-sections

The ground molecular state, which asymptotically corresponds to the $\text{Li}^+(1\text{S}) + \text{He}(1^1\text{S})$ interaction, has $^1\Sigma^+$ symmetry; see Table 1. The quantum chemical calculations indicate that this state has observable non-adiabatic couplings with excited states (Fig. 3 a), but the energy gaps between the ground-state potential and excited-state potentials are so big (of the order of 20 eV) that non-adiabatic transition probabilities from and to the ground molecular state are extremely small. The test quantum dynamical calculations confirm this fact. Thus, inelastic non-radiative collision processes involving the $\text{Li}^+(1\text{S}) + \text{He}(1^1\text{S})$ channel have negligible cross-sections and rate coefficients and can be disregarded.

The partial cross-sections for non-radiative inelastic endothermic processes in lithium–helium ion–atom collisions for different initial

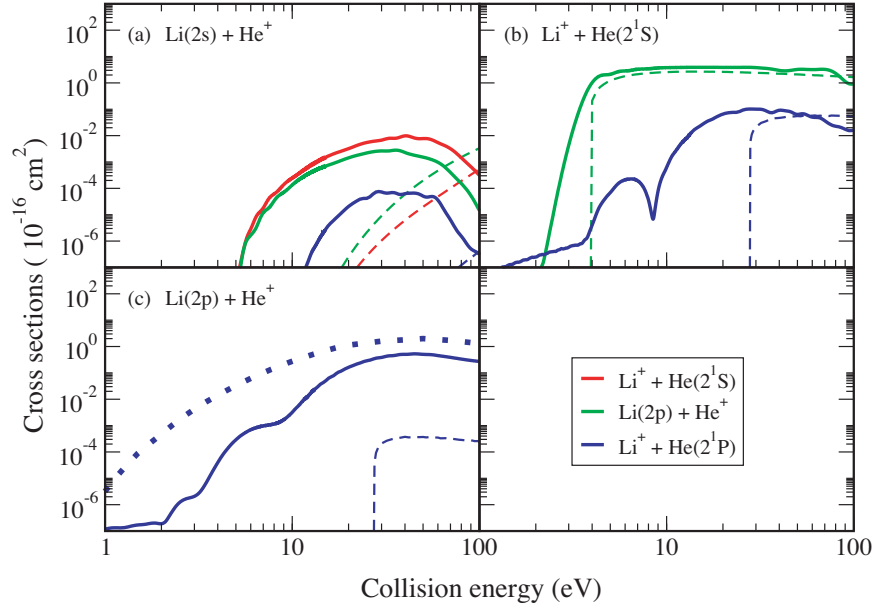


Figure 5. Non-radiative inelastic partial cross-sections within the singlet symmetry for different initial states. The initial collisional channel is indicated in each panel. The key for the final channels is common to all panels and shown in the right-hand bottom panel. Solid lines plot the quantum cross-sections for $^1\Sigma^+$, the dotted line the quantum cross-sections for $^1\Pi$ and the dashed lines the model cross-sections (Belyaev et al. 2014) for $^1\Sigma^+$. The statistical probability factors for the initial channels are taken into account in the cross-sections.

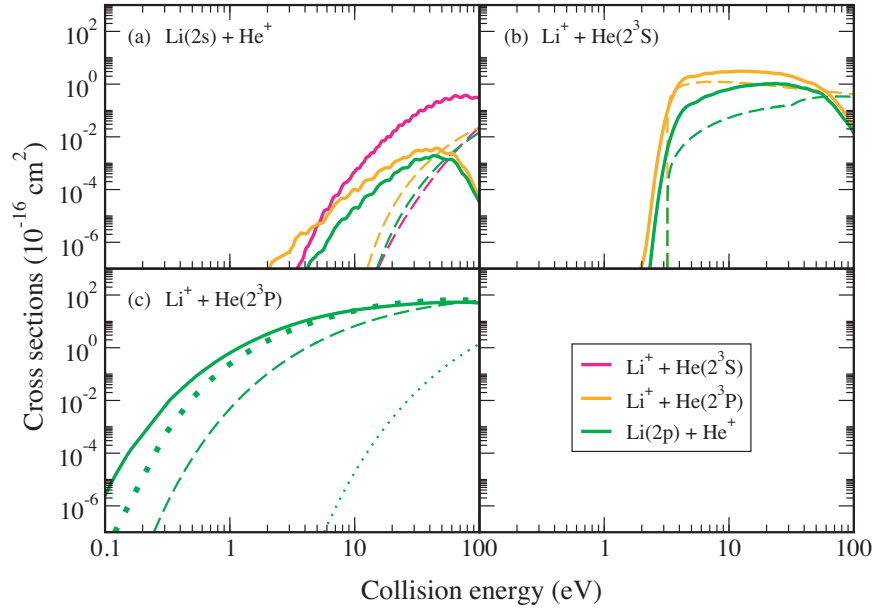
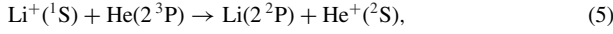


Figure 6. Non-radiative inelastic partial cross-sections within the triplet symmetry for different initial states. The initial collisional channel is indicated in each panel. The key for the final channels is common to all panels and shown in the right-hand bottom panel. Solid lines depict the quantum cross-sections for $^3\Sigma^+$, the thick dotted line the quantum cross-sections for $^3\Pi$, the dashed lines the model cross-sections (Belyaev et al. 2014) for $^3\Sigma^+$ and the thin dotted line the model cross-sections for $^3\Pi$. The statistical probability factors for the initial channels are taken into account in the cross-sections.

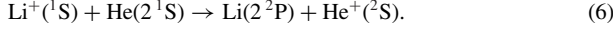
and final channels treated within the singlet, $^1\Sigma^+$ and $^1\Pi$, and the triplet, $^3\Sigma^+$ and $^3\Pi$, symmetries are shown in Figs 5 and 6, respectively, by thick solid and dotted lines. The cross-sections for the inverse (exothermic) processes can be inferred using detailed balance.

It is seen that the partial non-radiative cross-sections can attain experimentally measurable values. For different initial channels, the maximal values of the partial cross-sections vary from 10^{-2} to 53.5 \AA^2 . The cross-sections for the transitions between triplet states have typically larger values compared to those for the singlet

system. The highest cross-section, up to 53.5 \AA^2 , corresponds to the charge exchange process:



within the triplet system. Within the singlet system the highest cross-section is 3.9 \AA^2 and corresponds to the charge exchange process:



This is a result of different electronic structures of the $^1\Sigma^+$ and $^3\Sigma^+$ systems (see the previous subsection). Process (6) is determined by non-adiabatic transitions in the well-localized avoided crossing between the $B^1\Sigma^+$ and $C^1\Sigma^+$ states around the internuclear distance $R \approx 3.5 a_0$ (see Fig. 1); this is a Landau–Zener type of non-adiabatic region. Process (5) is determined by transitions in the broad non-adiabatic region around $R \approx 15 a_0$, see Figs 2 and 4. Note that the latter corresponds to the small splitting between two nearly parallel adiabatic potential energy curves of the $c^3\Sigma^+$ and $d^3\Sigma^+$ states; this is a Demkov type of non-adiabatic region. Within the triplet system, there are also non-adiabatic regions of the Landau–Zener type, e.g. between $b^3\Sigma^+$ and $c^3\Sigma^+$ states around $R \approx 4 a_0$ (see Fig. 2), but the non-adiabatic region around $R \approx 15 a_0$ provides the highest cross-section.

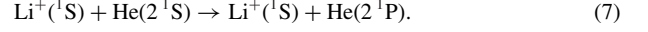
In principle, the calculated quantum cross-sections are indicative of different reaction mechanisms. Indeed, the electronic structure data, in particular, the non-adiabatic couplings, show that there are short- and long-range non-adiabatic regions leading to different energy dependences of the partial cross-sections. To clear up the influence of short- and long-range interactions, we have performed additional test dynamical calculations including only the short-range couplings, roughly with couplings at $R < 6 a_0$, and including only the long-range couplings, roughly at $R > 6 a_0$. These calculations clearly show which regions are responsible for which partial inelastic processes. In particular, these test calculations confirm that process (5) is determined by the long-range couplings, while process (6) is determined by the short-range couplings. In some cases, quantum interference between the short- and long-range couplings is important.

Another important feature is that short-range couplings take place at the repulsive parts of the adiabatic potential energy curves (see Figs 1 and 2). Therefore, for the short-range couplings to yield non-adiabatic transitions, the collision energy should be relatively high. On the other hand, at low collision energies, quantum tunnelling can also provide non-adiabatic transitions but with smaller values for probabilities. In contrast to this, in the long-range non-adiabatic regions, the adiabatic potentials are nearly flat, so that they are accessible at any collision energies above energy thresholds. These two features provide different values and different behaviour of the energy dependence of the cross-sections.

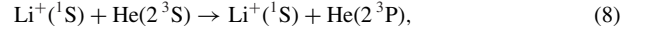
Many collisional channels produce molecular states only of singlet or triplet symmetry, but there are a couple of channels that create molecular states of both singlet and triplet symmetries, namely, the $\text{Li}(2^2\text{S}) + \text{He}^+(^2\text{S})$ and $\text{Li}(2^2\text{P}) + \text{He}^+(^2\text{S})$ channels; see Table 1. For this reason, the cross-section for the excitation process $\text{Li}(2^2\text{S}) + \text{He}^+(^2\text{S}) \rightarrow \text{Li}(2^2\text{P}) + \text{He}^+(^2\text{S})$, as well as for its inverse process, should be obtained as a sum over the corresponding partial cross-sections in the singlet and triplet symmetries.

The same Figs 5 and 6 compare the quantum cross-sections (thick solid and dotted curves) with ones obtained by Belyaev et al. (2014) using the model approach (thin dashed and dotted lines). The approach is based on the branching-probability-current method (Belyaev 2013), which requires information only about adi-

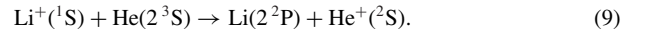
abatic potential energies and assumes that the Landau–Zener model is applicable. It is seen that for some partial processes the model cross-sections are in a very good agreement with the quantum ones, while for some partial processes there are marked deviations. The agreement is observed for the processes that are determined by well-localized avoided crossing non-adiabatic regions between adjacent molecular states. Within the $^1\Sigma^+$ system, the examples are the charge exchange process (6) and the excitation process:



Within the $^3\Sigma^+$ system, they are the charge exchange process (5), as well as the excitation process:



and the charge exchange process:



It is worth emphasizing that all these processes, (5)–(9), are those with the largest values of non-radiative cross-sections and, hence, they are of most interest in astrophysical applications.

It is seen that the deviations of the model cross-sections from the quantum ones occur typically at low collision energies. There are several main sources of such deviations: (i) quantum tunnelling, (ii) quantum interference, and (iii) non-adiabatic couplings between non-adjacent molecular states. Quantum tunnelling affects low-energy cross-sections substantially when a non-adiabatic region is located at a short-range repulsive part of the corresponding adiabatic potentials. As predicted by Belyaev et al. (2014), the quantum tunnelling effect can increase non-adiabatic transition probabilities and lower the energy thresholds compared to the model treatment. The examples are the non-adiabatic region between the $B^1\Sigma^+$ and $C^1\Sigma^+$ states around $R \approx 3.5 a_0$, which determines the process (6), and the non-adiabatic region between the $b^3\Sigma^+$ and $c^3\Sigma^+$ states around $R \approx 4 a_0$; see Figs 1 and 2. These avoided crossing regions are located energetically high above the asymptotic potential energies of the corresponding channels. In the model treatment, the system should have high enough collision energies to make non-adiabatic transitions. In the quantum treatment, quantum tunnelling allows the system to make non-adiabatic transitions at lower collision energies providing larger values of corresponding cross-sections at low energies.

Quantum interference can also yield deviations between the model and the quantum cross-sections, when several non-adiabatic regions exist between the same pair of molecular states, since the model approach does not take phase into account and the quantum treatment does. The existence of several non-adiabatic regions between the same pair of molecular states is clearly seen in Figs 3 and 4.

It has been shown by Belyaev et al. (2012) that non-adiabatic couplings between non-adjacent states can provide one of the mechanisms for non-radiative inelastic processes. In the present case, it is seen that some of the non-adiabatic couplings between non-adjacent molecular states have marked values, see Figs 3 and 4, and this also affects the quantum cross-sections.

As mentioned above, the LiHe^+ electronic structure provides Landau–Zener and the Demkov type of non-adiabatic regions. In contrast to the Landau–Zener type, the Demkov-type non-adiabatic regions do not have a local minima for adiabatic splittings. Within the $^3\Pi$ symmetry, this region was not included in the model calculation, because the latter is essentially based on a local minimum of adiabatic splittings. Within the $^1\Pi$ symmetry, a local minimum was observed, because the situation is between the Landau–Zener and

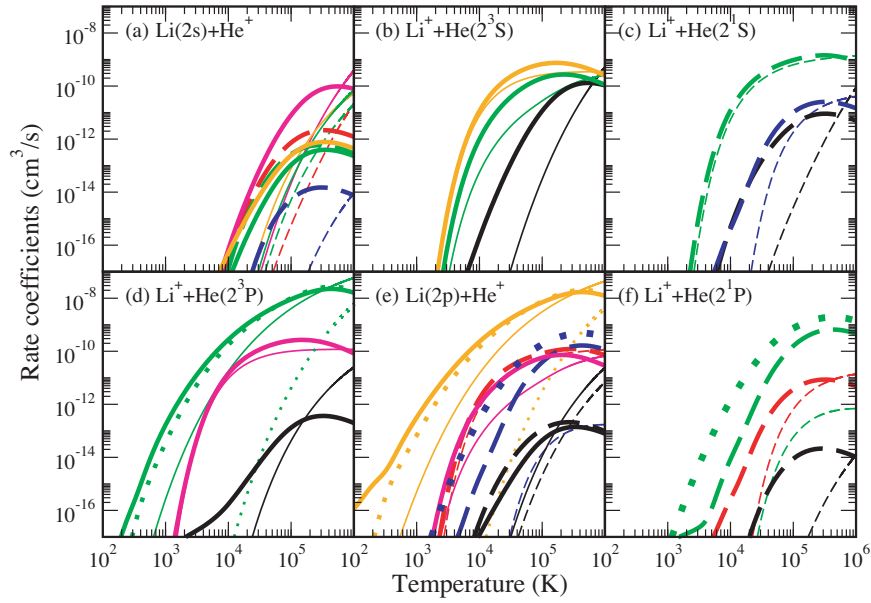


Figure 7. Partial inelastic rate coefficients for different non-radiative processes in lithium–helium ion–atom collisions as a function of the temperature. The initial collisional channel is indicated in each panel. The key for final channels is common to all panels and is labelled by colours: black lines correspond to $\text{Li}(2^2\text{S}) + \text{He}^+(2^2\text{S})$, red lines to $\text{Li}^+(1^1\text{S}) + \text{He}(2^1\text{S})$, green to $\text{Li}(2^2\text{P}) + \text{He}^+(2^2\text{S})$, blue to $\text{Li}^+(1^1\text{S}) + \text{He}(2^1\text{P})$, magenta to $\text{Li}^+(1^1\text{S}) + \text{He}(2^3\text{S})$ and orange to $\text{Li}^+(1^1\text{S}) + \text{He}(2^3\text{P})$. Dashed lines depict rate coefficients within the $^1\Sigma^+$ system, solid lines within the $^3\Sigma^+$ system, thick dotted lines within the $^1\Pi$ system and medium dotted lines within the $^3\Pi$ system. Thick lines show the present quantum results and thin lines the results of the model approach.

the Demkov types (it is instead the so-called Nikitin type), so the model calculation underestimated the corresponding cross-section. The present full quantum calculation handles this situation.

3.2 Inelastic rate coefficients

Inelastic rate coefficients $K_{if}(T)$ are determined from a cross-section as usual

$$K_{if}(T) = \sqrt{\frac{8}{\pi \mu (k_B T)^3}} \int_0^\infty \sigma_{if}(E) E \exp\left(-\frac{E}{k_B T}\right) dE, \quad (10)$$

where k_B is the Boltzmann constant and T the temperature.

Partial non-radiative inelastic rate coefficients for the different initial collisional channels obtained in the present quantum calculations are shown in Fig. 7. This includes all partial processes, endothermic and exothermic, starting from the six lowest (but not the ground) scattering channels; see Table 1. Following the energy dependence of the corresponding inelastic cross-sections shown in Figs 5 and 6, the rate coefficients of all these partial processes increase with increasing temperature.

It is seen in the figure that the largest values of the partial rate coefficients, with values up to $2.7 \times 10^{-8} \text{ cm}^3 \text{ s}^{-1}$, occur for the charge exchange process (5) and its inverse process. These partial processes take place in the $^3\Sigma^+$ and the $^3\Pi$ molecular symmetries, where the highest value of the rate coefficient corresponds to the process in the $^3\Pi$ symmetry. The other largest partial rate coefficients correspond to the charge exchange $\text{Li}^+(1^1\text{S}) + \text{He}(2^1\text{P}) \rightarrow \text{Li}(2^2\text{P}) + \text{He}^+(1^1\text{S})$ within the $^1\Pi$ symmetry and process (6) within the $^1\Sigma^+$ symmetry with maximum values of $1.9 \times 10^{-9} \text{ cm}^3 \text{ s}^{-1}$ and $1.4 \times 10^{-9} \text{ cm}^3 \text{ s}^{-1}$, respectively. Apart from these three most efficient partial depopulations, the rate coefficients of the remaining processes in Fig. 7 are much smaller. The two most efficient partial depopulation processes of Fig. 7 contribute more than 95 per cent

to the corresponding total values plotted in Fig. 8. Here the total rate coefficients for depopulation of $\text{Li}^+(1^1\text{S}) + \text{He}(2^3\text{P})$ collisions reach a maximum of $5 \times 10^{-8} \text{ cm}^3 \text{ s}^{-1}$ and for depopulation of $\text{Li}(2^2\text{P}) + \text{He}^+(2^2\text{S})$ collisions a maximal rate of $4 \times 10^{-8} \text{ cm}^3 \text{ s}^{-1}$.

Fig. 7 also compares the present quantum rate coefficients with the previous model results (Belyaev et al. 2014). The model calculation can obviously describe general trends in agreement with the quantum treatment, in some cases even nearly identical results are obtained. On the other hand, the present quantum study provides more accurate cross-sections and rate coefficients than the model approach, which is based on the Landau–Zener approximation.

The tabulated data for the calculated rate coefficients as a function of the temperature are available upon request and accessible online at the CDS. Each file contains the following information: column 1 gives the temperature T , other columns give the total (Table 2) and the partial (Table 3) rate coefficients for channel numbers defined in Table 1.

3.3 Comparison of radiative and non-radiative inelastic processes

Fig. 8 shows the temperature dependence of the total quantum non-radiative rate coefficients for all the initial channels considered in this study. They are compared with the available total radiative rate coefficients (Augustovičová et al. 2012, 2014a,b).

The comparison shows that the rate coefficients have a very different temperature dependence. Whereas the rate coefficients of the non-radiative processes increase rapidly with increasing temperature, the rate coefficients of the radiative processes drop slowly for high temperatures. This is in agreement with earlier findings (Zygelman et al. 1989; Belyaev et al. 2014). Critical temperatures at which the dominance of the two processes change are different for individual collision channels. In $\text{Li}(2^2\text{S}) + \text{He}^+(2^2\text{S})$ collisions,

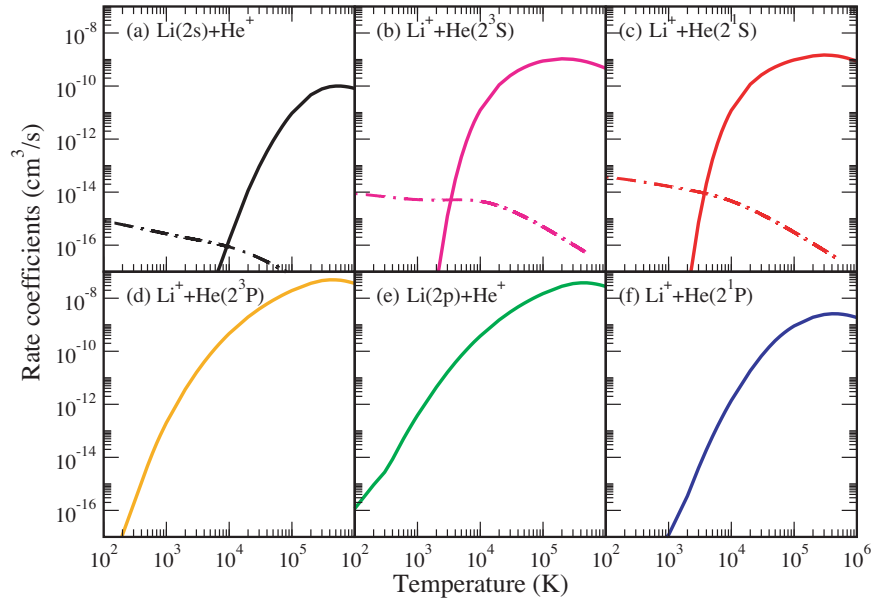


Figure 8. Total rate coefficients for non-radiative and radiative inelastic processes in lithium–helium ion–atom collisions for different initial channels as a function of the temperature. The initial collisional channel is indicated in each panel. Solid lines show total quantum rate coefficients for non-radiative processes and dot-dashed lines for radiative processes with the same initial channels. The data for radiative depopulation are taken from Augustovičová et al. (2012, 2014a,b).

for example, the non-radiative processes dominate over the radiative one at temperatures above $T \approx 9200$ K, for $\text{Li}^+(^1\text{S}) + \text{He}(2^1\text{S})$ collisions above $T \approx 3700$ K, and for $\text{Li}^+(^1\text{S}) + \text{He}(2^3\text{S})$ above $T \approx 3400$ K; the critical temperature becomes lower with increasing excitation of the He state.

Total rate coefficients for the radiative processes, as for the non-radiative processes (as shown above), are mostly determined by a single dominant depopulation process for each initial channel. The final main product channels are generally different for the two processes. For example, radiative association from the initial $\text{Li}(2^2\text{S}) + \text{He}^+(^2\text{S})$ collisional channel leads exclusively to the formation of the $(X^1\Sigma^+)$ electronic ground state of LiHe^+ (Augustovičová et al. 2012), which correlates asymptotically with $\text{Li}^+(^1\text{S}) + \text{He}(1^1\text{S})$, whereas according to Fig. 7 in the non-radiative process the dominating depopulation goes to the $\text{Li}^+(^1\text{S}) + \text{He}(2^3\text{S})$ channel, i.e. with He in its first excited state. Similar comparisons also hold for the other two initial collisional channels for which radiative rate coefficients are available for comparison: (i) depopulations via radiative processes lead in all cases to products that are energetically lower than the dominant product channels obtained for the corresponding non-radiative depopulation processes and (ii) the dominant non-radiative depopulation processes themselves are all endothermic.

4 CONCLUSION

In the present paper a full quantum study of non-radiative inelastic processes in lithium–helium ion–atom collisions is presented. The study uses the results of previous accurate *ab initio* electronic structure calculations of the 13 lowest-lying electronic molecular states of LiHe^+ for the $^1\Sigma^+$, $^3\Sigma^+$, $^1\Pi$, and $^3\Pi$ symmetries. These states adiabatically correlate to the seven lowest dissociation limits (the scattering channels) reaching from $\text{Li}^+(^1\text{S}) + \text{He}(1^1\text{S})$ to $\text{Li}^+(^1\text{S}) + \text{He}(2^1\text{P})$. The accurate adiabatic potential energies were

calculated together with radial non-adiabatic coupling matrix elements between these states. Based on these electronic structure calculations, the quantum non-adiabatic nuclear dynamics are studied by the reprojection method, which takes into account all non-adiabatic couplings, including those with non-vanishing asymptotic values. The accurate energy dependence of the cross-sections and the accurate temperature dependence of the rate coefficients for all partial processes between the scattering channels are calculated.

The computed non-radiative rate coefficients are compared with available radiative rate coefficients. It is shown that the temperature dependence for the non-radiative and the radiative processes are different: the non-radiative rate coefficients increase with increasing temperature, while the radiative rate coefficients decrease. This means that for the depopulation of the same scattering channel, the non-radiative processes dominate at high temperatures, whereas at low temperatures the radiative processes are typically the more efficient ones, such as in molecular clouds or in other cold astrophysical environments. The critical temperature separating radiative and non-radiative reactions is shown to be different for each individual initial scattering channel. From the results obtained here, it can be speculated that this temperature decreases with increasing excitation level of He. It can thus be concluded that for the depopulation of the $\text{Li}^+(^1\text{S}) + \text{He}(2^3\text{P})$ and the $\text{Li}(2^2\text{P}) + \text{He}^+(^2\text{S})$ channels, for which the present calculations obtain the largest rate coefficients, this bordering temperature should be still lower, probably even below 1000 K. That the non-radiative processes are more efficient at higher temperatures (which corresponds to the corresponding cross-sections dominating at high energies) together with the above finding that in these non-radiative processes the dominating partial depopulations are essentially endothermic, supports the expectation that non-radiative inelastic collisional processes become particularly important in high-temperature astrophysical environments.

One of the purposes of the present study is to compare the quantum results with those obtained previously in the model approach

(Belyaev et al. 2014). Detailed comparisons of the cross-sections are shown in Figs 5 and 6 and of the corresponding rate coefficients in Fig. 7, and the main sources for the deviations of the model approach from the quantum results are discussed. Some of the quantum effects responsible for the deviations were already predicted from an analysis of the relevant potential functions (Belyaev et al. 2014). Apart from systems where the quantum effects become essential, the comparison shows that the model approach can provide in many cases information about the main features in non-radiative collision processes. It can therefore be applied as a guide in more complex systems where detailed quantum calculations become impossible.

Among the reactions considered here, the depopulation reactions of excited helium states are of particular astrophysical interest. The consequences of the formation of metastable states of helium have long been discussed (Struve, Wurm & Henyey 1939) and collisional effects in these states were shown to be significant in high-temperature planetary nebulae (Clegg 1987). In particular, $\text{He}(2^3\text{S})$ with its extremely long lifetime of almost two hours (Hodgman, Dall & Byron 2009) plays an important role in astrophysical environments. It is assumed that it can be populated either by recombination of He^+ (cosmic-ray ionized) or by collisional excitations from the neutral ground state by thermal electrons (Zeldovich, Novikov & Sunyaev 1966). With its long lifetime it can act as an efficient base for the $\text{He I } \lambda 10830$ or the $\text{He I } \lambda 3889$ absorption lines, which are due to $(2s \rightarrow 2p)$ or $(2s \rightarrow 3p)$ excitations, respectively, in the metastable state. Observations of the $\lambda 10830$ absorption line have actually been reported for the Orion nebula (Boyce & Ford 1966) and for the Broad Absorption Line Quasar (BALQSO) (Leighly, Dietrich & Barber 2011); the $\lambda 3889$ line was seen towards ζ Ophiuchi (Galazutdinov & Krelowski 2012). Many of these absorption lines have also been used as probes of the cosmic-ray ionization rate in the interstellar medium (Indriolo et al. 2009). $\text{He}(2^3\text{P})$ with a lifetime of $\tau = 5.66$ ms comes into play as a product in $\lambda 10830$ absorption. It is also populated to a smaller extent in the recombination process from He^+ where it primarily undergoes spontaneous transfer to the $\text{He}(2^3\text{S})$ ground state of the triplet manifold or it can radiate in a two-photon decay down to the $\text{He}(1^1\text{S})$ ground state. Apart from radiative depopulation of the metastable states by cosmic radiation, depopulation can also take place via collisions in a denser photo-ionized plasma. Previous studies of the depopulation of helium metastable states in radiative association reactions with protons or lithium ions as collision partners (Augustovičová et al. 2012, 2014a,b) indicate that the processes with lithium ions are generally more efficient than with protons.

Generalizing the findings of the present study, at high temperatures the non-radiative reactions calculated here are, by far, especially dominant over the radiative reaction. This may open new perspectives in attempts to model the processes in stellar atmospheres. Inclusion of the non-radiative inelastic collision reactions of helium states with lithium ions might eventually improve the corresponding reaction schemes.

ACKNOWLEDGEMENTS

The authors thank Prof. Ronald McCarroll for careful reading of the manuscript. AKB and DSR thank S. A. Yakovleva for her help in calculations. AKB gratefully acknowledges support from the Russian Ministry for Education and Science and from the Max-Planck Institute for Astrophysics at Garching (Germany). PS and LA acknowledge support from the Czech Science Foundation - GAČR (Grant no. P209/15-10267S).

REFERENCES

- Asplund M., Lambert D. L., Nissen P. E., Primas F., Smith V. V., 2006, *ApJ*, 664, 229
- Audouze J., Silk J., 1989, *ApJ*, 342, L5
- Augustovičová L., Špirko V., Kraemer W. P., Soldán P., 2012, *Chemical Phys. Lett.*, 531, 59
- Augustovičová L., Kraemer W. P., Soldán P., 2014a, *ApJ*, 782, 46
- Augustovičová L., Kraemer W. P., Soldán P., 2014b, *J. Quant. Spectrosc. Radiative Transfer*, 148, 27
- Belyaev A. K., 2010, *Phys. Rev. A*, 82, 060701 (R)
- Belyaev A. K., 2013, *Phys. Rev. A*, 88, 052704
- Belyaev A. K., Egorova D., Grosser J., Menzel T., 2001, *Phys. Rev. A*, 64, 052701
- Belyaev A. K., Dalgarno A., McCarroll R., 2002, *J. Chemical Phys.*, 116, 5395
- Belyaev A. K., Barklem P. S., Spielfiedel A., Guitou M., Feautrier N., Rodionov D. S., Vlasov D. V., 2012, *Phys. Rev. A*, 85, 032704
- Belyaev A. K., Augustovičová L., Soldán P., Kraemer W. P., 2014, *A&A*, 565, A106
- Bovino S., Stoecklin T., Gianturco F. A., 2010, *ApJ*, 708, 1560
- Bovino S., Tacconi M., Gianturco F. A., Galli D., Palla F., 2011, *ApJ*, 731, 107
- Boyce P. B., Ford W. K., 1966, *PASP*, 78, 163
- Bransden B. H., McDowell M. R. C., 1992, *Charge Exchange and the Theory of Ion-Atom Collisions*. Clarendon, Oxford
- Clegg R. E. S., 1987, *MNRAS*, 229, 31
- Dalgarno A., Kirby K., Stancil P., 1996, *ApJ*, 458, 397
- Dubrovich V. K., 1993, *Astron. Lett.*, 19, 53
- Galazutdinov G. A., Krelowski J., 2012, *MNRAS*, 422, 3457
- Gianturco F., Gori-Giorgi P., 1997, *ApJ*, 479, 560
- González-Hernández J. I. et al., 2009, *A&A*, 505, L13
- Grosser J., Menzel T., Belyaev A. K., 1999, *Phys. Rev. A*, 59, 1309
- Hodgman S. S., Dall R. G., Byron L. J., 2009, *Phys. Rev. Lett.*, 103, 053002
- Howk J. C., Lehner N., Fields B. D., Mathews G., 2012, *Nature*, 489, 121
- Indriolo N., Hobbs L. M., Hinkle K. H., McCall B. J., 2009, *ApJ*, 703, 2131
- Iocco F., Magnano G., Miele G., Pisanti O., Serpico P., 2009, *Phys. Rep.*, 472, 1
- Iron M. A., Oren M., Martin J. M. L., 2003, *Molecular Phys.*, 101, 1345
- Israeli G., 2012, *Nature*, 37, 489
- Knowles P. J., Werner H.-J., 1985, *Chemical Phys. Lett.*, 115, 259
- Knowles P. J., Werner H.-J., 1988, *Chemical Phys. Lett.*, 145, 514
- Kramida A., Ralchenko Y., Reader J., NIST ASD Team 2014, NIST Atomic Spectra Database, version 5.2. See <http://physics.nist.gov/asd>
- Leighly K., Dietrich M., Barber S., 2011, *ApJ*, 728, 94
- Macías A., Riera A., 1982, *Phys. Rep.*, 90, 299
- Maoli R., Melciorri F., Tosti D., 1994, *ApJ*, 425, 372
- Mathews G. J., Alcock C. R., Fuller G. M., 1990, *ApJ*, 349, 449
- Mott N. F., Massey H. S. W., 1949, *The Theory of Atomic Collisions*. Clarendon, Oxford
- Puy D., Signore M., 1996, *A&A*, 305, 371
- Puy D., Signore M., 1998, *New Astron.*, 3, 27
- Reeves H., 1998, in Audouze J., Tran Than Van J., eds, *Dark Matter. Gif sur Yvette: Editions Frontieres*, p. 287
- Signore M. et al., 1994, *ApJS*, 92, 535
- Soldán P., Kraemer W. P., 2012, *Chemical Phys.*, 393, 135
- Stancil P. C., Dalgarno A., 1997, *ApJ*, 490, 76
- Struve O., Wurm K., Henyey L., 1939, *Proc. Natl. Acad. Sci. USA*, 25, 67
- van Mourik T., Wilson A. K., Dunning T. H., Jr, 1999, *Molecular Phys.*, 96, 529
- Werner H.-J., Knowles P. J., 1985, *J. Chemical Phys.*, 82, 5053
- Werner H.-J., Knowles P. J., 1988, *J. Chemical Phys.*, 89, 5803
- Werner H.-J. et al., 2010, *Molpro*, version 2010.2. <http://www.molpro.net>
- Zeldovich Y. B., Novikov I. D., Sunyaev R. A., 1966, *Astron. Circular USSR*, No.371
- Zygelman B., Dalgarno A., Kimura M., Lane N. F., 1989, *Phys. Rev. A*, 40, 2340

SUPPORTING INFORMATION

Additional Supporting Information may be found in the online version of this article:

partial_rates.dat

ReadMe.txt

total_rates.dat (<http://mnras.oxfordjournals.org/lookup/suppl/doi:10.1093/mnras/stv391/-/DC1>).

Please note: Oxford University Press are not responsible for the content or functionality of any supporting materials supplied by the authors. Any queries (other than missing material) should be directed to the corresponding author for the article.

This paper has been typeset from a $\text{\TeX}/\text{\LaTeX}$ file prepared by the author.

POTENTIAL MICROWAVE PROBES OF THE
PROTON-TO-ELECTRON MASS RATIO AT VERY
HIGH REDSHIFTS

Bibliographic record of the attached publication:

Augustovičová, L., P. Soldán, W. P. Kraemer, and V. Špirko (2014). “Potential microwave probes of the proton-to-electron mass ratio at very high redshifts.” In: *Monthly Notices of the Royal Astronomical Society* 439, pp. 1136–1139.
DOI: [10.1093/mnras/stu060](https://doi.org/10.1093/mnras/stu060).

Potential microwave probes of the proton-to-electron mass ratio at very high redshifts

L. Augustovičová,¹ P. Soldán,^{1*} W. P. Kraemer² and V. Špirko³

¹Department of Chemical Physics and Optics, Faculty of Mathematics and Physics, Charles University in Prague, Ke Karlovu 3, CZ-12116 Prague 2, Czech Republic

²Max-Planck Institute of Astrophysics, Postfach 1371, D-85741 Garching, Germany

³Institute of Organic Chemistry and Biochemistry, v.v.i., Academy of Sciences of the Czech Republic, Flemingovo nám. 2, CZ-16010 Prague 6, Czech Republic

Accepted 2014 January 8. Received 2013 December 23; in original form 2013 November 15

ABSTRACT

Recently, a stringent constraint on the change in the proton-to-electron mass ratio at a redshift of 0.89 has been established using theoretical predictions and radio observations of the methanol molecule. To get an insight at deeper look-back times, accurate determinations of variations of the proton-to-electron mass ratio at higher redshifts are needed. We propose a microwave probe of the proton-to-electron mass ratio employing the primordial molecular ions H_2^+ , D_2^+ , and He_2^+ considering redshifts from 0 to 70. Microwave rovibronic transitions of these ions, which are presented here, crucially exhibit high or very high sensitivities to a variation of the proton-to-electron mass ratio and could in principle be detected by the Atacama Large Millimeter/submillimeter Array.

Key words: molecular data – molecular processes.

1 INTRODUCTION

Critical investigations of the possibility that fundamental constants of nature could depend on time and space in the evolving Universe become more possible with the fast developing current experimental techniques (Uzan 2003). Attempts were made recently to establish constraints on the change of the proton-to-electron mass ratio $\mu = m_p/m_e$. Earlier strict constraints (Flambaum & Kozlov 2007; Murphy et al. 2008; Henkel et al. 2009; Kanekar 2011), obtained from inversion spectra of ammonia, were improved very recently by Bagdonaite et al. (2013a,b) to $\Delta\mu/\mu = (0.0 \pm 1.0) \times 10^{-7}$ (at the redshift $z = 0.89$) using theoretical predictions (Jansen et al. 2011; Levshakov, Kozlov & Reimers 2011) and new PKS 1830–211 radio observations for the methanol molecule.

The limit obtained there allows for a cosmological look-back time of roughly half of the age (7 billion years) of the Universe. In order to get an insight at deeper look-back times accurate determinations of μ at higher redshifts are needed. Apparently, information from the deepest look-back times can be expected using signals from the primordial molecules or molecular ions consisting of hydrogen, helium, and possibly lithium. So far all such monitorings were performed exclusively for the hydrogen molecule (see Bagdonaite et al. 2012, and references therein). However, as the pertinent spectra are not recorded with adequate accuracy, it appears worthwhile to probe also other molecular systems. The prospects of such monitorings

seem to be improved dramatically after launching the ALMA (Atacama Large Millimeter/submillimeter Array) project.

It turns out that the ALMA facilities can largely cover the frequency region of the microwave components of the H_2^+ and D_2^+ ($A^2\Sigma_u^+ \leftrightarrow X^2\Sigma_g^+$) and He_2^+ ($A^2\Sigma_g^+ \leftrightarrow X^2\Sigma_u^+$) rovibronic spectra measured by Carrington, Shaw & Taylor (1995a), Carrington, Pyne & Knowles (1995b), Carrington (1996), and also the forbidden electric dipole spectrum of the H_2^+ ($X^2\Sigma_g^+ \rightarrow X^2\Sigma_g^+$) predicted by Bunker & Moss (2000). Therefore, at least in principle, H_2^+ , D_2^+ , and He_2^+ appear as fairly suitable probes of the early expansion of the Universe. The use of H_2^+ , D_2^+ , and He_2^+ in astronomical searches is facilitated by the fact that these molecules can be studied theoretically at a very high accuracy level and that the corresponding highly accurate experimental data are available allowing a critical comparison and eventually adjustment of the theoretical findings.

The purpose of this study is to generate accurate estimates, so far unavailable, of the mass sensitivities of all the H_2^+ , D_2^+ , and He_2^+ $A \leftrightarrow X$ transitions, which may be of astronomical relevance and could be detected by the ALMA facility. So far the most distant galaxies were detected at redshifts of $z = 8.6$ (Lehnert et al. 2010) and $z = 9.6$ (Zheng et al. 2012). Because, the first observable star was most likely formed 30 million years after the big bang (at redshift $z \sim 65$; see Naoz, Noter & Barkana 2006), the calculations presented here are performed for the redshift range of $0 < z < 70$.

2 METHODS

It should be noted that the H_2^+ , HD^+ , and D_2^+ cations were considered as potential probes for temporal variations of the

* E-mail: pavel.soldan@mff.cuni.cz (PS)

proton-to-electron mass ratio already by Hilico et al. (2000, 2001); Karr & Hilico (2006). Treating these cations as three-body Coulomb systems, these authors have evaluated extremely accurate energies and pertinent mass sensitivities of the $N = 0, 1$, and 2 ro-vibrational states of the ground electronic states. To get these characteristics for the excited states, apparently, one can perform similar calculations and get the desired results with even higher accuracy (Ishikawa, Nakashima & Nakatsuji 2012). These calculations, however, are not feasible in the case of He_2^+ . Therefore, we have decided to adopt an indirect approach, in which we rely on less quantitative ab initio potential energy functions and their morphing by fitting to extremely accurate experimental data. Namely, we rely on the following ro-vibrational Hamiltonian (Herman & Asgharian 1966; Bunker & Moss 1977)

$$H_{\text{eff}} = T_{\text{kin}} + V_{\text{rot}}(R) + V_{\text{ad}}(R) + V'(R), \quad (1)$$

where

$$T_{\text{kin}} = -\frac{\hbar^2}{2M_{\text{red}}} \frac{d}{dR} f_v(R) \frac{d}{dR} \quad (2)$$

$$V_{\text{rot}}(R) = \frac{\hbar^2}{2M_{\text{red}}} f_r(R) \frac{N(N+1)}{R^2}, \quad (3)$$

$$f_x(R) = 1 + \mu g_x(R) \quad (x = v, r), \quad (4)$$

M_{red} is the appropriate atomic reduced mass, V_{ad} is the ‘adiabatic’ part of the molecular potential energy curve (assumed to include the Born–Oppenheimer, adiabatic, relativistic, quantum electro-dynamical, and residual retardation terms) and the terms $V'(R)$, $g_r(R)$ and $g_v(R)$ account for non-adiabatic effects. The so-called vibrational, $g_v(R)$, and rotational, $g_r(R)$, g -factors are assumed to acquire their ab initio values and the effective potential energy function $V_{\text{eff}}(R) = V_{\text{ad}}(R) + V'(R)$ is assumed to be determinable by fitting to the available experimental data. As the non-adiabatic functions $g_v(R)$ and $g_r(R)$ are not available for all the studied states, and also because the spectral data pertaining the excited states are too limited to allow for their detailed fitting, we have decided to simplify the above Hamiltonian by assuming that these functions can be approximated in the following way:

$$g_x(R) \doteq g_x^0 M_{\text{red}} \frac{(R - R_e)}{R^2} \quad (x = v, r), \quad (5)$$

where the constants g_x^0 are fitting parameters.

To respect the fact that the available experimental data are rather scarce, especially for the excited electronic states, we have decided to perform our fittings in the framework of the Jenč Reduced Potential Curve approach (Jenč 1983; Jenč et al. 1993), which appears as a suitable tool for a quantitative morphing of accurate ab initio potential energy curves in terms of only very few morphing parameters (Patkowski, Špirko & Szalewicz 2009).

In the case of H_2^+ , the reduced potential curves were constructed using the Born–Oppenheimer potential curves of Bishop & Wetmore (1973) and Peek (1965) and the adiabatic corrections of Bishop & Wetmore (1973) and Fabri et al. (2009). The potentials were interpolated using the cubic splines and extrapolated in the same way as in Schwenke (2001). In the case of He_2^+ , the reduced potential curves were constructed using the Born–Oppenheimer potential curves V_4 of Carrington et al. (1995b) and the adiabatic corrections of Xie, Poirier & Gellene (2005). The potentials were interpolated using the cubic splines and extrapolated using the expressions given in Xie et al. (2005). The corresponding transition dipole moments published very recently by Augustovičová et al. (2013) were used.

3 RESULTS AND DISCUSSION

In order to get an insight on the effects induced by the approximation defined by equation (5), we have first performed test calculations for HD, for which there are all needed data available in the literature (Ulivi, Natale & Inguscio 1991; Piszczatowski et al. 2009; Pachucki & Komasa 2010; Kassi & Campargue 2011; Dickenson et al. 2013). The results show practically quantitative agreement between the experimental data and their fitted counterparts (see online Supplementary Information).

The first step of the actual calculations consisted in the fitting of the theoretical ro-vibrational energies of Hilico et al. (2000) and Moss (1993), the experimental microwave data of Carrington et al. (1995b), and vibronic data of Raunhardt et al. (2008) for H_2^+ (D_2^+) and He_2^+ , respectively. The resulting potentials were in turn used to evaluate the sought sensitivities K_μ defined via

$$\frac{\Delta v}{\nu} = K_\mu \frac{\Delta \mu}{\mu}, \quad (6)$$

where Δv is the frequency shift of the probed transition induced by the variation of μ .

For a transition with frequency $\nu = (E_{v'N'} - E_{v''N''})/h$, we also calculated its line strength

$$S_{v'N', v''N''} = \mathcal{S}_{N', N''} |\langle \psi_{v'N'} | d_z | \psi_{v''N''} \rangle|^2 \quad (7)$$

and the corresponding Einstein coefficient

$$A_{v'N', v''N''} = \frac{64 \pi^4 \nu^3}{(4\pi\epsilon_0) 3h c^3} \frac{S_{v'N', v''N''}}{(2N' + 1)}, \quad (8)$$

where the only non-zero Hönl–London coefficients are $\mathcal{S}_{N', N'+1} = N' + 1$ and $\mathcal{S}_{N', N'-1} = N'$ and c is the speed of light in vacuum. For these calculations, we used our radiative-association code (Augustovičová et al. 2012) modified to accommodate bound-bound transitions.

Not surprisingly, as it can be surmised from the theoretical analysis of DeMille et al. (2008), the calculated sensitivities acquire magnitudes, which are comparable with their ‘record-breaking-methanol’ counterparts (see Tables 1–4 and their complete versions in the online Supplementary Information). Interestingly, the largest sensitivity constant evaluated in this study, $K = -407$, was obtained for the ($v_A = 0, N_A = 3 \leftarrow v_X = 26, N_X = 4$) transition of D_2^+ .

4 CONCLUSION

The predicted sensitivities are obtained here with positive or negative values which allows single molecular analyses without any reference molecules. Since the corresponding transitions have also fairly large line strengths, they could be promising candidates for astrophysical observations. On the other hand, although the H_2^+ , D_2^+ , and He_2^+ cations are assumed to play central roles in the primordial chemistry (Lepp, Stancil & Dalgarno 2002), they have not yet been detected in extraterrestrial environments and it has actually been argued that their detection would be a very difficult task (Shuter et al. 1986; Howells & Kennedy 1991). However, the radiative lifetimes of the H_2^+ states involved in the microwave transitions (with an upper radiative lifetime limit of 1000 s) are shorter than the time-scale estimated for the destructions of H_2^+ by collisional reactions with H_2 or H (Shuter et al. 1986; Howells & Kennedy 1991). H_2^+ ions formed in the upper levels of the discussed transitions may thus be expected to undergo spontaneous emission before being destroyed by chemical reactions, especially in low-density plasmas. It has further been reported that the Cassini–Huygens facility provided a

Table 1. The $A \leftrightarrow X$ microwave transitions of H_2^+ .

v', N'	v'', N''	ν_{fit}	ν_{exp}	S	A	K_μ
$A \rightarrow X$						
0, 0	18, 1	514 956.6		3.073	2.038×10^{-1}	31.669
0, 1	18, 0	645 722.3		2.484	1.083×10^{-1}	26.982
0, 1	18, 2	352 014.8		7.493	5.293×10^{-2}	39.683
0, 2	18, 1	593 778.1		4.452	9.055×10^{-2}	27.400
0, 2	18, 3	156 614.7	156 633	15.406	5.751×10^{-3}	65.568
$X \rightarrow A$						
19, 0	0, 1	52 907.5	52 895	8.884	6.400×10^{-4}	-17.594
19, 1	0, 0	96 431.6	96 432	5.268	7.659×10^{-4}	-5.739
19, 1	0, 2	17 610.2	17 610	24.113	2.135×10^{-5}	-29.230

Note. Frequencies ν are in MHz, line strengths S in D^2 , and Einstein coefficients A in s^{-1} ; the ν_{exp} column contains data from Carrington et al. (1995a).

Table 2. Forbidden electric dipole $X \rightarrow X$ microwave transitions of H_2^+ .

v', N'	v'', N''	ν_{fit}	ν_{theor}	S	A	K_μ
19, 1	19, 0	15 664.4	15 679.0	4.80×10^{-3}	0.3×10^{-8}	25.220
19, 1	18, 2	420 586.7	420 536.4	3.90×10^{-4}	4.7×10^{-6}	31.939
19, 0	18, 1	595 723.9	595 616.8	1.12×10^{-4}	1.15×10^{-5}	25.783
19, 1	18, 0	714 294.2	714 183.7	1.63×10^{-4}	9.6×10^{-6}	23.642

Note. Frequencies ν are in MHz, line strengths S in D^2 , and Einstein coefficients A in s^{-1} ; the ν_{theor} , S , and A columns contain data from Bunker & Moss (2000).

Table 3. The $A \leftrightarrow X$ microwave transitions of D_2^+ .

v', N'	v'', N''	ν_{fit}	ν_{exp}	S	A	K_μ
$A \rightarrow X$						
0, 0	26, 1	162 124.4	162 165.2	5.918	1.225×10^{-2}	59.209
0, 1	26, 0	215 438.7	215 484	5.595	9.060×10^{-3}	46.855
0, 1	26, 2	109 628.6	109 672.8	12.859	2.744×10^{-3}	78.142
0, 2	26, 1	211 802.5	211 847	11.477	1.060×10^{-2}	45.139
0, 2	26, 3	48 013.2	48 064.3	21.876	2.353×10^{-4}	145.883
0, 3	26, 2	189 639.2	189 681	18.329	8.676×10^{-3}	44.871
0, 4	26, 3	152 839.8	152 896.5	26.819	5.169×10^{-3}	45.453
1, 0	27, 1	11 117.9	11 138.1	22.896	1.529×10^{-5}	97.619
1, 1	27, 0	25 783.0	25 755.4	16.676	4.629×10^{-5}	50.245
$X \rightarrow A$						
26, 4	0, 3	11 978.9	11 928.0	35.183	3.265×10^{-6}	-406.966
27, 0	0, 1	118 294.6	118 296.7	2.291	1.843×10^{-3}	-10.337
27, 1	0, 2	95 215.2	95 222.5	4.826	6.746×10^{-4}	-10.400

Note. Frequencies ν are in MHz, line strengths S in D^2 , and Einstein coefficients A in s^{-1} ; the ν_{exp} column contains data from Carrington et al. (1995a).

strong evidence that H_2^+ is present in the Saturn's magnetosphere (Thomsen et al. 2010). Besides these arguments the unprecedented detection potential of the ALMA installation is finally decisive for the observation of the proposed microwave transitions.

Apart from the homonuclear diatomics H_2^+ , D_2^+ , and He_2^+ other primordial species could in principle also be chosen for the purpose of this study. For instance the deuterated species HD, H_2D^+ , or HD_2^+ could be promising candidates for astronomical observations due to the fact that they have actually been detected in extraterrestrial sources (see Caselli et al. 2003). Also HeH^+ , which has recently tentatively been identified in one of the highest redshift quasars with $z = 6.4$ (Zinchenko, Dubrovich & Henkel 2011) and which has always been expected to be abundant in interstellar environments, could be thought of in this context. It has to be stressed however that

the corresponding sensitivity coefficients K_μ of the ro-vibrational transitions between low-lying vibrational levels of a single electronic state (e.g. $X \rightarrow X$) of these ions are by orders of magnitude smaller than the sensitivity coefficients of the ro-vibronic $A \leftrightarrow X$ transitions, which are accessible for the homonuclear diatomics selected here.

ACKNOWLEDGEMENTS

LA acknowledges funding from the Grant Agency of the Charles University in Prague – GAUK (Grant no. 550112). VS appreciates support of the Ministry of Education of the Czech Republic – MŠMT (Grant KONTAKT-II-LH1 1022).

Table 4. The $A \leftrightarrow X$ microwave transitions of He_2^+ .

v', N'	v'', N''	ν_{fit}	ν_{exp}	S	A	K_{μ}
$A \rightarrow X$						
0, 0	22, 1	384 695.5		2.083	5.761×10^{-2}	33.071
0, 2	22, 1	438 939.4		3.984	3.271×10^{-2}	28.883
0, 2	22, 3	264 152.2		7.020	1.255×10^{-2}	42.473
0, 4	22, 3	382 670.8		8.177	2.473×10^{-2}	29.102
0, 4	22, 5	101 406.5	101 460	14.770	8.275×10^{-4}	81.484
1, 0	22, 1	603 065.1		0.095	1.016×10^{-2}	21.176
1, 0	23, 1	49 649.4	49 646	4.689	2.765×10^{-4}	44.371
1, 2	22, 1	622 318.2		0.142	3.309×10^{-3}	20.528
1, 2	22, 3	447 531.0		0.164	1.421×10^{-3}	25.287
1, 2	23, 1	68 902.5	68 924	6.261	1.946×10^{-4}	32.036
1, 2	23, 3	8926.8	8949	25.107	1.577×10^{-6}	144.214
$X \rightarrow A$						
23, 1	0, 0	168 720.1	168 709	1.628	1.265×10^{-3}	-12.770
23, 1	0, 2	114 476.3	114 539	3.932	9.562×10^{-4}	-18.432
23, 3	0, 2	174 452.0		3.577	1.314×10^{-3}	-6.822
23, 3	0, 4	55 933.4	55 880	9.287	1.108×10^{-4}	-19.792

Note. Frequencies ν are in MHz, line strengths S in D^2 , and Einstein coefficients A in s^{-1} ; the ν_{exp} column contains data from Carrington et al. (1995b).

REFERENCES

- Augustovičová L., Špirko V., Kraemer W. P., Soldán P., 2012, *Chem. Phys. Lett.*, 531, 59
- Augustovičová L., Špirko V., Kraemer W. P., Soldán P., 2013, *A&A*, 553, A42
- Bagdonaite J., Murphy M. T., Kaper L., Ubachs W., 2012, *MNRAS*, 421, 419
- Bagdonaite J., Daprà M., Jansen P., Bethlem H. L., Ubachs W., Muller S., Henkel C., Menten K. M., 2013a, *Phys. Rev. Lett.*, 111, 231101
- Bagdonaite J., Jansen P., Henkel C., Bethlem H. L., Menten K. M., Ubachs W., 2013b, *Science*, 339, 46
- Bishop D. M., Wetmore R. W., 1973, *Mol. Phys.*, 26, 145
- Bunker P. R., Moss R. E., 1977, *Mol. Phys.*, 33, 417
- Bunker P. R., Moss R. E., 2000, *Chem. Phys. Lett.*, 316, 266
- Carrington A., 1996, *Science*, 274, 1327
- Carrington A., Shaw A. M., Taylor S. M., 1995a, *J. Chem. Soc. Faraday Trans.*, 91, 3725
- Carrington A., Pyne C. H., Knowles P. J., 1995b, *J. Chem. Phys.*, 102, 5979
- Caselli P., van der Tak F. F. S., Ceccarelli C., Bacmann A., 2003, *Chem. Phys. Lett.*, 403, L37
- DeMille D., Sainis S., Sage J., Bergeman T., Kotochigova S., Tiesinga E., 2008, *Phys. Rev. Lett.*, 100, 043202
- Dickenson G. D., Niu M. L., Salumbides E. J., Komasa J., Eikema K. S. E., Pachucki K., Ubachs W., 2013, *Phys. Rev. Lett.*, 110, 193601
- Fabri C., Czako G., Tasi G., Császár A. G., 2009, *J. Chem. Phys.*, 130, 134314
- Flambaum V. V., Kozlov M. G., 2007, *Phys. Rev. Lett.*, 98, 240801
- Henkel C. et al., 2009, *A&A*, 500, 725
- Herman R. M., Asgharian A., 1966, *J. Mol. Spectrosc.*, 19, 305
- Hilico L., Billy N., Grémaud B., Delande D., 2000, *Eur. Phys. J. D*, 12, 449
- Hilico L., Billy N., Grémaud B., Delande D., 2001, *J. Phys. B: At. Mol. Opt. Phys.*, 34, 491
- Howells M. H., Kennedy R. A., 1991, *Chem. Phys. Lett.*, 184, 521
- Ishikawa A., Nakashima H., Nakatsuji H., 2012, *Chem. Phys.*, 401, 62
- Jansen P., Xu L.-H., Kleiner I., Ubachs W., Bethlem H. L., 2011, *Phys. Rev. Lett.*, 106, 100801
- Jenč F., 1983, *Adv. At. Mol. Phys.*, 19, 265
- Jenč F., Brandt B. A., Špirko V., Bludský O., 1993, *Phys. Rev. A*, 48, 1319
- Kanekar N., 2011, *ApJ*, 728, L12
- Karr J. P., Hilico L., 2006, *J. Phys. B: At. Mol. Opt. Phys.*, 39, 2095
- Kassi S., Campargue A., 2011, *J. Mol. Spectrosc.*, 267, 36

- Lehnert M. D. et al., 2010, *Nature*, 467, 940
- Lepp S., Stancil P. C., Dalgarno A., 2002, *J. Phys. B: At. Mol. Opt. Phys.*, 35, R57
- Levshakov S. A., Kozlov M. G., Reimers D., 2011, *ApJ*, 738, 26
- Moss R. E., 1993, *Mol. Phys.*, 80, 1541
- Murphy M. T., Flambaum V. V., Muller S., Henkel C., 2008, *Science*, 320, 1611
- Naoz S., Noter S., Barkana R., 2006, *MNRAS*, 373, L98
- Pachucki K., Komasa J., 2010, *Phys. Chem. Chem. Phys.*, 12, 9188
- Patkowski K., Špirko V., Szalewicz K., 2009, *Science*, 326, 1382
- Peek J. E., 1965, *J. Chem. Phys.*, 43, 3004
- Piszczatowski K., Lach G., Przybytek M., Komasa J., Pachucki K., Jeziorski B., 2009, *J. Chem. Theory Comput.*, 5, 3039
- Raunhardt M., Schäfer M., Vanhaecke N., Merkt F., 2008, *J. Chem. Phys.*, 128, 164310
- Schwenke D. W., 2001, *J. Chem. Phys.*, 114, 1693
- Shuter W. H. L., Williams D. R. W., Kulkarni S. R., Heiles C., 1986, *ApJ*, 306, 255
- Thomsen M. F. et al., 2010, *J. Geophys. Res.: Space Phys.*, 115, A10220
- Uliivi L., Natale P. D., Inguscio M., 1991, *ApJ*, 378, L29
- Uzan J.-P., 2003, *Rev. Mod. Phys.*, 75, 403
- Xie J., Poirier B., Gellene G., 2005, *J. Chem. Phys.*, 122, 184310
- Zheng W. et al., 2012, *Nature*, 489, 406
- Zinchenko I., Dubrovich V., Henkel C., 2011, *MNRAS*, 415, L78

SUPPORTING INFORMATION

Additional Supporting Information, containing complete transition tables and details of the potential fitting procedure, may be found in the online version of this article:

(<http://mnras.oxfordjournals.org/lookup/suppl/doi:10.1093/mnras/stu060/-/DC1>).

Please note: Oxford University Press is not responsible for the content or functionality of any supporting materials supplied by the authors. Any queries (other than missing material) should be directed to the corresponding author for the article.

This paper has been typeset from a $\text{\TeX}/\text{\LaTeX}$ file prepared by the author.

POTENTIAL MICROWAVE PROBES OF THE
PROTON-TO-ELECTRON MASS RATIO AT VERY
HIGH REDSHIFTS (SUPPLEMENTARY MATERIAL)

Bibliographic record of the attached publication:

Augustovičová, L., P. Soldán, W. P. Kraemer, and V. Špirko (2014).
“Potential microwave probes of the proton-to-electron mass ratio
at very high redshifts (supplementary material).” In: *Monthly No-*
tices of the Royal Astronomical Society, pp. 1–8.
DOI: [10.1093/mnras/stu060](https://doi.org/10.1093/mnras/stu060).

Potential microwave probes of the proton-to-electron mass ratio at very high redshifts (supplementary material)

Lucie Augustovičová, Pavel Soldán

Charles University in Prague, Faculty of Mathematics and Physics,
Department of Chemical Physics and Optics, Ke Karlovu 3, 12116 Prague 2, Czech Republic

Wolfgang P. Kraemer

Max-Planck-Institute of Astrophysics, Postfach 1371, 85741 Garching, Germany

Vladimír Špirko

Institute of Organic Chemistry and Biochemistry, v.v.i.,
Academy of Sciences of the Czech Republic, Flemingovo nám.2, 160 10 Prague 6, Czech Republic

(Dated: December 23, 2013)

Reduced Potential Curve Framework

The actual determination of the sought potential function is performed in two steps. In the first, a 'reference' *ab initio* potential energy function $V(R)$ is used to generate its reduced form $u(\rho)$, which is defined as follows (for details see Refs. [1, 2])

$$u(\rho) = V(R)/D_e, \quad (1)$$

where D_e is the depth of $V(R)$, and the reduced variable ρ is related to R via the expression

$$\rho(R) = \frac{R - \rho_{ij} [1 - \exp(-R/\rho_{ij})]}{R_e - \rho_{ij} [1 - \exp(-R/\rho_{ij})]}. \quad (2)$$

Here R_e is the position of the potential minimum and ρ_{ij} satisfies the transcendental equation

$$\rho_{ij} = \frac{R_e - \sqrt{\kappa D_e / k_e}}{1 - \exp(-R_e / \rho_{ij})}, \quad (3)$$

where

$$\kappa = (d^2V/dR^2)_{R=R_e} \quad (4)$$

is the so-called 'universal' reduced force constant (it is recommendable to fix it at the value which provides $\rho_{ij} \approx 1$).

In the second step, the reducing procedure is reverted by expressing $V(R)$ as the function of $u(\rho)$, namely

$$V(R) = D_e u(\rho), \quad (5)$$

with $\rho \equiv \rho(R)$ defined, for instance, by

$$\rho(R) = \frac{R - \rho_{ij} [1 - \alpha \exp(-\beta(1 + \gamma R)R/\rho_{ij})]}{R_e - \rho_{ij} [1 - \alpha \exp(-\beta(1 + \gamma R)R/\rho_{ij})]}, \quad (6)$$

and assuming $D_e, R_e, \rho_{ij}, \alpha, \beta$, and γ as fitting parameters. Apparently, the proposed reduced potential is a six-parameter empirical potential.

Comparisons

To get an insight on the effects induced by the approximation defined by Eq. (2), we have firstly performed our calculations for HD, for which there are all needed data available in the literature. It can be seen in TABLES S.I and S.II that the role of the non-adiabatic functions g_v and g_r in the given context is rather negligible.

A practically quantitative agreement between the exact values of the relative sensitivities of the $v \rightarrow v$ transitions and their approximate (RPC) counterparts evaluated in this study for the ground electronic state of H_2^+ is illustrated in FIG. S.1.

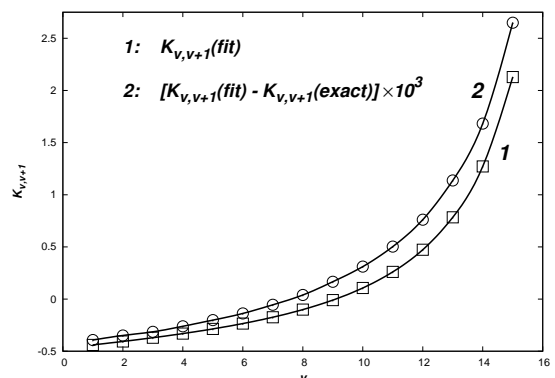


FIG. S.1. Dependence of the relative sensitivity, $K_{v,v+1}$, of the $v \rightarrow v+1$ transition frequencies on the proton-to-electron mass ratio. $K_{v,v+1}(fit)$ and $K_{v,v+1}(exact)$ were obtained from the present (RPC) fitting and numerically exact (non-adiabatic) calculations [8], respectively.

TABLE S.I. The RPC parameters of HD in its ground electronic state.^a

Method	R_e , Å	ρ_{ij} , Å	D_e , cm ⁻¹	α	β	γ
M1 ^b	0.74164855	0.018107093	38295.7535(36405.4974)	1	1	0
M2 ^c	0.74161292	0.018136730	38292.7059(36402.4450)	1	1	0

^aThe appropriate reduced potential curve was constructed using V_{eff} , g_v and g_r taken from Refs. [3, 4] and the 'correcting' RPC parameters α , β and γ were fixed at their reference values. The fitted data were taken from Refs. [5–7]. The values given in parentheses are the D_0 dissociation energies (the best literature value [3] reads 36405.7828(10)). ^bCalculated using ab initio g-factor functions. ^cCalculated using approximation given by Eq.(5) of the main part of the paper.

TABLE S.II. Comparison of the calculated and experimental frequencies (in cm⁻¹) and sensitivity constants of HD in its ground electronic state.^a

v', J'	v'', J''	ν_{exp}	ν_{M2}	K_{M2}	ν_{M1}	K_{M1}
0, 0	0, 1	89.227950(5) ^b	89.2280	-.9878	89.2280	-.9878
0, 1	0, 2	177.84172(16) ^b	177.8413	-.9843	177.8414	-.9844
0, 2	0, 3	265.24116(17) ^b	265.2398	-.9787	265.2399	-.9787
0, 3	0, 4	350.85295(12) ^b	350.8520	-.9708	350.8523	-.9708
0, 4	0, 5		434.1472	-.9609	434.1478	-.9609
0, 5	0, 6	514.656(1) ^b	514.6456	-.9491	514.6466	-.9491
0, 6	0, 7	591.9327(3) ^b	591.9260	-.9355	591.9275	-.9355
0, 0	1, 0	3632.16054(24) ^c	3632.1602	-.4752	3632.1632	-.4752
0, 5	2, 4	6576.8960	6576.9049	-.4179	6576.9037	-.4179
0, 2	2, 1	6901.4014	6901.4001	-.4479	6901.4004	-.4479
0, 1	2, 0	6997.6494	6997.6476	-.4558	6997.6480	-.4558
0, 0	2, 1	7168.4697	7168.4695	-.4679	7168.4698	-.4679
0, 1	2, 2	7241.8497	7241.8491	-.4721	7241.8492	-.4721
0, 2	2, 3	7306.4839	7306.4836	-.4749	7306.4835	-.4749
0, 3	2, 4	7361.9037	7361.9041	-.4763	7361.9037	-.4763
0, 4	2, 5	7407.7134	7407.7142	-.4762	7407.7138	-.4762
0, 5	2, 6	7443.5983	7443.5988	-.4748	7443.5986	-.4748
0, 6	2, 7	7469.3298	7469.3283	-.4718	7469.3287	-.4718
0, 7	2, 8	7484.7654	7484.7612	-.4675	7484.7625	-.4675
0, 8	2, 9	7489.8463	7489.8416	-.4618	7489.8445	-.4618
0, 1	2, 1	7079.2422	7079.2414	-.4614	7079.2417	-.4614
0, 2	2, 2	7064.0077	7064.0078	-.4592	7064.0078	-.4592
0, 3	2, 3	7041.2418	7041.2438	-.4559	7041.2435	-.4559
0, 4	2, 4	7011.0492	7011.0521	-.4515	7011.0514	-.4515
0, 0	2, 2	7331.0778	7331.0771	-.4784	7331.0772	-.4784
0, 1	2, 3	7484.3246	7484.3250	-.4870	7484.3248	-.4870
0, 2	2, 4	7627.1438	7627.1439	-.4937	7627.1437	-.4937
0, 3	2, 5	7758.5671	7758.5662	-.4986	7758.5661	-.4986
0, 4	2, 6	7877.7461	7877.7460	-.5015	7877.7464	-.5015

^aIf not stated otherwise, the data taken from Ref. [7]. ^bData taken from Ref. [5]. ^cData taken from Ref. [6].

[1] F. Jenč, Adv. At. Mol. Phys. **19**, 265 (1983).
[2] F. Jenč, B. A. Brandt, V. Špirko, and O. Bludský, Phys.Rev. A **48** 1319 (1993).
[3] K.Piszczatowski, G. Lach, M. Przybytek, J. Komasa, K. Pachucki, and B. Jeziorski, J. Chem. Theory Comput. **5**, 3039 (2009).

[4] K. Pachucki and J. Komasa, Phys. Chem. Chem. Phys. **12**, 9188 (2010).
[5] L. Ulivi, P. De Natale, and M. Inguscio, Astrophys. J. **378**, L29 (1991).
[6] G. D. Dickenson, M. L. Niu, E. J. Salumbides, J. Komasa, K. S. E. Eikema, K. Pachucki, and W. Ubachs, Phys.

TABLE S.III. The RPC parameters and effective g -factors of the $X^2\Sigma_g^+$ (electronic ground) and $A^2\Sigma_u^+$ (electronic excited) states of the H_2^+ cation.^a

Parameter	X: Theory	X: Fit	A: Theory	A: Fit
$R_e, \text{\AA}$	1.05715607	1.05681836	6.63763395	6.64513879
$\rho_{ij}, \text{\AA}$	0.66345346	0.66315624	1.39447240	1.3175 ^b
D_e, cm^{-1}	22528.5492	22528.5827	13.4395560	13.1983036
α	1.0	1.0	1.0	1.0
β	1.0	0.99958534	1.0	1.0
γ	0.0	0.00023 ^b	0.0	0.0
g_v^0	0.0	0.0	0.0	0.0
g_r^0	0.0	0.03442562	0.0	0.0

^aThe reduced potential curves were constructed using the Born-Oppenheimer potential curves of Bishop and Wetmore [9] and Peek [10] and the adiabatic corrections of Bishop and Wetmore [9] and Fabri [11]. The potentials were interpolated using the cubic splines and extrapolated in the same way as in Ref. [12]. ^bFixed after a preliminary determination.

TABLE S.IV. The RPC parameters and effective g -factors of the $X^2\Sigma_u^+$ (electronic ground) and $A^2\Sigma_g^+$ (electronic excited) states of the He_2^+ cation.^a

Parameter	X: Theory	X: Fit	A: Theory	A: Fit
$R_e, \text{\AA}$	1.081110	1.08052729	4.6173980	4.60238672
$\rho_{ij}, \text{\AA}$	0.43384369	0.43868588	2.8246201	2.78684500
D_e, cm^{-1}	19943.6597	19955.3963	17.304780	17.3460289
α	1.0	1.0	1.0	1.0
β	1.0	1.0	1.0	1.0
γ	0.0	0.0	0.0	0.0
g_v^0	0.0	0.0	0.0	0.0
g_r^0	0.0	-0.01156515	0.0	-0.993 ^b

^aThe reduced potential curves were constructed using the Born-Oppenheimer potential curves V_4 of Carrington *et al.* [13] and the adiabatic corrections of Xie *et al.* [14]. The potentials were interpolated using the cubic splines and extrapolated using the expressions given in Ref. [14]. ^bFixed after a preliminary determination.

- Rev. Lett. **110**, 193601 (2013).
- [7] S. Kassi and A. Campargue, J. Mol. Spectrosc. **267**, 36 (2011).
- [8] L. Hilico, N. Billy, B. Grémaud, and D. Delande, Eur. Phys. J. D **12**, 449 (2000).
- [9] D. M. Bishop and R. W. Wetmore, Mol. Phys. **26**, 145 (1973).
- [10] J. E. Peek, J. Chem. Phys. **43**, 3004 (1965).
- [11] C. Fabri, G. Czako, G. Tasi, and A. G. Császár, J. Chem. Phys. **130**, 134314 (2009).
- [12] D. W. Schwenke, J. Chem. Phys. **114**, 1693 (2001).
- [13] A. Carrington, C. H. Pyne, and P. J. Knowles, J. Chem. Phys. **102**, 5979 (1995).
- [14] J. Xie, B. Poirier, and G. I. Gellene, J. Chem. Phys. **122**, 184310 (2005).
- [15] A. Carrington, A. M. Shaw, and S. M. Taylor, J. Chem. Soc. Faraday Trans. **91**, 3725 (1995).
- [16] P. R. Bunker and R. E. Moss, Chem. Phys. Lett. **316**, 266 (2000).

TABLE S.V. The $A \leftrightarrow X$ microwave transitions of H_2^+ (frequencies ν in MHz, line strengths S in D^2 , Einstein coefficients A in s^{-1}).

v', N'	v'', N''	ν_{fit}	ν_{exp} [15]	S	A	K_μ
$A \rightarrow X$						
0,0	13,1	61470120.8		4.784×10^{-8}	5.398×10^{-3}	2.431
0,0	14,1	41267834.8		1.483×10^{-6}	5.065×10^{-2}	3.232
0,0	15,1	24874948.6		4.727×10^{-5}	3.534×10^{-1}	4.510
0,0	16,1	12486722.9		1.634×10^{-3}	$1.546 \times 10^{+0}$	6.835
0,0	17,1	4325672.3		6.667×10^{-2}	$2.621 \times 10^{+0}$	12.129
0,0	18,1	514956.6		$3.073 \times 10^{+0}$	2.038×10^{-1}	31.669
0,1	13,0	62155663.8		3.616×10^{-8}	1.406×10^{-3}	2.403
0,1	13,2	60191799.8		9.029×10^{-8}	3.188×10^{-3}	2.484
0,1	14,0	41860683.7		1.125×10^{-6}	1.337×10^{-2}	3.188
0,1	14,2	40174991.3		2.831×10^{-6}	2.974×10^{-2}	3.312
0,1	15,0	25368649.6		3.601×10^{-5}	9.520×10^{-2}	4.435
0,1	15,2	23980708.3		9.182×10^{-5}	2.050×10^{-1}	4.649
0,1	16,0	12872357.8		1.251×10^{-3}	4.321×10^{-1}	6.674
0,1	16,2	11809314.2		3.269×10^{-3}	8.718×10^{-1}	7.125
0,1	17,0	4590756.5		5.147×10^{-2}	8.064×10^{-1}	11.618
0,1	17,2	3890901.9		1.415×10^{-1}	$1.350 \times 10^{+0}$	13.013
0,1	18,0	645722.3		$2.484 \times 10^{+0}$	1.083×10^{-1}	26.982
0,1	18,2	352014.8		$7.493 \times 10^{+0}$	5.293×10^{-2}	39.683
0,2	13,1	61548942.2		4.636×10^{-8}	1.051×10^{-3}	2.427
0,2	13,3	58306282.2		1.009×10^{-7}	1.943×10^{-3}	2.565
0,2	14,1	41346656.3		1.465×10^{-6}	1.006×10^{-2}	3.224
0,2	14,3	38567946.6		3.232×10^{-6}	1.802×10^{-2}	3.437
0,2	15,1	24953770.0		4.792×10^{-5}	7.235×10^{-2}	4.494
0,2	15,3	22672393.5		1.083×10^{-4}	1.226×10^{-1}	4.868
0,2	16,1	12565544.3		1.724×10^{-3}	3.322×10^{-1}	6.789
0,2	16,3	10828109.6		4.077×10^{-3}	5.029×10^{-1}	7.597
0,2	17,1	4404493.8		7.592×10^{-2}	6.303×10^{-1}	11.903
0,2	17,3	3277836.2		1.987×10^{-1}	6.800×10^{-1}	14.574
0,2	18,1	593778.1		$4.452 \times 10^{+0}$	9.055×10^{-2}	27.400
0,2	18,3	156614.7	156632.8	$1.541 \times 10^{+1}$	5.751×10^{-3}	65.568
$X \rightarrow A$						
19,0	0,1	-52907.5	-52894.6	$8.884 \times 10^{+0}$	6.400×10^{-4}	-17.594
19,1	0,0	-96431.6	-96431.8	$5.268 \times 10^{+0}$	7.659×10^{-4}	-5.739
19,1	0,2	-17610.2	-17610.4	$2.411 \times 10^{+1}$	2.135×10^{-5}	-29.230

TABLE S.VI. Forbidden electric dipole $X \rightarrow X$ microwave transitions of H_2^+ (ν in MHz, S in D^2 , A in s^{-1}).

v', N'	v'', N''	ν_{fit}	ν_{theor} [16]	S [16]	A [16]	K_μ
19, 0	18, 1	595723.9	595616.8	1.12×10^{-04}	1.15×10^{-05}	25.783
19, 0	17, 1	4406439.6	4405914.7	3.94×10^{-06}	1.637×10^{-04}	11.691
19, 0	16, 1	12567490.1	12566813.1	1.03×10^{-07}	9.89×10^{-05}	6.716
19, 0	15, 1	24955715.8	24955065.2	3.07×10^{-09}	2.32×10^{-05}	4.458
19, 0	14, 1	41348602.1	41348038.1	9.61×10^{-11}	3.3×10^{-06}	3.202
19, 1	19, 0	15664.4	15679.0	4.80×10^{-03}	0.3×10^{-08}	25.220
19, 1	18, 0	714294.2	714183.7	1.63×10^{-04}	9.6×10^{-06}	23.642
19, 1	17, 0	4659328.4	4658814.5	4.73×10^{-06}	7.75×10^{-05}	11.332
19, 1	16, 0	12940929.7	12940285.5	1.23×10^{-07}	4.30×10^{-05}	6.597
19, 1	15, 0	25437221.5	25436617.9	3.56×10^{-09}	9.5×10^{-06}	4.402
19, 1	14, 0	41929255.6	41928749.3	1.09×10^{-10}	1.3×10^{-06}	3.171
19, 1	18, 2	420586.7	420536.4	3.90×10^{-04}	4.7×10^{-06}	31.939
19, 1	17, 2	3959473.8	3958972.8	1.31×10^{-05}	1.312×10^{-04}	12.652
19, 1	16, 2	11877886.1	11877197.1	3.37×10^{-07}	9.15×10^{-05}	7.039
19, 1	15, 2	24049280.2	24048590.2	9.28×10^{-09}	2.09×10^{-05}	4.613
19, 1	14, 2	40243563.2	40242940.2	2.94×10^{-10}	3.1×10^{-06}	3.293

TABLE S.VII. The $A \leftrightarrow X$ microwave transitions of He_2^+ (ν in MHz, S in D^2 , A in s^{-1}).

v', N'	v'', N''	ν_{fit}	ν_{exp} [13]	S	A	K_μ
			$A \rightarrow X$			
0, 0	14, 1	83057255.2		1.203×10^{-10}	5.165×10^{-06}	1.720
0, 0	15, 1	64504470.2		3.342×10^{-09}	6.719×10^{-05}	2.093
0, 0	16, 1	48248472.5		9.236×10^{-08}	7.767×10^{-04}	2.583
0, 0	17, 1	34321667.9		2.530×10^{-06}	7.653×10^{-03}	3.252
0, 0	18, 1	22757847.8		6.843×10^{-05}	6.031×10^{-02}	4.217
0, 0	19, 1	13589058.6		1.821×10^{-03}	3.414×10^{-01}	5.713
0, 0	20, 1	6837101.8		4.683×10^{-02}	$1.118 \times 10^{+00}$	8.307
0, 0	21, 1	2487772.4		$1.069 \times 10^{+00}$	$1.231 \times 10^{+00}$	13.708
0, 0	22, 1	384695.5		$1.346 \times 10^{+01}$	5.761×10^{-02}	33.071
0, 2	14, 1	83111499.0		1.865×10^{-10}	1.605×10^{-06}	1.718
0, 2	14, 3	82036181.3		3.124×10^{-10}	2.585×10^{-06}	1.746
0, 2	15, 1	64558714.1		5.220×10^{-09}	2.104×10^{-05}	2.091
0, 2	15, 3	63573232.2		8.784×10^{-09}	3.381×10^{-05}	2.127
0, 2	16, 1	48302716.3		1.454×10^{-07}	2.454×10^{-04}	2.579
0, 2	16, 3	47410973.4		2.461×10^{-07}	3.926×10^{-04}	2.630
0, 2	17, 1	34375911.7		4.023×10^{-06}	2.445×10^{-03}	3.246
0, 2	17, 3	33582640.1		6.850×10^{-06}	3.882×10^{-03}	3.320
0, 2	18, 1	22812091.6		1.102×10^{-04}	1.956×10^{-02}	4.205
0, 2	18, 3	22123146.3		1.891×10^{-04}	3.062×10^{-02}	4.322
0, 2	19, 1	13643302.4		2.981×10^{-03}	1.131×10^{-01}	5.687
0, 2	19, 3	13066110.3		5.172×10^{-03}	1.723×10^{-01}	5.896
0, 2	20, 1	6891345.6		7.858×10^{-02}	3.841×10^{-01}	8.235
0, 2	20, 3	6435634.1		1.384×10^{-01}	5.508×10^{-01}	8.686
0, 2	21, 1	2542016.2		$1.870 \times 10^{+00}$	4.594×10^{-01}	13.398
0, 2	21, 3	2220712.6		$3.359 \times 10^{+00}$	5.501×10^{-01}	14.791
0, 2	22, 1	438939.4		$2.574 \times 10^{+01}$	3.271×10^{-02}	28.883
0, 2	22, 3	264152.2		$4.535 \times 10^{+01}$	1.255×10^{-02}	42.473
0, 4	14, 3	82154699.9		2.082×10^{-10}	9.614×10^{-07}	1.743
0, 4	14, 5	80228422.5		3.179×10^{-10}	1.367×10^{-06}	1.794
0, 4	15, 3	63691750.8		5.956×10^{-09}	1.281×10^{-05}	2.122
0, 4	15, 5	61927618.8		9.175×10^{-09}	1.813×10^{-05}	2.190
0, 4	16, 3	47529492.0		1.702×10^{-07}	1.520×10^{-04}	2.621
0, 4	16, 5	45934677.2		2.649×10^{-07}	2.135×10^{-04}	2.716
0, 4	17, 3	33701158.7		4.851×10^{-06}	1.543×10^{-03}	3.305
0, 4	17, 5	32284392.0		7.643×10^{-06}	2.138×10^{-03}	3.444
0, 4	18, 3	22241664.9		1.380×10^{-04}	1.262×10^{-02}	4.295
0, 4	18, 5	21013816.0		2.209×10^{-04}	1.703×10^{-02}	4.517
0, 4	19, 3	13184628.9		3.933×10^{-03}	7.482×10^{-02}	5.837
0, 4	19, 5	12159622.2		6.435×10^{-03}	9.599×10^{-02}	6.242
0, 4	20, 3	6554152.8		1.120×10^{-01}	2.615×10^{-01}	8.516
0, 4	20, 5	5750563.8		1.894×10^{-01}	2.986×10^{-01}	9.426
0, 4	21, 3	2339231.2		$3.033 \times 10^{+00}$	3.226×10^{-01}	14.006
0, 4	21, 5	1782792.0		$5.408 \times 10^{+00}$	2.545×10^{-01}	17.086
0, 4	22, 3	382670.8		$5.283 \times 10^{+01}$	2.473×10^{-02}	29.102
0, 4	22, 5	101406.5	101460	$9.542 \times 10^{+01}$	8.275×10^{-04}	81.484

TABLE S.VIII. The $A \leftrightarrow X$ microwave transitions of He_2^+ (ν in MHz, S in D^2 , A in s^{-1}).

v', N'	v'', N''	ν_{fit}	ν_{exp} [13]	S	A	K_μ
$A \rightarrow X$						
1, 0	14, 1	83275624.7		3.523×10^{-11}	1.525×10^{-06}	1.716
1, 0	15, 1	64722839.8		9.697×10^{-10}	1.969×10^{-05}	2.087
1, 0	16, 1	48466842.0		2.646×10^{-08}	2.255×10^{-04}	2.572
1, 0	17, 1	34540037.5		7.121×10^{-07}	2.196×10^{-03}	3.233
1, 0	18, 1	22976217.3		1.876×10^{-05}	1.702×10^{-02}	4.179
1, 0	19, 1	13807428.1		4.778×10^{-04}	9.397×10^{-02}	5.627
1, 0	20, 1	7055471.3		1.127×10^{-02}	2.955×10^{-01}	8.057
1, 0	21, 1	2706141.9		2.032×10^{-01}	3.013×10^{-01}	12.620
1, 0	22, 1	603065.1		6.167×10^{-01}	1.016×10^{-02}	21.176
1, 0	23, 1	49649.4	49646	$3.029 \times 10^{+01}$	2.765×10^{-04}	44.371
1, 2	14, 1	83294877.8		3.060×10^{-11}	2.650×10^{-07}	1.716
1, 2	14, 3	82219560.1		5.122×10^{-11}	4.267×10^{-07}	1.744
1, 2	15, 1	64742092.9		8.493×10^{-10}	3.453×10^{-06}	2.086
1, 2	15, 3	63756611.0		1.429×10^{-09}	5.547×10^{-06}	2.123
1, 2	16, 1	48486095.1		2.341×10^{-08}	3.996×10^{-05}	2.571
1, 2	16, 3	47594352.2		3.960×10^{-08}	6.392×10^{-05}	2.622
1, 2	17, 1	34559290.6		6.382×10^{-07}	3.942×10^{-04}	3.231
1, 2	17, 3	33766018.9		1.086×10^{-06}	6.255×10^{-04}	3.304
1, 2	18, 1	22995470.5		1.710×10^{-05}	3.109×10^{-03}	4.175
1, 2	18, 3	22306525.1		2.931×10^{-05}	4.864×10^{-03}	4.290
1, 2	19, 1	13826681.3		4.458×10^{-04}	1.761×10^{-02}	5.619
1, 2	19, 3	13249489.2		7.716×10^{-04}	2.681×10^{-02}	5.822
1, 2	20, 1	7074724.5		1.092×10^{-02}	5.777×10^{-02}	8.035
1, 2	20, 3	6619013.0		1.913×10^{-02}	8.281×10^{-02}	8.460
1, 2	21, 1	2725395.0		2.133×10^{-01}	6.459×10^{-02}	12.532
1, 2	21, 3	2404091.5		3.740×10^{-01}	7.771×10^{-02}	13.704
1, 2	22, 1	622318.2		9.156×10^{-01}	3.309×10^{-03}	20.528
1, 2	22, 3	447531.0		$1.059 \times 10^{+00}$	1.421×10^{-03}	25.287
1, 2	23, 1	68902.5	68924	$4.045 \times 10^{+01}$	1.946×10^{-04}	32.036
1, 2	23, 3	8926.8	8949	$1.622 \times 10^{+02}$	1.577×10^{-06}	144.214
$X \rightarrow A$						
23, 1	0, 0	168720.1	168709	$1.052 \times 10^{+01}$	1.265×10^{-03}	-12.770
23, 1	0, 2	114476.3	114539	$2.540 \times 10^{+01}$	9.562×10^{-04}	-18.432
23, 3	0, 2	174452.0		$2.311 \times 10^{+01}$	1.314×10^{-03}	-6.822
23, 3	0, 4	55933.4	55880	$6.000 \times 10^{+01}$	1.108×10^{-04}	-19.792

TABLE S.IX. The $A \leftrightarrow X$ microwave transitions of D_2^+ (frequencies ν in MHz, line strengths S in D^2 , Einstein coefficients A in s^{-1}).

v', N'	v'', N''	ν_{fit}	ν_{exp} [15]	S	A	K_μ
$A \rightarrow X$						
0, 0	26, 1	162124.4	162165.2	5.918	1.225×10^{-2}	59.209
0, 1	26, 0	215438.7	215484	5.595	9.060×10^{-3}	46.855
0, 1	26, 2	109628.6	109672.8	12.859	2.744×10^{-3}	78.142
0, 2	26, 1	211802.5	211847	11.477	1.060×10^{-2}	45.139
0, 2	26, 3	48013.2	48064.3	21.876	2.353×10^{-4}	145.883
0, 3	26, 2	189639.2	189681	18.329	8.676×10^{-3}	44.871
0, 4	26, 3	152839.8	152896.5	26.819	5.169×10^{-3}	45.453
1, 0	27, 1	11117.9	11138.1	22.896	1.529×10^{-5}	97.619
1, 1	27, 0	25783.0	25755.4	16.676	4.629×10^{-5}	50.245
$X \rightarrow A$						
26, 4	0, 3	11978.9	11928.0	35.183	3.265×10^{-6}	-406.966
27, 0	0, 1	118294.6	118296.7	2.291	1.843×10^{-3}	-10.337
27, 1	0, 0	144893.3	144895.2	1.625	8.002×10^{-4}	-7.101
27, 1	0, 2	95215.2	95222.5	4.826	6.746×10^{-4}	-10.400
27, 2	0, 1	144290.0	144299.0	1.905	5.560×10^{-4}	-3.922
27, 2	0, 3	64279.4	64290.9	6.790	1.752×10^{-4}	-7.914

EFFECTIVE HYPERFINE STRUCTURE FUNCTIONS
OF AMMONIA

Bibliographic record of the attached publication:

Augustovičová, L., P. Soldán, and V. Špirko (2016). "Effective hyper-
fine structure functions of ammonia." In: *The Astrophysical Journal*
824, p. 147.

DOI: [10.3847/0004-637x/824/2/147](https://doi.org/10.3847/0004-637x/824/2/147).



EFFECTIVE HYPERFINE-STRUCTURE FUNCTIONS OF AMMONIA

L. AUGUSTOVIČOVÁ¹, P. SOLDÁN¹, AND V. ŠPIRKO^{1,2}

¹Charles University in Prague, Faculty of Mathematics and Physics, Department of Chemical Physics and Optics, Ke Karlovu 3, CZ-12116 Prague 2, Czech Republic; spirko@marge.uochb.cas.cz

²Institute of Organic Chemistry and Biochemistry, Academy of Sciences of the Czech Republic, Flemingovo nám. 2, CZ-16610 Prague 6, Czech Republic
Received 2015 October 27; revised 2016 April 15; accepted 2016 April 21; published 2016 June 23

ABSTRACT

The hyperfine structure of the rotation-inversion ($v_2 = 0^+, 0^-, 1^+, 1^-$) states of the $^{14}\text{NH}_3$ and $^{15}\text{NH}_3$ ammonia isotopomers is rationalized in terms of effective (ro-inversional) hyperfine-structure (hfs) functions. These are determined by fitting to available experimental data using the Hougen's effective hyperfine-structure Hamiltonian within the framework of the non-rigid inverter theory. Involving only a moderate number of mass independent fitting parameters, the fitted hfs functions provide a fairly close reproduction of a large majority of available experimental data, thus evidencing adequacy of these functions for reliable prediction. In future experiments, this may help us derive spectroscopic constants of observed inversion and rotation-inversion transitions deperturbed from hyperfine effects. The deperturbed band centers of ammonia come to the forefront of fundamental physics especially as the probes of a variable proton-to-electron mass ratio.

Key words: cosmological parameters – infrared: ISM – line: profiles – molecular data – submillimeter: ISM

1. INTRODUCTION

The hyperfine structure of ammonia in its rotation-inversion lines makes it an excellent tracer of density and temperature in a broad variety of interstellar environments (Ho & Townes 1983; Park 2001; Maret et al. 2009). However, the underlying hyperfine structure of ammonia distorts spectral lineshapes, which hinders the precise determination of transition frequencies (Cazzoli & Puzzarini 2013; Cazzoli & Puzzarini 2014), and consequently, the accuracy of the related physical data derived from these frequencies. A very illustrative example of a situation, in which a proper treatment of ammonia hyperfine structure is a *condicio sine qua non*, is given by the astronomical determination of the cosmological variability of the proton-to-electron mass ratio $\mu = m_p/m_e$ based on relating the wavelengths of astronomical spectral lines with their rest (laboratory) counterparts. The corresponding method relies on simultaneous fitting of the lines possessing different hyperfine structures, and, consequently, different line profiles too. It has been well documented in the literature that disregarding this fact might result in serious consequences (e.g., Murphy et al. 2008 and Kanekar et al. 2015). For instance, neglecting the non-LTE effects on the NH_3 hyperfine structure may cause about 40% of the total systematic error in the result of Murphy et al. (2008).

Even though ammonia has been detected in a great variety of interstellar regions, both in our Galaxy (Levshakov et al. 2010) and also at high-redshift objects (Riechers et al. 2013), currently only two redshifted ammonia absorbers (at $z \sim 0.685$ toward B0218+357 and $z \sim 0.886$ toward B1830-210 (Henkel et al. 2005, 2008)) provide spectral lines that allow for critical constraints on the changes in μ (Kanekar 2011). These lines pertain to the metastable ($J, K = J$) inversion transitions that form a subset of those transitions with resolved hyperfine structure already studied in the literature (Kukolich 1965, 1967; Kukolich & Wofsy 1970; Ruben & Kukolich 1974; Kukolich 1975; Ouhayoun et al. 1977; Marshall & Muentner 1981; Hüttner &

Majer 1984; Belov et al. 1998; Fichoux et al. 1998; van Veldhoven et al. 2002, 2004; Cazzoli et al. 2009; Lemarchand et al. 2011).

The inversion transitions between the metastable states of NH_3 , although possessing the most favorable spectral properties, are not the most sensitive probes of μ . As was recently shown by Jansen et al. (2014), Špirko (2014), and Owens et al. (2015), several rotation-inversion transitions have large line strength, which could allow for their astronomical detection while exhibiting significantly higher mass sensitivities than the currently observed metastable lines. It should be noted, however, that not all of these promising lines have been studied with resolved hyperfine structures. Thus, in order to assist future experimental studies, we find it worthwhile to predict the corresponding hyperfine-structure spectroscopic constants theoretically. The approach we adopt consists of globally fitting all of the available experimental data in terms of the ro-inversional hyperfine-structure property functions that arise from a simple averaging of the Hougen's effective hyperfine-structure Hamiltonian (Hougen 1972) within the framework of the non-rigid inverter theory (Špirko 1983).

2. THEORY

In order to describe the probed data theoretically we follow the approach from our previous studies on the inversional dependence of the hyperfine quadrupole coupling and rotational g -factors of ammonia (Špirko 1979, 1981). The following effective Hamiltonian is used:

$$H = H_{\text{ir}} + H_{\text{hfs}}, \quad (1)$$

where H_{ir} is the vibration-inversion-rotation Hamiltonian described by Špirko (1983). H_{hfs} is the effective hyperfine-

structure Hamiltonian (Hougen 1972)

$$\begin{aligned}
H_{\text{hfs}} = & Q[3(\mathbf{I}_N \cdot \mathbf{J})^2 + \frac{3}{2}(\mathbf{I}_N \cdot \mathbf{J}) - I_N^2 J^2]/[2I_N(2I_N - 1)] \\
& \times (2J - 1)(2J + 3)] + R(\mathbf{I}_N \cdot \mathbf{J}) + S(\mathbf{I}_H \cdot \mathbf{J}) \\
& + T[2/(2J - 1)(2J + 3)] \left[\frac{3}{2}(\mathbf{I}_N \cdot \mathbf{J})(\mathbf{I}_H \cdot \mathbf{J}) \right. \\
& \left. + \frac{3}{2}(\mathbf{I}_H \cdot \mathbf{J})(\mathbf{I}_N \cdot \mathbf{J}) - (\mathbf{I}_N \cdot \mathbf{I}_H)J^2 \right] \\
& + U[2/(2J - 1)(2J - 3)] \left[3(\mathbf{I}_H \cdot \mathbf{J})^2 \right. \\
& \left. + \frac{3}{2}(\mathbf{I}_H \cdot \mathbf{J}) - I_H^2 J^2 \right], \tag{2}
\end{aligned}$$

where J and K are rotational quantum numbers, \mathbf{J} , \mathbf{I}_N , and \mathbf{I}_H represent, respectively, the total rotational angular momentum of the ammonia molecule, the spin of the nitrogen nucleus, and the total nuclear spin of the three protons. The corresponding dot products are expressed using laboratory-fixed vector components. The spectroscopic constants Q , R , S , T , and U express the magnitude of the ^{14}N quadrupole coupling, N spin-rotation coupling, H spin-rotation coupling, N–H spin–spin interaction, and H–H spin–spin interaction, respectively.

As the magnetic part of H_{hfs} can be accurately treated as a small perturbation of H_{ir} , the corresponding magnetic spectroscopic constants R , S , T , and U can be expressed in the following way (Gunther-Mohr et al. 1954; Sauer et al. 1991; Oddershede et al. 1992):

$$\begin{aligned}
R = & -\overline{M}_{xx}(N) - [\overline{M}_{zz}(N) - \overline{M}_{xx}(N)]K^2/J(J + 1), \\
S = & -\frac{1}{2}[\overline{M}_{xx}(H) + \overline{M}_{yy}(H)] \\
& + \frac{1}{2}[\overline{M}_{xx}(H) - \overline{M}_{yy}(H)]\delta_{K1}(-1)^{J+p} \\
& - [2\overline{M}_{zz}(H) - \overline{M}_{xx}(H) - \overline{M}_{yy}(H)]K^2/J(J + 1), \\
T = & \overline{D}_1[1 - 3K^2/J(J + 1)] - \frac{1}{2}\overline{D}_2\delta_{K1}(-1)^{J+p}, \\
U = & -\frac{1}{4}\overline{D}_3[1 - 3K^2/J(J + 1)],
\end{aligned}$$

where $p = 0/1$ for the lower/upper inversion state, and the nuclear spin–spin interaction \overline{D}_1 , \overline{D}_2 , \overline{D}_3 , and spin-rotation $\overline{M}_{\alpha,\alpha}(N/H)$ (where $\alpha = x, y, \text{ or } z$) constants are ro-inversional averages

$$\overline{P}_{v_2,J,K} = \langle \psi_{v_2,J,K} | P | \psi_{v_2,J,K} \rangle. \tag{3}$$

Here, P are known functions of vibrational coordinates, ($P = D_1, D_2, D_3, M_{xx}, M_{yy}, \text{ or } M_{zz}$), and $\psi_{v_2,J,K}$ are normalized eigenfunctions of H_{ir} .

The geometrically defined functions P can be evaluated from first principles, which allows predictions of the sought hyperfine-structure energy patterns in a purely ab initio way. Indeed, such predictions have already been carried out (Fowler & Špirko 1990; Sauer et al. 1991; Oddershede et al. 1992). The actual calculations revealed that a one-dimensional (rigid

inverter) power series,

$$P = \sum_{k=0} P_k h^{2k}, \tag{4}$$

provides a sufficient description of the magnetic parts of the hyperfine structures of the lowest $v_2 = 0^+, 0^-, 1^+, 1^-$ states. Here h is the distance of the atom N from the plane formed by H atoms, and the expansion coefficients P_k are fitting parameters. To achieve a comparable description of the quadrupole coupling part of the probed hyperfine structure, which dominates the hyperfine-structure spectral pattern of $^{14}\text{NH}_3$, one should go beyond the limits of the rigid-inverter approximation by incorporating the centrifugal distortion effects.

According to the theory developed by Hougen (1972), the hyperfine quadrupole couplings can be described by means of the state-dependent quadrupole coupling constants, given as

$$Q = \langle \psi_{v_2,J,K} | eQ_N q_{zz} | \psi_{v_2,J,K} \rangle + Q^{\text{dist}} Z(J, K), \tag{5}$$

where Q_N is the nuclear quadrupole moment of ^{14}N , q_{zz} is the zz component of the molecule fixed electric field gradient tensor q , Q^{dist} is a correction constant, and

$$Z(J, K) = K^2(4K^2 - 1)/[3K^2 - J(J + 1)] - 2K^2. \tag{6}$$

Although the ab initio determined property functions provide a qualitatively reliable rationalization of all of the observed hyperfine-structure data (Fowler & Špirko 1990; Sauer et al. 1991; Oddershede et al. 1992), they fail to provide a quantitative reproduction. To create a more accurate description, we assume that the matrix elements $\langle \psi_{v_2,J,K} | h^{2k} | \psi_{v_2,J,K} \rangle$ are known and treat the parameters P_k as free parameters of the following system of equations:

$$\overline{P}_{v_2,J,K} = \sum_{k=0} P_k \langle \psi_{v_2,J,K} | h^{2k} | \psi_{v_2,J,K} \rangle, \tag{7}$$

where $\overline{P}_{v_2,J,K}$ are the experimental counterparts of the averages $\overline{P}_{v_2,J,K}$, which we assume for a physically correct solution of this system. Unlike the standard spectroscopic constants $\overline{P}_{v_2,J,K}$, which are fitted separately for each spectral line and which can hardly be determined without a priori imposed constraints (see e.g., (Lemarchand et al. 2011)), the expansion coefficients P_k are both mass and state independent, thus providing a much more numerically robust simultaneous fitting.

3. RESULTS AND DISCUSSION

In order to fit the ammonia hyperfine-structure property functions, one needs both the ro-inversional matrix elements $\langle \psi_{v_2,J,K} | h^{2k} | \psi_{v_2,J,K} \rangle$ and an adequate set of appropriate experimental characteristics. While the needed matrix elements can easily be evaluated using the literature ro-inversional wavefunctions for any imaginable state (in this study we rely on the functions taken from Špirko 1983), the actual fittings are prevented by the lack of accurate data for excited vibrational states. So far, the only excited states for which there are available adequate data are the $v_2 = 1^\pm$ inversional states. Thus, the fittings are safely limited to the subset of the $v_2 = 0^\pm$ and 1^\pm inversional states only. To get an insight of the vibrational effects on the probed hyperfine structures, we first performed a fitting of the magnetic parameters (the ^{14}N quadrupole coupling has already been examined by Špirko 1979; Fowler & Špirko 1990) under assumption that they are constant (i.e., assuming $\langle \psi_{v_2,J,K} | h^{2k} | \psi_{v_2,J,K} \rangle = 0$). For the ground vibrational state the fit achieves experimental uncertainty using eight fitting parameters

only (we note that $^{15}R/^{14}R \cong ^{15}T/^{14}T \cong ^{15}g/^{14}g = -1.402$; see also Kukolich (1975) and Drouin et al. for similar fits). However, on the other hand, the fit fails to provide any information on the inversional effects.

According to a purely ab initio study (Oddershede et al. 1992), the magnetic hyperfine-structure constants exhibit inversional dependence, which may perhaps be overlooked for the vibrational ground states but certainly not for the $v_2 = 1$ excited states. In principle, thanks to a very high accuracy of the beam maser measurement data of Kukolich (1965, 1967), Kukolich & Wofsy (1970), Ruben & Kukolich (1974), and Marshall & Muenter (1981), a certain insight could be achieved by fitting this data without imposing $\langle \psi_{v_2, J, K} | h^{2k} | \psi_{v_2, J, K} \rangle = 0$. Unfortunately, such fits are rather unstable, calling thus for data that are more sensitive to the inversional effects. Thanks to Ch. Bordé and coworkers such data are available (Bordé et al. 1985; Lemarchand et al. 2011); namely the saturation spectroscopy data for the $saQ(6, 3)$ transition of $^{14}\text{NH}_3$ and the $asR(2, 0)$ transition of $^{15}\text{NH}_3$. Extending our inputs with these data has made the fits, performed simultaneously for $^{14}\text{NH}_3$ and $^{15}\text{NH}_3$, much more robust and still fairly quantitative, despite their lesser accuracy. The final results are represented by the following equations:

$$R = [-7.410154 - 41.70885 \langle v_2, J, K | h^2 | v_2, J, K \rangle + 170 \langle v_2, J, K | h^4 | v_2, J, K \rangle - (0.4753610 - 3.8 \langle v_2, J, K | h^2 | v_2, J, K \rangle) \times K^2/J(J+1)]/f, \quad (8)$$

$$S = -15.93747 - 20.68011 \langle v_2, J, K | h^2 | v_2, J, K \rangle + 50 \langle v_2, J, K | h^4 | v_2, J, K \rangle - (2.57032 - 0.8 \langle v_2, J, K | h^2 | v_2, J, K \rangle) \times K^2/(2J(J+1)) + 14.49483 \delta_{K1}(-1)^{J+p}, \quad (9)$$

$$T = [(11.4522 - 340 \langle v_2, J, K | h^4 | v_2, J, K \rangle) \times (1 - 3K^2/J(J+1)) + (14.66723 - 8.5 \langle v_2, J, K | h^4 | v_2, J, K \rangle) \times \delta_{K1}(-1)^{J+p}]/f, \quad (10)$$

$$U = -(20.46231 + 48 \langle v_2, J, K | h^2 | v_2, J, K \rangle) \times (1 - 3K^2/J(J+1))/4, \quad (11)$$

where the constants set in boldface were determined approximately by tabulating, and held constant during the fits, $f = -1.402/1$ for the cases of $^{14}\text{NH}_3/^{15}\text{NH}_3$, respectively, and $p = 0/1$ for the lower/upper inversion state.

The $saQ(6, 3)$ and $asR(2, 0)$ data from Lemarchand et al. (2011), Bordé et al. (1985) are not the only data carrying the sought information on the hyperfine structure of excited ammonia. In addition, for $^{14}\text{NH}_3$ there are also saturation spectroscopy data for the $asQ(8, 7)$ transition (Ouhayoun et al. 1977), Doppler-limited data for the $v_2 = 1, (J, K) = (1, 1)^- \rightarrow (2, 1)^+$ transition, (Hüttner & Majer 1984) saturation spectroscopy data for the $v_2 = 1, (J, K) = (1, 0)^+ \rightarrow (0, 0)^-, (1, 1)^- \rightarrow (2, 1)^+, (2, 0)^- \rightarrow (3, 0)^+, (2, 1)^- \rightarrow (3, 1)^+,$ and $(2, 2)^- \rightarrow (3, 2)^+$ rotation-inversion transitions (Belov et al. 1998), and finally, the IR-IR double

resonance data for the sums and differences of the $saQ(3, 3)$ (allowed) and $ss^{-3}Q(3, 3)$ (forbidden) transitions and also standard saturation spectroscopy data for the allowed $saQ(3, 3)$ transition (Fichoux et al. 1998). As the accuracy of this data is of the same order of magnitude as the magnitudes of the magnetic hyperfine-structure parameters, they do not allow for an accurate determination of these parameters. However, fixing these parameters at the values obtained in the above presented analysis allows for an evaluation of the ^{14}N quadrupole coupling characteristics. In principle, thanks to the centrifugal distortion effects, already the ground-state data may enable a determination of a quadrupole coupling function, which predicts estimates of the $v_2 = 1$ characteristics in reasonable agreement with their experimental counterparts (Špirko 1979, Fowler & Špirko 1990). In the present case, this holds only for the parameters derived in Ouhayoun et al. (1977) and Hüttner & Majer (1984). The parameters derived in Belov et al. (1998) and Fichoux et al. (1998) markedly disagree with our theoretical predictions. To resolve this problem, we have refined the corresponding data with the magnetic hyperfine parameters fixed at their predicted values, and obtained the fitted quadrupole constants Q in close harmony with our incipient predictions. A global fit of all available data provides the following effective quadrupole coupling function:

$$Q = -5682.077 + 0.4584517J(J+1) - 0.5464027K^2 + 11565.48 \langle v_2, J, K | h^2 | v_2, J, K \rangle - 4400 \langle v_2, J, K | h^4 | v_2, J, K \rangle - 1.080 Z(J, K). \quad (12)$$

Numerical values of the $Q, R, S, T,$ and U constants for different J and K are provided in the supplementary material. These can be used for the construction of Hamiltonian H_{hfs} and thus for the calculation of required hyperfine spectra.

Though involving only a moderate number of fitting parameters, the hyperfine-structure functions (8–12) reproduce all the probed experimental data fairly accurately, as seen in Tables 1 and 2, and in the inset of Figure 1, thus evidencing their adequacy for reliable predicting for a large number of the rotational states pertaining to the lowest inversional states ($v_2 = 0^+, 0^-, 1^+, 1^-$) of the $^{14}\text{NH}_3$ and $^{15}\text{NH}_3$ isotopomers. In particular, the predictions can be used to assess the importance of the hfs interactions in the astronomical determination of the cosmological variability of the proton-to-electron mass ratio $\mu = m_p/m_e$ based on the use of the ammonia transitions.

Probably the simplest way of assessing this importance consists of deriving the differences between the line centers of the ro-inversional bands deperturbed from the hfs effects and the corresponding spectral maxima of these bands. The envelope of absorption hyperfine resolved lines was calculated from each individual absorption line center, the position of which was determined by fitting a variety of laboratory spectra. These calculations were carried out for spectral lines with Doppler half-width at the kinetic temperature $T = 55$ K for a molecular gas toward B0218+357 (Henkel et al. 2005). As a matter of fact (see Figure 2 and Table 3) the hyperfine effects exhibit a nonlinear dependence on the cosmological redshift and for the $K = 1$ states may acquire non-negligible magnitudes. This is especially interesting in the case of the $v_2 = 1, (J, K) = (2, 1)^+ \rightarrow (1, 1)^-$ and $v_2 = 1, (J, K) =$

Table 1
Calculated and Experimental Hyperfine Frequencies of the $^{14}\text{NH}_3 (J, K) = (3, 1)^+ \rightarrow (2, 1)^-$ Transition in the Excited v_2 Vibrational State

F_1'	F'	F_1	F	Calculated	Experimental ^a	Intensity ^b	Intensity ^a
3	3.5	3	2.5	762 851.4248	...	0.004535	...
3	3.5	3	3.5	762 851.4939	762 851.494(020)	0.122449	46.67
3	2.5	3	2.5	762 851.5329	...	0.090703	...
3	2.5	3	3.5	762 851.6020	...	0.004535	...
3	3.5	2	2.5	762 852.2217	762 852.204(001)	1.01587	373.33
3	2.5	2	1.5	762 852.2570	...	0.711111	...
3	2.5	2	2.5	762 852.3298	...	0.050794	...
2	2.5	1	1.5	762 852.5532	...	0.72	...
2	1.5	1	0.5	762 852.5886	...	0.4	...
4	4.5	3	3.5	762 852.5896	762 852.622(020)	1.42857	540.00
4	3.5	3	2.5	762 852.6224	762 852.622(020)	1.10204	252.00
2	1.5	1	1.5	762 852.6720	...	0.08	...
4	3.5	3	3.5	762 852.6915	...	0.040816	...
2	2.5	3	2.5	762 852.8496	...	0.000181	...
2	2.5	3	3.5	762 852.9187	762 852.940(050)	0.003628	1.33
2	1.5	3	2.5	762 852.9683	...	0.002540	...
2	1.5	3	3.5	762 853.0374	...	0.	...
2	2.5	2	1.5	762 853.5736	...	0.008889	...
2	2.5	2	2.5	762 853.6465	...	0.124444	...
2	1.5	2	1.5	762 853.6923	762 853.670(005)	0.08	46.67
2	1.5	2	2.5	762 853.7652	...	0.008889	...

Notes. Frequencies are given in MHz.

^a Frequencies and relative intensities as published in Belov et al. (1998).

^b Relative intensities calculated for electric dipole transitions according to Kukolich (1967).

Table 2
Predicted Doppler Shifted $^{14}\text{NH}_3 v_2 = 1, (J, K) = (1, 0)^+ \rightarrow (0, 0)^-$ Lines for Different Redshifts z

F_1'	F'	F_1	F	$z = 0$	$z = 0.685$	$z = 0.886$	$z = 2$	$z = 4$	$z = 6$
1	1.5	0	1.5	466 243.610	276 702.439	247 212.943	155 414.537	93 248.722	66 606.230
1	2.5	0	1.5	466 243.610	276 702.439	247 212.943	155 414.537	93 248.722	66 606.230
1	1.5	2	1.5	466 245.558	276 703.595	247 213.976	155 415.186	93 249.112	66 606.508
1	2.5	2	1.5	466 245.558	276 703.595	247 213.976	155 415.186	93 249.112	66 606.508
1	1.5	2	0.5	466 245.558	276 703.595	247 213.976	155 415.186	93 249.112	66 606.508
1	1.5	2	2.5	466 245.570	276 703.602	247 213.982	155 415.190	93 249.114	66 606.510
1	2.5	2	2.5	466 245.570	276 703.602	247 213.982	155 415.190	93 249.114	66 606.510
1	1.5	2	3.5	466 245.617	276 703.630	247 214.007	155 415.206	93 249.123	66 606.517
1	2.5	2	3.5	466 245.617	276 703.630	247 214.007	155 415.206	93 249.123	66 606.517
1	1.5	1	0.5	466 246.901	276 704.392	247 214.688	155 415.634	93 249.380	66 606.700
1	1.5	1	1.5	466 246.929	276 704.409	247 214.703	155 415.643	93 249.386	66 606.704
1	2.5	1	1.5	466 246.929	276 704.409	247 214.703	155 415.643	93 249.386	66 606.704
1	1.5	1	2.5	466 246.936	276 704.413	247 214.706	155 415.645	93 249.387	66 606.705
1	2.5	1	2.5	466 246.936	276 704.413	247 214.706	155 415.645	93 249.387	66 606.705

Note. The upper (dashed) and lower state quantum numbers are considered from the coupling scheme $F_1 = J + I_N$ and $F = F_1 + I_H$. Frequencies are given in MHz.

$(1, 0)^+ \rightarrow (0, 0)^-$ transitions, which exhibit fairly anomalous mass sensitivities ($T_{s(2,1)-a(1,1)} \sim 17.2$, $T_{a(0,0)-s(1,0)} \sim -6.6$) and which have already been observed extraterrestrially (for details see Owens et al. 2015), thus belonging among the most promising probes of the cosmological variability of the proton-to-electron mass ratio $\mu = m_p/m_e$.

4. CONCLUSION

In summary, inversional hyperfine-structure functions of ammonia have been determined by a simultaneous fitting of the literature experimental hyperfine spectroscopic constants, which were determined separately for each inversion-rotation transition. Using only a moderate number of mass- and state-independent fitting parameters, the fit

achieves experimental uncertainty for a large majority of the fitted characteristics, thus evidencing its adequacy for reliable predicting. The acquired results allow accurate accounting of the hyperfine interactions for a large number of thus-far unmeasured ro-inversional states of $^{14}\text{NH}_3$ and $^{15}\text{NH}_3$, and also for a critical revision of the fits based on the use of mass- and state-dependent spectroscopic constants. Knowledge of the hyperfine-structure parameters allow for a physically correct determination of the genuine energy patterns in the Doppler profile of the roinversion transitions and thus also a correct rationalization of the physical characteristics depending on these patterns. For instance, an accurate determination of the Boltzmann constant by means of Doppler spectroscopy (Lemarchand et al. 2011), or

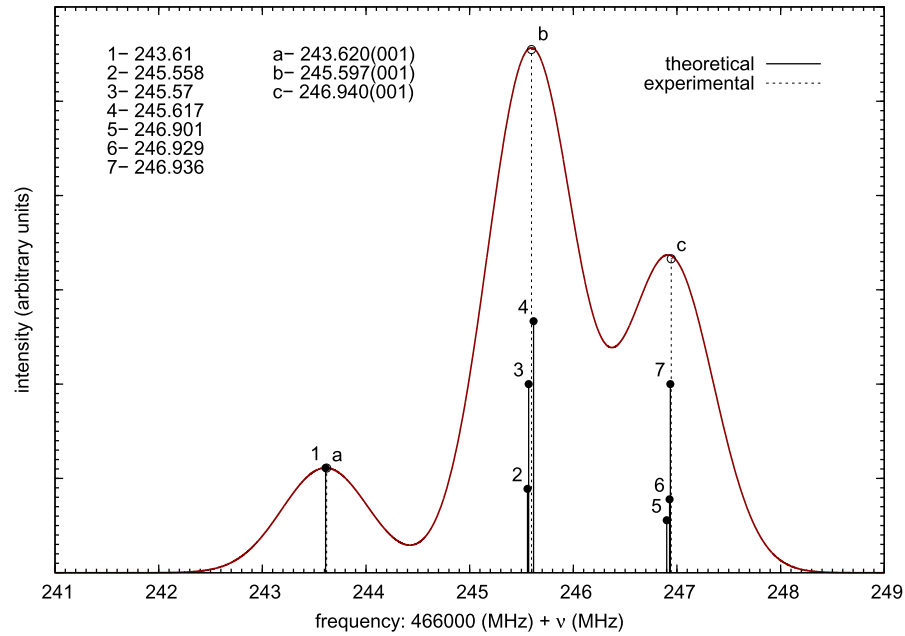


Figure 1. Theoretical ammonia $^{14}\text{NH}_3$ $v_2 = 1, (J, K) = (1, 0)^+ \rightarrow (0, 0)^-$ spectrum vs. saturation dip position lines of the hyperfine components from Belov et al. (1998) at temperature 150 K. Frequencies in MHz relative to the value of 466,000 MHz.

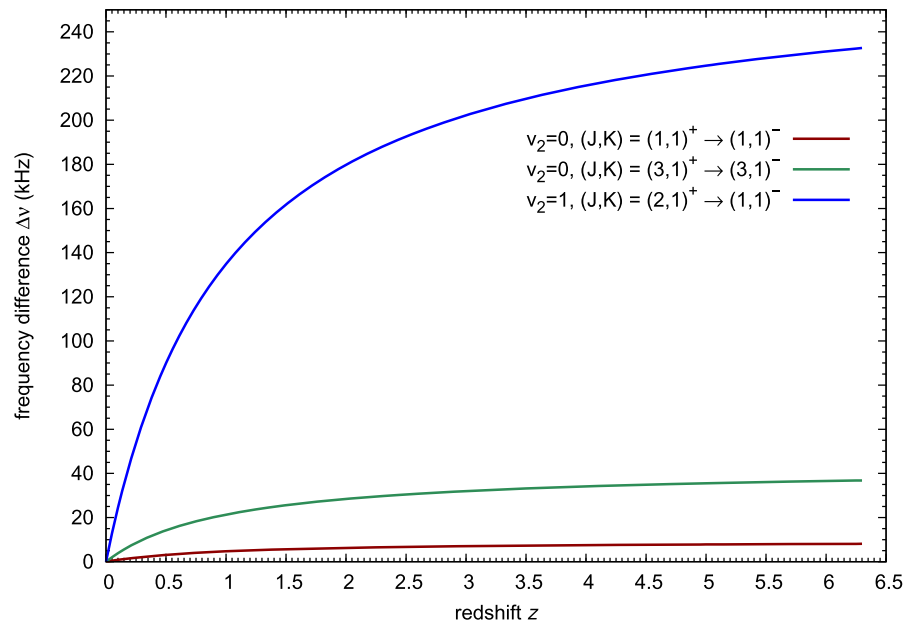


Figure 2. Selected differences $\Delta\nu \equiv [\nu_{v_2=0} - \nu_{v_2}]_{\text{max}} - [\nu_{v_2=0} - \nu_{v_2}]_{\text{band c.}}$ of the spectral maxima and the band centers deperturbed from the hfs effects.

a realistic modeling of the population transfers induced by infrared lasers (Dietiker et al. 2015). In particular, the predictions can be used for deriving the genuine band centers of the astronomical lines, which appear to be promising for a critical probing of the cosmological variability of the proton-to-electron mass ratio.

This manuscript is dedicated to Jon T. Hougen on the occasion of his 80th birthday. The authors would also like to thank Alec Owens for carefully reading this manuscript. This work was a part of the research project RVO:61388963 (IOCB) and was kindly supported by the Czech Science Foundation (grant P209/15-10267S).

Table 3

The Deperturbed Band Centers^a of the Rotational-inversion Transitions (First Row), the Positions of the Corresponding Spectral Maxima^b (Second Row) for Different Redshifts z at Given Temperature, and their Mutual Shift (Third Row) in km s^{-1}

$z = 0$	$z = 0.685$	$z = 0.886$	$z = 2$	$z = 4$	$z = 6$
$v_2 = 0, (J, K) = (1, 1)^+ \rightarrow (1, 1)^- (T = 55 \text{ K})$					
23 694 495.481(6)	14 062 015.122(4)	12 563 359.216(3)	7 898 165.160(2)	4 738 899.096(1)	3 384 927.926(1)
23 694 504.872	14 062 020.696	12 563 364.195	7 898 168.291	4 738 900.974	3 384 929.267
1.188×10^{-1}	7.052×10^{-2}	6.300×10^{-2}	3.961×10^{-2}	2.376×10^{-2}	1.697×10^{-2}
$v_2 = 0, (J, K) = (2, 1)^+ \rightarrow (2, 1)^- (T = 55 \text{ K})$					
23 098 819.011(13)	13 708 497.929(8)	12 247 518.033(7)	7 699 606.337(4)	4 619 763.802(3)	3 299 831.287(2)
23 098 791.912	13 708 481.847	12 247 503.665	7 699 597.304	4 619 758.382	3 299 827.416
-3.517×10^{-1}	-2.087×10^{-1}	-1.865×10^{-1}	-1.172×10^{-1}	-7.034×10^{-2}	-5.024×10^{-2}
$v_2 = 0, (J, K) = (2, 2)^+ \rightarrow (2, 2)^- (T = 55 \text{ K})$					
23 722 633.336(4)	14 078 714.146(2)	12 578 278.545(2)	7 907 544.445(1)	4 744 526.667(1)	3 388 947.619(1)
23 722 633.363	14 078 714.162	12 578 278.559	7 907 544.454	4 744 526.673	3 388 947.623
3.401×10^{-4}	2.018×10^{-4}	1.803×10^{-4}	1.134×10^{-4}	6.802×10^{-5}	4.858×10^{-5}
$v_2 = 0, (J, K) = (3, 1)^+ \rightarrow (3, 1)^- (T = 55 \text{ K})$					
22 234 505.850(30)	13 195 552.433(18)	11 789 239.581(16)	7 411 501.950(10)	4 446 901.170(6)	3 176 357.979(4)
22 234 548.501	13 195 577.745	11 789 262.195	7 411 516.167	4 446 909.700	3 176 364.072
5.751×10^{-1}	3.413×10^{-1}	3.049×10^{-1}	1.917×10^{-1}	1.150×10^{-1}	8.215×10^{-2}
$v_2 = 0, (J, K) = (3, 3)^+ \rightarrow (3, 3)^- (T = 55 \text{ K})$					
23 870 129.185(8)	14 166 248.774(5)	12 656 484.191(4)	7 956 709.728(3)	4 774 025.837(2)	3 410 018.455(1)
23 870 129.190	14 166 248.777	12 656 484.194	7 956 709.730	4 774 025.838	3 410 018.456
6.290×10^{-5}	3.733×10^{-5}	3.335×10^{-5}	2.097×10^{-5}	1.258×10^{-5}	8.985×10^{-6}
$v_2 = 1, (J, K) = (2, 1)^+ \rightarrow (1, 1)^- (T = 55 \text{ K})$					
140 141.8067(230)	83 170.2117(136)	74 306.3662(122)	46 713.9356(77)	28 028.3613(46)	20 020.2581(33)
140 142.0763	83 170.3717	74 306.5092	46 714.0254	28 028.4153	20 020.2966
5.768×10^{-1}	3.423×10^{-1}	3.058×10^{-1}	1.923×10^{-1}	1.154×10^{-1}	8.239×10^{-2}
$v_2 = 1, (J, K) = (1, 0)^+ \rightarrow (0, 0)^- (T = 150 \text{ K})$					
466 245.8133(16)	276 703.7468(9)	247 214.1110(8)	155 415.2711(5)	93 249.16266(3)	66 606.5448(2)
466 245.5960	276 703.6178	247 213.9958	155 415.1987	93 249.1192	66 606.5137
-1.397×10^{-1}	-8.292×10^{-2}	-7.408×10^{-2}	-4.657×10^{-2}	-2.794×10^{-2}	-1.996×10^{-2}

Notes. Frequencies are given in kHz for $v_2 = 0$, and in MHz for $v_2 = 1$ inversion transitions, respectively.

^a Rotation-inversion frequencies taken from Hougen (1972) and Belov et al. (1998) for $v_2 = 0$ and $v_2 = 1$, respectively.

^b This work.

APPENDIX

MATRIX ELEMENTS $\langle \psi_{v_2, J, K} | h^{2k} | \psi_{v_2, J, K} \rangle$

The matrix elements $\langle \psi_{v_2, J, K} | h^{2k} | \psi_{v_2, J, K} \rangle$ used in this study (see (8–12)), and given below, were evaluated using non-rigid-inverter theory (Špirko 1983):

¹⁴NH₃

$$\begin{aligned} \langle 0^+, J, K | h^2 | 0^+, J, K \rangle &= 0.146555 + 0.561286 \\ &\times 10^{-4} J(J+1) - 0.939964 \times 10^{-4} K^2 \\ \langle 0^+, J, K | h^4 | 0^+, J, K \rangle &= 0.237773 \times 10^{-1} \\ &+ 0.138640 \times 10^{-4} J(J+1) - 0.258439 \times 10^{-4} K^2 \\ \langle 0^+, J, K | h^6 | 0^+, J, K \rangle &= 0.437755 \times 10^{-2} \\ &+ 0.349177 \times 10^{-5} J(J+1) - 0.654997 \times 10^{-5} K^2 \\ \langle 0^-, J, K | h^2 | 0^-, J, K \rangle &= 0.146948 + 0.548447 \times 10^{-4} \\ &\times J(J+1) - 0.916797 \times 10^{-4} K^2 \\ \langle 0^-, J, K | h^4 | 0^-, J, K \rangle &= 0.238600 \times 10^{-1} \\ &+ 0.136093 \times 10^{-4} J(J+1) - 0.253928 \times 10^{-4} K^2 \end{aligned}$$

$$\begin{aligned} \langle 0^-, J, K | h^6 | 0^-, J, K \rangle &= 0.439479 \times 10^{-2} \\ &+ 0.344209 \times 10^{-5} J(J+1) - 0.646296 \times 10^{-5} K^2 \\ \langle 1^+, J, K | h^2 | 1^+, J, K \rangle &= 0.116171 + 0.834249 \times 10^{-4} \\ &\times J(J+1) - 0.141828 \times 10^{-3} K^2 \\ \langle 1^+, J, K | h^4 | 1^+, J, K \rangle &= 0.216725 \times 10^{-1} \\ &+ 0.192492 \times 10^{-4} J(J+1) - 0.348637 \times 10^{-4} K^2 \\ \langle 1^+, J, K | h^6 | 1^+, J, K \rangle &= 0.497749 \times 10^{-2} \\ &+ 0.533994 \times 10^{-5} J(J+1) - 0.978084 \times 10^{-5} K^2 \\ \langle 1^-, J, K | h^2 | 1^-, J, K \rangle &= 0.130110 + 0.511772 \times 10^{-4} \\ &\times J(J+1) - 0.855298 \times 10^{-4} K^2 \\ \langle 1^-, J, K | h^4 | 1^-, J, K \rangle &= 0.246869 \times 10^{-1} \\ &+ 0.127964 \times 10^{-4} J(J+1) \\ &- 0.239061 \times 10^{-4} K^2 \\ \langle 1^-, J, K | h^6 | 1^-, J, K \rangle &= 0.570963 \times 10^{-2} \\ &+ 0.388773 \times 10^{-5} J(J+1) \\ &- 0.735440 \times 10^{-5} K^2 \end{aligned}$$

¹⁵NH₃

$$\begin{aligned}
\langle 0^+, J, K | h^2 | 0^+, J, K \rangle &= 0.146611 + 0.570977 \times 10^{-4} \\
&\quad \times J(J+1) - 0.949121 \times 10^{-4} K^2 \\
\langle 0^+, J, K | h^4 | 0^+, J, K \rangle &= 0.237785 \times 10^{-1} \\
&\quad + 0.141454 \times 10^{-4} J(J+1) - 0.261155 \times 10^{-4} K^2 \\
\langle 0^+, J, K | h^6 | 0^+, J, K \rangle &= 0.437480 \times 10^{-2} \\
&\quad + 0.356260 \times 10^{-5} J(J+1) - 0.661749 \times 10^{-5} K^2 \\
\langle 0^-, J, K | h^2 | 0^-, J, K \rangle &= 0.146986 + 0.558393 \times 10^{-4} \\
&\quad \times J(J+1) - 0.926613 \times 10^{-4} K^2 \\
\langle 0^-, J, K | h^4 | 0^-, J, K \rangle &= 0.238575 \times 10^{-1} + 0.138959 \times 10^{-4} \\
&\quad \times J(J+1) - 0.256772 \times 10^{-4} K^2 \\
\langle 0^-, J, K | h^6 | 0^-, J, K \rangle &= 0.439124 \times 10^{-2} + 0.351381 \times 10^{-5} \\
&\quad \times J(J+1) - 0.653285 \times 10^{-5} K^2 \\
\langle 1^+, J, K | h^2 | 1^+, J, K \rangle &= 0.116623 + 0.847064 \times 10^{-4} \\
&\quad \times J(J+1) - 0.142884 \times 10^{-3} K^2 \\
\langle 1^+, J, K | h^4 | 1^+, J, K \rangle &= 0.217434 \times 10^{-1} + 0.195906 \times 10^{-4} \\
&\quad \times J(J+1) - 0.351720 \times 10^{-4} K^2 \\
\langle 1^+, J, K | h^6 | 1^+, J, K \rangle &= 0.498937 \times 10^{-2} + 0.543581 \times 10^{-5} \\
&\quad \times J(J+1) - 0.986722 \times 10^{-5} K^2 \\
\langle 1^-, J, K | h^2 | 1^-, J, K \rangle &= 0.130136 + 0.523519 \times 10^{-4} \\
&\quad \times J(J+1) - 0.868616 \times 10^{-4} K^2 \\
\langle 1^-, J, K | h^4 | 1^-, J, K \rangle &= 0.246643 \times 10^{-1} + 0.131147 \times 10^{-4} \\
&\quad \times J(J+1) - 0.242555 \times 10^{-4} K^2 \\
\langle 1^-, J, K | h^6 | 1^-, J, K \rangle &= 0.569812 \times 10^{-2} + 0.397832 \times 10^{-5} \\
&\quad \times J(J+1) - 0.744856 \times 10^{-5} K^2
\end{aligned}$$

REFERENCES

Belov, S. P., Urban, Š., & Winnewisser, G. 1998, *JMoSp*, 189, 1

- Bordé, Ch. J., Bordé, J., Bréant, Ch., et al. 1985, Seventh International Conference on Laser Spectroscopy, Laser Spectrosc. VII, ed. T. W. Hänsch, & Y. R. Shen (Berlin Heidelberg: Springer-Verlag), 108
- Cazzoli, G., Dore, L., & Pazzarini, C. 2009, *A&A*, 507, 1707
- Cazzoli, G., & Pazzarini, C. 2013, *JPCA*, 117, 13759
- Cazzoli, G., & Pazzarini, C. 2014, *JMoSp*, 298, 31
- Dietiker, P., Miloglyadov, E., Quack, M., Schneider, A., & Seyfang, G. 2015, *JChPh*, 143, 244305
- Drouin, B. J., Yu, S. Y., & Pearson, J. C. 2010, see <http://hdl.handle.net/1811/46077/>
- Fichoux, H., Khelkhal, M., Rusinek, E., et al. 1998, *JMoSp*, 192, 169
- Fowler, P. W., & Špirko, V. 1990, *J. Chem. Soc. Faraday Trans.*, 86, 1991
- Gunther-Mohr, G. R., Townes, C. H., & Van Vleck, J. H. 1954, *PhRv*, 94, 1191
- Henkel, C., Braatz, J. A., Menten, K. M., & Ott, J. 2008, *A&A*, 485, 451
- Henkel, C., Jethava, N., Kraus, A., et al. 2005, *A&A*, 440, 893
- Ho, P. T. P., & Townes, C. H. 1983, *ARA&A*, 21, 239
- Hougen, J. T. 1972, *JChPh*, 57, 4207
- Hüttner, W., & Majer, W. 1984, *MolPh*, 52, 631
- Jansen, P., Bethlem, H. L., & Ubachs, W. 2014, *JChPh*, 140, 010901
- Kanekar, N. 2011, *ApJL*, 728, L12
- Kanekar, N., Ubachs, W., Menten, K. M., et al. 2015, *MNRAS*, 448, L104
- Kukulich, S. G. 1965, *PhRv*, 138, A1322
- Kukulich, S. G. 1967, *PhRv*, 156, 83
- Kukulich, S. G. 1975, *JChS*, 97, 5704
- Kukulich, S. G., & Wofsy, S. C. 1970, *JChPh*, 52, 5477
- Lemarchand, C., Triki, M., Darquié, B., et al. 2011, *NJPh*, 13, 073028
- Levshakov, S. A., Molaro, P., Lapinov, A. V., et al. 2010, *A&A*, 512, A32
- Maret, S., Faure, A., Scifoni, E., & Wiesenfeld, L. 2009, *MNRAS*, 399, 425
- Marshall, M. D., & Muentzer, J. S. 1981, *JMoSp*, 85, 322
- Murphy, T., Flambaum, V. V., Müller, S., & Henkel, C. 2008, *Sci*, 320, 1611
- Oddershede, J., Páidarová, I., & Špirko, V. 1992, *JMoSp*, 152, 342
- Ouhayoun, M., Bordé, C. J., & Bordé, J. 1977, *MolPh*, 33, 597
- Owens, A., Yurchenko, S. N., Thiel, W., & Špirko, V. 2015, *MNRAS*, 450, 3191
- Park, Y.-S. 2001, *A&A*, 376, 348
- Riechers, D. A., Bradford, C. M., Clements, D. L., et al. 2013, *Natur*, 496, 329
- Rubén, D. J., & Kukulich, S. G. 1974, *JChPh*, 61, 3780
- Sauer, S. P. A., Špirko, V., & Oddershede, J. 1991, *CP*, 153, 189
- Špirko, V. 1979, *MolPh*, 38, 1761
- Špirko, V. 1981, *MolPh*, 43, 723
- Špirko, V. 1983, *JMoSp*, 101, 30
- Špirko, V. 2014, *JPhCh Lett.*, 5, 919
- Thompson, R. I. 1975, *ApL&C*, 16, 3
- van Veldhoven, J., Jongma, R. T., Sartakov, B., Bongers, W. A., & Meijer, G. 2002, *PhRvA*, 66, 032501
- van Veldhoven, J., Küpper, J., Bethlem, H. L., et al. 2004, *EPJD*, 31, 337

NO EVAPORATIVE COOLING OF NITRIC OXIDE IN ITS GROUND STATE

Bibliographic record of the attached publication:

Augustovičová, L. D. and J. L. Bohn (2017). “No evaporative cooling of nitric oxide in its ground state.” In: *Physical Review A* 96, p. 042712.
DOI: [10.1103/PhysRevA.96.042712](https://doi.org/10.1103/PhysRevA.96.042712).

No evaporative cooling of nitric oxide in its ground state

Lucie D. Augustovičová* and John L. Bohn

JILA, NIST, and Department of Physics, University of Colorado, Boulder, Colorado 80309-0440, USA

(Received 8 August 2017; published 18 October 2017)

Cold collisions of $^{14}\text{N}^{16}\text{O}$ molecules in the $^2\Pi_{1/2}$ ground state, subject to electric and magnetic fields, are investigated. It is found that elastic collision rates significantly exceed state-changing inelastic rates only at temperatures above 0.5 K at laboratory-strength fields. It is found, however, that in very large fields, $>10^4$ V/cm, inelastic rates can be somewhat suppressed. Magnetic fields have a negligible influence on scattering for this nearly nonmagnetic state.

DOI: [10.1103/PhysRevA.96.042712](https://doi.org/10.1103/PhysRevA.96.042712)

I. INTRODUCTION

Progress in the production of ultracold molecules continues to accelerate, thanks especially to very recent experimental developments such as molecular laser cooling [1–6] and buffer-gas-loaded beams [7]. The former technique entails the real possibility of producing submicrokelvin molecular samples, although it is at present limited to a particular subset of molecules. By contrast, the buffer-gas-loaded beams make for very general sources but are still limited to sample temperatures of hundreds of millikelvins. At such temperatures the molecules are merely “very cold,” not yet ultracold. The true ultracold regime would produce molecules with such low translational temperatures that they collide in only a single partial wave, thus realizing the “ultimate molecular beam experiment”—that is, state preparation in a single quantum number of all degrees of freedom, including the partial wave of relative motion of reactants [8].

Thus for a number of chemically relevant species, notably radicals such as OH, CH, NH, and NO, additional cooling seems desirable and may potentially be achieved by evaporative cooling. This well-established technique selectively removes the highest-energy atoms from the sample and allows the rest to rethermalize at a lower temperature. It requires a relatively high elastic collision rate and, at the same time, a relatively low rate of inelastic or chemical collisions. The technique works well for alkali atoms, where it was noted long ago that the ratio of elastic-to-inelastic collision rates should exceed ~ 100 for evaporation to be effective [9].

For molecules, it has been somewhat problematic to achieve this ratio, owing to the rotational structure and dipole moments of the molecules, which provide many avenues for rearranging the energy and angular momentum, thus propelling molecules from trappable, weak-field-seeking states to untrapped strong-field-seeking states. Evaporative cooling is not completely out of the question for molecular radicals, however; evidence for evaporative cooling has been reported in OH [10,11].

Inelastic rates for many molecules have been studied at low temperatures in this context, as recently reviewed in [12]. Thus far, to our knowledge no one has investigated the situation

for the important atmospheric radical NO, which could be tamed by Stark deceleration [13] or other means [14,15]. Accordingly, here we undertake estimates of elastic and inelastic collisions of NO radicals at low temperature, in their $^2\Pi_{1/2}$ ground state. We focus on weak-electric-field-seeking states in the upper component of the zero-field parity doublet, as these would prove electrostatically trappable. Inelastic collisions are then those that leave one or both molecules in the untrapped-strong-field-seeking state after the collision.

In general, we find that inelastic collision rates are high for NO molecules in their $^2\Pi_{1/2}$ state, likely preventing evaporative cooling to temperatures below tens of millikelvins for this state. The rates are seen to vary slightly upon the application of an electric field but remain high for typically achievable laboratory fields $<10^4$ V/cm. We note, however, a lowering of the inelastic rates for fields higher than this. We note also that magnetic fields have little effect on the $^2\Pi_{1/2}$ state, as it possesses a minuscule magnetic moment.

II. THEORY

A. Molecular Hamiltonian

A single $^2\Pi$ molecule, treated as a rigid rotor and immersed in electric and magnetic fields, can be described by the effective Hamiltonian

$$H = H_{\text{SO}} + H_{\text{ROT}} + H_{\text{SR}} + H_{\text{HFS}} + H_{\text{S}} + H_{\text{Z}}, \quad (1)$$

where the individual terms represent the electronic spin-orbit coupling H_{SO} , rotational Hamiltonian H_{ROT} , spin-rotation coupling H_{SR} , hyperfine structure H_{HFS} , and Stark and Zeeman Hamiltonians H_{S} and H_{Z} . For ^{14}NO in its lowest vibronic state the spin-orbit coupling constant $A_{\text{SO}} = 123.146$ cm $^{-1}$ and the rotational constant $B_{\text{ROT}} = 1.696$ cm $^{-1}$ [16], thus satisfying the requirement that $A_{\text{SO}}\Lambda \gg B_{\text{ROT}}J$ for Hund’s case (a) to be a good representation. In the absence of Λ doubling, each J, M angular momentum state is doubly degenerate in the projection Ω of the angular momentum on the molecular axis,

$$\begin{aligned} |^2\Pi_{3/2}^{\pm}\rangle &= |n, \Lambda = \pm 1, S, \Sigma = \pm 1/2\rangle |\Omega = \pm 3/2, J, M\rangle, \\ |^2\Pi_{1/2}^{\pm}\rangle &= |n, \Lambda = \pm 1, S, \Sigma = \mp 1/2\rangle |\Omega = \pm 1/2, J, M\rangle, \end{aligned} \quad (2)$$

*Present address: Faculty of Mathematics and Physics, Department of Chemical Physics and Optics, Charles University, Ke Karlovu 3, CZ-12116 Prague 2, Czech Republic.

where n refers to any other unspecified quantum numbers. In the presence of H_{SO} and H_{SR} , the appropriate zero-field energy eigenstates are also eigenstates of parity $p = \pm$:

$$|^2\Pi_{3/2}p\rangle = \frac{1}{\sqrt{2}}(|^2\Pi_{3/2}^+\rangle + p(-1)^{J-S}|^2\Pi_{3/2}^-\rangle), \quad (3)$$

$$|^2\Pi_{1/2}p\rangle = \frac{1}{\sqrt{2}}(|^2\Pi_{1/2}^+\rangle + p(-1)^{J-S}|^2\Pi_{1/2}^-\rangle). \quad (4)$$

Of these states, the $\Omega = 1/2$ is the ground state of NO, with the lowest-lying $\Omega = 3/2$ around 170 K higher in energy. The dominant inelastic processes at ultralow temperatures will be state-changing collisions within the $J = 1/2$, $\Omega = 1/2$ manifold, which we focus on here.

Moreover, the ^{14}N nucleus has spin $I = 1$ (the spin of the ^{16}O nucleus is 0), whereby the appropriate quantum numbers are those of the hyperfine interaction, where \vec{J} and \vec{I} are coupled to form \vec{F} in the laboratory frame. Thus the $J = 1/2$ level of interest here splits into two hyperfine levels, $F = 1/2$ and $F = 3/2$. So we work in the basis set $|\eta, \Omega, J, I, F, M_F; p\rangle$, where M_F is F 's projection onto the laboratory axis and η is a general index which represents all other considered quantum numbers. For simplicity in the following, we abbreviate this state vector $|FM_F, p\rangle$. We adopt the hyperfine levels for the $^2\Pi_{1/2}$, $J = 1/2$ rotational level from Ref. [17].

In an applied homogeneous electric field, $\vec{\mathcal{E}}$, whose direction specifies the space-fixed z axis, the effective Hamiltonian is augmented by the Stark-effect term $H_S = -\vec{d}_s \cdot \vec{\mathcal{E}}$, whose matrix elements are given elsewhere [18,19]. The electric dipole moment of NO in its ground state is relatively small, $d = 0.15872$ D [20]. For this reason, fairly large electric fields are required to influence collisions of NO molecules, as we see below.

Finally, in the presence of an external magnetic field the molecule experiences a Zeeman interaction with Hamiltonian $H_Z = -\vec{\mu} \cdot \vec{B}$. However, in the $\Omega = 1/2$ state, contributions to the molecular magnetic moment due to the electron's orbital motion and spin nearly cancel, leaving this state with a negligible g factor, ~ 0.0007 [21]. We therefore neglect this interaction in most of what follows.

Figure 1 demonstrates the Stark effect for a single NO molecule in the $^2\Pi_{1/2}$ ground state. States of opposite parity repel as the field is increased, and the Stark effect transitions from quadratic to linear at a characteristic electric field $\mathcal{E}_0 = \Delta_\Lambda/2d \sim 2500$ V/cm. The states in this figure are labeled with the quantum numbers \vec{F} and $|M_F\rangle$, noting that M_F referred to the electric-field axis is a good quantum number, but F is not, and that $\pm M_F$ states remain degenerate in an electric field. Those states whose energies rise with the electric field are the weak-field-seeking states that can be trapped electrostatically. Their collisions that result in molecules in the lower-energy, high-field-seeking states are the collisions that the experiment wishes to avoid, at least for evaporative cooling purposes.

B. Molecular scattering

In general, collisions that remove molecules from the weak-field-seeking states can take two forms: inelastic collisions from the upper to the lower states depicted in Fig. 1 and chemical reactions. Taken together, these processes—referred

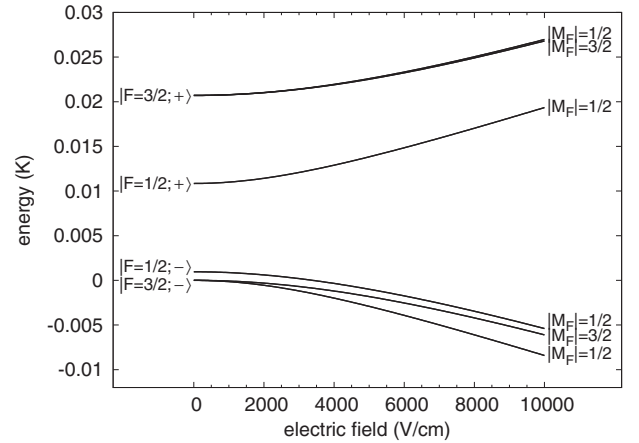


FIG. 1. Stark energies of the hyperfine $|\vec{F}, M_F, +/\rangle$ and Λ -doublet levels for $J = 1/2$ of the $^2\Pi_{1/2}$ state of the NO molecule.

to collectively as “quenching”—are generally indistinguishable, resulting only in loss of molecules from the trap, unless products are detected. From the thermodynamic point of view, NO molecules are certainly exoergic in collision and can undergo the reaction $2\text{NO} \rightarrow \text{N}_2 + \text{O}_2$ with enthalpy change $\Delta H = -180$ kJ/mol, thus releasing 21 000 K of kinetic energy, a devastating blow to trapping. However, from the kinetics point of view, this reaction is rendered unlikely due to the very high activation energy 209 kJ/mol $\doteq 25$ 000 K [22]. The reaction probability will therefore be taken as negligible, although of course it could conceivably be enhanced by resonant tunneling [23].

We therefore replace the short-range physics with a hard-wall boundary condition at $R = 30 a_0$. State-changing physics is then described by the long-range van der Waals and dipole-dipole interactions. The former is taken to be isotropic and is given by $-C_6/R^6$, where we take $C_6 = 35.2 E_h a_0^6$ as a lower estimate of the actual C_6 obtained from the London formula, using the mean static polarizability for NO [24]. The long-range dipole-dipole interaction is given by

$$\begin{aligned} V_{\text{dd}}(\vec{R}) &= -\frac{3(\hat{R} \cdot \vec{d}_1)(\hat{R} \cdot \vec{d}_2) - \vec{d}_1 \cdot \vec{d}_2}{4\pi\epsilon_0 R^3} \\ &= -\frac{\sqrt{6}}{4\pi\epsilon_0 R^3} \sum_{q=-2}^2 (-1)^q C_q^2(\hat{R})(d_1 \otimes d_2)_{-q}^2 \end{aligned} \quad (5)$$

where $\vec{R} = R\hat{R}$ is the intermolecular separation vector in relative coordinates, and $(d_1 \otimes d_2)_{-q}^2$ is the $-q$ component of the compound irreducible second-rank tensor product of the rank-1 tensors that act as the electric dipole moment operators on the individual variables of molecules 1 and 2.

Basis functions for scattering calculations consist of states of the separated molecules, plus partial waves in the expansion of the relative motion. These states are denoted $|\vec{F}_1, M_{F1}; p_1\rangle |\vec{F}_2, M_{F2}; p_2\rangle |L, M_L\rangle$, where the \vec{F} notation is used to emphasize that these states are eigenstates of the molecules in an electric field, where F is not, strictly, a good quantum number. For simplicity in the following, we employ the shorthand notation $|\vec{F}, M_F; p\rangle \equiv |\eta, \Omega, J, I, \vec{F}, M_F; p\rangle$ for

individual molecules. Basis functions symmetrized under particle exchange are given by (for $\tilde{F}_1 \neq \tilde{F}_2$ or $M_{F1} \neq M_{F2}$ or $p_1 \neq p_2$)

$$\begin{aligned} & |\tilde{F}_1, M_{F1}; p_1\rangle |\tilde{F}_2, M_{F2}; p_2\rangle |L, M_L\rangle_S \\ &= \frac{1}{\sqrt{2}} \{ |\tilde{F}_1, M_{F1}; p_1\rangle |\tilde{F}_2, M_{F2}; p_2\rangle |L, M_L\rangle \\ & \pm (-1)^L |\tilde{F}_2, M_{F2}; p_2\rangle |\tilde{F}_1, M_{F1}; p_1\rangle |L, M_L\rangle \}, \quad (6) \end{aligned}$$

with a plus sign for bosonic molecules and a minus sign for fermionic molecules. For the indistinguishable hyperfine kets this relation immediately ensures that only even partial waves are allowed for indistinguishable bosons and only odd partial waves for indistinguishable fermions. In the present case of fermionic NO molecules, it means that a totally antisymmetric wave function can be expanded onto odd L components.

The total wave function $\Psi(\vec{R})$ is represented as a column vector having the n th component of the form

$$\Psi_n(\vec{R}) = \frac{\psi_n(R)}{R} [|\tilde{F}_1, M_{F1}; p_1\rangle |\tilde{F}_2, M_{F2}; p_2\rangle |L, M_L\rangle_S]_n,$$

where ψ_n is the diabatic solution of the set of coupled radial equations

$$\left[\sum_{m=1}^{N_{\text{ch}}} \left(-\frac{\hbar^2}{2m_{\text{red}}} \frac{d^2}{dR^2} + E_m \right) \delta_{nm} + V_{nm} \right] \psi_m = E_{\text{tot}} \psi_n, \quad (7)$$

with E_m being the threshold energy of the pair of molecules in channel m and $E_{\text{tot}} = E_c + E_n$ the total energy written in terms of the collision energy E_c above the threshold energy of channel n . Here V includes the dipole-dipole interaction, whose matrix elements are described elsewhere [25], and the centrifugal energy, which is diagonal with matrix elements $\hbar^2 L(L+1)/(2m_{\text{red}}R^2)$. This Hamiltonian preserves the projection of the total molecular angular momentum onto the field axis, $M_{\text{tot}} = M_{F1} + M_{F2} + M_L$.

The set of coupled Schrödinger equations, (7), in multichannel scattering is solved using the log-derivative propagator method [26]. Matching the log-derivative matrix with the asymptotic solution for open channels at large R yields the open-open submatrix of the reaction K matrix and, subsequently, the scattering matrices S and T . For a given incident channel i , we identify the partial-wave cross sections

$$\sigma_{L,i \rightarrow f}(E) = 2 \times \frac{\pi}{k_i^2} \sum_{M_L} \sum_{f, L', M'_L} |\langle i, L, M_L | T | f, L', M'_L \rangle|^2,$$

where $f = i$ for elastic scattering and $f \neq i$ for inelastic scattering, and the factor of 2 is required for indistinguishable collision partners. These cross sections, in turn, are added to yield total cross sections averaged over all incident collision directions,

$$\sigma_{i \rightarrow f}(E) = \sum_L \sigma_{L,i \rightarrow f}(E).$$

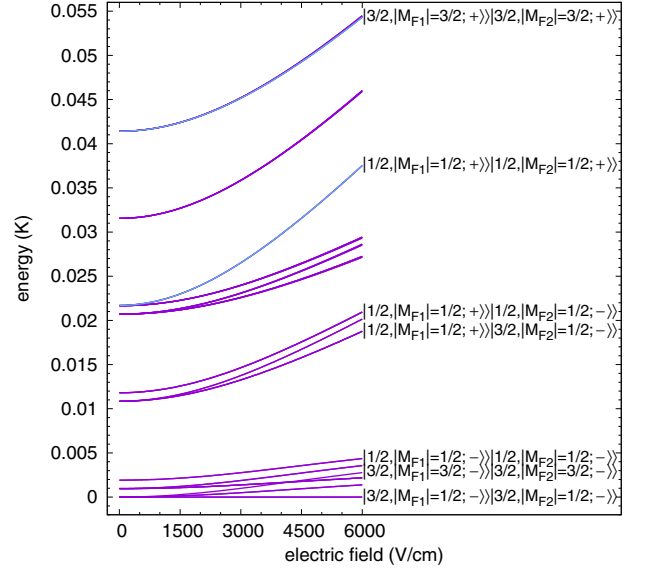


FIG. 2. Threshold energies for two NO collisional molecules related to the $|3/2, |M_{F1}|=1/2; -\rangle\rangle |3/2, |M_{F2}|=1/2; -\rangle\rangle_S$ lowest threshold. The light lines indicate the collision channels of our interest: the $|1/2, |M_{F1}|=1/2; +\rangle\rangle |1/2, |M_{F2}|=1/2; +\rangle\rangle_S$ and $|3/2, |M_{F1}|=3/2; +\rangle\rangle |3/2, |M_{F2}|=3/2; +\rangle\rangle_S$ channels.

III. RESULTS AND DISCUSSION

The main goal of the present work is to predict theoretically whether evaporative cooling of $^{14}\text{N}^{16}\text{O}$ molecules in their ground rovibrational $^2\Pi_{1/2}$ state trapped in electrostatic traps is feasible. To this end, we consider the weak-field-seeking states, namely, those whose energy rises with the electric field in Fig. 1. The molecules in this case have the quantum numbers $|\tilde{F}M_F; p\rangle = |3/2, 1/2; +\rangle$ and $|3/2, 3/2; +\rangle$. Scattering calculations shown below are computed for these states using partial waves up to $L = 5$, which converge with the shown cross sections within approximately 20%, adequate for our present purposes.

Based on models similar to the one we use here, cold collisions of $^2\Pi_{3/2}$ molecules have been studied previously [18, 19, 25, 27]. Generally speaking, elastic cross sections can be made large in these states by applying an electric field, given the generically high cross sections of dipolar scattering. However, it was also found that inelastic scattering grows in an electric field, as the molecules, once polarized, can exert torques on one another, thereby changing their orientation and driving inelastic collisions.

Prospects for mitigating this loss have been considered. For $^2\Pi_{3/2}$ molecules, it was found that applying a magnetic field could drive the rates down, partly by decreasing the effective coupling between entrance and exit channels [19] and partly due to a novel long-range shielding potential [10]. This mechanism is, however, ineffective in the $^2\Pi_{1/2}$ state, which has a negligible magnetic moment. For Σ molecules, an additional shielding mechanism is predicted to occur when the energy of the incident threshold crosses the energy of another threshold of states with opposite parity [28–31]. Looking at

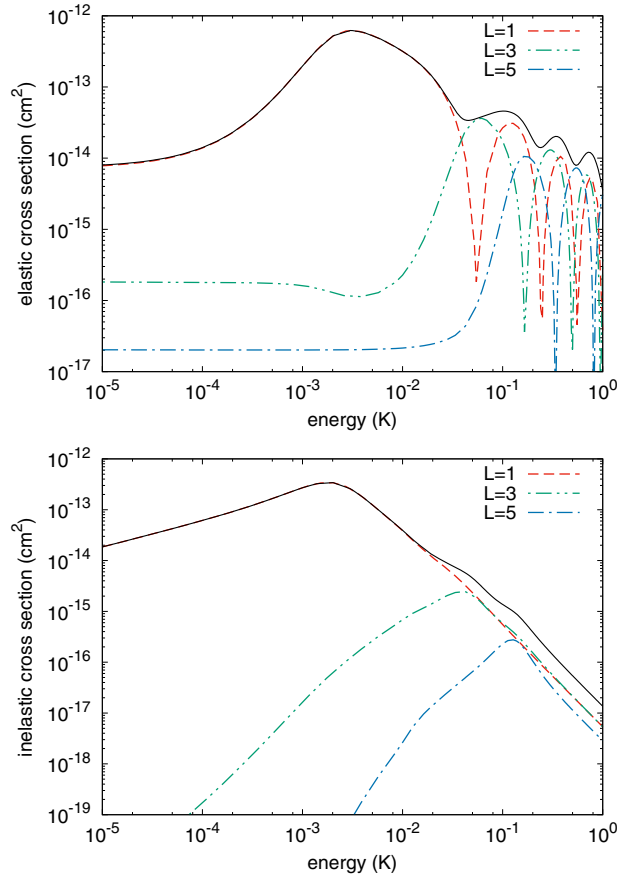


FIG. 3. Elastic (upper) and inelastic (lower) cross sections versus the collision energy for an applied electric field of 6000 V/cm, showing individual partial-wave contributions $L = 1, 3, 5$ for incident channel $|1/2, 1/2; +\rangle|1/2, 1/2; +\rangle|1, 0\rangle_S$. The solid line denotes the full cross section.

the thresholds of interest for NO, however (Fig. 2), this event seems not to occur at realistic electric-field values.

Thus the only hope for suppressing inelastic collisions in the $^2\Pi_{1/2}$ state of NO seems to be to exploit the fact that this molecule is a fermion. This means that identical NO molecules will necessarily collide with the incident partial wave $L = 1$, in which case the centrifugal barrier associated with this channel can provide a certain shielding against inelastic scattering. This shielding mechanism would be effective below the p -wave centrifugal barrier, about 4 mK in zero field.

Examples of total and partial cross sections, as subjected to an electric field of 6000 V/cm, are shown in Fig. 3. Elastic cross sections are shown in the upper panel, while inelastic cross sections are shown in the lower panel. The collision energy within the wide range 10 μ K through 1 K is considered; note that Stark deceleration down to ~ 100 mK temperatures is possible experimentally. At energies below ~ 1 mK, cross sections scale according to the usual Wigner threshold laws. Elastic cross sections are independent of energy in all partial waves, as appropriate to dipolar scattering, while inelastic cross sections scale with the collision energy E_c as $\sigma_{\text{inel}} \sim E_c^{L-1/2}$. Thus elastic scattering will eventually

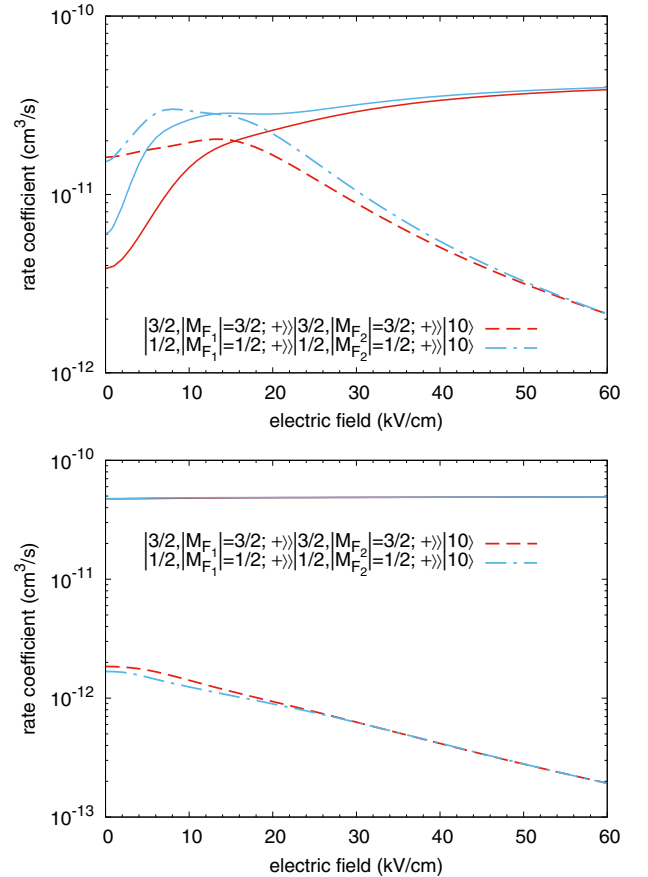


FIG. 4. Rate coefficients for elastic (solid curves) and inelastic (dashed curves) scattering as a function of the electric field for the two incident channels considered in the text. The collision energy is fixed at the value $E_c = 1$ mK (upper panel) and $E_c = 100$ mK (lower panel).

dominate inelastic scattering at sufficiently low temperatures, but Fig. 3 shows that 10^{-5} K is not yet low enough.

At temperatures above 10 mK, the energy dependence of the cross sections is different. For elastic scattering of dipoles, once the energy is above the threshold region and several partial waves contribute, the cross section is expected to scale according to the eikonal approximation, $\sigma_{\text{el}} \sim 1/\sqrt{E_c}$ [32]. This behavior is seen to approximately hold, even in the energy range shown, where a small number of partial waves is relevant and the cross sections exhibit Ramsauer-Townsend minima in each partial wave. In this energy range the inelastic cross section decreases even more rapidly, as $\sigma_{\text{inel}} \sim 1/E_c^2$. This behavior is different from the $1/E_c^{2/3}$ scaling predicted by the Langevin capture model. This is not in itself surprising, since only a small number of partial waves are relevant at this energy, yet the Langevin approximation is more appropriate for the many-partial wave, semiclassical regime.

In any event, elastic scattering is seen to exceed inelastic scattering only at collision energies well above 10 mK. This temperature therefore presents a bottleneck for evaporative

cooling from Stark decelerator temperatures down to the threshold regime.

It is worthwhile to study whether an electric field can alter the $\sigma_{\text{el}}/\sigma_{\text{inel}}$ ratio. Accordingly, Fig. 4 shows the elastic and inelastic rate constants, defined by $K = v_i\sigma$ in terms of the incident velocity v_i , as a function of the electric field. Both a low energy (1 mK; upper panel) and a higher energy (100 mK; lower panel) are shown. After an initial rise of the inelastic rates, a new effect appears, namely, that the inelastic rate coefficients decrease in large fields. At these higher fields the elastic rates remain high and constant, as expected of the scattering of polarized dipoles.

This dependence on the electric field at high field can be seen in the Born approximation. Consider scattering from an incident channel with wave number k_i to a distinct final

channel with wave number k_f . The T -matrix element giving the probability amplitude of the transition is [25]

$$\langle i|T|f\rangle = 2\left(\frac{2m_{\text{red}}}{\hbar^2}\right)\sqrt{k_i k_f} \times \int_0^\infty R^2 dR j_{L_i}(k_i R) \frac{C_{i,f}}{R^3} j_{L_f}(k_f R), \quad (8)$$

where L_i and L_f are the partial waves of the incident and final channels, j_L 's are spherical Bessel functions, and $C_{i,f}/R^3$ is the matrix element of the long-range dipolar interaction between the two channels. Note that $C_{i,f}$ is, in general, a function of the electric field, since the channel indices refer to molecular states as dressed by the electric field. Working out the integral, the T -matrix elements are

$$\langle i|T|f\rangle = \frac{2\pi m_{\text{red}} C_{i,f}}{\hbar^2} \left[\frac{\Gamma\left(\frac{L_i+L_f}{2}\right)}{4\Gamma\left(\frac{-L_i+L_f+3}{2}\right)\Gamma(L_i+3/2)} \right] \frac{k_i^{L_i+1/2}}{k_f^{L_f-1/2}} F\left(\frac{L_i+L_f}{2}, \frac{L_i-L_f-1}{2}; L_i+3/2; \left(\frac{k_i}{k_f}\right)^2\right), \quad (9)$$

where F is a hypergeometric function. In the limit of low collision energy, scattering occurs primarily from outside the classical turning points of the potentials, whereby a perturbative Born approximation that captures the long-range physics is relevant.

For ultracold collisions, k_i remains small, while k_f continues to grow with the electric field. Quantitatively, the outgoing wave number scales with the field \mathcal{E} , for large fields, as

$$k_f = \sqrt{(2m_{\text{red}}/\hbar^2)(E_{\text{tot}} - E_f)} \propto \sqrt{d\mathcal{E}}, \quad (10)$$

given that the threshold energy is proportional to the field in the linear Stark regime. Moreover, in this limit the argument

$(k_i/k_f)^2$ of the hypergeometric function vanishes, whereby $F = 1$ and, for $L_f = 1$ final channels, the ultracold inelastic rate should scale as $K_{\text{inel}} \propto 1/k_f \propto 1/\sqrt{\mathcal{E}}$.

This behavior is approached in the field regime where the molecules are fully polarized and the potential couplings $C_{i,f}$ saturate with the field. As shown in Fig. 5, this saturation has not yet quite occurred for fields as large as 40 kV/cm. In any event, the suppression effect would require fields greater than 10 kV/cm, which are likely unfeasible in electrostatic traps.

Finally, we note that we have carried out scattering calculations under the influence of a magnetic field. The cross sections show negligible dependence on the magnetic field up to 1000 G, owing to the small g factor of the $^2\Pi_{1/2}$ state. A greater influence of magnetic field may be expected for the metastable $^2\Pi_{3/2}$, $J = 3/2$ state. This remains a subject for future investigations.

IV. CONCLUSION

We have performed an analysis of the possibility of evaporative cooling of NO molecules in their ground electronic $\Omega = 1/2$ state and computed scattering cross sections and rate coefficients under the influence of electric fields. We find that the ratio of elastic-to-inelastic rates is favorable at higher temperatures, ~ 0.5 K, and it appears that applying an electric field can improve the prospects for evaporative cooling even at 100 mK. However, the required fields are probably unrealistically high with the traps as currently built.

ACKNOWLEDGMENTS

We acknowledge funding from the U.S. Army Research Office under ARO Grant No. W911NF-12-1-0476 and useful discussions with B. van der Meerakker.

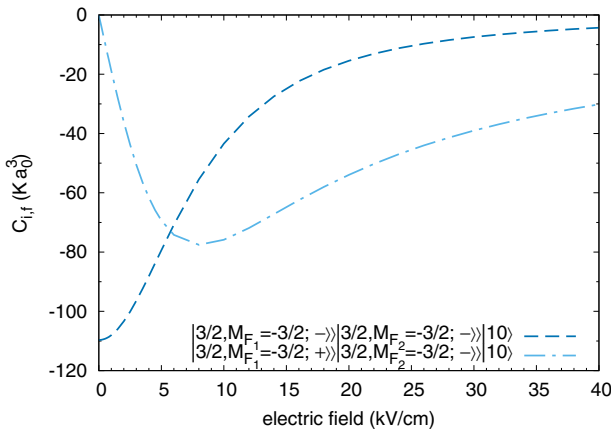


FIG. 5. Off-diagonal matrix elements $C_{i,f}$ of dipole-dipole interaction without a radial dependence as functions of the electric field for outbound channels indicated in the legend and inbound channel $|3/2, -3/2; +\rangle|3/2, -3/2; +\rangle|1, 0\rangle_S$.

- [1] E. S. Shuman, J. F. Barry, and D. DeMille, *Nature* **467**, 820 (2010).
- [2] J. F. Barry, D. J. McCarron, E. B. Norrgard, M. H. Steinecker, and D. DeMille, *Nature* **512**, 286 (2014).
- [3] M. Yeo, M. T. Hummon, A. L. Collopy, B. Yan, B. Hemmerling, E. Chae, J. M. Doyle, and J. Ye, *Phys. Rev. Lett.* **114**, 223003 (2015).
- [4] I. Kozyryev, L. Baum, K. Matsuda, and J. M. Doyle, *Chem. Phys. Chem.* **17**, 3641 (2016).
- [5] E. Chae, L. Anderegg, B. L. Augenbraun, A. Ravi, B. Hemmerling, N. R. Hutzler, A. L. Collopy, J. Ye, W. Ketterle, and J. M. Doyle, *New J. Phys.* **19**, 033035 (2017).
- [6] L. Anderegg, B. Augenbraun, E. Chae, B. Hemmerling, N. R. Hutzler, A. Ravi, A. Collopy, J. Ye, W. Ketterle, and J. Doyle, *Phys. Rev. Lett.* **119**, 103201 (2017).
- [7] N. R. Hutzler, H.-I. Lu, and J. M. Doyle, *Chem. Rev.* **112**, 4803 (2012).
- [8] S. Ospelkaus, K.-K. Ni, D. Wang, M. H. G. de Miranda, B. Neyenhuis, G. Quéméner, P. S. Julienne, J. L. Bohn, D. S. Jin, and J. Ye, *Science* **327**, 853 (2010).
- [9] C. R. Monroe, E. A. Cornell, C. A. Sackett, C. J. Myatt, and C. E. Wieman, *Phys. Rev. Lett.* **70**, 414 (1993).
- [10] B. K. Stuhl, M. T. Hummon, M. Yeo, G. Quéméner, J. L. Bohn, and J. Ye, *Nature* **492**, 396 (2012).
- [11] D. Reens, H. Wu, T. Langen, and J. Ye, [arXiv:1706.02806](https://arxiv.org/abs/1706.02806).
- [12] N. Balakrishnan, *J. Chem. Phys.* **145**, 150901 (2016).
- [13] S. N. Vogels, J. Onvlee, S. Chefdeville, A. van der Avoird, G. C. Groenenboom, and S. Y. T. van de Meerakker, *Science* **350**, 787 (2015).
- [14] B. J. Bichsel, M. A. Morrison, N. Shafer-Ray, and E. R. I. Abraham, *Phys. Rev. A* **75**, 023410 (2007).
- [15] M. S. Elioff, J. J. Valentini, and D. W. Chandler, *Science* **302**, 1940 (2003).
- [16] T. D. Varberg, F. Stroh, and K. M. Evenson, *J. Mol. Spectrosc.* **196**, 5 (1999).
- [17] W. Meerts and A. Dymanus, *J. Mol. Spectrosc.* **44**, 320 (1972).
- [18] A. V. Avdeenkov and J. L. Bohn, *Phys. Rev. A* **66**, 052718 (2002).
- [19] C. Ticknor and J. L. Bohn, *Phys. Rev. A* **71**, 022709 (2005).
- [20] D. R. Lide, *CRC Handbook of Chemistry and Physics*, 84th ed. (CRC Press, Boca Raton, FL, 2003).
- [21] M. Mizushima, J. T. Cox, and W. Gordy, *Phys. Rev.* **98**, 1034 (1955).
- [22] G.-D. Zhou, *Fundamentals of Structural Chemistry* (World Scientific, Singapore, 1993).
- [23] E. Bodo, F. A. Gianturco, N. Balakrishnan, and A. Dalgarno, *J. Phys. B* **37**, 3641 (2004).
- [24] N. J. Bridge and A. D. Buckingham, *Proc. R. Soc. A* **295**, 334 (1966).
- [25] A. V. Avdeenkov and J. L. Bohn, *Phys. Rev. A* **71**, 022706 (2005).
- [26] B. R. Johnson, *J. Comput. Phys.* **13**, 445 (1973).
- [27] G. Quéméner and J. L. Bohn, *Phys. Rev. A* **88**, 012706 (2013).
- [28] A. V. Avdeenkov, M. Kajita, and J. L. Bohn, *Phys. Rev. A* **73**, 022707 (2006).
- [29] G. Wang and G. Quéméner, *New J. Phys.* **17**, 035015 (2015).
- [30] G. Quéméner and J. L. Bohn, *Phys. Rev. A* **93**, 012704 (2016).
- [31] M. L. González-Martínez, J. L. Bohn, and G. Quéméner, *Phys. Rev. A* **96**, 032718 (2017).
- [32] J. L. Bohn, M. Cavagnero, and C. Ticknor, *New J. Phys.* **11**, 055039 (2009).

NO EVAPORATIVE COOLING IN THE $^2\Pi_{3/2}$ STATE

Bibliographic record of the attached publication:

Augustovičová, L. D. and J. L. Bohn (2018). "NO evaporative cooling in the $^2\Pi_{3/2}$ state." In: *Physical Review A* 97, p. 062703.
DOI: [10.1103/PhysRevA.97.062703](https://doi.org/10.1103/PhysRevA.97.062703).

NO evaporative cooling in the ${}^2\Pi_{3/2}$ state

Lucie D. Augustovičová* and John L. Bohn

JILA, NIST, and Department of Physics, University of Colorado, Boulder, Colorado 80309-0440, USA



(Received 9 March 2018; published 8 June 2018)

The scattering at ultralow temperatures of fermionic ${}^{14}\text{N}{}^{16}\text{O}$ molecules in the metastable ${}^2\Pi_{3/2}$ is considered, under the influence of parallel electric and magnetic fields. It is found that a magnetic field of several thousand Gauss can enhance the ratio of elastic-to-inelastic collision rates. The magnetic field can therefore assist the electric field in increasing this ratio. Evaporative cooling of NO is feasible only in the presence of combined magnetic and electric fields and for temperatures above about 70 mK.

DOI: [10.1103/PhysRevA.97.062703](https://doi.org/10.1103/PhysRevA.97.062703)

I. INTRODUCTION

In a recent paper [1], we discussed the collision cross sections of ground-state nitric oxide (NO) molecules at low temperatures, below 1 K. This work was motivated by the possibility of evaporatively cooling this species, if it were to be produced in a sub-Kelvin sample by buffer-gas cooling, Stark deceleration, or other means [2–5]. In Ref. [1] it was found that elastic rate constants greatly exceed inelastic rate constants only at temperatures above about one hundred millikelvin. Evaporative cooling would therefore be limited to temperatures on this order, thus succumbing to the “millikelvin catastrophe” common in cold molecules [6–8].

In the ${}^2\Pi_{1/2}$ ground state considered in Ref. [1], the application of a very large electric field (of order tens of kV/cm) was found to suppress the inelastic rates, but this field is likely too large to usefully do so in the laboratory. The application of a magnetic field would do little to suppress collisions in this state, which has a negligible magnetic moment. By contrast, the metastable excited ${}^2\Pi_{3/2}$ state of NO does possess a magnetic moment and could in principle be influenced by magnetic, as well as electric, fields. Magnetic fields have been predicted to suppress inelastic scattering of ${}^2\Pi_{3/2}$ OH molecules [9–11], leading to ongoing efforts to achieve evaporative cooling in this radical [12].

In this paper we therefore extend the work of Ref. [1] to the metastable state of NO, studying the influence of combined (parallel) electric and magnetic fields on collision rates. While the addition of a magnetic field has some modest additional effect, the conclusion remains that evaporative cooling of NO below 100 mK is problematic.

II. THEORY

A. NO molecular structure in absence of external field

In this section we briefly describe the structure of the NO molecule. The NO ground-state structure is considered in

Ref. [1], to which we refer readers for details. In the rigid-rotor approximation, the internal structure of the ground ${}^2\Pi$ electronic state, ground vibrational state includes the spin-orbit (SO) interaction, rotation (ROT), spin-rotation (SR) interaction, Λ -doubling structure, and nitrogen hyperfine interaction (HFS) in ${}^{14}\text{N}{}^{16}\text{O}$. The well-defined axial components Λ and Σ are combined to define Ω , a good quantum number in the Hund’s case-(a) representation. Components of Λ doubling are $|\Omega| = 1/2$ and $|\Omega| = 3/2$, both doubly degenerate, of which ${}^2\Pi_{3/2}$ is the higher-lying state. Their separation is determined by a spin-orbit fitting parameter of 123.146 cm^{-1} [13], far enough for neglecting the lower state in our cold-collision calculation. For these purposes the nearest rotational level $J = 5/2$ can be neglected because the ${}^{14}\text{NO}$ rotational constant is 1.696 cm^{-1} [13].

The total angular momentum of the molecule \vec{J} has definite projections on the space-fixed axis M and on the molecule-fixed axis Ω . The eigenvectors of $H_{\text{SO}} + H_{\text{ROT}} + H_{\text{SR}}$ for each J, M are doubly degenerate in Ω :

$$|{}^2\Pi_{3/2}^{\pm}\rangle = |\Lambda = \pm 1, S, \Sigma = \pm 1/2\rangle |\Omega = \pm 3/2, J, M\rangle. \quad (1)$$

In zero electric field, these states are combined into a parity doublet $+/-$. The parity basis is a linear combination of (1) that is labeled according to their total parity under the inversion operation E^* for each rotational level,

$$|{}^2\Pi_{3/2}(+/-)\rangle = \frac{1}{\sqrt{2}}(|{}^2\Pi_{3/2}^+\rangle \pm (-1)^{J-S}|{}^2\Pi_{3/2}^-\rangle). \quad (2)$$

These functions can also be classified according to $p = e$ or f symmetry, total parity exclusive of a $(-1)^{J-1/2}$ rotational factor. The Λ -doubling constant is $\Delta_{\Lambda} = 5 \times 10^{-5}\text{ K}$ [14] which is about 350 times smaller than for the ${}^2\Pi_{1/2}$ state.

In addition, the ${}^{14}\text{N}$ nucleus has spin $I = 1$ (the spin of the ${}^{16}\text{O}$ nucleus is zero), we extend the basis function set to also include \vec{I} , coupled to \vec{J} to form \vec{F} in the laboratory frame, thus the $J = 3/2$ level of our interest splits into three hyperfine components $F = 1/2$, $F = 3/2$, and $F = 5/2$. This identifies the molecular basis set as $|\eta, |\Omega\rangle, J, I, F, M_F; p\rangle$, where M_F is the projection of F onto the laboratory axis, and η is a general index which represents all other quantum numbers. Within the ${}^2\Pi_{3/2}$, $J = 3/2$ manifold, we employ the shorthand notation $|F, M_F; p\rangle \equiv |\eta, |\Omega\rangle, J, I, F, M_F; p\rangle$.

*Present address: Charles University, Faculty of Mathematics and Physics, Department of Chemical Physics and Optics, Ke Karlovu 3, CZ-12116 Prague 2, Czech Republic.

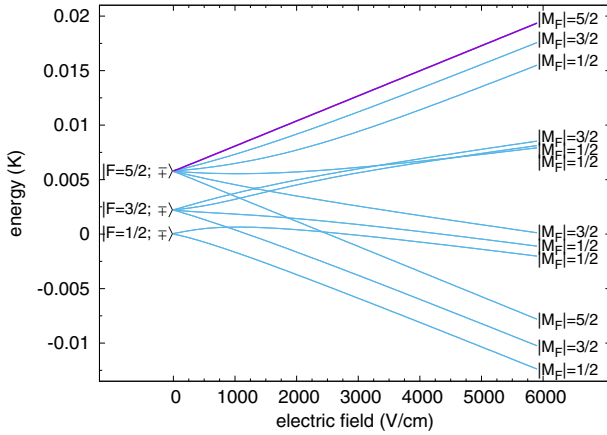


FIG. 1. Stark energies of the hyperfine $|F, M_F; e/f\rangle$ and Λ -doublet levels for $J = 3/2$ of the ${}^2\Pi_{3/2}$ state of the NO molecule at zero magnetic field. Each line is doubly degenerate in M_F . The hyperfine state of our interest $|5/2, 5/2; f\rangle$ is highlighted.

B. Stark and Zeeman field interactions with NO

In the presence of a homogeneous electric field $\vec{\mathcal{E}}$ whose direction specifies the space-fixed Z axis, the effective Hamiltonian is augmented by the Stark-effect term $H_S = -\vec{d}_s \cdot \vec{\mathcal{E}}$. The space-fixed component of the electric-dipole moment of the molecule $d_s^Z = T_0^1(\vec{d}_s)$ needs to be rotated to the molecule-fixed axis, to which the electric-dipole moment \vec{d}_m is referred by using a Wigner D matrix, $T_0^1(\vec{d}_s) = \sum_q D_{q0}^{(1)*} T_q^1(\vec{d}_m)$. The electric-field Hamiltonian becomes

$$H_S = -\mathcal{E} \sum_q D_{q0}^{(1)*} T_q^1(\vec{d}_m).$$

In the $|J, M, \Omega\rangle$ basis, matrix elements of H_S are well known, and with the use of the Wigner–Eckart theorem these terms are finally recast into the $F M_F$ -parity basis. We will not explicitly express terms here but refer to, e.g., Ref. [9].

The Stark effect for a single NO molecule in its first-excited electronic state, $J = 3/2$ is demonstrated in Fig. 1. In the absence of a magnetic field, the hyperfine components are degenerate for $|M_F|$ levels. The opposite-parity states repel as the field is increased. In the large- \mathcal{E} limit parity ceases to be a good quantum number. In this case we follow convention and label the lower and upper states of the doublet as e and f states, respectively (see below). The critical field where the Stark effect transforms from quadratic to linear is around $\mathcal{E}_0 = \Delta_\Lambda/2d \sim 7$ V/cm, based on the dipole moment of NO, $d = 0.15872$ D [15]. For fields larger than \mathcal{E}_0 the H_S term dominates over the hyperfine H_{HFS} term in the molecular effective Hamiltonian and F is no longer a good quantum number. However, H_S commutes with F_Z , resulting in a block-diagonal Hamiltonian matrix elements with respect to the magnetic quantum number M_F .

To transform smoothly from the zero-field Λ -doubling Hamiltonian basis to the strong field basis for fixed values of J and M , it is convenient to introduce a mixing angle δ_M

and denote lower and upper states of Λ -doublet pairs by

$$|e\rangle = \cos \delta_M |{}^2\Pi_{3/2}^+\rangle - \sin \delta_M |{}^2\Pi_{3/2}^-\rangle, \quad (3)$$

$$|f\rangle = \sin \delta_M |{}^2\Pi_{3/2}^+\rangle + \cos \delta_M |{}^2\Pi_{3/2}^-\rangle. \quad (4)$$

The Stark Hamiltonian in the $\{|e\rangle, |f\rangle\}$ basis can be represented by

$$H_S = -\frac{d\mathcal{E}M|\Omega|}{J(J+1)} \begin{bmatrix} \cos 2\delta_M & \sin 2\delta_M \\ \sin 2\delta_M & -\cos 2\delta_M \end{bmatrix}.$$

In the limiting cases $\delta_M = 0$, which corresponds to a very high field, the Stark Hamiltonian matrix is a diagonal matrix in the basis $\{|e\rangle = |{}^2\Pi_{3/2}^+\rangle, |f\rangle = |{}^2\Pi_{3/2}^-\rangle\}$, and for $\delta_M = \pi/4$ that corresponds to the zero-field limit the Stark Hamiltonian is off-diagonal in the basis $\{|e\rangle = (|{}^2\Pi_{3/2}^+\rangle - |{}^2\Pi_{3/2}^-\rangle)/\sqrt{2}, |f\rangle = (|{}^2\Pi_{3/2}^+\rangle + |{}^2\Pi_{3/2}^-\rangle)/\sqrt{2}\}$. By contrast, the Λ -doubling Hamiltonian

$$H_\Lambda = \Delta_\Lambda/2 \begin{bmatrix} -\sin 2\delta_M & \cos 2\delta_M \\ \cos 2\delta_M & \sin 2\delta_M \end{bmatrix}$$

is diagonal in the low-field limit $\delta_M = \pi/4$.

In an applied homogenous magnetic field the molecular magnetic moment interacts with the field and consequently the energy levels are subjected to the Zeeman effect with the Zeeman interaction Hamiltonian operator $H_Z = -\vec{\mu}_s \cdot \vec{B}$, where $\vec{\mu}_s$ is the magnetic moment in the space-fixed reference frame. Unlike the $|\Omega| = 1/2$ state for which the orbital and spin contribution to the molecular magnetic moment nearly cancel, the magnetic moment of the $|\Omega| = 3/2$ state ($J = 3/2$) is large. The Landé factor $g_J = (g_L\Lambda + g_S\Sigma)\Omega/[J(J+1)] = 0.777246$ [16], where g_L and g_S are electron orbital and spin g factors, respectively. The Zeeman splitting is shown in Fig. 2 for the field range 0–200 G at which the stretched molecular states are split by an energy shift comparable to the Stark shift at the range of 0–6000 V/cm. We focus on the low-field seeking state of highest energy which is the stretched state with quantum numbers $|5/2, 5/2; f\rangle$ for collisions.

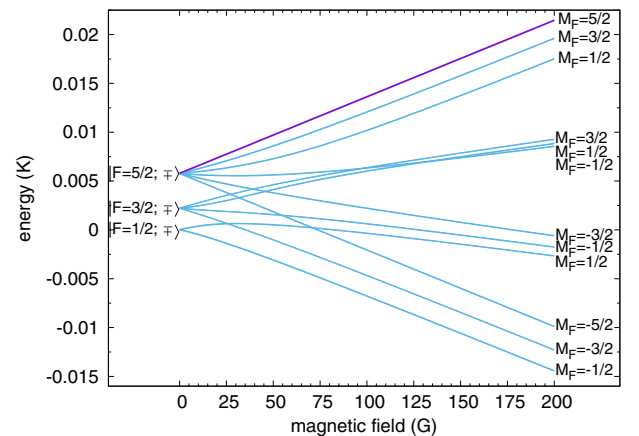


FIG. 2. Zeeman energies of the hyperfine $|F, M_F; e/f\rangle$ and Λ -doublet levels for $J = 3/2$ of the ${}^2\Pi_{3/2}$ state of the NO molecule at zero electric field. In a detailed resolution each line would be p -doubly split. The hyperfine state of interest, $|5/2, 5/2; f\rangle$, is highlighted.

The electric- and magnetic-field configuration can be arbitrary with an angle $\theta_{\varepsilon B}$ between them. In the following we set $\theta_{\varepsilon B} = 0$ because the electric dipoles are more easily induced when electric and magnetic moments are parallel [10] and also because M_F is a conserved quantum number.

Figures 1 and 2 appear remarkably similar on the scale shown, showing the range over which the two fields produce comparable energy shifts. However, the states belonging to these spectra are quite different. Consider the stretched state $|5/2, 5/2; f\rangle$ of interest. This state is doubly degenerate between states with $M_F = \pm 5/2$ and the same f . The states immediately lower in energy, in large electric field, differ by changing M_F , but still retain the f parity. By contrast, the stretched state at high field in Fig. 2 is nearly degenerate in e or f parity, but has a unique, positive value of $M_F = +5/2$. The state immediately lower in energy changed M_F , but still has both parity states e and f . These differences will matter below, in determining the dominant inelastic-scattering channels.

C. NO-NO interaction Hamiltonian

Let us now consider scattering due to the collision of two NO molecules of mass m , and located at \vec{r}_1, \vec{r}_2 , respectively. We restrict our discussion to two-body scattering in the center-of-mass frame by considering the relative position $\vec{R} = \vec{r}_1 - \vec{r}_2$ of body 1 with respect to body 2, and reduced mass $m_{\text{red}} = m/2$ associated with the relative motion. In spherical coordinates we are able to solve the scattering problem by using a separation of angular and radial variables of the total wave function $\Psi(R, \theta, \phi)$; the system is subjected to the centrifugal potential $\hbar^2 L(L+1)/(2m_{\text{red}}R^2)$.

For a pair of $^{14}\text{N}^{16}\text{O}$ fermionic molecules the wave function is antisymmetric with respect to interchange of the molecules. The effect of the inversion of the coordinates of all particles in the molecular center of mass is given by $E^*(R, \theta, \phi) = (R, \pi - \theta, \phi + \pi)$, thus the exchange properties of the partial waves are governed strictly by the properties of the spherical harmonics. Spherical harmonics have a definite parity $(-1)^L$ with respect to inversion about the origin, which means that the spatial wave function is inversion-antisymmetric for odd L and vice versa.

Considering collisions of identical species we must use the symmetrized combinations of the uncoupled hyperfine representation $|F_1, M_{F1}; p_1\rangle |F_2, M_{F2}; p_2\rangle |L, M_L\rangle$. The symmetrized functions (for $F_1 \neq F_2$ or $M_{F1} \neq M_{F2}$ or $p_1 \neq p_2$) are

$$\begin{aligned} & |F_1, M_{F1}; p_1\rangle |F_2, M_{F2}; p_2\rangle |L, M_L\rangle_S \\ &= \frac{1}{\sqrt{2}} \{ |F_1, M_{F1}; p_1\rangle |F_2, M_{F2}; p_2\rangle |L, M_L\rangle \\ & \quad \pm (-1)^L |F_2, M_{F2}; p_2\rangle |F_1, M_{F1}; p_1\rangle |L, M_L\rangle \}, \quad (5) \end{aligned}$$

with the $+$ sign for bosonic molecules and the $-$ sign for fermionic molecules. In the case of indistinguishable fermionic NO molecules this relation immediately ensures that only odd partial waves are allowed in a totally antisymmetric wave function.

The potential-energy surface between the molecules includes a van der Waals interaction and is represented as $-C_6/R^6$, which we assume is isotropic in the present calculation. We take $C_6 = 35.2E_h a_0^6$ as a lower estimate of actual C_6

obtained from the London formula and the mean dipole static polarizability for the NO molecule [17]. We are interested in the effects of long-range forces, and in particular dipole-dipole interactions, which are dominant at long range in ultracold scattering. For this reason we simply replace the short-range physics with a hard-wall boundary condition at $R = 30a_0$. On this distance scale, the higher-excited rotational states are unlikely to be relevant.

The long-range interaction is dominated by electric dipole-dipole interaction between the two molecules:

$$\begin{aligned} V_{\text{dd}}(\vec{R}) &= -\frac{3(\hat{R} \cdot \vec{d}_1)(\hat{R} \cdot \vec{d}_2) - \vec{d}_1 \cdot \vec{d}_2}{4\pi \varepsilon_0 R^3} \\ &= -\frac{\sqrt{30}d^2}{4\pi \varepsilon_0 R^3} \sum_{q_1, q_2} (-1)^q C_q^2 \begin{pmatrix} 2 & 1 & 1 \\ q & -q_1 & -q_2 \end{pmatrix} C_{q_1}^1 C_{q_2}^1, \quad (6) \end{aligned}$$

where $\vec{R} = R\hat{R}$ is the intermolecular separation vector in relative coordinates, and \vec{d}_i is the electric dipole of molecule i . $C_{q_1}^1$ and $C_{q_2}^2$ are components of first- and second-rank spherical tensors, which are given by reduced spherical harmonics. The term V_{dd} can be given in a matrix representation in the symmetrized hyperfine basis (5), as written, e.g., in Ref. [18] with a remaining dependence on the radial coordinate R .

The space-fixed reference frame collisional Hamiltonian for the NO-NO molecular system whose point mass is located at the center of mass is

$$H_{\text{tot}} = -\frac{\hbar^2}{2m_{\text{red}}} \frac{d^2}{dR^2} + H_{1,2} + V, \quad (7)$$

where $H_{1,2} = H_1 \otimes \mathbb{1}_2 + \mathbb{1}_1 \otimes H_2$ is the sum of the one-molecule effective Hamiltonians, V is the general term of potential energy including centrifugal barrier, long-range isotropic van der Waals interactions, and anisotropic dipole-dipole interactions.

The total wave function $\Psi(\vec{R})$ is represented by a column vector having the n th component of the form

$$\Psi_n(\vec{R}) = \frac{\psi_n(R)}{R} [|F_1, M_{F1}; p_1\rangle |F_2, M_{F2}; p_2\rangle |L, M_L\rangle_S],$$

where n is a collective index denoting all the channel indices in the square brackets, and ψ_n is the diabatic solution of the set of coupled radial equations

$$\left[\sum_{m=1}^{N_{\text{ch}}} \left(-\frac{\hbar^2}{2m_{\text{red}}} \frac{d^2}{dR^2} + E_m \right) \delta_{nm} + V_{nm} \right] \psi_m = E_{\text{tot}} \psi_n, \quad (8)$$

with E_m being the threshold energy of channel m , which is defined as the eigenenergy of $H_{1,2}$ in the $R \rightarrow \infty$ limit. E_{tot} represents the total collision energy, which is a conserved quantity during the collision. The total energy $E_{\text{tot}} = E_c + E_n$, where E_c is the collision energy relative to the threshold energy E_n of the incident channel.

In addition to symmetric properties of the wave functions another molecular symmetry of great importance for the interaction Hamiltonian is the total molecular angular-momentum projection onto an electric-field axis, $M_{\text{tot}} = M_{F1} + M_{F2} + M_L$. This quantum number is conserved in an electric field by dipole-dipole interactions and the same holds for magnetic fields.

The set of coupled Schrödinger equations (8) in multi-channel scattering was solved by employing the log-derivative propagator method [19]. Matching the log-derivative matrix with the asymptotic solution for open channels at large R yields the open-open submatrix of the reaction K matrix, and subsequently the scattering matrices S and T . The partial scattering cross section for a collision process between an inbound channel i and any of the outbound channels f is given by

$$\sigma_{L,i \rightarrow f}(E) = 2 \times \frac{\pi}{k_i^2} \sum_{M_L} \sum_{f, L', M'_L} |(i, L, M_L | T | f, L', M'_L)|^2,$$

where $f = i$ for elastic processes and $f \neq i$ for inelastic processes, $k_i^2 = 2m_{\text{red}}(E_{\text{tot}} - E_i^{1,2})/\hbar^2 = 2m_{\text{red}}E_c/\hbar^2$ a square of the wave number of an incident channel, and the numerical factor of two is required because of permutation symmetry in collisions of identical particles in indistinguishable hyperfine states. The total cross section is a sum of partial cross sections over all possible incoming partial waves L

$$\sigma_{i \rightarrow f}(E) = \sum_L \sigma_{L,i \rightarrow f}(E).$$

We also consider scattering rate constants, defined as $K = v_i \sigma$, where v_i is the incident collision velocity.

In practice, we consider only scattering within the $|\Omega| = 3/2$ manifold and disregard possible collision events where molecules scatter into $|\Omega| = 1/2$ states, which are far away in energy. Within this approximation, and for the $|5/2, 5/2; f\rangle |5/2, 5/2; f\rangle$ initial state of interest, we find that including partial waves $L = 1, 3, 5$ is sufficient to converge the cross sections to perhaps 20 percent at the highest energies considered, a sufficient convergence for our computation purposes. At the lowest collision energy of 10^{-5} K a right bound of $15\,000a_0$ is sufficient to have a converged cross section below 5%. Within these approximations there are $N_{\text{ch}} = 258$ total scattering channels.

III. SCATTERING RESULTS

We have calculated the elastic and inelastic cross sections for colliding molecules subjected to magnetic and electric fields. Note that, by elastic is meant collisions during which the internal state $|F, M_F; p\rangle$ of both molecules remains unchanged, whereas by inelastic is meant collisions in which at least one molecule converts its internal state to another. The collision energy within the wide range of $10 \mu\text{K}$ through 1 K is considered. As a rule of thumb, we seek circumstances where the ratio of elastic to inelastic collision rates is 100 or greater, to facilitate evaporative cooling.

Figure 3 shows cross sections for $\mathcal{E} = 6000 \text{ V/cm}$ and $B = 1000 \text{ G}$ with partial-wave contributions to the total cross sections. Below 1.5 mK the inelastic collisions dominate over the elastic collisions. At around 10^{-4} K the inelastic cross section features a maximum. Below this energy lies the threshold regime where σ_{inel} scales with collision energy E_c as $E_c^{1/2}$. Above this energy, $\sigma_{\text{inel}} \sim E_c^{-2}$. For the indicated values of the electric and magnetic field the favorable ratio of at least one hundred elastic events to one inelastic collision event seems to hold from 100 mK to higher collision energies, thus allowing NO molecules to be cooled by collisions to this limit.

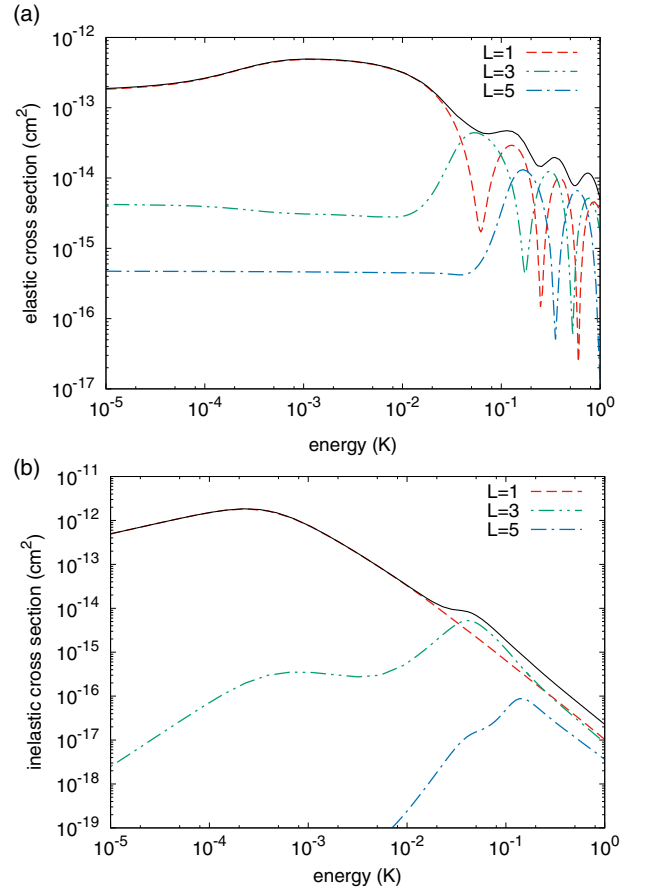


FIG. 3. (a) Elastic and (b) inelastic cross sections versus the collision energy for 6000 V/cm applied electric field and 1000 G applied magnetic field. Also shown are the individual partial-wave contributions $L = 1, 3, 5$ to the total cross section calculated in the inbound channel $|5/2, 5/2; f\rangle |5/2, 5/2; f\rangle |1, 0\rangle_s$.

Figure 3 closely resembles the similar Fig. 3 in Ref. [1], which showed the result for the $|\Omega| = 1/2$ state of the NO molecule, also in an electric field $\mathcal{E} = 6000 \text{ V/cm}$. It differs, of course, in that the $|\Omega| = 1/2$ had no magnetic moment and would not have been influenced by a magnetic field. The fact that the overall magnitude and variation of the cross sections is similar between the $|\Omega| = 3/2$ and $|\Omega| = 1/2$ states, is reasonable since the principal physics being explored here is due to the electric-dipole interactions between the molecules. There are also differences in the two cases, which likely arise from details of angular-momentum coupling in the $|\Omega| = 3/2$ versus $|\Omega| = 1/2$ state, and particularly in the hyperfine structure.

The effect of the magnetic field on the $|\Omega| = 3/2$ state can be significant. To see this, we examine scattering-rate coefficients in zero electric field, as shown in Fig. 4, for collision energies $E_c = 100 \text{ mK}$ and $E_c = 1 \text{ mK}$. Figure 4 plots rate coefficients versus magnetic-field strength. At the low collision energy of 1 mK , the inelastic rate actually exceeds the elastic rate, until a field of about 2000 G is applied. At still higher fields, the inelastic rate continues to diminish. Nevertheless, the ratio of

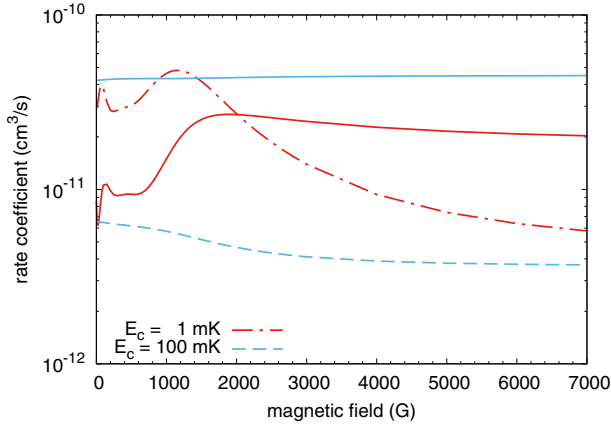


FIG. 4. Rate coefficient for elastic (solid curves) and inelastic (dashed curves) as a function of magnetic field at $E = 0$ V/cm for the two different collision energies: $E_c = 1$ mK (red, dark curve) and $E_c = 100$ mK (blue, light curve).

elastic to inelastic scattering remains less than an order of magnitude for the fields considered. Qualitatively, the same behavior is seen for $E_c = 100$ mK, although elastic scattering already exceeds inelastic scattering in zero field. The general conclusion, from the point of view of evaporative cooling, is that a magnetic field does not sufficiently increase the ratio of elastic to inelastic scattering.

The presence of a magnetic field can also strongly influence the behavior of rate constants when an electric field is present. This influence is indicated in Fig. 5. Panel (a) of this figure shows rate coefficients versus electric field for a low collision energy, $E_c = 1$ mK. In the absence of a magnetic field (black lines), the inelastic rate actually far exceeds the elastic rate for most of the range; a situation similar to the case in the $|\Omega| = 1/2$ state (see Fig. 4 of Ref. [1]). Incorporating a magnetic field parallel to the electric field can ameliorate this difference: elastic and inelastic rates are comparable for all electric fields if the magnetic field is 1000 G (red lines); while the elastic rate exceeds the inelastic rate for all electric fields if $B = 3000$ G (blue lines). Moreover, large electric fields tend to suppress the inelastic rates while leaving the elastic rates alone, an effect already emphasized for the $|\Omega| = 1/2$ state. Admittedly, the fields required for this suppression are unrealistically large to be a useful means of achieving evaporative cooling at millikelvin temperatures.

The situation is somewhat more promising in the case of 100 mK collision energy [Fig. 5(b), zoom to small electric field in Fig. 5(c)]. Here inelastic scattering is already suppressed in zero field and becomes further suppressed as the magnetic field is increased. Meanwhile, the elastic-scattering rate is essentially unchanged by the magnetic fields. In a $B = 3000$ G magnetic field, it is conceivable that merely polarizing the atoms ($\mathcal{E} > 40$ V/cm) is sufficient to promote evaporative cooling to this temperature.

IV. SEMI-QUANTITATIVE ANALYSIS

Regardless of some inelastic suppression at large fields and at temperatures above 10 mK, inelastic scattering is

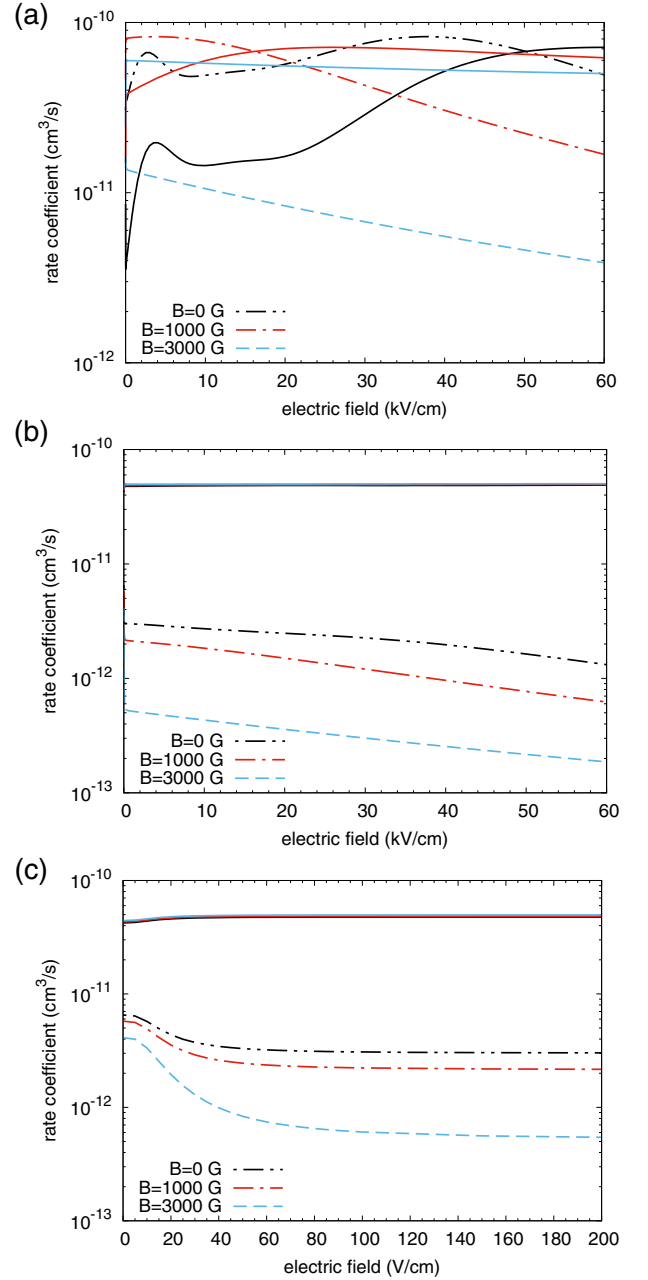


FIG. 5. Rate coefficients for elastic (solid curves) and inelastic (dashed curves) scattering as a function of electric field at $B = 0$ G (black curve), $B = 1000$ G (red curve), and $B = 3000$ G (light blue curve). The collision energy is fixed at the value (a) $E_c = 1$ mK, (b) $E_c = 100$ mK. (c) The same as in panel (b) but in detailed electric-field range.

nevertheless a fact of life for these radicals. It is worthwhile to look at the mechanism of inelastic scattering, both to see why this scattering occurs, and why it is suppressed.

Starting from the stretched state $|5/2, 5/2; f\rangle|5/2, 5/2; f\rangle$, collisions can be inelastic, thereby releasing energy, by transformations of two types: either the molecules can change

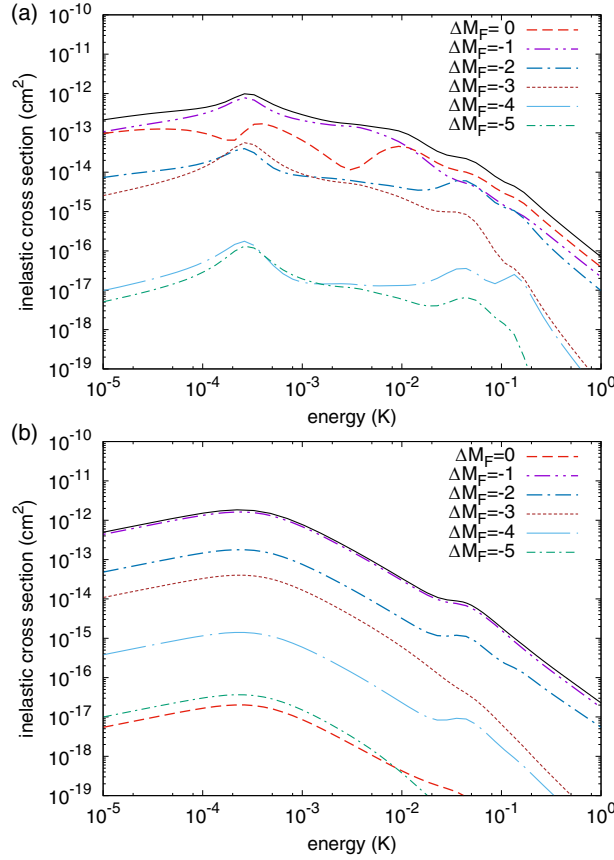


FIG. 6. Inelastic cross sections versus collision energy (a) in the absence of field, (b) subjected to an electric field of $\mathcal{E} = 6000$ V/cm and a magnetic field of $B = 1000$ G. The collisions occur in the incident state $|5/2, M_{F1} = 5/2; f\rangle|5/2, M_{F2} = 5/2; f\rangle|1, 0\rangle_S$ and individual partial cross sections represent losses to channels that change M_{F1} and M_{F2} . The notation $\Delta M_F = M'_{F1} - M_{F1} + M'_{F2} - M_{F2}$.

the total projection of angular momentum on the field axis, $\Delta M_F = \Delta M_{F1} + \Delta M_{F2}$, with the shed angular momentum transferred to partial-wave angular momentum; or else one or both molecules can change parity state from f to e .

The partial cross sections for the various ΔM_F channels are shown in Fig. 6, both in the absence of applied field [Fig. 6(a)] and in fields of $\mathcal{E} = 6000$ V/cm and $B = 1000$ G [Fig. 6(b)]. Quite generally, these partial cross sections exhibit a propensity rule, whereby larger changes in angular momentum, ΔM_F , are suppressed relative to smaller changes. A notable exception is the partial cross section for $\Delta M_F = 0$. In zero field this process is somewhat suppressed with respect to $\Delta M_F = -1$ for energies below ~ 10 mK, while in strong fields it is suppressed to be the least significant cross section of all.

The ability of the molecules to scatter into different ΔM_F and parity channels depends qualitatively on two things: the initial-to-final-state coupling, and the energy released in the collision. This can be seen in the plane-wave Born approximation, where the transition amplitude between initial channel i with wave number k_i and parities p_{1i}, p_{2i} , to final channel f

with wave number k_f and parities p_{1f}, p_{2f} , is given by [7]

$$\begin{aligned} \langle i|T|f\rangle &= \frac{4m_{\text{red}}}{\hbar^2} C_{i,f} \sqrt{k_i k_f} \int_0^\infty \frac{j_{L_i}(k_i R) j_{L_f}(k_f R)}{R} dR \\ &= A C_{i,f} \sqrt{k_i k_f} \frac{k_i^{L_i}}{k_f^{L_f}} F(a, b, c; (k_i/k_f)^2). \end{aligned} \quad (9)$$

Here k_i and k_f are the wave numbers of the initial and final channels; F is a hypergeometric function whose indices depend on angular-momentum quantum numbers; and C_{if} are matrix elements of the dipole coupling in the dressed states of the molecules, exclusive of the $1/R^3$ scaling.

The matrix elements C_{if} depend strongly on electric field, which can be seen as follows: In the expression (6) for the dipolar interactions, the matrix elements of the individual $C_{q_i}^1$ components is given by

$$C_{q_i}^1 = \langle J, M, |\Omega| | C_{q_i}^1 | J, M, |\Omega\rangle \begin{bmatrix} \cos 2\delta_M & \sin 2\delta_M \\ \sin 2\delta_M & \cos 2\delta_M \end{bmatrix},$$

using [20]

$$\langle J, M, \Omega | C_{q_i}^1 | J, M, \Omega' \rangle = \frac{\delta_{\Omega, \Omega'} \Omega}{J(J+1)} \begin{cases} M, & q_i = 0 \\ \pm \sqrt{\frac{J^2 - M^2}{2}}, & q_i = \mp 1. \end{cases}$$

Thus in the two-molecule field-dressed basis the $C_{i,f}$ matrix elements depend on the parity states and the electric field (via δ_M) as

$$\begin{aligned} \langle ee|C|ee\rangle &\propto \cos^2(2\delta_M), \\ \langle ee|C|ef\rangle &\propto \sin(4\delta_M), \\ \langle ee|C|ff\rangle &\propto \sin^2(2\delta_M), \end{aligned} \quad (10)$$

Thus in the zero-electric-field limit, $\delta_M \rightarrow \pi/4$, the initial channel with $p_{1i} = p_{2i} = f$ is directly coupled only to the final channel with $p_{1f} = p_{2f} = e$; both molecules must change parity. Whereas in the high-electric-field limit, $\delta_M \rightarrow 0$ and the initial channel $p_{1i} = p_{2i} = f$ couples only to channels where $p_{1f} = p_{2f} = f$ also; that is, the f character of the state is preserved.

The second effect, that of the energy released in the collision, follows from the Born-approximation result, noting that in the threshold limit $k_i/k_f \rightarrow 0$, the hypergeometric function in Eq. (9) is reduced to unity. The energy dependence is therefore in the prefactor $\sqrt{k_i k_f} k_i^{L_i} / k_f^{L_f}$. For final wave numbers given by the energy released, $k_f = (2m_{\text{red}} \Delta E / \hbar^2)^{1/2}$, where ΔE is the energy between incident and final thresholds, and for p waves $L_f = 1$, we have $\sigma_{if} \propto 1/\sqrt{\Delta E}$, which is suppressed as the gap ΔE gets larger. This idea was used to explain the electric-field suppression of inelastic rates in Ref. [1].

Selected rate constants in the Born approximation, with $\Delta M_F = -1, 0$, are shown in Fig. 7. The rates show the smooth transition between ee final states that are the dominant result at zero field, to the ff final states that dominate at large field. At small electric field, both $\Delta M_F = -1, 0$ channels with opposite ee parity are readily available, with gap ΔE remaining small, on the order of the Λ -doubling energy. Both possibilities are therefore approximately equally likely.

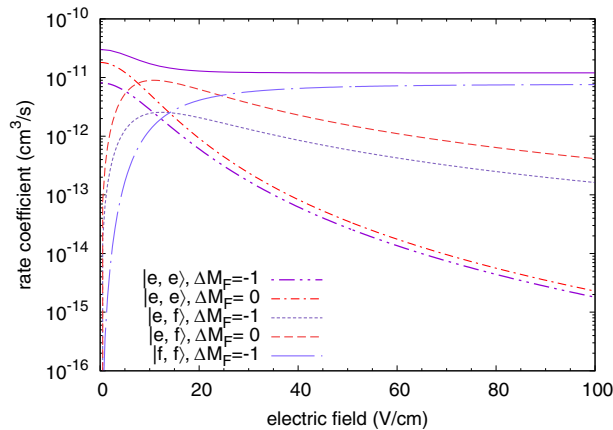


FIG. 7. Rate coefficients in Born approximation for inelastic scattering as a function of electric field at $B = 0$ G between the incident channel $|f, f\rangle \equiv |5/2, M_{F1} = 5/2; f\rangle|5/2, M_{F2} = 5/2; f\rangle|1, 0\rangle_S$ and final channels indicated in the legend that are either of different e (or f) parity or different M_F . The collision energy is fixed at the value $E_c = 1$ mK. The solid purple curve corresponds to a sum of all $\Delta M_F = -1$ state-changing collisions, where only selected dominant $K_{i \rightarrow f}$ are shown. Only the $L_f = 1$ outgoing partial wave is considered.

On the other hand, at large field, a parity-conserving $\Delta M_F = -1$ transition, $|5/2, 5/2; f\rangle|5/2, 5/2; f\rangle \rightarrow |5/2, 5/2; f\rangle|5/2, 3/2; f\rangle$ is easily allowed, with a gap corresponding to approximately the hyperfine splitting (Fig. 1), so this transition proceeds rapidly. But for a $\Delta M_F = 0$ transition, the only parity-preserving operation is $|5/2, 5/2; f\rangle|5/2, 5/2; f\rangle \rightarrow |5/2, 5/2; f\rangle|5/2, 5/2; f\rangle$; that is, elastic scattering. The $\Delta M_F = 0$ inelastic transition is therefore highly suppressed.

Finally, we note that, for any allowed transition, such as the $\Delta M_F = -1$ transition, $|5/2, 5/2; f\rangle|5/2, 5/2; f\rangle \rightarrow$

$|5/2, 5/2; f\rangle|5/2, 3/2; f\rangle$ at high field, the addition of a magnetic field further splits the energy between the $|5/2, 5/2\rangle$ and $|5/2, 3/2\rangle$ states, increasing the gap ΔE and further somewhat suppressing the inelastic rates. This is the result seen in Fig. 5.

V. CONCLUSIONS

We analyzed the possibility of evaporative cooling of NO molecules in their $|\Omega| = 3/2, J = 3/2$ state and computed scattering cross sections and rate coefficients under the influence of electric and magnetic fields. We find that evaporative cooling is viable only for collision energies E_c no lower than ~ 100 mK, which is similar to a result obtained for NO in the $^2\Pi_{1/2}$ state [1]. Without the influence of an external magnetic field, the ratio of elastic to inelastic rates is highly unfavorable and does not exceed 100 at $E_c = 100$ mK even when an unrealistically high electric field is applied. Magnetic fields of a few thousand gauss are necessary for effective cooling, the suppression of the inelastic rate can then be controlled by an additional electric field, which is in accordance with the phenomenon found for the $^2\Pi_{1/2}$ state [1].

As a result, no matter what field is applied and of what magnitude, the most probable inelastic process is the one that changes the sum of total-angular-momentum projection ΔM_F for both collision species by one.

Finally, we discussed the role of molecular state parity that is during inelastic processes preferred to be changed or conserved with respect to the magnitude of the electric field.

ACKNOWLEDGMENTS

We acknowledge funding from the U.S. Army Research Office under ARO Grant No. W911NF-12-1-0476 and from the JILA NSF Physics Frontier Center, PHY-1734006. L.D.A. acknowledges the financial support of the Czech Science Foundation (Grant No. P209/18-00918S).


- [1] L. D. Augustovičová and J. L. Bohn, *Phys. Rev. A* **96**, 042712 (2017).
- [2] S. N. Vogels, J. Onvlee, S. Chefdeville, A. van der Avoird, G. C. Groenenboom, and S. Y. T. van de Meerakker, *Science* **350**, 787 (2015).
- [3] Z. Gao, S. N. Vogels, M. Besemer, T. Karman, G. C. Groenenboom, A. van der Avoird, and S. Y. T. van de Meerakker, *J. Phys. Chem. A* **121**, 7446 (2017).
- [4] X. Wang, M. Kirste, G. Meijer, and S. Y. T. van de Meerakker, *Z. Phys. Chem.* **227**, 1595 (2013).
- [5] K. E. Strecker and D. W. Chandler, *Phys. Rev. A* **78**, 063406 (2008).
- [6] L. M. C. Janssen, A. van der Avoird, and G. C. Groenenboom, *Phys. Rev. Lett.* **110**, 063201 (2013).
- [7] A. V. Avdeenkov and J. L. Bohn, *Phys. Rev. A* **71**, 022706 (2005).
- [8] J. L. Bohn, A. M. Rey, and J. Ye, *Science* **357**, 1002 (2017).
- [9] C. Ticknor and J. L. Bohn, *Phys. Rev. A* **71**, 022709 (2005).
- [10] G. Quéméner and J. L. Bohn, *Phys. Rev. A* **88**, 012706 (2013).
- [11] B. K. Stuhl, M. T. Hummon, M. Yeo, G. Quéméner, J. L. Bohn, and J. Ye, *Nature (London)* **492**, 396 (2012).
- [12] D. Reens, H. Wu, T. Langen, and J. Ye, *Phys. Rev. A* **96**, 063420 (2017).
- [13] T. D. Varberg, F. Strohm, and K. M. Evenson, *J. Mol. Spectrosc.* **196**, 5 (1999).
- [14] W. Meerts and A. Dymanus, *J. Mol. Spectrosc.* **44**, 320 (1972).
- [15] D. R. Lide, *CRC Handbook of Chemistry and Physics*, 84th ed. (CRC Press, Boca Raton, FL, 2003).
- [16] R. L. Brown and H. E. Radford, *Phys. Rev.* **147**, 6 (1966).
- [17] N. J. Bridge and A. D. Buckingham, *Proc. R. Soc. London, Ser. A* **295**, 334 (1966).
- [18] A. V. Avdeenkov and J. L. Bohn, *Phys. Rev. A* **66**, 052718 (2002).
- [19] B. R. Johnson, *J. Comput. Phys.* **13**, 445 (1973).
- [20] J. L. Bohn, in *Cold Molecules: Theory Experiment, Applications*, edited by R. V. Krems, B. Friedrich, and W. C. Stwalley (CRC Press, Taylor & Francis Group, Boca Raton, FL, 2010), Chap. 2, p. 39.

MANIFESTATION OF QUANTUM CHAOS IN
FANO-FESHBACH RESONANCES

Bibliographic record of the attached publication:

Augustovičová, L. D. and J. L. Bohn (2018). "Manifestation of quantum chaos in Fano-Feshbach resonances." In: *Physical Review A* 98, p. 023419.

DOI: [10.1103/PhysRevA.98.023419](https://doi.org/10.1103/PhysRevA.98.023419).

Manifestation of quantum chaos in Fano-Feshbach resonancesLucie D. Augustovičová¹ and John L. Bohn²¹*Charles University, Faculty of Mathematics and Physics, Department of Chemical Physics and Optics, Ke Karlovu 3, CZ-12116 Prague 2, Czech Republic*²*JILA, NIST, and Department of Physics, University of Colorado, Boulder, Colorado 80309-0440, USA* (Received 27 June 2018; published 20 August 2018)

A model is presented that mimics the nearest-neighbor-spacing (NNS) distribution of chaotic molecules such as Dy_2 and Er_2 just below their dissociation threshold. In this model the degree of chaos is controlled by choosing suitable Hamiltonian matrices from random ensembles. It is found that, in versions of the model that are not completely chaotic, the NNS of observable Fano-Feshbach resonances exhibits greater level repulsion, hence more chaos, than the corresponding NNS of a typical energy spectrum of the molecule at a fixed magnetic field.

DOI: [10.1103/PhysRevA.98.023419](https://doi.org/10.1103/PhysRevA.98.023419)**I. INTRODUCTION**

Recently, evidence of quantum chaos has been reported in ultracold collisions of both erbium and dysprosium atoms [1–5]. The states contributing to chaotic spectra are those that lie immediately below the dissociation threshold of the Dy_2 or Er_2 molecule. This is unusual: chaos is predicted to be present in triatomic systems at or just below dissociation, such as Ar_3 clusters [6], as well as ultracold collisions of $\text{Li}+\text{CaH}$ [7] or $\text{Rb}+\text{K}_2$. However, it is less obvious that diatomic molecules could present chaotic behavior.

The observation of chaos in Dy_2 and Er_2 was assisted by the circumstance of extremely low temperatures, on the order of hundreds of nK. This circumstance enabled high-resolution spectroscopy of distinct states, which revealed quantum chaos by the usual measures of nearest-neighbor-spacing statistics or spectral rigidity.

There is, however, a novelty in the observations of Refs. [1–5], at least from the point of view of quantum chaos. The resonant states were observed as a function of magnetic field, rather than as a function of energy, as would be the case in conventional spectroscopy. This is a very natural consequence of spectroscopy in ultracold gases, where the energy of a pair of colliding atoms is fixed, essentially at zero, while the resonant states can be moved, in this case by means of the magnetic field, through this energy, where they are observed as $E = 0$ scattering resonances.

The spectra of the near-dissociation molecules generally appear as in Fig. 1. This figure is the result of a schematic model of Dy_2 energy levels, to be described in Sec. II. The point here is that, at each value of the magnetic field B , there exists a spectrum of bound-state energies that may exhibit some degree of quantum chaos. As the magnetic field is increased, this spectrum evolves, in such a way that the energy states move closer to, and eventually cross, the dissociation threshold, taken here to be $E = 0$. This threshold corresponds to the lowest-energy states of a pair of free atoms, each in the $|jm\rangle = |8, -8\rangle$ state in this case. At each magnetic field where one of these bound state crosses the threshold, a scattering resonance appears, which is observed by means of the excessive three-body recombination that accompanies

it. The resulting set of magnetic field values constitutes a spectrum, which can be analyzed by means of the usual tools of quantum chaos.

The measured spectra of Dy_2 and Er_2 are therefore unusual, inasmuch as they consist of magnetic field values, rather than energies. What is recovered is not the energy spectrum of a chaotic molecule, but rather a spectrum consisting of a *single* energy level from each of *many different* chaotic molecules, since the molecular Hamiltonian giving rise to these bound states is different for each magnetic field.

This distinction raises questions regarding the interpretation of the measurement. If chaos is found in the spectra of magnetic field values, does it imply the same degree of chaos would be found in the energy spectrum at any fixed magnetic field? If not, which is “more chaotic,” and how do we quantify the difference?

In this article we make a preliminary investigation into these questions. In Sec. II we construct a fairly realistic model of Dy_2 molecules and extract from it spectra of energies at constant magnetic field, and spectra of magnetic field values at constant energy. These spectra are analyzed in terms of their nearest-neighbor spacing (NNS) and quantified by the free parameters of their respective Brody distribution [8]. It is found that both spectra yield Brody parameters near unity, i.e., that both the energy and magnetic field spectra are fully chaotic.

In Sec. III we introduce a family of extended models in such a way that effective channel couplings in the molecule can be reduced, making the molecules less chaotic. We find that for any given member of this family that is not completely chaotic, the Brody parameter of the magnetic field spectrum is generally greater than that for the energy spectrum $\nu_B > \nu_E$, implying that the magnetic field spectrum may exhibit a greater degree of chaos. In Sec. III we also simplify the model further to garner insight into why this might be so. We conclude in Sec. IV.

II. MODEL OF THE DIATOMIC SPECTRA

We begin with a simplified model of these molecules, which incorporates features of about the right quality and scale. It is a

simplified version of a complete scattering calculation carried out by [1]. The essence of this approximate calculation is to separate the basic structure of rovibrational energy levels, and spins, from the strong anisotropic couplings that ultimately generate the chaos.

A. Hamiltonian

This model describes a pair of ^{162}Dy atoms in their ground state with spin $j = 8$ and g factor $g = 1.2508$ [9]. The nuclear spin of these atoms is zero. (A similar model can be constructed for Er, of course.) The model Hamiltonian is taken to be

$$H = H_{\text{rv}} + H_{\text{mag}} + V_{\text{an}}. \quad (1)$$

Briefly, H_{rv} describes the rovibrational degrees of freedom, H_{mag} their shifts in a magnetic field, and V_{an} the coupling of these states due to the anisotropic potential energy surface. V_{an} is regarded as the part that engenders chaos in the spectra.

In more detail: We begin with a Lennard-Jones potential that describes an approximately correct long-range interaction between the atoms, so that the spacing of rovibrational levels is realistic. This potential, including a centrifugal potential, is

$$V_{\text{LJ}} = \frac{C_{12}}{R^{12}} - \frac{C_6}{R^6} + \frac{\hbar^2 L(L+1)}{2\mu R^2}, \quad (2)$$

where R is the distance between the atoms, μ the reduced mass of the atom pair, and $C_6 = 2003$ au [1] is the isotropic van der Waals coefficient of Dy_2 . C_{12} is chosen so that the depth of the potential is set to 785.7 cm^{-1} [10].

From this potential, a set of radial basis functions $|L, v\rangle = \phi_{L,v}(R)$ is numerically constructed as eigenfunctions of H_{rv} :

$$-\frac{\hbar^2}{2\mu} \frac{d^2 \phi_{L,v}}{dR^2} + V_{\text{LJ}} \phi_{L,v} = E_{L,v} \phi_{L,v}. \quad (3)$$

Taken together with the spins of the two atoms and the partial wave angular momentum, these states define the basis of this model

$$|L, v\rangle |LM_L\rangle |j_1 m_1\rangle |j_2 m_2\rangle. \quad (4)$$

$$\langle L' v' | \langle L' M'_L | \langle j_1 m'_1 | \langle j_2 m'_2 | V_{\text{an}} | L, v \rangle | LM_L \rangle | j_1 m_1 \rangle | j_2 m_2 \rangle$$

$$= \sum_{q=-2}^2 (-1)^{q+1} \langle L' M'_L | C_{2q} | LM_L \rangle \left\{ \sqrt{6} \left(\frac{g\alpha}{2} \right)^2 \langle L' v' | \frac{1}{R^3} | L, v \rangle \langle j_1 m'_1 | \langle j_2 m'_2 | (j_1 \otimes j_2)_{2,-q} | j_1 m_1 \rangle | j_2 m_2 \rangle \right. \\ \left. + C_{\text{ad}} \langle L' v' | \frac{1}{R^6} | L, v \rangle \langle j_1 m'_1 | \langle j_2 m'_2 | (j_1 \otimes j_1)_{2,-q} + (j_2 \otimes j_2)_{2,-q} | j_1 m_1 \rangle | j_2 m_2 \rangle \right\}, \quad (9)$$

where $(j_1 \otimes j_2)_{2,-q}$ is the $-q$ component of the compound irreducible second-rank tensor product of tensors of rank 1 (vectors) that act as the total angular momentum operators on the individual variables in spaces 1 and 2. C_{kq} is the modified spherical harmonic. The value of $C_{\text{ad}} = 0.168 E_{\text{h}} a_0^6$ [10].

B. Spectrum and chaos

Thus, the Hamiltonian matrix can be constructed and diagonalized for any desired value of magnetic field B . The

Further, in this basis the magnetic field Hamiltonian is diagonal, with energies given by

$$H_{\text{mag}} |j_1 m_1\rangle |j_2 m_2\rangle = g\mu_B (m_1 + m_2) B |j_1 m_1\rangle |j_2 m_2\rangle, \quad (5)$$

where μ_B is the Bohr magneton.

The observations occur upon scattering atoms in their ground state, $|jm\rangle = |8, -8\rangle$ at ultracold temperatures, whereby the initial partial wave angular momentum is $L = 0$. Starting from this state, we consider all basis states (4) consistent with conservation of angular momentum and boson exchange symmetry. Moreover, we consider the energy of two free atoms in the $|8, -8\rangle$ state to define the zero of energy at all values of magnetic field. As a consequence, the energies of the basis states in (4) have the magnetic field dependence

$$E_{L,v} + g\mu_B [(m_1 + 8) + (m_2 + 8)] B. \quad (6)$$

This ensures that the energies of all the bound states are rising functions of magnetic field, and that the magnetic field spectrum will be identified with these levels crossing $E = 0$. These energies are more or less independent from one potential to the next, and ensure a random, nonchaotic spectrum, characterized by a nearest-neighbor distribution having Poisson statistics.

To generate chaos in such a spectrum requires strong off-diagonal coupling, represented here by V_{an} . This potential can contain the magnetic dipole-dipole interaction between the atoms,

$$V_{\text{dd}}(\vec{R}) = -\left(\frac{g\alpha}{2}\right)^2 3 \frac{(\hat{R} \cdot \vec{j}_1)(\hat{R} \cdot \vec{j}_2) - \vec{j}_1 \cdot \vec{j}_2}{R^3}, \quad (7)$$

where α is the fine-structure constant; and an anisotropic dispersion interaction

$$V_{\text{ad}}(\vec{R}) = -\frac{C_{\text{ad}}}{\sqrt{6}} \sum_{i=1}^2 \frac{3(\hat{R} \cdot \vec{j}_i)(\hat{R} \cdot \vec{j}_i) - \vec{j}_i \cdot \vec{j}_i}{R^6}. \quad (8)$$

Here, $\vec{R} = R\hat{R}$ is the interatomic separation vector in relative coordinates. It has been observed previously that V_{dd} is primarily responsible for anisotropic coupling in Dy_2 , while V_{ad} is more important for Er_2 [1,11].

In the basis (4) these interactions have the matrix elements

resulting map of eigenenergies versus B is shown in Fig. 1. To achieve this figure, 7103 basis functions having their partial-wave function of even L up to $L_{\text{max}} = 28$ were needed to reach convergence of eigenstates of H . The energies change substantially for $L_{\text{max}} < 22$, but in turn as L_{max} increases their positions converge and for $L_{\text{max}} = 28$ they do not deviate from their converged values by more than 8×10^{-6} K in the range of energy shown.

This spectrum shows several remarkable features. Mainly, it consists of a collection of nearly parallel curves, with

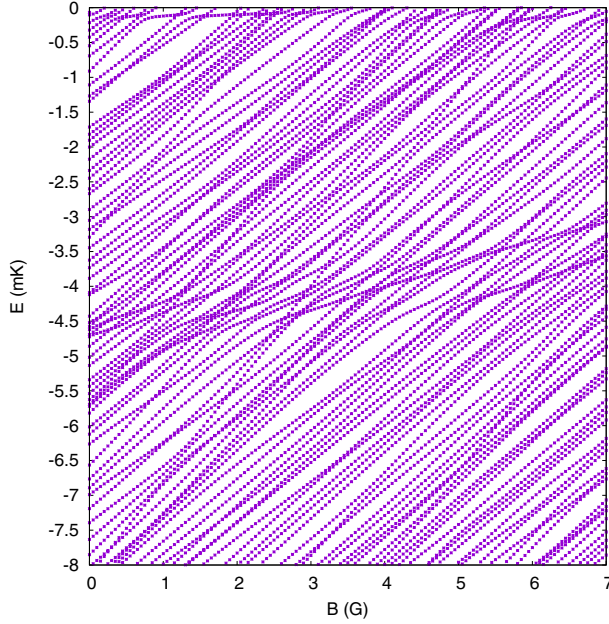


FIG. 1. Simulated spectrum of Dy_2 molecules, versus magnetic field, generated as described in the text. Each energy level at $B = 0$ evolves as the magnetic field is increased, eventually finding its way to zero energy, where it appears as a scattering resonance.

occasional avoided crossings. The mean slope of these lines is approximately 1 mK/G, corresponding to about $15\mu_B$. This is comparable to the mean value of all the bare magnetic moments described by (6), whose average value would be $20\mu_B$ if all values of m were equally likely. The point is that strong interchannel couplings in this case lead to a remarkably uniform set of magnetic moments for all states. If the lines in Fig. 1 were all straight lines with the same slope, then the magnetic field spectrum at $E = 0$ would be a faithfully rescaled copy of the energy spectrum at $B = 0$, and the two spectra would exhibit exactly the same degree of chaos. That these curves are not perfectly parallel is the first hint that the chaos in the two spectra may not be equivalent.

In addition, several lines in Fig. 1 have a considerably smaller slope. These are likely due to broad “halo” resonances tied to the incident channel as were discovered in Ref. [3] and that are expected to persist across many narrower, chaotic lines in the spectrum. While such states are interesting, they are in the minority and do not significantly affect the conclusions we draw here.

We seek to quantify the degree of chaos present in the two kinds of spectra: one, an energy spectrum at a fixed value of B ; and the other, a magnetic field spectrum at $E = 0$. To do so, we employ the basic tool widely used for this purpose, namely, we fit the nearest-neighbor spacing (NNS) distribution [8], normalized so that the mean NNS is equal to one. As is conventional, we then fit this distribution to the Brody function:

$$P(v, s) = (1 + v)\alpha s^v \exp(-\alpha s^{v+1}), \quad (10)$$

where $\alpha = \{\Gamma[(v + 2)/(v + 1)]\}^{v+1}$, s is the normalized NNS, and v is the Brody parameter. This parameter is considered to

be a measure of the chaos on the spectrum: $v = 0$ corresponds to a random, nonchaotic, Poisson spectrum, while $v = 1$ corresponds to a fully chaotic spectrum whose levels are chaotic and characteristic of the eigenvalues of matrices from the Gaussian orthogonal ensemble (GOE). We will extract two kinds of Brody parameters, v_E for a spectrum of energy values, and v_B for a spectrum of magnetic field values.

The NNS and the Brody parameter represent only one approach to quantifying chaos in a quantum mechanical system. The methods of statistical analysis of spectra are many and diverse, and subsequent analyses have looked more deeply at the experimental spectra. Reference [12] analyzed the original Er data set in [2], finding that the NNS distribution is likely to underestimate the degree of chaos if levels are missing from the spectra, that is, if they are too narrow to be observed. This is shown by an analysis of the power spectrum of long-range correlations in far apart spectral levels [13] as well as by analyzing the distribution of resonance widths in comparison with the Porter-Thomas distribution. This analysis is consistent with the data if all resonances narrower than ~ 10 mG are unobserved, which amounts to about 20% of them. The suggestion was that the spectrum was indeed chaotic, but the resolution of the data was not yet sufficient to draw this conclusion. The analysis is further complicated by the sensitive temperature dependence of observable effects of the resonances [1].

Nevertheless, in our theoretical study we are able to resolve all resonances and use the Brody parameter exclusively as a measure of chaos. In Fig. 2 are shown two histograms of the data in Fig. 1. Figure 2(a) is drawn from the $B = 0$, energy spectrum, and yields a Brody parameter $v_E = 1_{-0.23}^{+0}$. Figure 2(b) is drawn from the $E = 0$, magnetic field spectrum, and yields $v_B = 0.93_{-0.28}^{+0.07}$. In both cases, the histograms are generated from 250 levels of the spectrum. The uncertainties are the $1\text{-}\sigma$ uncertainties due to the fit to the Brody function (10). This uncertainty arises due to the counting statistics of data in the histogram. It is compelling to assert that both these spectra are “fairly chaotic,” and that therefore chaos is preserved in the mapping from energy spectra to magnetic field spectra. However, the large fit uncertainties make a quantitative statement difficult. With these uncertainties, the value of v_B is somewhat higher than, but nearly consistent with, the values $\sim 0.5\text{--}0.75$ extracted from the original ^{164}Dy data [1].

C. Simulation of lesser-strength anisotropy

In order to beat down the large error bars associated to a single statistical evaluation of the spectra ensemble, we exploit the theory of random matrices. The nonzero matrix elements of V_{an} for a chaotic molecule are viewed as random variables distributed around zero with a variance w_0 . This allows us to simulate the molecule more generically by using the matrix elements distributed according to the probability densities [14]

$$P(w, V_{ii}) = \frac{1}{\sqrt{2\pi w}} \exp\left(-\frac{V_{ii}^2}{2w}\right),$$

$$P(w, V_{ij}) = \frac{1}{\sqrt{\pi w}} \exp\left(-\frac{V_{ij}^2}{w}\right), \quad i \neq j. \quad (11)$$

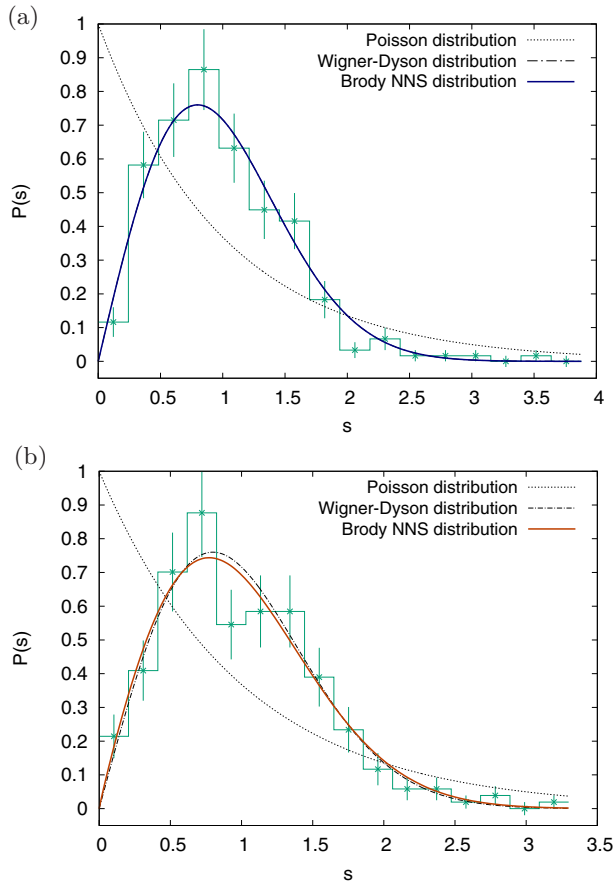


FIG. 2. Nearest-neighbor-spacing (NNS) distributions for the spectrum shown in Fig. 1. In (a) is shown the $B = 0$ spectrum, while in (b) is shown the $E = 0$ spectrum.

To approximate the Dy_2 model given in the previous section, we set the width w to the root-mean-squared width determined from the nonzero matrix elements computed above. This width is $w_0 = 24.7$ mK.

The interaction matrix is constructed by filling those elements that are not zero by symmetry with random variables determined from the GOE distributions (11), while treating the diagonal elements of H_{rv} and H_{mag} as before. In this way we can generate many realizations of models of Dy_2 and find an ensemble of independent Brody parameters that can be averaged to reduce the collective uncertainty of the set. Approximately 30 such realizations are required to reduce the uncertainty to 5%. The resulting Brody parameters are then $\nu_E = 0.94 \pm 0.05$ and $\nu_B = 0.98 \pm 0.05$, respectively. We conclude that our basic model of Dy_2 is fully chaotic, and is equally chaotic in energy and magnetic field spectra.

The random matrix version of the theory affords also the opportunity to turn off the chaos in a controlled way. Namely, as the value of w is reduced, the magnitudes of the matrix elements of V_{an} are reduced, generating less level repulsion in the eigenvalues of H , and bringing the spectrum closer to the essentially random spectrum of $H_{rv} + H_{mag}$. That is, the Brody parameters are generally expected to be increasing functions

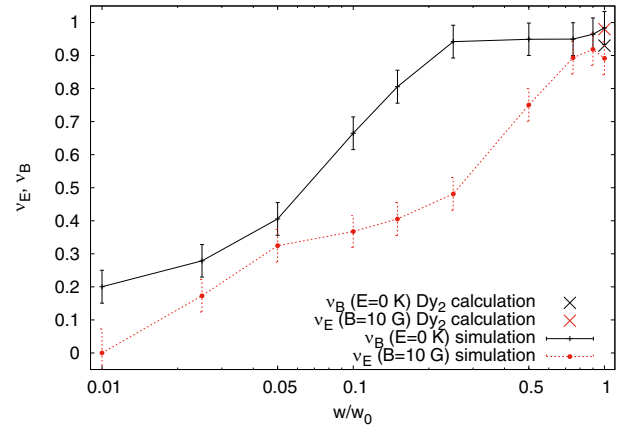


FIG. 3. Brody parameters ν_E and ν_B for the simulation of “subdysprosium” as a function of the width parameter w in the units of $w_0 = 24.7$ mK, and for Dy_2 calculation (shown in Fig. 1) evaluated from discrete energy values for $B = 10$ G [red (dark gray) cross at $0.98^{+0.02}_{-0.25}$], and from resonance positions at $E = 0$ K [black cross at $0.93^{+0.07}_{-0.28}$]. Error bars for values at large crosses are not shown.

of w . We refer to such a model, with less chaos than a more realistic dysprosium model, as the “subdysprosium” model.

We note that a similar model was described in Ref. [1]. There are some significant differences, however. Reference [1] distributed the magnetic moments randomly and, more significantly, allowed the diagonal spectrum to have its own Brody parameter, independent of the size of random off-diagonal matrix elements. A main conclusion from that calculation was that the Brody parameter of the magnetic field resonance spectrum rose as a function of channel coupling just the same, regardless of the original diagonal Brody parameter. This was strong evidence that the chaos in the observed spectra lay in the avoided crossings in figures such as Fig. 3(d) of Ref. [1], or Fig. 1 of this paper. Reference [1] did not, however, make a direct comparison between energy and magnetic field spectra for a given channel coupling, as we do here.

For our model, the resulting parameters ν_E for magnetic field $B = 10$ G (for reasons explained below) and ν_B for energy $E = 0$ are shown versus w in Fig. 3. For full strength of anisotropic coupling, $w = w_0$, both spectra have essentially unit Brody parameters and are both fully chaotic, and agree with the results of the model in the previous section (solid points). Both Brody parameters drop rapidly as w decreases, but ν_E drops much more rapidly. Therefore, for a given version of subdysprosium that is not completely chaotic, the magnetic field spectrum of Fano-Feshbach resonances would appear more chaotic than would the energy spectrum at a given magnetic field. For much smaller values of w the spectra both return to random, Poisson-type NNS, and do not differ as dramatically.

A caveat in preparing this Fig. 3 is that the energy spectrum is computed at a magnetic field $B = 10$ G, rather than $B = 0$. This is because, for small B , the spectrum has two characteristic energy scales. There is a small energy scale given by the very regular spacing of Zeeman levels, and a larger energy spacing given by the characteristic rovibrational energies. This

leads to a bimodal NNS that is not well described by a Brody distribution for any value of ν_E . Once a field is applied and Zeeman energy splitting becomes comparable to rovibrational splittings, this is no longer an issue.

III. SCHEMATIC MODEL OF MAGNETIC FIELD DEPENDENCE

Examination of the onset of chaos in subdysprosium in Fig. 3 suggests that the Brody parameter curves $\nu_E(w)$ and $\nu_B(w)$ have the same shape, namely, a sigmoidal dependence that rises at first then saturates at unity. The two curves can be made to nearly overlap by shifting one of them along the logarithmic w axis. Another way to say this is that for a given value of w in the model, the two kinds of spectra have different *effective* values of w , scaled by some factor. In this section we explore this idea.

To do so, it is worthwhile to construct an even simpler model that incorporates the essential features of the subdysprosium model, but that lends itself better to analytical understanding. These essential features are as follows: an underlying spectrum of pseudovibrational states representing the molecule in zero field; a collection of pseudomagnetic moments that map these energies to magnetic field values; and a strong mixing that generates chaos.

A. It's only a model

To this end, we contemplate a set of N_v energy levels E_i to represent the $B = 0$ molecule. These energies have mean spacing E_0 , which defines the unit of energy. They are chosen randomly in the energy interval $[-N_v E_0, 0]$, appropriate to pseudovibrational states lying below a threshold at $E = 0$. Each of these is assumed to have a d -fold degeneracy of pseudomagnetic levels, bringing the total number of states in the model to $N = N_v d$. These degenerate states are enumerated by pseudomagnetic quantum numbers, $m = 1, 2, \dots, d$. The degeneracy of these states is lifted in a magnetic field, which each one getting an additional energy $m\mu B$, which represents all the states rising in energy with magnetic field. The combination μB effectively defines the magnetic field unit $B_0 = E_0/\mu$.

The Hamiltonian of the model is then given in matrix form as

$$H_{\text{schematic}} = D + V + \mu B M, \quad (12)$$

where D and M are diagonal matrices,

$$D = \text{diag}(E_1, E_1, \dots, E_1, E_2, E_2, \dots, E_2, \dots, E_{N_v}), \quad (13)$$

where each energy E_i is repeated d times; and

$$M = \text{diag}(1, 2, \dots, d, 1, 2, \dots, d, \dots, d). \quad (14)$$

In this way, all the original pseudovibrational levels move to intercept the $E = 0$ axis somewhere in the interval $B \in [0, N_v E_0/\mu]$ [see Fig. 4(a)]. The energy and magnetic field spectra are therefore characterized by mean spacing of, respectively,

$$\Delta E = \frac{N_v E_0}{N_v d} = \frac{E_0}{d}, \quad \Delta B = \frac{E_0/\mu}{d}. \quad (15)$$

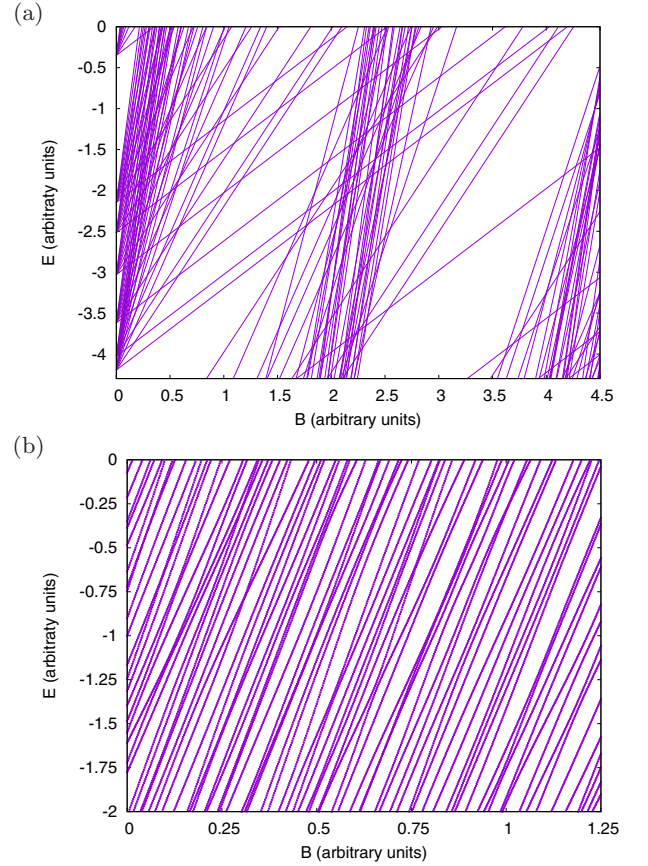


FIG. 4. Simulated spectra for the schematic model of chaotic molecules in a magnetic field in the case of 10-fold degeneracy. In (a) is shown the nonchaotic version $w = 0$, illustrating the movement of levels from the energy axis to the magnetic field axis. In (b) is shown a chaotic spectrum with $w = 0.8$; compare to Fig. 1.

Chaos is introduced into the model via the coupling matrix V , in the same way it was for the subdysprosium model. That is, the elements of V will be drawn from the Gaussian orthogonal ensemble given in (11). Sample spectra for $w = 0.8 E_0$ are shown in Fig. 4(b). These spectra reproduce, at least qualitatively, the features of the more realistic model in Fig. 1. Note especially that the lines are nearly, but not quite, parallel, representing the regularization of magnetic moments of all the states.

B. Chaos in the model

Using this schematic model, we compute the Brody parameters $\nu_E(w)$ and $\nu_B(w)$ as functions of w , and for several different values of spin degeneracy d . The results are shown in Fig. 5. In general, all curves show the familiar sigmoidal dependence that shows how the chaos turns on as w is increased.

The specific curves are different, however. In general, larger spin degeneracies d cause the curves $\nu_E(w)$ and $\nu_B(w)$ to shift to smaller values of w , indicating an earlier onset of chaos. Moreover, for a given value of $d > 1$, ν_B is shifted to smaller

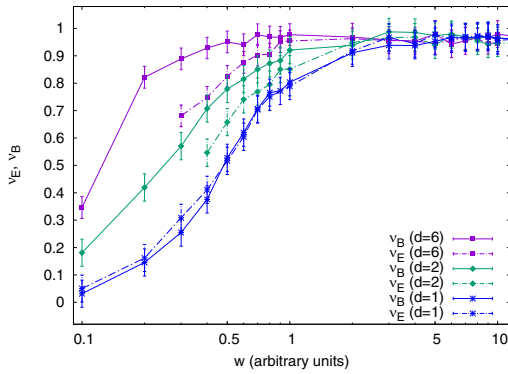


FIG. 5. Brody parameters ν_E and ν_B for the schematic model presented in Sec. II A as a function of the width parameter w .

w than ν_E , as in the subdysprosium model, suggesting that for a given model with a given value of w , the magnetic field spectrum exhibits a greater degree of chaos by this measure. For $d = 1$, the two Brody parameters coincide.

Qualitatively, these features can be understood in simple terms. For example, in the energy spectra the mean energy spacing is $\Delta E = E_0/d$. The spectrum, random when $w = 0$, starts to see significant mixing and level repulsion when off-diagonal matrix elements in the Hamiltonian, of order w , become comparable to the mean spacing of the diagonal elements. Thus, for $d = 1$ the transition to chaos is nearly complete when $w = 1$ (recall that w is given in units of E_0 in the plot). But, for larger values of d , the coupling w should be compared to a smaller mean spacing E_0/d , so that the level repulsion, hence chaos, appears at smaller values of $w \sim E_0/d$. Thus, the Brody parameters ν_E (dashed curves in Fig. 5) are shifted leftward in the figure for larger d .

Similarly, for a given degeneracy d , the magnetic field spectrum becomes chaotic for smaller w than does the corresponding energy spectrum. This suggests that the magnetic field spectrum possesses a larger ratio of effective coupling to mean level spacing, at least in the range explored, than does the energy spectrum. We can see this as follows.

To find the $B = 0$, energy spectrum, we solve the matrix diagonalization

$$(D + V)x^{(\alpha)} = e_\alpha x^{(\alpha)} \quad (16)$$

for the energy eigenvalues e_α and eigenstates $x^{(\alpha)}$. The size of w in the matrix V , as compared to the mean spacing ΔE of the diagonal elements of D , controls the degree of chaos and the value of the Brody parameter.

Similarly, the $E = 0$, magnetic field spectrum is given by setting the energy to zero, thereby solving

$$(D + V + \mu BM)y = 0 \quad (17)$$

for the spectrum of B values. Since M is a positive-definite matrix, $M^{1/2}$ and $M^{-1/2}$ exist, and this matrix equation is equivalent to the diagonalization

$$(\tilde{D} + \tilde{V})\tilde{y}^{(\alpha)} = b_\alpha \tilde{y}^{(\alpha)}, \quad (18)$$

where the transformed matrices, in units of magnetic field, read as

$$\tilde{D} = -\frac{1}{\mu} M^{-1/2} D M^{-1/2}, \quad \tilde{V} = -\frac{1}{\mu} M^{-1/2} V M^{-1/2}, \quad (19)$$

and the eigenstate is changed to

$$\tilde{y} = M^{1/2} y. \quad (20)$$

The magnetic field spectrum derives from a qualitatively different eigenvalue problem (18) than the one in Eq. (17) that gives the energy spectrum. For one thing, the unperturbed spectrum (diagonal elements of \tilde{D}) no longer have a uniform density of states. To see this, note that the diagonal elements of \tilde{D} have the form $B_i = -E_i/(m\mu)$. Thus, the spectrum is squeezed to smaller values of B for larger values of m , as can be seen in Fig. 4(a). The small region of magnetic field in the interval $B \in [0, N_v B_0/d]$, contains a number of states given by

$$\sum_{m=1}^d \frac{N_v}{d} m = \frac{N_v}{d} \frac{d(d+1)}{2}. \quad (21)$$

The density of states in this near-zero-field interval is then

$$\rho_B = \frac{d(d+1)}{2B_0}. \quad (22)$$

This is higher than the value d/B_0 given by taking the total number and dividing by the total magnetic field range. It is worthwhile to restrict attention to this magnetic field region where the density of states is relatively uniform. Such a region can cover as many magnetic field resonance values as desired, by simply increasing N_v .

Similarly, the matrix \tilde{V} is no longer necessarily drawn from the GOE since its matrix elements become $-V_{ij}/(\mu\sqrt{mm'})$, and are diminished by the m quantum numbers of the states involved. In this case, the matrix element distributions no longer share a common width as implied by (11). Rather, for each given pair of numbers m, m' , the matrix elements V_{ij} are Gaussian distributed, with an effective width $w_{mm'} = w/(\mu\sqrt{mm'})$.

The net distribution of all matrix elements will no longer be Gaussian, in general, but for the sake of approximation we can define a Gaussian distribution whose width is defined by the root-mean-square deviation of the matrix elements. That is, given the mean-squared width $\langle V_{ij}^2 \rangle = w^2/2$, the mean-squared width of any off-diagonal element of \tilde{V} is

$$\frac{\tilde{w}^2}{2} = \frac{1}{d^2} \sum_m \sum_{m'} \frac{w^2}{2\mu^2} \frac{1}{mm'} = \frac{w^2}{2\mu^2} \frac{1}{d^2} \left(\sum_{m=1}^d \frac{1}{m} \right)^2. \quad (23)$$

For the sake of estimation, we will pretend that \tilde{V} is a member of a GOE with width \tilde{w} .

Then, roughly, the degree of chaos in the magnetic field spectrum is determined by the ratio of \tilde{w} to the mean level spacing in the magnetic field range of interest,

$$\frac{\tilde{w}}{1/\rho_B} = \frac{w}{\mu B_0} \frac{d+1}{2} \sum_{m=1}^d \frac{1}{m}. \quad (24)$$

The corresponding parameter determining the degree of chaos in the energy spectrum is $w/(1/\rho_E)$, where $\rho_E = E_0/d$ is the density of states for the energy levels. The relation between these two is therefore

$$\frac{\tilde{w}}{1/\rho_B} = \frac{w}{1/\rho_E} f_c(d), \quad (25)$$

where f_c is a correction function given by

$$f_c(d) = \frac{d+1}{2d} \sum_{m=1}^d \frac{1}{m}. \quad (26)$$

This factor is unity for $d = 1$, i.e., for no spin degeneracy. In this case, the energy spectrum is just rescaled by the magnetic moment to become the magnetic field spectrum, and the Brody parameter ought therefore to come out the same. For nonzero spin degeneracy $d > 1$, however, $f_c > 1$, implying that the magnetic field spectrum should be *more chaotic* (larger Brody parameter) than the energy spectrum. This conclusion is restricted to the near-zero-field region $B \in [0, N_v B_0/d]$. In this region, the density of states ρ_B grows rapidly as a function of degeneracy ($\sim d^2$), faster than the comparatively slow growth of the width parameter $\tilde{w} \sim \ln d/d$.

IV. CONCLUSIONS

In summary, we have verified, by numerical and semianalytic considerations, that a molecule that exhibits partial chaos in its energy spectrum below its dissociation threshold, may appear to exhibit a greater degree of chaos as measured in

its spectrum of Fano-Feshbach resonances. This conclusion, drawn from the nearest-neighbor-spacing distribution, is consistent with the general models of Ref. [1]. In both models, the transition from the $B = 0$ energies to the $E = 0$ magnetic field resonance positions involves a series of avoided crossings or, alternatively, nontrivial magnetic moment fluctuations of the molecular states.

It is of course difficult to change the degree of chaos in a given molecule and to make a full study of the dependencies in Fig. 3. Nevertheless, the Dy_2 molecule as measured in Ref. [1] has Brody parameters ν_B somewhat less than unity. It is therefore conceivable that a measurement of the energy spectrum of Dy_2 at fixed magnetic field, for example by microwave spectroscopy, would be capable of testing the hypothesis that $\nu_E < \nu_B$ for this molecule. Effectively varying the degree of chaos native to a molecule may have to wait until similar spectra are measured in alternative, less chaotic molecules elsewhere in the periodic table.

ACKNOWLEDGMENTS

We acknowledge useful discussions with J. d’Incao and M. Sze. We also acknowledge funding from the US Army Research Office under ARO Grant No. W911NF-12-1-0476 and from the JILA NSF Physics Frontier Center, Grant No. PHY-1734006. L.D.A. acknowledges the financial support of the Czech Science Foundation (Grants No. P209/18-00918S and No. P208/17-26751Y).

-
- [1] T. Maier, H. Kadau, M. Schmitt, M. Wenzel, I. Ferrier-Barbut, T. Pfau, A. Frisch, S. Baier, K. Aikawa, L. Chomaz *et al.*, *Phys. Rev. X* **5**, 041029 (2015).
 - [2] A. Frisch, M. Mark, K. Aikawa, F. Ferlaino, J. L. Bohn, C. Makrides, A. Petrov, and S. Kotochigova, *Nature (London)* **507**, 475 (2014).
 - [3] T. Maier, I. Ferrier-Barbut, H. Kadau, M. Schmitt, M. Wenzel, C. Wink, T. Pfau, K. Jachymski, and P. S. Julienne, *Phys. Rev. A* **92**, 060702 (2015).
 - [4] K. Baumann, N. Q. Burdick, M. Lu, and B. L. Lev, *Phys. Rev. A* **89**, 020701 (2014).
 - [5] K. Aikawa, A. Frisch, M. Mark, S. Baier, A. Rietzler, R. Grimm, and F. Ferlaino, *Phys. Rev. Lett.* **108**, 210401 (2012).
 - [6] D. M. Leitner, R. S. Berry, and R. M. Whitnell, *J. Chem. Phys.* **91**, 3470 (1989).
 - [7] M. D. Frye, M. Morita, C. L. Vaillant, D. G. Green, and J. M. Hutson, *Phys. Rev. A* **93**, 052713 (2016).
 - [8] T. A. Brody, *Lett. Nuovo Cimento* **7**, 482 (1973).
 - [9] B. R. Judd and I. Lindgren, *Phys. Rev.* **122**, 1802 (1961).
 - [10] A. Petrov, E. Tiesinga, and S. Kotochigova, *Phys. Rev. Lett.* **109**, 103002 (2012).
 - [11] B. C. Yang, J. Pérez-Ríos, and F. Robicheaux, *Phys. Rev. Lett.* **118**, 154101 (2017).
 - [12] J. Mur-Petit and R. A. Molina, *Phys. Rev. E* **92**, 042906 (2015).
 - [13] R. A. Molina, J. Retamosa, L. Muiñoz, A. Relaño, and E. Faleiro, *Phys. Lett. B* **644**, 25 (2007).
 - [14] K. Życzkowski, M. Lewenstein, M. Kuś, and F. Izrailev, *Phys. Rev. A* **45**, 811 (1992).

ULTRACOLD COLLISIONS OF POLYATOMIC
MOLECULES: CAO₂

Bibliographic record of the attached publication:

Augustovičová, L. D. and J. L. Bohn (2019). "Ultracold collisions of polyatomic molecules: CaOH." In: *New Journal of Physics* 21.10, p. 103022.
DOI: [10.1088/1367-2630/ab4720](https://doi.org/10.1088/1367-2630/ab4720).



PAPER

Ultracold collisions of polyatomic molecules: CaOH

OPEN ACCESS

RECEIVED
21 June 2019REVISED
13 September 2019ACCEPTED FOR PUBLICATION
24 September 2019PUBLISHED
9 October 2019Lucie D Augustovičová¹ and John L Bohn²¹ Charles University, Faculty of Mathematics and Physics, Department of Chemical Physics and Optics, Ke Karlovu 3, CZ-12116 Prague 2, Czech Republic² JILA, NIST, and Department of Physics, University of Colorado, Boulder, CO 80309-0440, United States of AmericaE-mail: augustovicova@karlov.mff.cuni.cz**Keywords:** ultracold molecules, evaporative cooling, stark effect, dipole–dipole interaction

Original content from this work may be used under the terms of the [Creative Commons Attribution 3.0 licence](https://creativecommons.org/licenses/by/4.0/).

Any further distribution of this work must maintain attribution to the author(s) and the title of the work, journal citation and DOI.

**Abstract**

Ultracold collisions of the polyatomic species CaOH are considered, in internal states where the collisions should be dominated by long-range dipole–dipole interactions. The computed rate constants suggest that evaporative cooling can be quite efficient for these species, provided they start at temperatures achievable by laser cooling. The rate constants are shown to become more favorable for evaporative cooling as the electric field increases. Moreover, long-range dimer states $(\text{CaOH})_2^*$ are predicted to occur, having lifetimes on the order of microseconds.

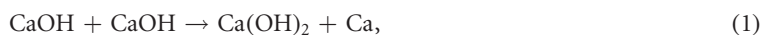
1. Introduction

The technology to laser cool molecules leads the way to a wave of truly ultracold molecular species, achieving temperatures on the microKelvin scale rather than the milliKelvin scale [1]. These temperatures are low enough that the molecules can be confined in magnetic [2, 3] or optical dipole traps [4, 5], can be produced in individual quantum states, tend to collide in individual partial waves, and have collisions that respond strongly to laboratory electric and magnetic fields [6]. These are all ingredients that enhance the experimental ability to control ultracold molecules. The newest members on the list of laser-coolable species are polyatomic species [7–10]. The linear triatomic species SrOH is a good candidate for laser cooling [11], and has been deflected by optical forces [12], opening the way for similar species such as CaOH and CaOCH_3 [13], and more besides. These species should expand opportunities for quantum information, sensing, and fundamental physics [9].

Central to the properties of an ultracold gas are the collision cross sections of its constituent molecules. As in any ultracold environment, high elastic scattering rates are desirable to bring the gas to thermal equilibrium, while low inelastic scattering rates are essential to protect the gas from two-body losses. Understanding collision cross sections and their response to applied electromagnetic fields is also vital for controlling collisions, with attendant applications to ultracold chemistry. The species SrOH has been studied experimentally in collisions with helium buffer gas atoms at 2.2 K, finding that vibrational quenching occurs rapidly in these collisions [14]. In addition, collisions of SrOH with lithium atoms has been investigated theoretically, concluding that sympathetic cooling of the molecule with this atom is feasible [15].

In this article we extend cold collision theory of linear polyatomic molecules, considering CaOH molecules colliding with each other. Central to our approach is that, for certain collisions at ultralow temperature, the scattering rates and their field dependence rely on physics that occurs when the molecules are far apart, that is, on scales larger than the range of the exchange potentials between them. For molecules such as OH in weak-electric-field seeking states, these long range forces often exert torques that drive the colliding molecules into strong-field-seeking states, instigating unacceptable loss rates. A main point we raise here is that laser-cooled molecules can be optically trapped in strong-field-seeking states, making them far more immune to these state-changing collisions.

We therefore focus on such long-range processes, and in particular ignore possibilities such as the chemical reaction



which is exothermic by some 13 000 K. $\text{Ca}(\text{OH})_2$ is a stable compound used in industrial applications like paper production and sewage treatment. It is not known whether the reaction (1) occurs at low temperatures in the gas phase. If it does, this is obviously a detriment to producing and maintaining a stable, ultracold gas of CaOH . We will disregard the possibility that the reaction occurs, both because the potential energy surface is unknown, and because, in the appropriate internal states, the molecules are expected to be shielded by the repulsive parts of the dipole–dipole interaction.

This circumstance simplifies the description of scattering, and leads to certain common behaviors. In this article, exploiting the electric dipole moment of CaOH and considering a state that has a small parity doublet, we find that these behaviors still occur. The behaviors that we single out are: (1) a suppression of inelastic scattering at sufficiently high electric field and sufficiently low temperature, for states that can be optically trapped; and (2) a set of electric-field resonances, previously described as ‘field linked states’, [16, 17] that could serve as an additional platform for controlling these species and their interaction.

2. The molecule

The molecule CaOH (or the closely related SrOH) has a linear geometry in its $^2\Sigma^+$ electronic ground state. Around this linear geometry, the molecule has vibrational modes in the Ca-O and O-H bonds, denoted by quantum numbers ν_1 and ν_3 , respectively; and a bending vibration denoted ν_2 . The collective state of the vibration is then labeled (ν_1, ν_2, ν_3) [18]. The bending mode is lower in energy in these molecules, whereby at low temperatures we focus on the states $(0, \nu_2, 0)$.

For small vibrational quanta ν_2 , we regard the molecule as a rigid asymmetric rotor, defined by a principal axis that we think of as the Ca-H axis. Owing to the bending vibration, the O atom is displaced a small distance off this axis. Suitable linear combinations of vibrations in the molecule-fixed x and y directions amount to rotation of the O atom around the molecular axis, with component l on this axis, where l is a signed integer. If the electron were to have angular momentum projection Λ on this axis, then the relevant quantum number in Hund’s case a would be $K = l + \Lambda$, but for the Σ electronic state, $\Lambda = 0$ and $K = l$. To specify the value of $|l|$ given ν_2 , one writes the vibrational state as $(\nu_1, \nu_2^{|l|}, \nu_3)$.

The asymmetric rigid rotor is therefore described using the usual rotor wave functions

$$\langle \alpha\beta\gamma | l N M_N \rangle = \sqrt{\frac{2N+1}{8\pi^2}} D_{M_N l}^{N*}(\alpha\beta\gamma) \quad (2)$$

in terms of the Euler angles (α, β, γ) giving the orientation of the molecule, where $N \geq |l|$ and therefore $N = 1$ is the ground rotational state of the $(0, 1^1, 0)$ state of interest. The vibrational rotation quantum number l , tied to the molecular axis, is treated like one would treat the projection of the electron angular momentum in Hund’s case a. This extends even to notation: states with angular momenta $|l| = 0, 1, 2, \dots$ are labeled $^2\Sigma, ^2\Pi, ^2\Delta, \dots$ (It is understood that the electron remains in a Σ state.) For $|l| > 0$, the degeneracy of two states is broken, producing an l -doubling analogous to Λ -doubling in a case a molecule. Meanwhile, the electronic and nuclear spin states are well described by Hund’s case b. An appropriate uncoupled basis state for the rotor wave functions is then

$$|l N M_N \rangle |S M_S \rangle |I M_I \rangle. \quad (3)$$

This basis forms the foundation upon which all the results are computed and interpreted in what follows. Appropriate basis sets may, however, require different superpositions of these states in the low- and high-electric field limits.

In this paper we focus on a particular state, the lowest bending excitation with $\nu_2 = 1$. This is because it is the lowest-lying state with an l -doublet, and hence can be polarized easily in a small electric field. Thus the low temperature scattering behavior is expected to be dominated by dipolar forces between the molecules, enabling control over the collisions.

2.1. Field-free hamiltonian

In the absence of an applied field, the states (3) are coupled into a total angular momentum scheme, first adding \mathbf{N} and \mathbf{S} to produce \mathbf{J} , then adding \mathbf{I} to produce the total spin \mathbf{F} :

$$|l[(NS)JI]FM_F\rangle = \sum_{M_N M_S M_I} |l N M_N \rangle |S M_S \rangle |I M_I \rangle \langle N M_N S M_S | J M_J \rangle \langle J M_J I M_I | F M_F \rangle. \quad (4)$$

When $l \neq 0$, these states are combined into parity eigenstates

$$||l, \epsilon [(NS)JI]FM_F\rangle = \frac{1}{\sqrt{2}} [|(l)[(NS)JI]FM_F\rangle + \epsilon |(-l)[(NS)JI]FM_F\rangle] \quad (5)$$

with the parity $p = \epsilon(-1)^{N-l}$. The complete basis set is then

$$|(\nu_1, \nu_2^l, \nu_3); |l, \epsilon; [(NS)II]FM_F\rangle. \quad (6)$$

For a given electronic state and a given vibrational state (ν_1, ν_2^l, ν_3) , the Hamiltonian of the molecule is written as a sum of several terms, in roughly descending order of energy:

$$H = H_{\text{vib}} + H_{\text{rot}} + H_{\text{sr}} + H_{\text{ld}} + H_{\text{hf}}, \quad (7)$$

denoting, respectively, the vibrational and rotational energies, the spin-rotation coupling, the l -doubling, and the hyperfine interaction.

For $\nu_2 = 1$ states, the model Hamiltonian H is diagonal in the basis chosen, with the matrix elements as given in [19]. In higher states this is not the case, for example, for $\nu_2 = 2$ there can be mixing between the $^2\Sigma$ and $^2\Delta$ states, but this will not concern us here. The rotational Hamiltonian, ignoring centrifugal distortion, is

$$H_{\text{rot}} = B_v[N(N+1) - I^2]. \quad (8)$$

The spin-rotation Hamiltonian, again ignoring centrifugal distortion, is diagonal in the basis (6) and is given by

$$H_{\text{sr}} = \gamma \mathbf{N} \cdot \mathbf{S} = \frac{\gamma}{2}[J(J+1) - N(N+1) - S(S+1)]. \quad (9)$$

The l -doubling arises due to Coriolis coupling of the state l to states with $l \pm 1$, and grows with N . Using the conventions established in [19, 20], the l -doubling Hamiltonian is diagonal in (6), with matrix elements

$$H_{\text{ld}} = \frac{q_l \epsilon}{2} N(N+1). \quad (10)$$

These states are labeled by the spectroscopic designation, letters e and f , assigned by the convention

$$p = \begin{cases} +(-1)^{J-1/2}, & e \\ -(-1)^{J-1/2}, & f \end{cases} \quad (11)$$

Finally, the hyperfine interaction is the smallest perturbation to the molecule, taking the form

$$H_{\text{hf}} = b \mathbf{J} \cdot \mathbf{I} = \frac{b}{2}[F(F+1) - J(J+1) - I(I+1)], \quad (12)$$

where $I = 1/2$ is the spin of the hydrogen atom, the only relevant nuclear spin in the $^{40}\text{Ca}^{16}\text{OH}$ molecule.

Most of the spectroscopic constants are reported in [19]. For the $|l| = 1$ state of CaOH, we use $B = 9996.75184$ MHz, $\gamma = 35.051$ MHz, $q_l = -21.6492$ MHz. The hyperfine constant has not been measured, to our knowledge. We therefore use the value measured for the $l = 0, N = 1$ level, $E_{F=1} - E_{F=0} = 7 \times 10^{-3}$ MHz [21].

2.2. The electric field

Polar molecules like CaOH will obviously respond to an electric field. A magnetic field is perhaps less relevant at this point, since the electron is only weakly coupled to the molecular axis. We therefore focus on the Stark effect. Its Hamiltonian is

$$H_{\text{E}} = -\mathbf{d} \cdot \mathcal{E} = -d\mathcal{E}C_{10}(\cos\beta), \quad (13)$$

where β is the angle between \mathbf{d} (which coincides with the molecular axis) and \mathcal{E} . For use later on, we compute the matrix elements of C_{1q} for arbitrary q . These are given in terms of the reduced matrix element as

$$\begin{aligned} & \langle l, \epsilon; [(NS)II]FM_F | C_{1q} | l, \epsilon'; [(N'S)J'I]F'M_F' \rangle \\ &= (-1)^{F-M_F} \sqrt{2F+1} \begin{pmatrix} F & 1 & F' \\ -M_F & q & M_F' \end{pmatrix} \\ & \times \langle l, \epsilon; [(NS)II]F | C_{1q} | l, \epsilon'; [(N'S)J'I]F' \rangle. \end{aligned} \quad (14)$$

The reduced matrix element is computed in the usual way [22, 23]

$$\begin{aligned} & \langle l, \epsilon; [(NS)II]F | C_{1q} | l, \epsilon'; [(N'S)J'I]F' \rangle \\ &= (-1)^{F'+J'+S+I+l} \left(\frac{1 + \epsilon\epsilon'(-1)^{N+N'+1}}{2} \right) [F'] [J] [J'] [N] [N'] \\ & \times \begin{Bmatrix} J & J' & 1 \\ N' & N & S \end{Bmatrix} \begin{Bmatrix} F & F' & 1 \\ J' & J & I \end{Bmatrix} \begin{pmatrix} N & 1 & N' \\ -l & 0 & l \end{pmatrix}, \end{aligned} \quad (15)$$

where $[J] = \sqrt{2J+1}$, etc. The magnitude of the dipole moment has been measured as $d = 1.465$ D [24].

2.3. High-field limit

Although the scattering calculations presented below are performed by casting the two-body Hamiltonian in the zero-field basis (6), to describe the states in the high-field limit it is useful to specify the quantum numbers that are good there. In this limit the dominant term in the Hamiltonian is the Stark effect, which in the uncoupled basis (3) has matrix elements diagonal in N_M and l , as well as the spins:

$$\begin{aligned} & \langle lNM_N | \langle SM_S | \langle IM_I | -d \cdot \mathcal{E} | l'N'M'_N \rangle | SM'_S \rangle | IM'_I \rangle \\ & = -d\mathcal{E}(-1)^{M_N-l} [N][N'] \begin{pmatrix} N & 1 & N' \\ -M_N & 0 & M'_N \end{pmatrix} \begin{pmatrix} N & 1 & N' \\ -l & 0 & l \end{pmatrix} \delta_{M_S M'_S} \delta_{M_I M'_I}. \end{aligned} \quad (16)$$

Moreover, we are primarily interested in the $N = 1$ rotational ground state. This state is mixed with the nearby $N = 2$ state for fields on the order of $4B_v/d \approx 5 \times 10^4 \text{ V cm}^{-1}$. So long as we remain well below this field, the Stark Hamiltonian is diagonal in N as well, and its matrix elements simplify to

$$\langle lNM_N | \langle SM_S | \langle IM_I | -d \cdot \mathcal{E} | l'NM'_N \rangle | SM'_S \rangle | IM'_I \rangle = -d\mathcal{E} \frac{lM_N}{N(N+1)} \delta_{M_S M'_S} \delta_{M_I M'_I}, \quad (17)$$

which harbors a double degeneracy for each value of lM_N .

Next is the spin-rotation Hamiltonian, which couples different M_N and M_S . Since

$$H_{sr} = \gamma \mathbf{N} \cdot \mathbf{S} = \gamma \sum_q (-1)^q N_q S_{-q}, \quad (18)$$

we have in the uncoupled basis

$$\begin{aligned} \langle lNM_N | \langle SM_S | \langle IM_I | H_{sr} | l'NM'_N \rangle | SM'_S \rangle | IM'_I \rangle & = \gamma (-1)^{q+N-M_N+S-M_S} \sqrt{N(N+1)(2N+1)S(S+1)(2S+1)} \\ & \times \begin{pmatrix} N & 1 & N \\ -M_N & q & M'_N \end{pmatrix} \begin{pmatrix} S & 1 & S \\ -M_S & -q & M'_S \end{pmatrix} \delta_{M_I M'_I}, \end{aligned} \quad (19)$$

with $q = M_N - M'_N = M'_S - M_S$. Finally, the l -doubling Hamiltonian is off-diagonal in the l quantum number:

$$\langle lNM_N | \langle SM_S | \langle IM_I | H_{ld} | l'NM'_N \rangle | SM'_S \rangle | IM'_I \rangle = (1 - \delta_{ll'}) \frac{q_l}{2} N(N+1) \delta_{M_N M'_N} \delta_{M_S M'_S} \delta_{M_I M'_I}, \quad (20)$$

The hyperfine Hamiltonian is even smaller, and we will not call it out in the high-field limit.

The Stark effect of the $(0, 1^1, 0)$, $N = 1$ levels is shown in figure 1. The range shown spans the transition from low- to high-field behavior, which occurs due to mixing of the zero-field parity states by the electric field. The transition between these two limits occurs at a field of approximately $\mathcal{E}_0 = |q_l|/d \approx 29 \text{ V cm}^{-1}$. States in the zero-field limit, $\mathcal{E} < \mathcal{E}_0$, are labeled by their good quantum numbers J , F , and parity. States in the high-field limit, $\mathcal{E} > \mathcal{E}_0$, split into three main groups, characterized by the value of lM_N , that rise in energy with field, fall with energy, or remaining relatively constant, in accordance with (17). These states are further split by H_{sr} and H_{ld} . Diagonal elements of H_{sr} allow the identification of the dominant values of M_N , whereby these states can be labeled by the value of M_J . Also shown is the total projection of angular momentum, M_F , which will allow us to identify spin-stretched states where necessary.

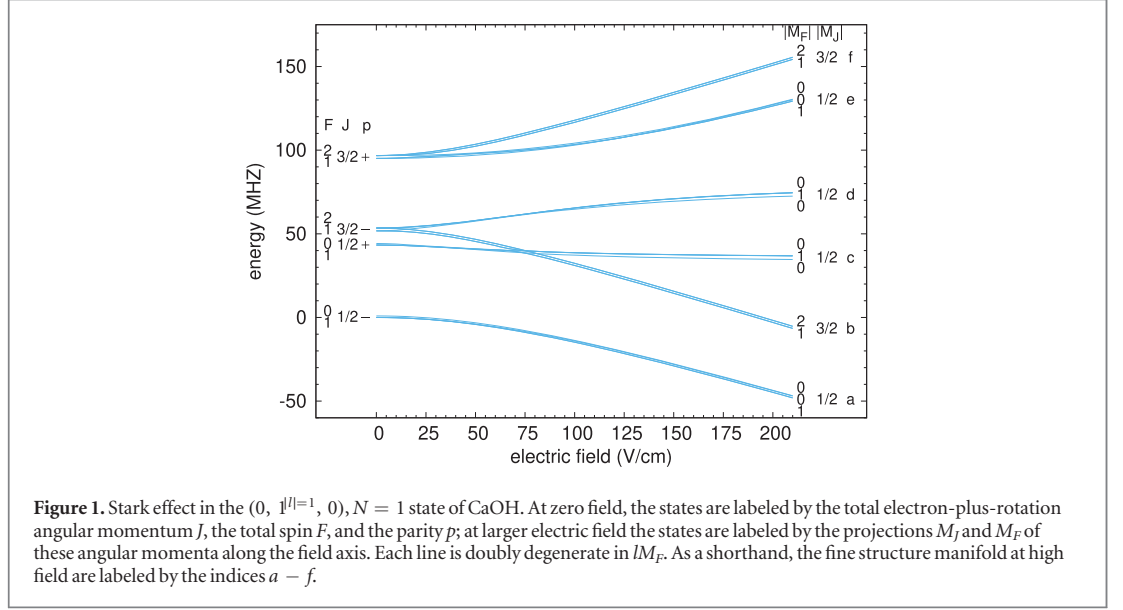
For simplicity of notation, the six relevant manifolds shown at high field are labeled simply in order of increasing energy as a, b, c, d, e, f . Here e and f do not have the usual parity meaning (equation (11)), but are merely putting energies in order, as shown. In what follows, it will be relevant to describe scattering events in terms of the rotation and spin quantum numbers, along with the fine structure manifold. Thus we will employ the shorthand notation for the used basis set

$$|x, l; M_N M_S \rangle, \quad (21)$$

where $x = a, b, \dots, f$. If needed, we will also specify the total spin M_F , but the nuclear spin plays a minor role in scattering.

3. The scattering hamiltonian

At ultralow collision energies, we focus on the long-range interactions between the molecules. This includes a van der Waals interaction $-C_6/R^6$, which we take to be isotropic. This force is weak on the scale of R where the main dipole-dipole interactions are relevant, and even a larger variation of C_6 that include rotational contribution seems not to change the overall rate constants by more than 20%. A significant contribution to inelastic scattering of dipolar molecules is that the molecules exert torques on one another due to their long-range dipole-dipole interaction, changing their internal state without requiring them to get close enough to



react chemically. Our main result, to be shown below, is that this effect can be mitigated in CaOH molecules prepared in the appropriate initial, strong-field-seeking state. To emphasize this point, we have disregarded any possibility of chemical reactions, and perform scattering calculations assuming a hard wall boundary condition at $R = 30a_0$. We are guided here by the results of [25], where the long-range shielding due to an electrostatic field was shown to suppress chemical reactivity as well as long-range inelastic scattering. Going ahead, it will of course be valuable to incorporate the influence of any potential chemical reactivity, for example by means of absorbing boundary conditions [26, 27].

Scattering at long range is driven by the dipole–dipole interaction,

$$V_d = -\frac{\sqrt{30}d^2}{R^3} \sum_{q_1 q_2} \begin{pmatrix} 2 & 1 & 1 \\ q & -q_1 & -q_2 \end{pmatrix} C_{2-q}(\theta\phi) C_{1q_1}(\beta_1\alpha_1) C_{1q_2}(\beta_2\alpha_2). \quad (22)$$

Here (θ, ϕ) are the polar angles of the intermolecular vector \mathbf{R} , and (β_i, α_i) are the polar angles giving the orientation of molecule i .

For a pair of molecules, the unsymmetrized, low-field basis functions are written

$$|\eta_1 F_1 M_{F_1}\rangle |\eta_2 F_2 M_{F_2}\rangle |LM_L\rangle \equiv |l, \epsilon_1[(N_1 S) J_1 I] F_1 M_{F_1}\rangle |l, \epsilon_2[(N_2 S) J_2 I] F_2 M_{F_2}\rangle |LM_L\rangle. \quad (23)$$

The matrix elements of the interaction are then given by

$$\begin{aligned} & \langle \eta_1 F_1 M_{F_1} | \langle \eta_2 F_2 M_{F_2} | \langle LM_L | V_d | \eta'_1 F'_1 M'_{F_1} \rangle | \eta'_2 F'_2 M'_{F_2} \rangle | L' M'_L \rangle \\ &= -\frac{\sqrt{30}d^2}{R^3} \begin{pmatrix} 2 & 1 & 1 \\ q & -q_1 & -q_2 \end{pmatrix} \langle LM_L | C_{2-q} | L' M'_L \rangle \\ & \times \langle \eta_1 F_1 M_{F_1} | C_{1q_1} | \eta'_1 F'_1 M'_{F_1} \rangle \langle \eta_2 F_2 M_{F_2} | C_{1q_2} | \eta'_2 F'_2 M'_{F_2} \rangle. \end{aligned} \quad (24)$$

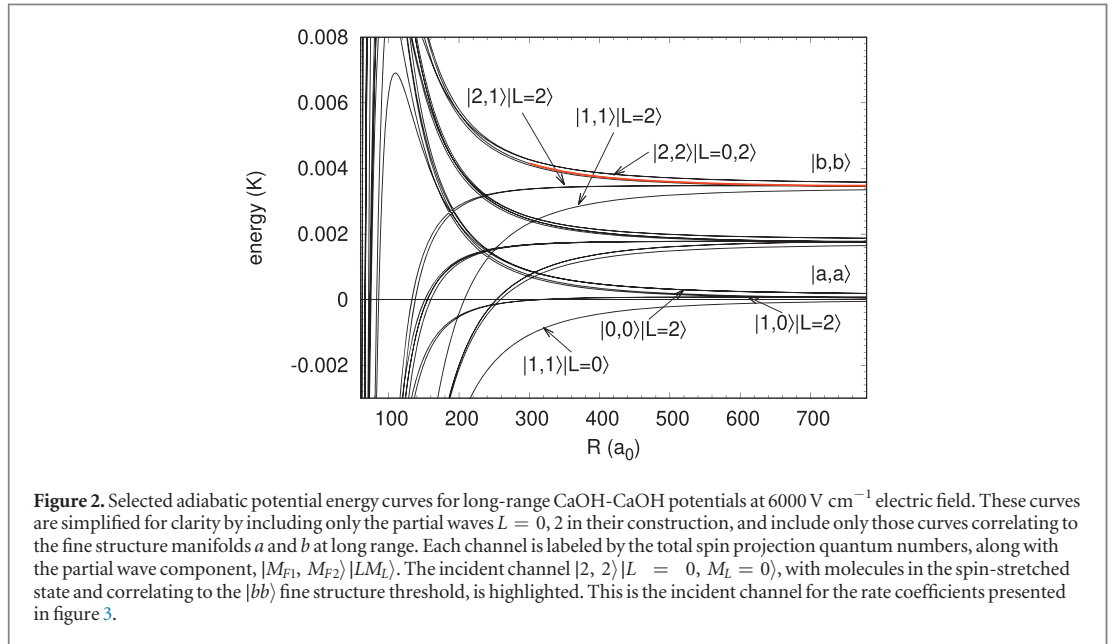
The matrix elements within molecular states are given by (14), while the partial wave matrix element is

$$\langle LM_L | C_{2-q} | L' M'_L \rangle = (-1)^{M_L} [L][L'] \begin{pmatrix} L & 2 & L' \\ 0 & 0 & 0 \end{pmatrix} \begin{pmatrix} L & 2 & L' \\ -M_L & -q & M'_L \end{pmatrix}. \quad (25)$$

In practice, matrix elements in this basis are transformed into the basis of eigenstates in the desired electric field, and form the physical scattering states. The matrix elements must moreover be symmetrized for particle exchange. In what follows here, we will consider molecules colliding in initially identical quantum states, whereby we consider only even partial waves for these bosonic molecules.

3.1. Scattering calculations

Calculations of collision cross sections are performed by first casting the Hamiltonian into the low-field basis as described above. The Hamiltonian of the two molecules is diagonalized in the presence of the applied field, if any, to define the asymptotic scattering channels. The incident channel selects one of these to describe the states of the colliding molecules. The molecules are identical bosons, so if we consider scattering two molecules in identical initial states, we incorporate even partial waves $L = 0, \dots, L_{\max}$. We find the calculations are converged with $L_{\max} = 18$.



In practice, inelastic collisions of polar molecules are subject to propensity rules that favor small values of ΔM_L , that is, it is difficult to change the projection of orbital angular momentum significantly. This propensity was explored in [28]. In the calculations that follow, we restrict that basis set to $|\Delta M_L| \leq 3$. This results in a set of typically $\sim 10^3$ channels per scattering calculation. We perform this calculation using a log-derivate propagator method [29]. The total cross section is a sum of partial cross sections over all even incoming partial-wave angular momentum, $\sigma_{i \rightarrow f}(E) = \sum_L \sigma_{L, i \rightarrow f}(E)$.

4. Results

We here report two significant properties of ultracold collisions of $(0, 1^1, 0)$ CaOH molecules, at least among those that are dominated by long-range physics. The first is the possibility of evaporative cooling in an appropriate state. The second is the occurrence of field-linked states, short-lived dimers consisting of a pair of CaOH molecules weakly bound by dipolar forces.

4.1. Prospects for evaporative cooling in the b state

Evaporative cooling is efficient only to the extent that elastic collisions occur at far higher rates than inelastic collisions. One good strategy for reducing inelastic collision rates is to never let the molecules get close together. This idea is illustrated in figure 2, which shows a simplified version of the adiabatic potential energy curves between the molecules, for molecules initially in the a or b fine structure manifolds (in the notation of figure 1), and in a field of $\mathcal{E} = 6000 \text{ V cm}^{-1}$.

Molecules in the a manifold would have no lower-energy fine structure state to scatter into, and thus are immune to fine-structure-changing collisions. However, the lowest $L = 0$ partial wave adiabatic curve is attractive and encourages the molecules to ‘go into the lion’s den’ at small R , where they may react chemically or else suffer the vibrational transition $\nu_2 = 1 \rightarrow \nu_2 = 0$.

The situation is different for molecules in the fine structure states b . Adiabatic curves for this limit, in the spin-stretched states $|M_{F_1} M_{F_2}\rangle = |22\rangle$ are repulsive, as seen in figure 2. This repulsion originates in the dipole-dipole interaction inducing couplings to the lower energy states. Level repulsion ensures that the upper states rise in energy at smaller R where the dipole-dipole interaction grows in strength. This is the principle of electrostatic shielding [25, 30–32].

We therefore focus on spin-stretched molecules with $M_F = 2$ in the b state. Figure 3 shows rate coefficients versus field strength at two different collision energies, $1 \mu\text{K}$ and 1 mK . The elastic rate constants remain high at all values of electric field, due to generically strong scattering of dipoles. A remarkable feature is an overall decreasing trend of loss rates with applied electric field at both energies. As a rule of thumb, evaporation is efficient when $K_{\text{el}}/K_{\text{inel}} \geq 100$, which occurs for experimentally reasonable fields. Our calculations indicate that for $E_c = 1 \text{ mK}$ such a field is $\mathcal{E} \sim 3500 \text{ V cm}^{-1}$ and for $E_c = 1 \mu\text{K}$ it is $\mathcal{E} \sim 2500 \text{ V cm}^{-1}$.

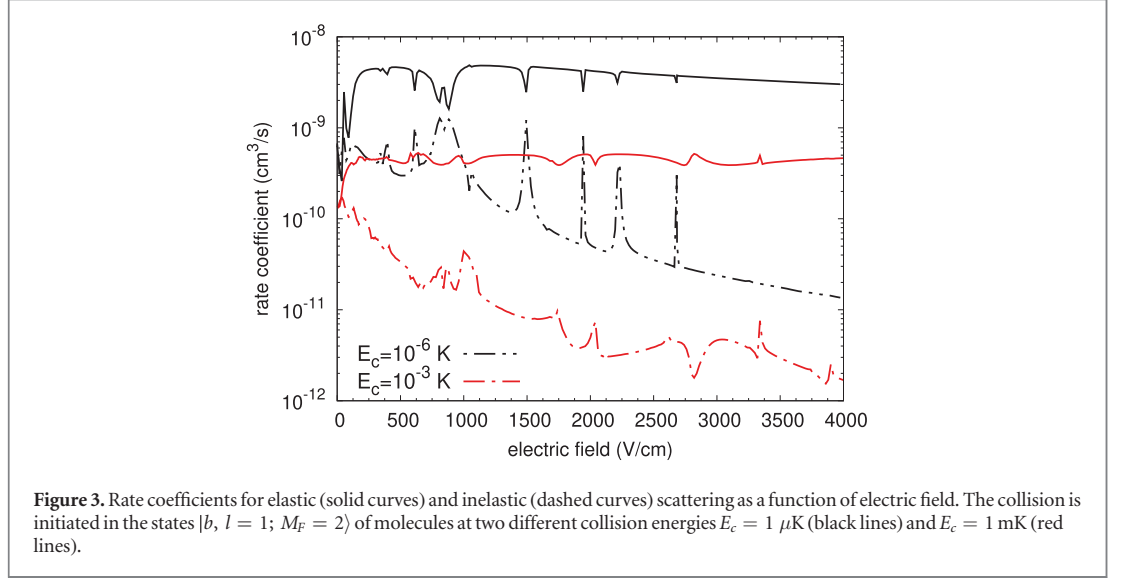


Table 1. Selected quantum numbers of states in the lowest two fine structure manifolds. For the scattering calculations, the state in the first line is the incident channel.

Manifold	l	M_N	M_S
b	1	1	1/2
b	-1	-1	-1/2
a	1	1	-1/2
a	-1	-1	1/2

The cause of this suppression of K_{inel} at high electric fields is described in detail in [28, 33], which estimates transition amplitudes in the Born approximation. Central to this approximation is the proportionality

$$T_{\text{initial,final}} \propto \langle \text{initial} | C_3 | \text{final} \rangle, \quad (26)$$

where T is the transition matrix element between initial and final scattering channels, and $\langle \text{initial} | C_3 | \text{final} \rangle$ is the matrix element of the dipole coupling between the field-dressed initial and final states. Not shown explicitly here is a radial integral over the scattering wave functions. Selection rules for the direct transitions in the first Born approximation reside in the angular factor C_3 .

Quantum numbers for states in the a and b fine structure manifolds are given in table 1; we disregard the nuclear spin as a spectator degree of freedom and denote the states as in (21). In this uncoupled basis relevant at high electric field, angular matrix elements of the dipole–dipole interaction read

$$\begin{aligned} & \langle l_1 N_1 M_{N_1} S M_{S_1} | \langle l_2 N_2 M_{N_2} S M_{S_2} | \langle L M_L | C_3 | l'_1 N'_1 M'_{N_1} S M'_{S_1} \rangle | l'_2 N'_2 M'_{N_2} S M'_{S_2} \rangle | L' M'_L \rangle \\ &= \begin{pmatrix} 2 & 1 & 1 \\ q & -q_1 & -q_2 \end{pmatrix} \langle L M_L | C_q | L' M'_L \rangle \\ & \times \langle l_1 N_1 M_{N_1} | C_{q_1} | l'_1 N'_1 M'_{N_1} \rangle \langle l_2 N_2 M_{N_2} | C_{q_2} | l'_2 N'_2 M'_{N_2} \rangle \delta_{M_{S_1} M'_{S_1}} \delta_{M_{S_2} M'_{S_2}}, \end{aligned} \quad (27)$$

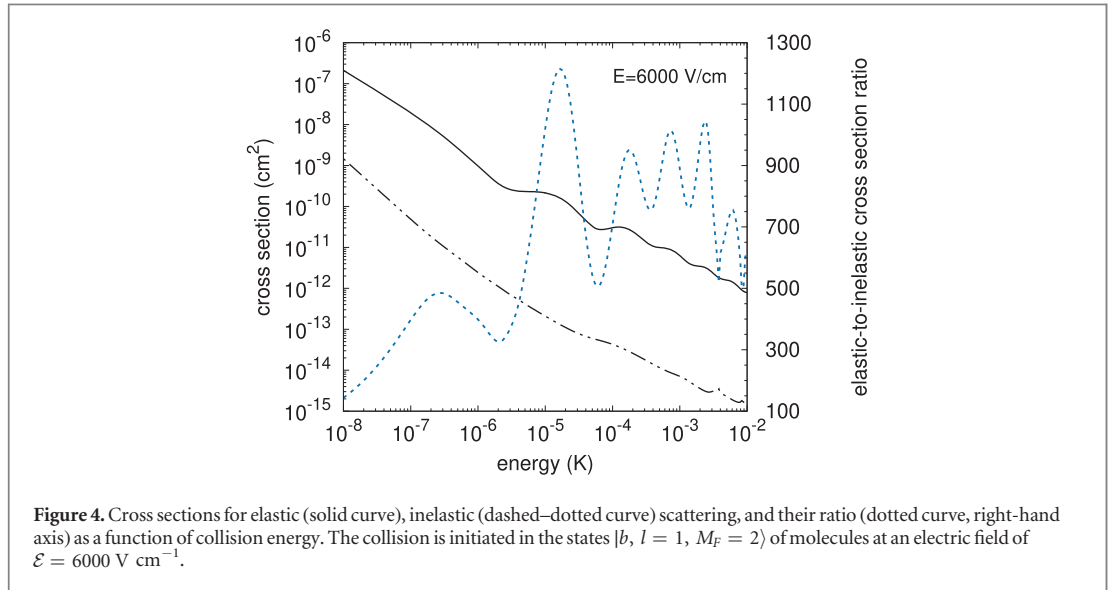
where $q = M_L - M'_L$, $q_1 = M'_{N_1} - M_{N_1}$, $q_2 = M'_{N_2} - M_{N_2}$; the matrix element in partial wave quantum numbers is given in (25); and the molecular matrix elements are given by

$$\langle l_i N_i M_{N_i} | C_q | l'_i N'_i M'_{N_i} \rangle = (-1)^{M_{N_i} - l_i} [N] [N'_i] \begin{pmatrix} N_i & 1 & N'_i \\ -l_i & 0 & l'_i \end{pmatrix} \begin{pmatrix} N_i & 1 & N'_i \\ -M_{N_i} & q_i & M'_{N_i} \end{pmatrix} \quad (28)$$

for $i = 1, 2$. The matrix elements of C_3 therefore satisfy the selection rules

$$\Delta l = 0, \quad |\Delta M_N| \leq 1, \quad \Delta M_S = 0, \quad (29)$$

and so, too, does direct scattering in the Born approximation. It is therefore clear that the dipole interaction will not directly couple the initial state approximated as $|b, +1; 1, 1/2\rangle$ to any of the other energetically accessible



states listed in the table. To make the transition within the Born approximation would require changing the electronic spin.

However, the electron spin is coupled to the molecular axis, by means of the spin-rotation coupling. This means that the state nominally labeled $|a, +1; 1, -1/2\rangle$ in table 1 is actually perturbed by another states, i.e.

$$|a\rangle \approx |a, +1; 1, -1/2\rangle - \frac{\sqrt{2}\gamma}{d\mathcal{E} + \gamma} |d, +1; 0, 1/2\rangle - \frac{q_l}{d\mathcal{E}} |e, -1; 1, -1/2\rangle. \quad (30)$$

Suppose, then, that the initial scattering channel, including partial wave, is

$$\begin{aligned} |\text{initial}\rangle &= |bb\rangle \approx \left(|b, +1; 1, 1/2\rangle - \frac{q_l}{d\mathcal{E}} |f, -1; 1, 1/2\rangle \right) \left(|b, +1; 1, 1/2\rangle - \frac{q_l}{d\mathcal{E}} |f, -1; 1, 1/2\rangle \right) \\ &\times |L = 0, M_L = 0\rangle \end{aligned} \quad (31)$$

while the final channel is

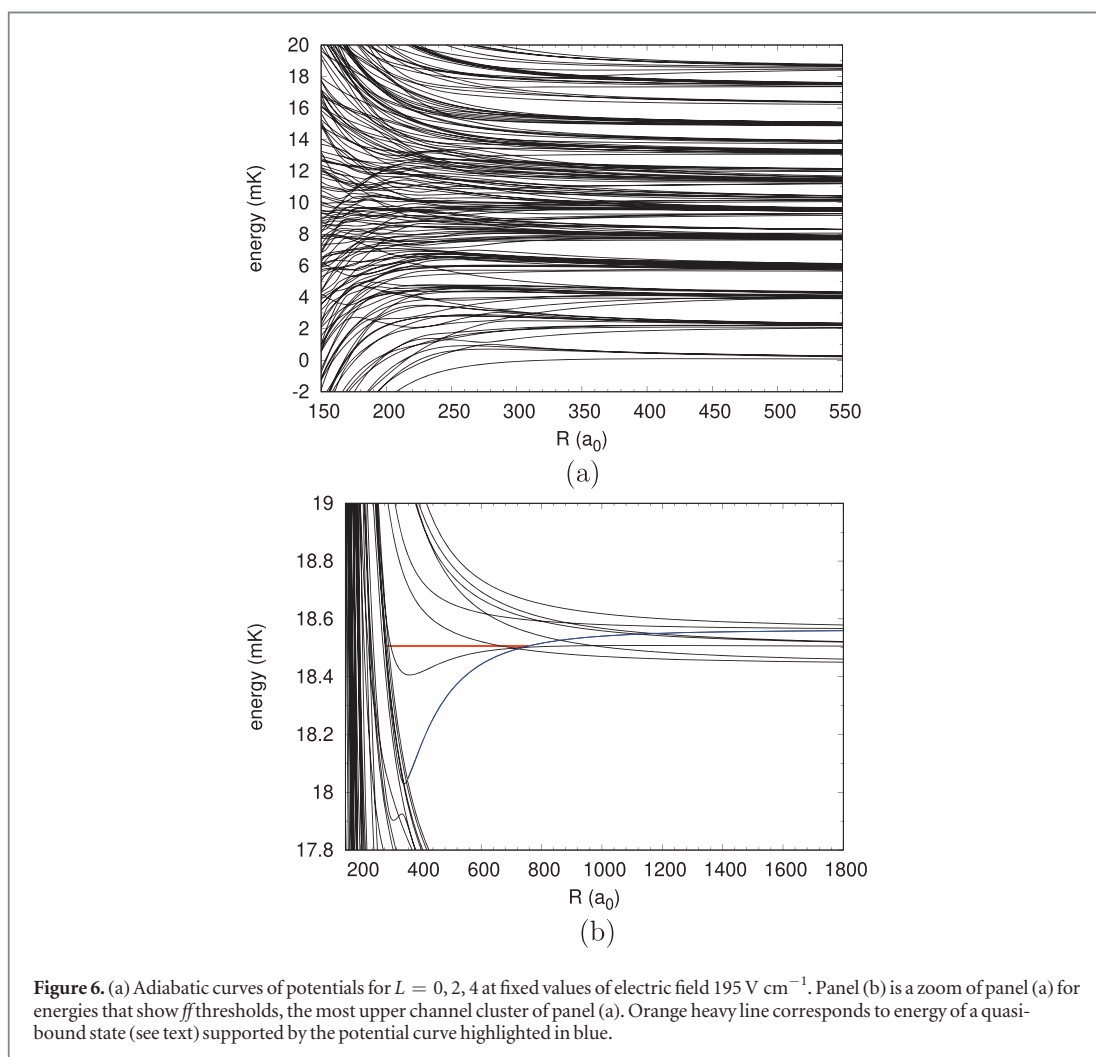
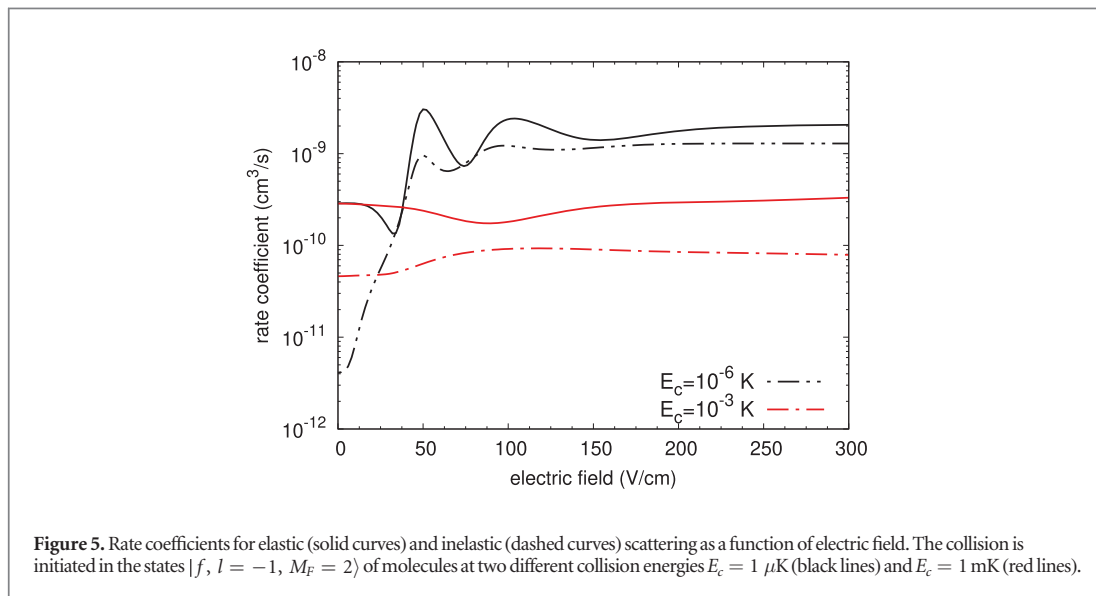
$$\begin{aligned} |\text{final}\rangle &= P_{12}|ab\rangle \approx P_{12} \left(|a, +1; -1/2\rangle - \frac{\sqrt{2}\gamma}{d\mathcal{E} + \gamma} |d, +1; 0, 1/2\rangle - \frac{q_l}{d\mathcal{E}} |e, -1; 1, -1/2\rangle \right) \\ &\times \left(|b, +1; 1, 1/2\rangle - \frac{q_l}{d\mathcal{E}} |f, -1; 1, 1/2\rangle \right) |L = 2, M_L = 1\rangle, \end{aligned} \quad (32)$$

where P_{12} denotes the exchange operator of the two molecules. Given these states and the selection rules, it is clear that the matrix element $T_{\text{initial,final}}$ is nonzero and is proportional to $\gamma/(d\mathcal{E} + \gamma)$, that is to say, inversely proportional to the electric field. This final channel is indeed the one that dominates inelastic scattering in the full numerical calculation. Applying the electric field thus has the effect of reducing the effective spin-rotation coupling of the molecules. This diminution of effective spin-rotation coupling has been noted previously, in the context of atom-molecule scattering [34], and is an important implement in the experimental toolbox for controlling inelastic scattering.

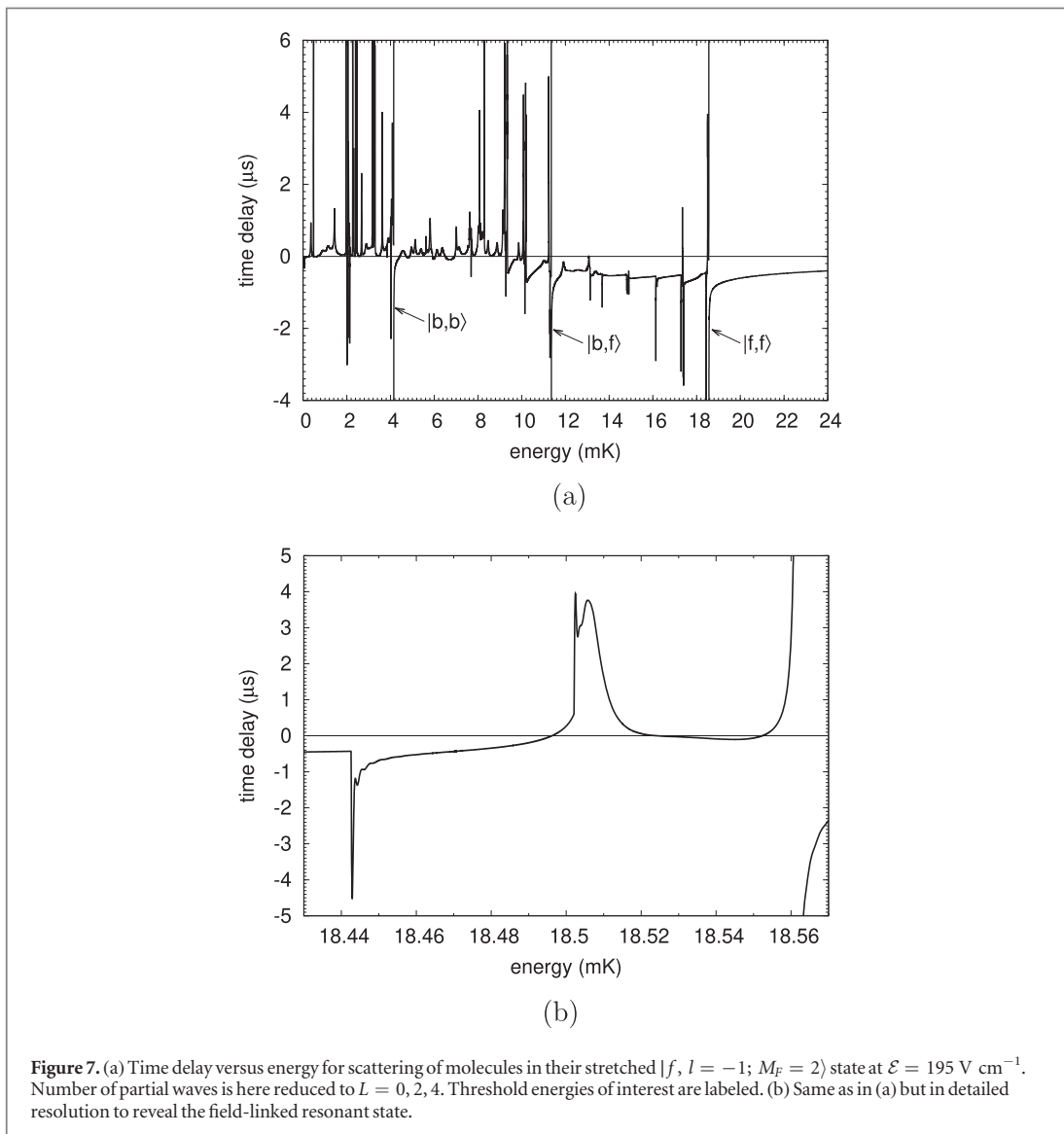
Because of this suppression, it appears that optically trapped CaOH in the $|b, +1; 1, 1/2\rangle$ fine structure manifold might be a suitable candidate for evaporation. This optimistic message is supported by figure 4, demonstrating elastic σ_{el} versus inelastic σ_{inel} cross sections as functions of collision energy when the electric field is fixed at 6000 V cm^{-1} . Over the whole energy range, 10 mK down to 10 nK, the ratio $\sigma_{\text{el}}/\sigma_{\text{inel}}$ exceeds 100, even reaching as high as 1000. This ratio becomes smaller towards lower energies because of the Wigner threshold laws that declares σ_{el} approaches a constant, while $\sigma_{\text{inel}} \propto E_c^{-1/2}$ for exothermic collisions.

4.2. Field-linked states on collisions of f -state molecules

Collisions in the weak-field-seeking f states are subject to rapid inelastic decay into lower energy states, such as c and d states. Still, these collisions are interesting for their variation with electric field, seen as a set of broad peaks in figure 5. It is shown there that elastic rate coefficients for the $|f\rangle$ states at $E_c = 1 \text{ mK}$ are larger than inelastic rate coefficients but not by much, certainly not enough for evaporative cooling to occur. For the lower collision



energy $E_c = 1 \mu\text{K}$ the inelastic scattering rates increase rapidly at low electric field then level off at about 100 V cm^{-1} . This behavior attests to the induction of dipole moments by the field, which then increase the ability of the molecules to exert torques on one another and change their internal state.



In addition, the collision rates exhibit modulations as the field is turned on, which are more pronounced at the lower energy. These modulations correspond to a set of ‘field-linked’ resonant states, anticipated in scattering of dipolar $^2\Pi$ molecules [16]. They correspond to long-range, quasi-bound states of the two molecules. The resulting $(\text{CaOH})_2$ dimer is held by a delicate balance between the attractive and repulsive aspects of the dipole–dipole interaction, and exists only in the presence of an electric field that activates these dipoles; hence the name field-linked. Details on the structure of these dimers are described in [17].

These resonant states represent an oasis of relative simplicity amid the chaos of ultracold molecule interactions. Figure 6(a) shows a partial set of the adiabatic curves at an electric field $\mathcal{E} = 195 \text{ V cm}^{-1}$, above the fields where the main oscillations of the rate coefficients occur (figure 5). For clarity, only those channels dominated by the partial waves $L = 0, 2, 4$ are shown. A great deal of fine- and hyperfine structure appears, along with many multiple crossings. However, in the vicinity of the very highest threshold, correlating to pairs of molecules in the $|f, -1; 1, 1/2\rangle$ state, one sees a potential energy curve with a minimum at around $340 a_0$ and an inner turning point near $280 a_0$ (figure 6(b)). This potential cradles the field linked states, which are relatively isolated from the rest of the spectrum.

Field-linked $(\text{CaOH})_2$ dimers could presumably be produced, by ramping the electric field from low to high values across the resonance, adiabatically converting molecules to dimers in the same way that alkali atoms are converted to Feshbach molecules upon sweeping a magnetic field. The dimers could then serve as a platform for further manipulation of molecular interactions, for example, selective laser excitation that could probe the reaction barrier, or else Raman processes that could create selected states of the dimer. A key feature of the field-linked dimer is that its lifetime is short, since the polarized molecules continue to exert torques on one another.

To determine this lifetime, we compute the Wigner-Smith time delay [35]. We begin by computing the energy-dependent eigenvalues $K_i(E)$ of the scattering K -matrix to obtain the eigenphase shifts $\delta_i(E) = \tan^{-1} K_i(E)$. The eigenphase sum,

$$\delta(E) = \sum_i \delta_i(E) \quad (33)$$

is a quantity that rises by $\sim\pi$ as the energy crosses a resonance. The sharper this rise, the narrower the resonance, and the longer the lifetime. Formally, the time delay is given by

$$\tau = 2\hbar \frac{d\delta}{dE}. \quad (34)$$

The time delay peaks at resonant energies, and its value at the peak is associated with the lifetime of the resonance.

Figure 7(a) presents τ at $\mathcal{E} = 195 \text{ V cm}^{-1}$ over an energy range up to 24 mK. For reference, three fine-structure thresholds are shown. At low energies, many resonances are seen. These are primarily Fano-Feshbach resonances with the many hyperfine states. The resonant wave functions in this energy range penetrate to small R , given the many attractive adiabatic curves in this range (figure 6(a)), and are therefore poorly characterized by the model. For energies larger than about 10 mK, time delay is generally negative because the particle spends less time in the short range as it is reflected from the repulsive potential energy curves shown in figure 6(a).

At the energy ~ 18.506 mK, just below the $|f, -1; 1, 1/2\rangle|f, -1; 1, 1/2\rangle$ threshold of interest, the time delay exhibits a striking resonance peak isolated from other resonances. This is the signature of the field-linked state, and its peak time delay is $\sim 4 \mu\text{s}$. We conclude that, upon formation, the $(\text{CaOH})_2$ field-linked dimer would live for several microseconds, giving the experimenter time to further manipulate the molecules.

5. Conclusions

Various aspects of the long-range physics between dipolar molecules, predicted but never observed for dimers like OH, are shown to occur also in the $(0, 1^1, 0) N = 1$ states of CaOH. The big difference is that previously considered molecules have been produced by buffer gas cooling, Stark deceleration, or other methods that limited their ultimate temperature to the 10–100 mK regime. By contrast, the novel ability to laser cool species such as CaOH opens the possibility that these intricate effects can be measured and exploited to further the development of ultracold molecular science.

We have focused on two of the main features of these ultracold collisions. On the one hand, by choosing spin-stretched b state molecules, the elusive goals of evaporative cooling and even dipolar molecular quantum degenerate gases may be achieved. In addition, by choosing f state molecules, novel field-linked dimers become possible, opening new implications for studying and manipulating the molecules.

Acknowledgments

This material is based upon work supported by the National Science Foundation under Grant Number PHY 1125844 and Grant Number PHY 1806971. LDA acknowledges the financial support of the Czech Science Foundation (Grant No. 18-00918S).

References

- [1] McCarron D J, Steinecker M H, Zhu Y and DeMille D 2018 *Phys. Rev. Lett.* **121** 013202
- [2] Williams H J, Caldwell L, Fitch N J, Truppe S, Rodewald J, Hinds E A, Sauer B E and Tarbutt M R 2018 *Phys. Rev. Lett.* **120** 163201
- [3] McCarron D J, Steinecker M H, Zhu Y and DeMille D 2018 *Phys. Rev. Lett.* **121** 013202
- [4] Anderegg L, Augenbraun B L, Bao Y, Burchesky S, Cheuk L W, Ketterle W and Doyle J M 2018 *Nat. Phys.* **14** 890–3
- [5] Cheuk L W, Anderegg L, Augenbraun B L, Bao Y, Burchesky S, Ketterle W and Doyle J M 2018 *Phys. Rev. Lett.* **121** 083201
- [6] Krems R V 2019 *Molecules in Electromagnetic Fields* (Hoboken, NJ: Wiley)
- [7] Isaev T A and Berger R 2016 *Phys. Rev. Lett.* **116** 063006
- [8] Isaev T A and Berger R 2018 *Chimia* **72** 375–8
- [9] Kozyryev I, Baum L, Matsuda K and Doyle J M 2016 *Chem. Phys. Chem.* **17** 3641–8
- [10] Kozyryev I, Baum L, Matsuda K, Augenbraun B L, Anderegg L, Sedlack A P and Doyle J M 2017 *Phys. Rev. Lett.* **118** 173201
- [11] Li M, Klos J, Petrov A and Kotochigova S 2019 Emulating optical cycling centers in polyatomic molecules arXiv:1904.11579
- [12] Kozyryev I, Baum L, Aldridge L, Yu P, Eyler E E and Doyle J M 2018 *Phys. Rev. Lett.* **120** 063205
- [13] Kozyryev I, Steimle T C, Yu P, Nguyen D T and Doyle J M 2019 *New J. Phys.* **21** 052002
- [14] Kozyryev I, Baum L, Matsuda K, Olson P, Hemmerling B and Doyle J M 2015 *New J. Phys.* **17** 045003
- [15] Morita M, Klos J, Buchachenko A A and Tscherbil T V 2017 *Phys. Rev. A* **95** 063421
- [16] Avdeenkov A V and Bohn J L 2003 *Phys. Rev. Lett.* **90** 043006
- [17] Avdeenkov A V, Bortolotti D C E and Bohn J L 2004 *Phys. Rev. A* **69** 012710

- [18] Townes C and Schawlow A 1975 *Microwave Spectroscopy Dover Books on Physics* vol 2 (New York: Dover) ch 2
- [19] Fletcher D A, Anderson M A, Barclay W L and Ziurys L M 1995 *J. Chem. Phys.* **102** 4334–9
- [20] Kopp I and Hougen J T 1967 *Can. J. Phys.* **45** 2581–96
- [21] Scurlock C, Fletcher D and Steimle T 1993 *J. Mol. Spectrosc.* **159** 350–6
- [22] Brink D and Satchler G 1993 *Angular Momentum Oxford Science Publications* (Oxford: Clarendon)
- [23] Ticknor C and Bohn J L 2005 *Phys. Rev. A* **71** 022709
- [24] Steimle T C, Fletcher D A, Jung K Y and Scurlock C T 1992 *J. Chem. Phys.* **96** 2556–64
- [25] Quéméner G and Bohn J L 2016 *Phys. Rev. A* **93** 012704
- [26] Karman T and Hutson J M 2018 *Phys. Rev. Lett.* **121** 163401
- [27] Lassablière L and Quéméner G 2018 *Phys. Rev. Lett.* **121** 163402
- [28] Augustovičová L D and Bohn J L 2018 *Phys. Rev. A* **97** 062703
- [29] Johnson B R 1973 *J. Comput. Phys.* **13** 445–9
- [30] Avdeenkov A V, Kajita M and Bohn J L 2006 *Phys. Rev. A* **73** 022707
- [31] Wang G and Quéméner G 2015 *New J. Phys.* **17** 035015
- [32] González-Martínez M L, Bohn J L and Quéméner G 2017 *Phys. Rev. A* **96** 032718
- [33] Augustovičová L D and Bohn J L 2017 *Phys. Rev. A* **96** 042712
- [34] Tscherbil T V and Krems R V 2006 *J. Chem. Phys.* **125** 194311
- [35] Smith F T 1960 *Phys. Rev.* **118** 349–56

ZEEMAN MOLECULAR PROBE FOR TESTS OF
FUNDAMENTAL PHYSICAL CONSTANTS

Bibliographic record of the attached publication:

Augustovičová, L. D. and V. Špirko (2020). “Zeeman molecular probe for tests of fundamental physical constants.” In: *Monthly Notices of the Royal Astronomical Society* 494.2, pp. 1675–1680.
DOI: [10.1093/mnras/staa792](https://doi.org/10.1093/mnras/staa792).

Zeeman molecular probe for tests of fundamental physical constants

Lucie D. Augustovičová¹★ and Vladimír Špirko^{1,2}★

¹Faculty of Mathematics and Physics, Department of Chemical Physics and Optics, Charles University, Ke Karlovu 3, CZ-12116 Prague 2, Czech Republic

²Institute of Organic Chemistry and Biochemistry, Academy of Sciences of the Czech Republic, Flemingovo nám. 2, CZ-16610 Prague 6, Czech Republic

Accepted 2020 March 17. Received 2020 March 16; in original form 2020 January 4

ABSTRACT

The impact of the Zeeman effect on the Λ -doublet spectra of diatomic radicals is analysed from the point of view of a possible cosmological variation of the proton-to-electron mass ratio, μ . The actual model calculations performed for the $^2\Pi_{3/2}$ and $^2\Pi_{1/2}$ states of ^{16}OH reveal that the Λ -doublet energy levels of diatomic radicals can be tuned to degeneracy by means of the Zeeman effect using realistic magnetic fields. Tuning this degeneracy allows for a dramatic enhancement of the relative mass sensitivity coefficients of the corresponding transitions and for a substantial reduction of their Doppler broadening. Moreover, unlike their field-free counterparts associated with the degeneracies arising due to the $A \sim 4B$ situations (A and B being the spin–orbit and rotation constant, respectively), the electric dipole allowed $e \leftrightarrow f$ Zeeman-tuned transitions exhibit favourable intensities, thus evidencing their promising potential.

Key words: magnetic fields – molecular data – molecular processes.

1 INTRODUCTION

The search for a temporal variation of the fine structure constant (α) and the proton-to-electron mass ratio ($\mu = m_p/m_e$) using atomic and molecular spectroscopy (see e.g. Webb et al. 1999; Jansen, Bethlem & Ubachs 2014) is an important way for a critical probing of physics beyond the Standard Model (Safronova et al. 2018). The search is based on comparing the measured frequencies of different spectral transitions over a certain period of time and the surmise that the temporal shifts of these frequencies may significantly differ. The actual searches rely either on astronomical observations (see e.g. Thompson 1975; Bagdonaite et al. 2013) or laboratory experiments (see e.g. Kobayashi, Ogino & Inouye 2019). Similarly, a possible gravitational variation of α and μ can be probed by comparing the laboratory spectra with their astronomical counterparts observed towards white dwarf stars that undergo a gravitational collapse (Berengut et al. 2013; Bagdonaite et al. 2014). The white dwarf stars provide a unique environment in which to search not only for possible gravitational variations in fundamental physics, but also the environment exhibiting the second strongest magnetic field in the Universe. The white dwarfs may thus provide another tool for probing the fundamental constants. Since there is no rotating object in the Universe that is devoid of a magnetic field, and the ratio of the electromagnetic force to the gravitational force is 39 orders of magnitude, the magnetic effects have potentially observable effects on all astronomical spectra of all the objects in the Universe. The

strengths of the magnetic fields of these objects vary over a very wide range of values, and are found to lie typically in the range of 1–1 000 μG (Crutcher et al. 2010) for interstellar molecular clouds, 1–40 mG (Slysh & Migenes 2006) for star-forming regions embedded in dense molecular clouds, 0–5 G (Schubert & Soderlund 2011) for solar planets, 2–350 G (Long et al. 2013; Kuridze et al. 2019) for solar outer atmospheres (such as flares, eruptions, and coronal loops), 0.1–1 kG (Machida, Inutsuka & Matsumoto 2007) for protostars at their formation epoch, 1–7 kG (van Noort et al. 2013; Afram & Berdyugina 2015; Kao et al. 2018) for starspots and brown dwarfs, 10^3 – 10^9 G (Ferrario, de Martino & Gänsicke 2015) for white dwarfs, and 10^8 – 10^{15} G (Konar 2017) for neutron stars. [The strongest magnetic field produced so far in laboratory is 1.2 MG (Nakamura et al. 2018)].

The promising potential of the use of the magnetic effects in probing the cosmological variation of the fundamental constants has already been recognized by Chin & Flambaum (2006), who have proposed using the magnetic Feshbach resonances of ultracold molecules to increase the sensitivity of their scattering lengths to the variation of μ . An even higher sensitivity has been predicted for this variation derived from the photoassociation rate of ultracold molecules in the vicinity of the magnetic Feshbach resonances by Gacesa & Côté (2014). The aim of this study is to probe the effects of the magnetic fields on the mass sensitivities of the spectral transitions of the molecular radicals possessing energy level structures exhibiting observable Zeeman splittings. Quite a few of these radicals are fairly abundant in the interstellar medium and circumstellar shells (e.g. OH, CH, CN, SO, SiO, NO, NH, C₂H, C₃H, ...); thanks to near-degeneracies in their energy level patterns, the mass sensitivities of the corresponding transitions may become

* E-mail: augustovicova@karlov.mff.cuni.cz (LDA); vladimir.spirko@marge.uochb.cas.cz (VŠ)

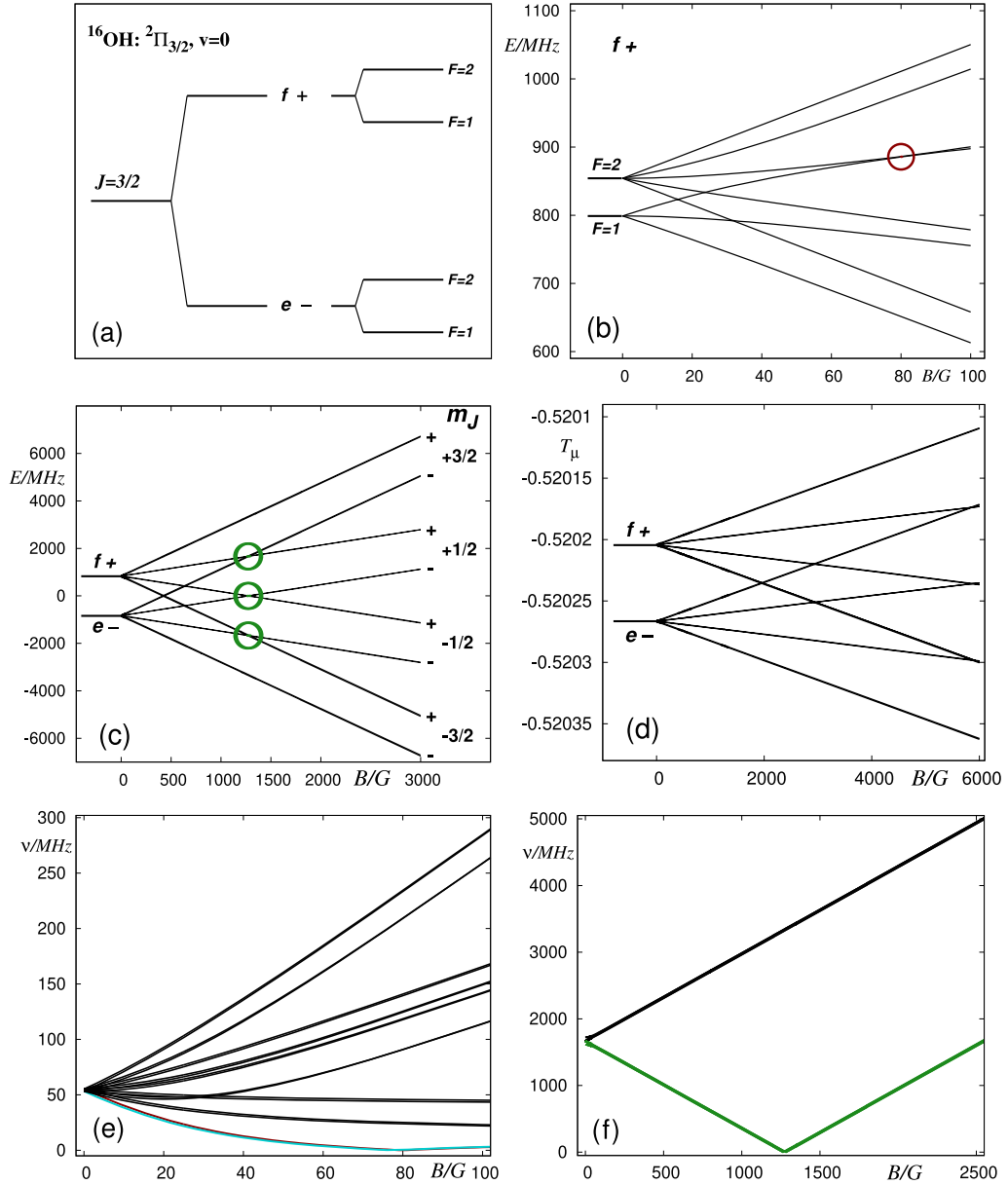


Figure 1. Energy level patterns E [panels (a), (b), and (c)], mass derivatives of energies T_μ [panel (d); $T_\mu = E^{-1}dE/d\mu$] and allowed transition frequencies ν [panels (e) and (f)] of ^{16}OH in its $J=3/2$ rotational state. Coloured circles [panels (b) and (c)] and curves [panels (e) and (f)] label level-crossing states supporting allowed transitions; dark red (dark grey), cyan (light grey), and green (mid grey) pertaining to the ff , ee , and ef transitions, respectively.

strongly enhanced (Kozlov & Levshakov 2013; Jansen et al. 2014); and, very importantly, the structure of their energy level patterns makes it possible to tune their states to a needed degeneracy by using an appropriate magnetic field (Cahn et al. 2014).

The actual probing is accomplished by performing model calculations for the Λ -doublet transitions of the $X^2\Pi$ ground state of ^{16}OH within the framework of the effective Hamiltonian of Brown and coworkers (Brown et al. 1978) (for details see Supplementary Material). Using these transitions are advantageous because: they have already been used to probe the cosmological variability of α and μ with a fairly competitive accuracy (Kanekar, Ghosh & Chengalur 2018); the Zeeman splitting of the OH megamaser

emissions allows for reliable determination of magnetic field strengths even in truly hostile objects of the Universe (Slysh & Miggenes 2006); the laboratory data needed for comparisons with their astronomical counterparts and for a reliable evaluation of the mass sensitivity coefficients are known fairly accurately (Maeda, Wall & Carr 2015); and, the nature of the obtained results allows for quite general conclusions.

The Standard Model of electroweak and strong interactions implies that a variation of α should be accompanied by a much larger change in μ (Calmet & Fritzsche 2002), showing thus μ as a much more sensitive probe. Therefore, this study is limited only to this quantity.

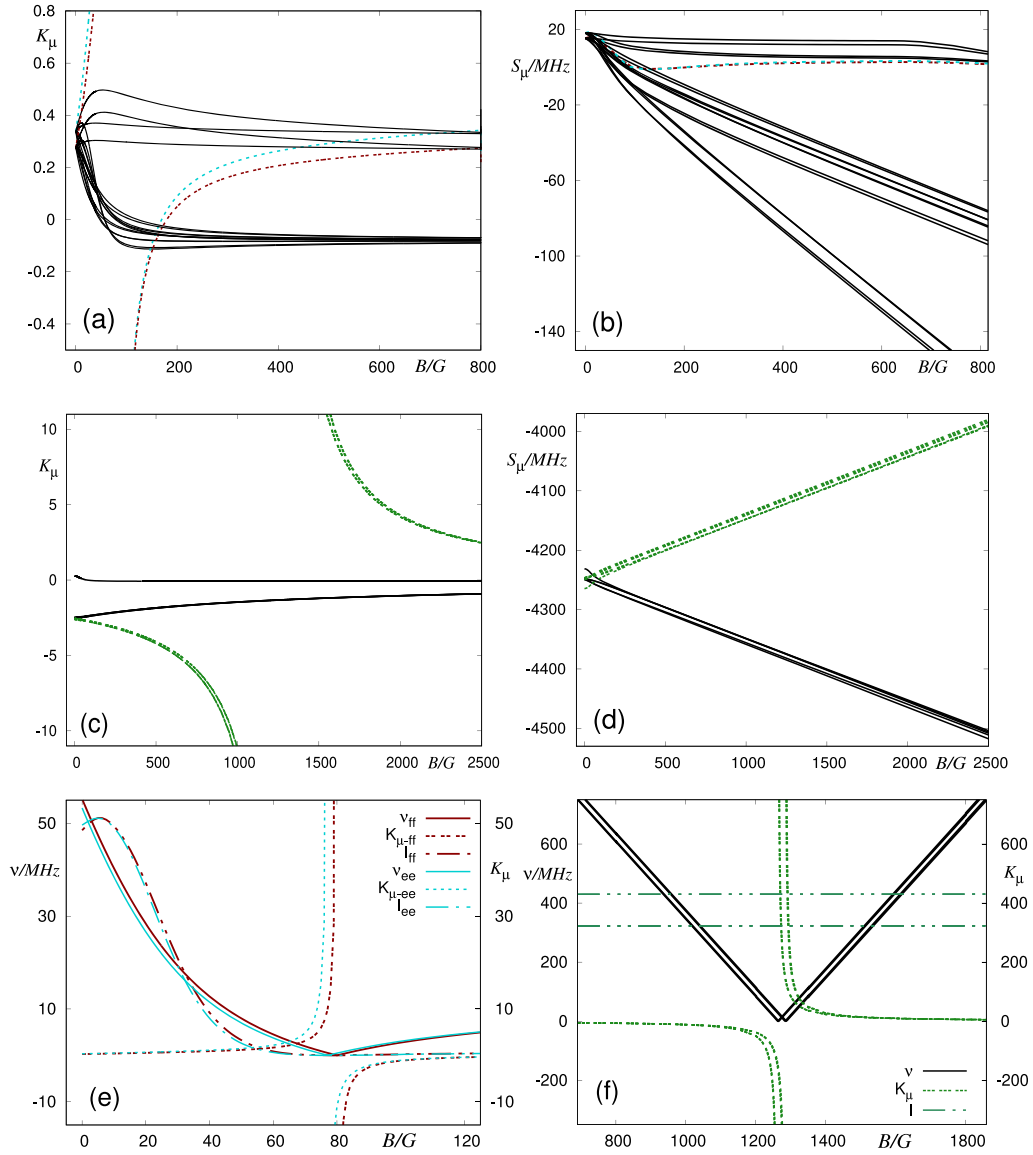


Figure 2. Mass sensitivities K_μ and S_μ , transition frequencies ν , and relative intensities I (in arbitrary units) of ^{16}OH in its $J=3/2$ rotational state for selected allowed transitions as in Figs 1(e) and (f). Coloured and multiple dotted curves label characteristics pertaining to the level-crossing states.

2 METHODS

To rationalize the frequency shift ($\Delta\nu$) of a spectroscopic transition due to a temporal variation ($\Delta\mu$), it is usual to rely on a linear proportionality (Jansen et al. 2014)

$$K_{u,l} = \frac{\mu}{E_u - E_l} \left(\frac{dE_u}{d\mu} - \frac{dE_l}{d\mu} \right), \quad (1)$$

where E_u and E_l are the energy of the appropriate upper and lower states, respectively; the so-called sensitivity coefficient K_μ quantifies the effect that a possible variation of μ would have for this transition is related to the frequency shift through the expression

$$\Delta\nu = \nu K_\mu \frac{\Delta\mu}{\mu} = (E_u - E_l) K_\mu \frac{\Delta\mu}{\mu} = S_\mu \frac{\Delta\mu}{\mu}, \quad (2)$$

where $\Delta\nu = \nu_{\text{obs}} - \nu_0$ is the change in the frequency and $\Delta\mu = \mu_{\text{obs}} - \mu_0$ is the change in μ , both with respect to their present day values ν_0 and μ_0 .

Apparently, the mass sensitivity coefficient K_μ is inversely proportional to the transition frequency ν , becoming thus strongly enhanced if there is an accidental degeneracy of the corresponding levels u and l . Therefore, tuning this energy level degeneracy can allow for a fairly dramatic tuning of K_μ . One way of achieving desirable degeneracy tunings can be based on the Zeeman-tuned level-crossing spectroscopy (Cahn et al. 2014). Importantly, a suitable magnetic field not only enhances the sensitivity coefficient K_μ of a ‘near-degeneracy’ transition, but also strongly reduces its Doppler broadening, which usually hampers the astrophysical observations. Nevertheless, as K_μ determines only the relative frequency change, its actual value may not be fully decisive for the laboratory Doppler-free spectroscopy tests, which rely on the absolute accuracy of the

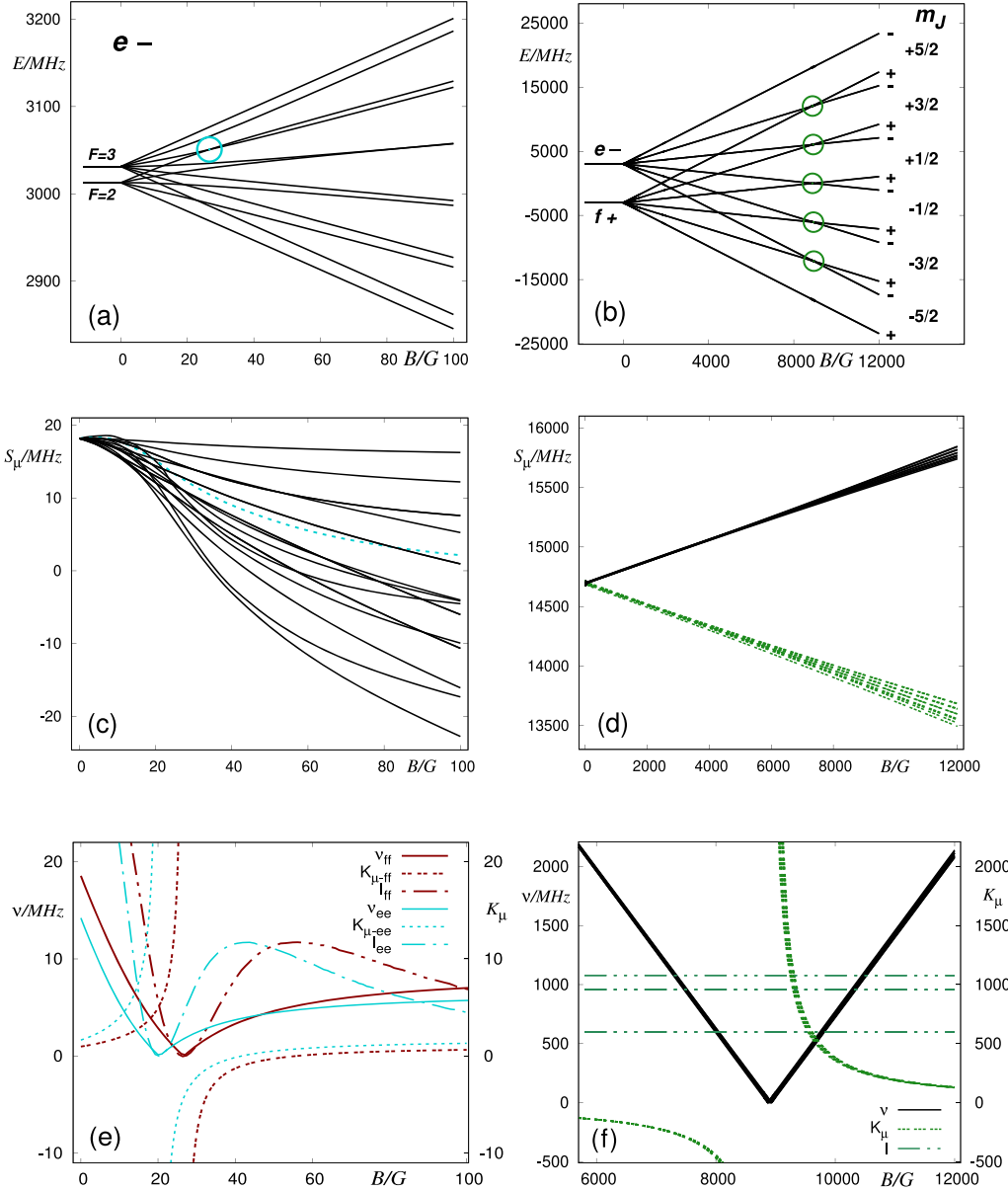


Figure 3. Energy level patterns E [panels (a) and (b)], mass sensitivities K_μ [panels (e) and (f)], and S_μ [panels (c) and (d)], allowed transition frequencies ν and relative intensities I [panels (e) and (f)] of ^{16}OH in its $J=5/2$ rotational state. Coloured circles [in panels (a) and (b)] label level-crossing states supporting allowed transitions with their mass characteristics [displayed as coloured and multiple dotted curves in panels (c), (d), (e), and (f)].

frequency measurements. In such a case, apparently, the factor S_μ becomes more relevant (Kozlov & Budker 2019).

3 RESULTS AND DISCUSSION

The electronic ground state of the OH radical has a $X^2\Pi$ configuration. Each rotational level, labelled by J , consists of a Λ doublet with components possessing + and - parities (labelled by the usual spectroscopic labels f and e , respectively) and each of these components splits into hyperfine multiplets (labelled by F). In the presence of a magnetic field, the hyperfine states are split into $4(2J+1)$ of the corresponding Zeeman sublevels (labelled by m_F), with the exception $2(2J+1)$ for $J=1/2$.

In the $J=3/2$ rotational ground state of ^{16}OH , each of the Λ -doublet states splits into a hyperfine triplet ($F=1$) and a hyperfine quintet ($F=2$) [Fig. 1(a)]. In the presence of a magnetic field, the $F=2$ and $F=1$ states split into 5 and 3 Zeeman sublevels [Fig. 1(b)]. The $F=2$ levels are higher than the $F=1$ levels by 53 and 55 MHz for the e and f states, respectively. Thus, as the dominant part of the Zeeman effect is the same for both parities, the corresponding e and f Zeeman level patterns topologically almost coincide [Fig. 1(c)]. Similarly [see Fig. 1(d)], the e and f states exhibit nearly coinciding magnetic dependences of their ‘reduced’ mass sensitivities $T_\mu = E^{-1}dE/d\mu$ (note that these dependences are much weaker than their ‘energy’ counterparts). Consequently, both the magnetic dipole allowed (low-frequency) transitions $|e, -, F$

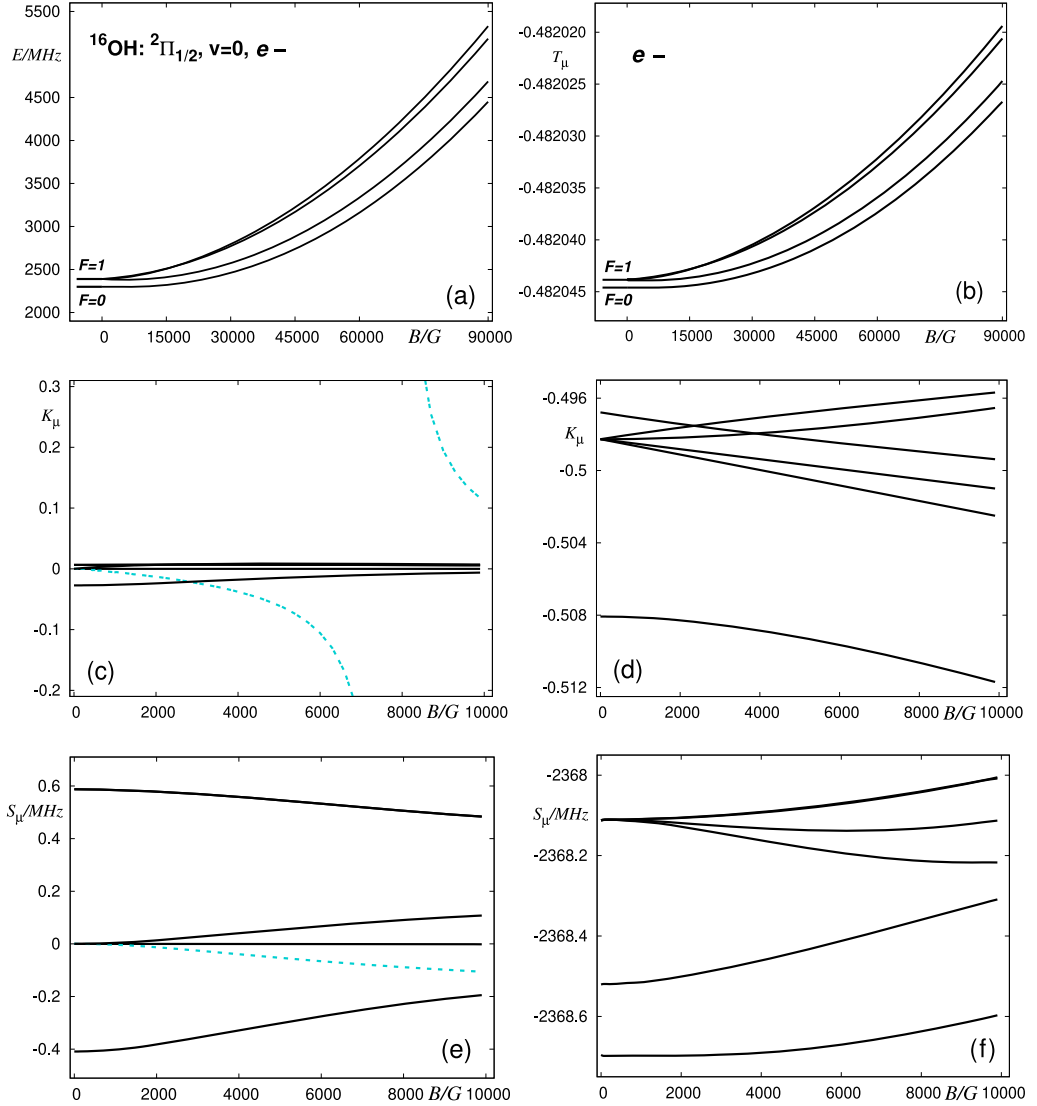


Figure 4. Energy level patterns E , mass derivatives of energies T_μ ($T_\mu = E^{-1}dE/d\mu$), mass sensitivities K_μ and S_μ , transition frequencies ν , and relative intensities I of ^{16}OH in its $J=1/2$ rotational state. Coloured and dotted curves label level-crossing states supporting ee allowed transition.

$= 2, m_F) \leftrightarrow |e, -, F=1, m_F\rangle$ and $|f, +, F=2, m_F) \leftrightarrow |f, +, F=1, m_F\rangle$ [Fig. 1(e)] and their mass sensitivity coefficients K_μ and S_μ [see Figs 2(a) and (c)] and both the electric dipole allowed (high-frequency) transitions $|f, +, m_J) \leftrightarrow |e, -, m_J - 1\rangle$, and $|e, -, m_J) \leftrightarrow |f, +, m_J - 1\rangle$ [Fig. 1(f)], and their mass sensitivity coefficients [Figs 2(b) and 2(d)] exhibit closely coinciding magnetic dependences.

As it is seen in Figs 2(a) and (b), the transitions supported by the crossing states acquire strongly enhanced mass sensitivity coefficients K_μ , appearing thus as promising tools for probing the temporal variability of μ . However, just as in the case of the transitions connecting the ‘field-free’ $F_1(J)$ and $F_2(J)$ levels of the $^2\Pi$ states possessing $A \sim 4B$ (de Nijs, Ubachs & Bethlem (2012); A and B being the spin-orbit and rotational constant, respectively), the enhancements of K_μ are associated with suppressing the $e \leftrightarrow e$ and $f \leftrightarrow f$ transition strengths [Fig. 2(e)]. Moreover, the ‘absolute’ sensitivity factor S_μ of these transitions exhibit rather constant dependence on the imposed magnetic field [Fig. 2(c), coloured curves].

On the other hand, importantly, the strengths of the $e \leftrightarrow f$ and $f \leftrightarrow e$ transitions are found to be practically field-independent, evidencing thus promising potential of these transitions for astronomical studies [Fig. 2(f)].

The results obtained for another $^2\Pi_{3/2}$ low-lying rotational states were found to be qualitatively just very same as the results obtained for the $J=3/2$ state (see Figs 3 and 4). They differ significantly only by the number of the corresponding Zeeman sublevels and thus also by the number of the level-crossings supporting the allowed spectral transitions. Note also that the magnetic dependence of the $^2\Pi_{1/2}$ state is rather negligible as its orbital and spin contributions to the molecular magnetic moment nearly cancel.

4 SUMMARY

The Zeeman energy and mass sensitivity patterns of the rotational states of the OH radical in its $^2\Pi$ ground electronic state are composed of two very similar parts pertaining to the opposite

+ and – parities of these states (Λ -doublets). The shapes of the corresponding Zeeman spectra and the mass dependences of the transitions forming these spectra also exhibit very similar dependences on the imposed magnetic field. Rather non-linear dependences for the fields that are too weak to compete with the hyperfine interactions, on the one side, and, a fairly linear dependences for the fields dominating the hyperfine interactions, on the other hand. Importantly, the magnetic field is a function that is even under spatial inversion and cannot thus mix parity states. So, as the slopes of the individual magnetic dependences may acquire positive and negative values, the Zeeman energy levels may undergo level crossings. The reducing of the transition frequencies associated with these crossovers not only strongly enhances the mass sensitivity coefficients K_μ of these transitions, but also strongly reduces their Doppler broadenings. Unfortunately, the reducing of the frequencies is also associated with a strong intensity suppressing of the corresponding ee and ff magnetic dipole allowed transitions, thus limiting their use probably only to laboratory radio-frequency microwave double resonance analyses (see e.g. Destombes & Marlière 1975). Moreover, the ‘absolute’ sensitivities S_μ of the Λ -doublet transitions can hardly acquire magnitudes that would allow for competing with the laboratory atomic clock studies. On the other hand, the intensities of the ef ‘electric’ transitions depend on the imposed field only very weakly. The ef transitions are also much stronger than their ‘magnetic’ counterparts and appear thus as very promising astronomical probes of the proton-to-electron mass ratio μ cosmological variability. Also importantly, as the magnetic variations of the sensitivity coefficients S_μ exhibit opposite signs, significantly different magnitudes for different rotational states and fairly different magnitudes for the $^2\Pi_{3/2}$ and $^2\Pi_{1/2}$ states, they could allow for analyses exclusively based on using spectral lines originating from a single species at the same physical location. Apparently, as the real magnetic fields can be expected to be very complicated structures, this is of a crucial importance for any astronomical study.

As especially interesting appears the analysis of spectra of paramagnetic molecules acquired in the presence of extremely strong magnetic fields. The absolute values of the sensitivity coefficients S_μ of the corresponding transitions grow monotonically with the strength of the field and it is thus not unthinkable that these analyses could improve the present limit on the temporal variation of μ . It should be stressed, however, that the present results were obtained for a homogeneous magnetic field using constant molecular g -factors with a complete neglect of the higher order diamagnetic contributions. The diamagnetic contributions are quadratic in the magnetic field and their role in the case of extremely strong magnetic fields may thus become crucially important. Investigation of the very strong field effects will be the subject of future research.

ACKNOWLEDGEMENTS

This work was supported by the Czech Science Foundation (Grant 18-00918S) and institutional support was provided by Czech Academy of Sciences under Project RVO:61388963 (IOCB).

REFERENCES

- Afram N., Berdyugina S. V., 2015, *A&A*, 576, A34
 Bagdonaite J., Daprà M., Jansen P., Bethlem H. L., Ubachs W., Muller S., Henkel C., Menten K. M., 2013, *Phys. Rev. Lett.*, 111, 231101
 Bagdonaite J., Salumbides E. J., Preval S. P., Barstow M. A., Barrow J. D., Murphy M. T., Ubachs W., 2014, *Phys. Rev. Lett.*, 113, 123002
 Berengut J. C., Flambaum V. V., Ong A., Webb J. K., Barrow J. D., Barstow M. A., Preval S. P., Holberg J. B., 2013, *Phys. Rev. Lett.*, 111, 010801
 Brown J., Kaise M., Kerr C., Milton D., 1978, *Mol. Phys.*, 36, 553
 Cahn S. B. et al., 2014, *Phys. Rev. Lett.*, 112, 163002
 Calmet X., Fritzsche H., 2002, *Phys. Lett.*, 540, 173
 Chin C., Flambaum V. V., 2006, *Phys. Rev. Lett.*, 96, 230801
 Crutcher R. M., Wandelt B., Heiles C., Falgarone E., Troland T. H., 2010, *ApJ*, 725, 466
 de Nijs A. J., Ubachs W., Bethlem H. L., 2012, *Phys. Rev. A*, 86, 032501
 Destombes J., Marlière C., 1975, *Chem. Phys. Lett.*, 34, 532
 Ferrario L., de Martino D., Gänsicke B. T., 2015, *Space Sci. Rev.*, 191, 111
 Gacesa M., Côté R., 2014, *J. Mol. Spectrosc.*, 300, 124
 Jansen P., Bethlem H. L., Ubachs W., 2014, *J. Chem. Phys.*, 140, 010901
 Kanekar N., Ghosh T., Chengalur J. N., 2018, *Phys. Rev. Lett.*, 120, 061302
 Kao M. M., Hallinan G., Pineda J. S., Stevenson D., Burgasser A., 2018, *ApJS*, 237, 25
 Kobayashi J., Ogino A., Inouye S., 2019, *Nat. Commun.*, 10, 3771
 Konar S., 2017, *J. Astrophys. Astron.*, 38, 47
 Kozlov M. G., Budker D., 2019, *Ann. Phys.*, 531, 1800254
 Kozlov M. G., Levshakov S. A., 2013, *Ann. Phys.*, 525, 452
 Kuridze D. et al., 2019, *ApJ*, 874, 126
 Long D. M., Williams D. R., Régnier S., Harra L. K., 2013, *Sol. Phys.*, 288, 567
 Machida M. N., Inutsuka S., Matsumoto T., 2007, *ApJ*, 670, 1198
 Maeda K., Wall M. L., Carr L. D., 2015, *New J. Phys.*, 17, 045014
 Nakamura D., Ikeda A., Sawabe H., Matsuda Y. H., Takeyama S., 2018, *Rev. Sci. Instrum.*, 89, 095106
 Safronova M. S., Budker D., DeMille D., Kimball D. F. J., Derevianko A., Clark C. W., 2018, *Rev. Mod. Phys.*, 90, 025008
 Schubert G., Soderlund K., 2011, *Phys. Earth Planet. Inter.*, 187, 92
 Slysh V. I., Migens V., 2006, *MNRAS*, 369, 1497
 Thompson R. I., 1975, *Astrophys. Lett.*, 16, 3
 van Noort M., Lagg A., Tiwari S. K., Solanki S. K., 2013, *A&A*, 557, A24
 Webb J. K., Flambaum V. V., Churchill C. W., Drinkwater M. J., Barrow J. D., 1999, *Phys. Rev. Lett.*, 82, 884

SUPPORTING INFORMATION

Supplementary data are available at *MNRAS* online.

Table S1. Vibrational energies of ^{16}OH (in cm^{-1}).

Table S2. Zero-field fine-structure $X_{v,v'} = \langle v(r)|X(r)|v'(r)\rangle$ matrix elements for ^{16}OH (in cm^{-1}).

Table S3. Zero-field hyperfine-structure $x_{v,v'} = \langle v(r)|x(r)|v'(r)\rangle$ matrix elements for ^{16}OH (in MHz).

Please note: Oxford University Press is not responsible for the content or functionality of any supporting materials supplied by the authors. Any queries (other than missing material) should be directed to the corresponding author for the article.

This paper has been typeset from a $\text{\TeX}/\text{\LaTeX}$ file prepared by the author.